Materials Under Extreme Conditions Series

Journal of Innovative Materials in Extreme Conditions

Volume 4

Technicum Scientific Publishing
Stuttgart, 2024

Bibliografische Information Der Deutschen Bibliothek

Die Deutsche Bibliothek verzeichnet diese Publikation in der Deutschen Nationalbibliografie; detaillierte bibliografische Daten sind im Internet über http://dnb.ddb.de abrufbar.

Bibliographic information published by Die Deutsche Bibliothek

Die Deutsche Bibliothek lists this publication in the Deutsche Nationalbibliografie; detailed bibliographic data are available on the Internet at http://dnb.ddb.de.

Editors:
Dr. rer. nat. Branko Matović
Dr. Vesna Maksimović
Dr. Ivana Cvijović-Alagić
Dr. rer. nat. Dejan Zagorac
Dr. Jelena Zagorac

Verlag / Publisher:
Technicum Scientific Publishing
Dachswaldweg 99, 70569 Stuttgart, Germany
Phone: +49 (0)177 241 4257
E-mail: contact@opentechnicum.com
Web: www.opentechnicum.com

ISBN: 978-3-9817635-5-3

Coverbild / Cover image: www.pixabay.com

Copyright © 2024 Technicum Scientific Publishing
Alle Rechte vorbehalten. / All rights reserved.
Stuttgart 2024

Journal of Innovative Materials in Extreme Conditions

Volume 4, Issue 1, Year 2023

Published by:

SIM-EXTREME

Serbian Society for Innovative Materials in Extreme Conditions

Journal name

Journal of Innovative Materials in Extreme Conditions (*abbr*. JIMEC)

Publisher

Serbian Society for Innovative Materials in Extreme Conditions (SIM-EXTREME), Belgrade, Serbia.

Bibliographic Information

ISSN (Online) 2738-0882

Review Type

Single Blind Peer Review Process

No publication fees

Publication in the Journal is free for all authors and there are **no article processing charges.**

Open access statement

This is an open access journal which means that **all content is freely available without charge** to the user or his/her institution. Users are allowed to read, download, copy, distribute, print, search, or link to the full texts of the articles in this journal without asking prior permission from the publisher or the author. This is in accordance with the BOAI definition of open access.

All papers published in Journal of Innovative Materials in Extreme Conditions are licensed under a
Creative Commons Attribution-NonCommercial-NoDerivatives 4.0 International License.

Editorial Board

Editor-in-chief

Dr. rer. nat. Branko Matović
Center of Excellence "CEXTREME LAB", Institute of Nuclear Sciences "Vinča", University of Belgrade, Serbia
e-mail: mato@vinca.rs

Editors

Dr. Vesna Maksimović
Center of Excellence "CEXTREME LAB", Institute of Nuclear Sciences "Vinča", University of Belgrade, Serbia
e-mail: maksimovic-editor@jimec.edu.rs

Dr. Ivana Cvijović-Alagić
Center of Excellence "CEXTREME LAB", Institute of Nuclear Sciences "Vinča", University of Belgrade, Serbia
e-mail: cvijovic-alagic-editor@jimec.edu.rs

Dr. rer. nat. Dejan Zagorac
Center of Excellence "CEXTREME LAB", Institute of Nuclear Sciences "Vinča", University of Belgrade, Serbia
e-mail: zagorac-editor@jimec.edu.rs

Journal Manager

Dr. Jelena Zagorac
Center of Excellence "CEXTREME LAB", Institute of Nuclear Sciences "Vinča", University of Belgrade, Serbia
e-mail: manager@jimec.edu.rs

Editorial Board

Prof. Dr. Rer. Nat. N.V. Ravi Kumar
Indian Institute of Technology Madras, India

Dr. Tetiana Prikhna
V. Bakul Institute for Superhard Materials, National Academy of Sciences of Ukraine, Ukraine

Dr. Enikő Volceanov
Metallurgical Research Institute, Politehnica University of Bucharest, Romania

Dr Peter Tatarko
Institute of Inorganic Chemistry, Slovak Academy of Sciences, Slovak Republic

Dr. Miladin Radović
Department of Materials Science and Engineering, Texas A&M University, USA

Assoc. Prof. Dr. Claus Rebholz
Department of Mechanical and Manufacturing Engineering, University of Cyprus, Cyprus

Dr. rer. nat. Günter Motz
Ceramic Materials Engineering, University of Bayreuth, Germany

Dr. Vladimir Urbanovich, *Centre of Science and Practice of Materials, National Academy of Sciences of Belarus, Belarus*

Prof. Dr. Boštjan Markoli
Department of Materials and Metallurgy, Faculty of Natural Sciences and Engineering, University of Ljubljana, Slovenia

Prof. Dr. Miloš Đukić
Faculty of Mechanical Engineering, University of Belgrade, Serbia

Dr. Jelena Stašić
Center of Excellence "CEXTREME LAB", Institute of Nuclear Sciences "Vinča", University of Belgrade, Serbia

Prof. Dr. K.C. Hari Kumar
Indian Institute of Technology Madras, India

Prof. Dr. Branislav Jelenković
corresponding member of the Serbian Academy of Science and Art (SASA), Center of Excellence "Photonic Center", Institute of Phyiscs, University of Belgrade, Serbia

Prof. Dr. Zoran Popović
full member of the Serbian Academy of Science and Art (SASA), Institute of Physics, University of Belgrade, Serbia

Prof. Dr. Dasari L. V. K. Prasad
Department of Chemistry, IIT Kanpur, India

Prof. Vladimir Ivanov
corresponding member of the Russian Academy of Sciences (RAS), Kurnakov Institute of General and Inorganic Chemistry, Russian Federation

Prof. Katsumi Yoshida
Institute of Innovative Research, Tokyo Institute of Technology, Japan

Prof. Pei-zhong Feng
School of Materials Science and Engineering, China University of Mining and Technology, PR China

Prof. Michele Calì
Electric, Electronics and Computer Engineering Department, University of Catania, Italia

Prof. Sanjay Mathur
Department of Inorganic and Materials Chemistry, University of Cologne, Germany

Prof. Pavol Šajgalìk
Institute of Inorganic Chemistry, Slovak Academy of Sciences, Slovak Republic

Prof. Dr. Shuiquan Deng
Fujian Institute of Research on the Structure of Matter, Chinese Academy of Sciences, China

Journal of Innovative Materials in Extreme Conditions (*abbr*. JIMEC)

Volume 4, Issue 1, Year 2023

Volume 4, year 2023

JIMEC: Table of Contents

Volume 4, Issue 1, Year 2023

Cover Picture

Macro-images of the surface of the ZrB_2-25vol.%SiC materials with different types and content of the additives after the oxyacetylene ablation test at ~ 2670 °C for 60 s. All of the samples had a diameter of 20 mm. Published in: Hakan Ünsal, Zuzana Fürdősová, Zdeněk Chlup, Monika Tatarková, Alexandra Kovalčíková, Michal Hičák, Naser Hosseini, Inga Zhukova, Ivo Dlouhý, Pavol Šajgalík, Peter Tatarko, ZrB_2-SiC COMPOSITES WITH RARE-EARTH OXIDE ADDITIVES, *Journal of Innovative Materials in Extreme Conditions*, **Vol. 4**, Issue 1, pages 22-29 (2023).

-Issue 1

1. **EFFECTS OF LASER RADIATION AT 10^{13} W/cm^2 INTENSITY ON FERRITIC ODS STEEL WITH AND WITHOUT Hf IN HELIUM AND VACUUM**
   Milan Trtica, Jelena Stasic, Xizhang Chen, Jiri Limpouch, Andrijana Zekic, *Journal of Innovative Materials in Extreme Conditions*, **Vol. 4**, Issue 1, page 1-9 (2023).
   (PDF Free Download)

2. **THE ORIGIN OF ^{99}Tc IN THE ENVIRONMENT AND ITS REMOVAL**
   Đorđe Petrović, Ljiljana Matović, Marija Egerić, Mia Omerašević, Radojka Vujasin, Snežana Ilić-Stojanović, Sanja Krstić, *Journal of Innovative Materials in Extreme Conditions*, **Vol. 4**, Issue 1, page 10-21 (2023).
   (PDF Free Download)

3. **ZrB_2-SiC COMPOSITES WITH RARE-EARTH OXIDE ADDITIVES**
   Hakan Ünsal, Zuzana Fürdősová, Zdeněk Chlup, Monika Tatarková, Alexandra Kovalčíková, Michal Hičák, Naser Hosseini, Inga Zhukova, Ivo Dlouhý, Pavol Šajgalík, Peter Tatarko, *Journal of Innovative Materials in Extreme Conditions*, **Vol. 4**, Issue 1, page 22-29 (2023).
   (PDF Free Download)

4. **DFT STUDY OF CRYSTALLINE TiO_2 PHASE TRANSITIONS APPLICABLE IN EXTREME ENVIRONMENTS**
   Dušica Jovanović, Dejan Zagorac, Aleksandra Zarubica, Matej Fonović, Jelena Zagorac, *Journal of Innovative Materials in Extreme Conditions*, **Vol. 4**, Issue 1, page 30-37(2023).
   (PDF Free Download)

5. **DATA MINING *AB INITIO* STUDY OF GYPSUM AND $CaCO_3$ MODIFICATIONS AT STANDARD AND EXTREME CONDITIONS**
   Tamara Škundrić, Branko Matović, Aleksandra Zarubica, Dorota Chudoba, Dejan Zagorac, *Journal of Innovative Materials in Extreme Conditions*, **Vol. 4**, Issue 1, page 38-51 (2023).
   (PDF Free Download)

Journal of Innovative Materials in Extreme Conditions
2023
Volume 4
Issue 1

EFFECTS OF LASER RADIATION AT 10^{13} W/cm^2 INTENSITY ON FERRITIC ODS STEEL WITH AND WITHOUT Hf IN HELIUM AND VACUUM

Milan Trtica[1,*], Jelena Stasic[1,2,*], Xizhang ChenN[3], Jiri Limpouch[4], Andrijana Zekic[5]

[1] VINCA Institute of Nuclear Sciences - National Institute of the Republic of Serbia, University of Belgrade, P.O. Box 522,11001 Belgrade, Serbia

[2] Center of Excellence "CEXTREME LAB", VINCA Institute of Nuclear Sciences - National Institute of the Republic of Serbia, University of Belgrade, Mike Petrovića Alasa 12-14, 11001 Belgrade, Serbia

[3] School for Mechanical and Electrical Engineering, Wenzhou University,Wenzhou City, PC 325035, PR China

[4] Faculty of Nuclear Sciences and Physical Engineering, Czech Technical University inPrague,CZ-115 19 Prague, Czech Republic

[5] University of Belgrade, Faculty of Physics, Studentski trg 12, 11001 Belgrade, Serbia

Corresponding authors: etrtica@vinca.rs/jelsta@vinca.rs*

Abstract: *Ferritic 16Cr3Al ODS steel, with and without the addition of hafnium, was exposed to high-intensity laser radiation of the order of 10^{13} W/cm^2. Irradiation was conducted in the environments of helium and vacuum and the obtained surface effects were observed in the sense of morphology and chemical changes. This class of steels is being developed primarily for structural applications in nuclear reactors, which is why their behavior under harsh conditions, including high power densities, is of utmost importance. The obtained results show mostly superficial changes even at a high number of pulses, which points toward the successful implementation of these materials in a number of applications involving severe work conditions.*

Keywords: *High laser intensity; ODS steel; surface modification.*

1. Introduction

Various oxide dispersion-strengthened (ODS) alloys are being developed in laboratories worldwide with the aim of withstanding high temperatures while retaining excellent mechanical properties. These materials are comprised of a metal matrix reinforced with nanosized oxide particles, usually rare earth metal oxides (such as Y_2O_3). ODS alloys are generally produced via powder metallurgy technique [1,2], however novel procedures are increasingly studied - selective laser melting [3], cold spray [4], arc plasma sintering [5]. The aim is to obtain uniformly distributed, non-agglomerated oxide particles. ODS steels, particularly, possess high irradiation and oxidation resistance and are mainly developed as structural materials for nuclear applications, in generation IV fission reactors (fuel cladding), as well as for future fusion reactors [6,7]. It is envisaged that they will be used in other areas, for example in aerospace engineering. Most of the research is based on ferritic types of steels [1,2,5,6], such as the one used in this work. Al in 16Cr3Al ODS steel contributes to corrosion resistance, however, it also leads to the formation of coarser oxide particles. This is why IVB group elements (here hafnium) are added, promoting finer-grained structure of the base material, formation of smaller reinforcing Y-Hf-O particles, and improving corrosion behavior.

The aim of this study was: to analyze surface effects induced on 16Cr3Al ODS steel with and without Hf by high-intensity laser pulses at ~10^{13} W/cm^2 in controlled ambiances of helium and vacuum. In the main, the behavior of the material under high laser intensity, in this case 10^{13} W/cm^2, is still insufficiently known so in this context these investigations are vital. Also, it should be mentioned that studies employing pulsed laser radiation, particularly ultrashort pulses on these types of steel are scarce in literature [8-10] and the results are expected to be useful for further development of these materials.

2. Experimental

ODS steel samples used in experiments, synthesized using the standard powder metallurgy method (mechanical alloying followed by hot isostatic pressing, HIP), had the following compositions: (i) Fe-16Cr-3Al-1.5W-0.35Y_2O_3 (wt%), and (ii) Fe-16Cr-3Al-1.5W-0.35Y_2O_3-0.5Hf (wt%). Details on material preparation and experimental setup with Ti: sapphire femtosecond laser are given in [9,10]. The laser, emitting at the wavelength of 804 nm, was working in fundamental mode and the energy of pulses (65 fs long) in this work was kept constant at 0.25 mJ. A laser beam was focused to ~20 μm and samples were irradiated slightly in front of the focal plane. Irradiation was done in helium (1013 mbar) and vacuum (10^{-4} mbar), and the surface was analyzed using a scanning electron microscope (SEM) with an energy-dispersive X-ray analyzer (EDX), and optical profilometer.

3. Results and Discussion

3.1. Irradiation of ferritic ODS steel

Irradiation of ferritic ODS steel in helium

Effects occurring on the surface of ODS steel after the action of 1, 10, and 100 femtosecond pulses with energy E_p = 0.25 mJ (energy density 2.4 J/cm^2, intensity 3.6×10^{13} W/cm^2) in helium are presented in Figure 1. Figure shows SEM images of the obtained damages, as well as locations of EDX chemical analysis and 2D profilometric view of the damage after 100 delivered pulses.

After one laser pulse damage is barely visible (Figure 1A), while after 10 pulses damage is more prominent (Figure 1B1). In the central part subwavelength laser-induced periodic surface structures (LIPSS) can be detected, also termed *ripples*, i.e. LIPSS with the periodicity of the order of laser wavelength or lower, can be detected (B2). These ripples are the so-called low spatial frequency LIPSS (LSFL) with periodicity between λ/2 and λ (~600 nm in this case). They are seen more clearly on the periphery of the spot (B3). After 100 accumulated pulses there is visible melting, and *grooves* (LIPSS with periodicity over λ, here ~3 μm) can be seen in the center, as well as LSFL aligned 90° to grooves which are always parallel to light polarization (linear vertical in the present study). Profilometric analysis confirms superficial damage, with a depth of around 2 μm and numerous protrusions of up to 3.5 and even 5 μm.

The process of laser interaction with metal material starts with the absorption of incoming radiation by free electrons during several tens of femtoseconds. After the thermalization of the electron subsystem, energy is transferred to the lattice (scale of several hundred fs to several ps). Finally, ablation of the material occurs on a time scale of tens of picoseconds after termination of the laser pulse.

Laser irradiation at high intensities, such as the ones used here, causes the formation of high-temperature plasma above the material. However, unlike in the case of longer laser pulses in the nanosecond or picosecond range, the *plasma shielding* effect, i.e. loss of some of the incoming radiation due to plasma absorption, is absent or negligible here. The reason for this is that ultrashort femtosecond laser pulse ends before the plasma occurs so most of the laser energy is delivered to the surface. It should be emphasized that this subsequently generated plasma, according to some studies [11], can have effects on the target surface.

Particularly, the interaction of laser radiation with metals in the helium atmosphere is scarcely studied. Based on earlier research, this interaction has certain advantages - damage is more defined, depth of the damage, as a rule, is higher than in air.

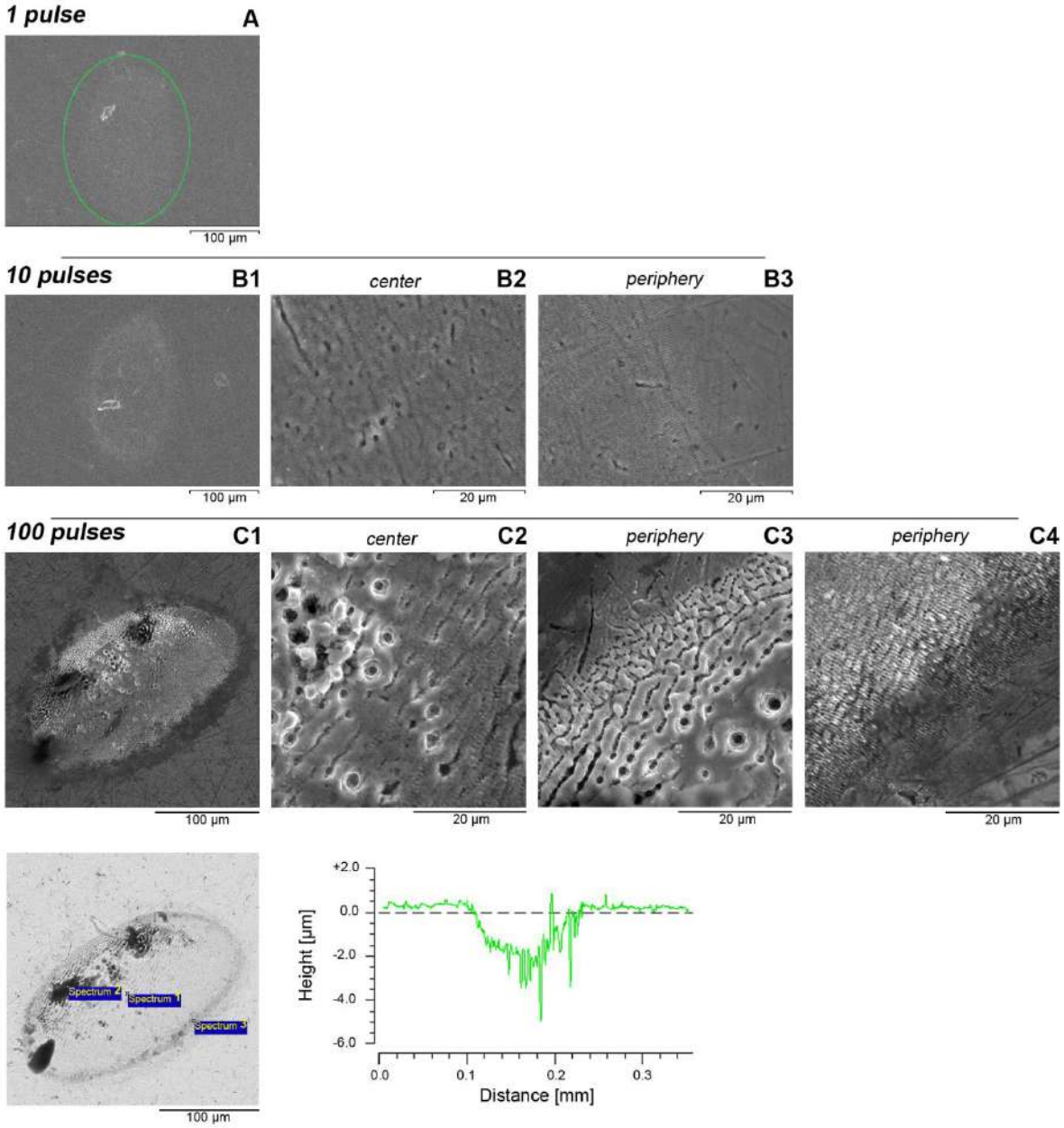

Figure 1. SEM analysis of ferritic ODS steel surface after irradiation in He with 1 (A), 10 (B), and 100 (C) fs laser pulses at ~10^{13} W/cm^2. EDX locations and profilometric analysis after 100 accumulated pulses.

The results of the EDX analysis are given in Table 1.

Table 1. EDX elemental analysis of ferritic ODS steel after irradiation in He with 100 fs laser pulses.

Spectrum	O	Al	Cr	Fe	Y	W
Non-irradiated	1.5	1.7	16.6	75.4	1.0	3.8
Spectrum 1 (*center*)	0.8	2.1	16.4	76.4	1.0	3.3
Spectrum 2 (*periphery*)	25.2	1.2	13.9	52.5	2.5	4.7
Spectrum 3 (*periphery*)	11.3	1.4	15.2	68.4	0.6	3.1

* Values are given in wt%.

Chemical analysis revealed the presence of all elements contained in the 16Cr3Al steel, and their concentrations vary depending on the location of the analysis. The central part of the damage shows

no significant changes, while only in characteristic locations, there is a more prominent increase in oxygen content, followed by a decrease of Cr and Fe. The possible explanation could involve the decomposition of internal oxides due to high laser intensity, followed by the formation of new oxides of the constituting elements (e.g. Fe, Cr).

Irradiation of ferritic ODS steel in vacuum

Figure 2 shows the ODS steel surface after fs laser irradiation in vacuum ambiance at E_p = 0.25 mJ (energy density 2.1 J/cm^2, intensity 3.2·10^{13} W/cm^2).

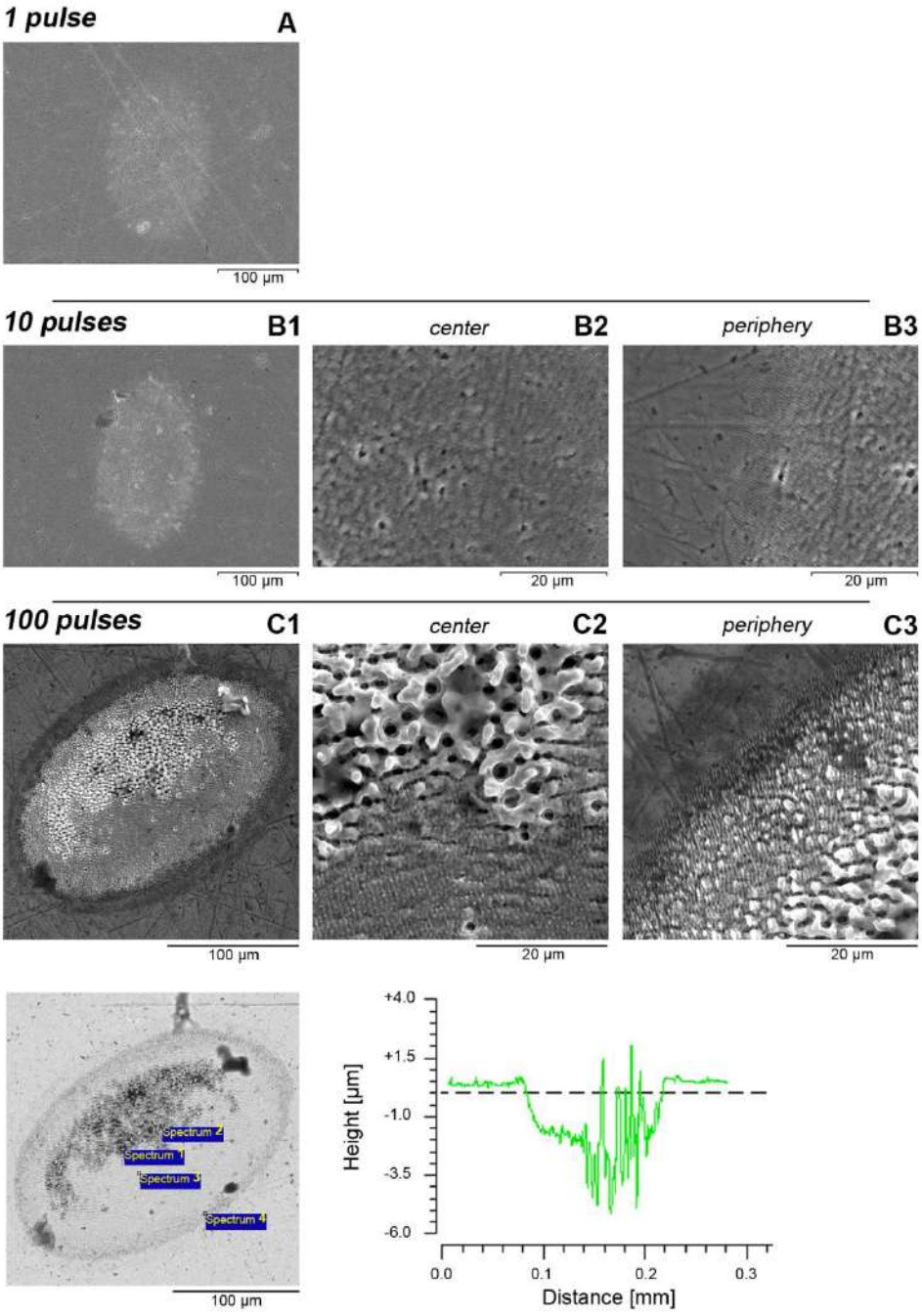

Figure 2. SEM analysis of ferritic ODS steel surface after irradiation in a vacuum with 1 (A), 10 (B), and 100 (C) fs laser pulses at ~10^{13} W/cm^2. EDX locations and profilometric analysis after 100 accumulated pulses.

One pulse has caused mild, but more visible damage compared to helium atmosphere (Figure 2A). Effects after 10 pulses have similar nature to those in He (2B). A hundred pulses cause more intensive melting in the spot center compared to He, with a coral-like structure formed as a result of disturbed grooves. LSFL structures are present in the central and peripheral zone. Profilometric analysis shows irregular damage form with a depth of ~3.5 to 5 μm.

EDX elemental analysis results after the action of 100 pulses are provided in Table 2. Changes in the central zone are insignificant, except in characteristic locations (dark areas, Spectrum 1) where oxygen content is increased with the lowering of Cr and Fe, similar as in helium. Composition in the peripheral (LIPSS) zone is close to the non-irradiated area (see Table 1).

Table 2. EDX elemental analysis of ferritic ODS steel after irradiation in vacuum with 100 fs laser pulses.

Spectrum	**O**	**Al**	**Cr**	**Fe**	**Y**	**W**
Spectrum 1 (*center)*	11.6	1.6	13.8	68.1	1.5	3.4
Spectrum 2 *(center)*	1.0	0.4	18.5	78.7	0.2	1.2
Spectrum 3 *(center)*	0.5	1.6	16.4	76.8	0.7	4.0
Spectrum 4 *(periphery)*	3.4	1.5	16.8	74.3	1.0	3.0

* Values are given in wt%.

3.2. Irradiation of ferritic ODS steel with Hf

Irradiation of ferritic ODS steel with the addition of hafnium in helium

Figure 3 summarizes surface features obtained on ODS steel with Hf after fs laser irradiation in helium, at E_p = 0.25 mJ (energy density 1.8 J/cm^2, intensity 2.8·10^{13} W/cm^2). LSFL-type ripples are visible already after one pulse, and generally, damages after 1, 10, and 100 pulses show more superficial character favorized probably by the addition of Hf, with less melting compared to ODS steel with no Hf added. The central part of the damage shows the presence of spherical pores due to local vaporization, with not fully developed grooves (only a few at the edge of the damage). The average damage depth is around 2 micrometers and few protrusions up to 2.5-3 μm.

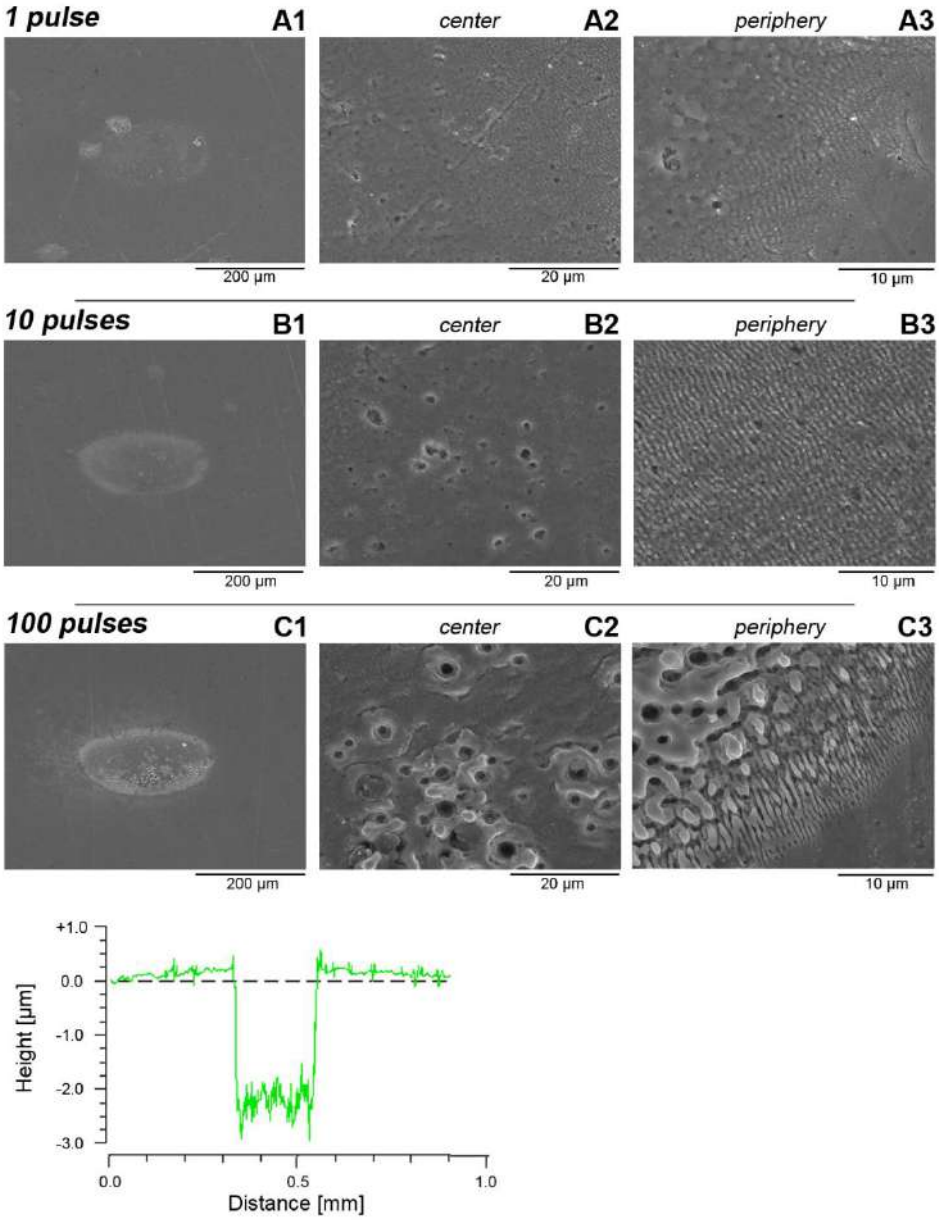

Figure 3. SEM analysis of ferritic ODS-steel with Hf surface after irradiation in He with 1 (A), 10 (B), and 100 (C) fs laser pulses at ~10^{13} W/cm^2. Profilometric analysis after 100 pulses.

Irradiation of ferritic ODS steel with the addition of hafnium in vacuum

SEM and profilometric analysis of the surface of ODS steel with added Hf after fs laser irradiation in vacuum, at 0.25 mJ (energy density 3.6 J/cm^2, intensity $5.7 \cdot 10^{13}$ W/cm^2), is given in Figure 4. No LSFL-type ripples are visible after one pulse, unlike in helium, as damage is somewhat more intense due to better coupling of the laser beam with the target in a vacuum atmosphere. Grooves are hardly visible (periphery at 100 pulses applied), and melting with a coral-like structure is less prominent compared to ODS steel without Hf. Profilometry shows a crater with a conical shape, ~2.1 µm deep, with a lot of redeposited material on one side. Based on SEM and profilometric analysis in a vacuum, it can be concluded that damages in the case of ODS steel with Hf are shallower, with less prominent melting, which is attributed to the Hf effect.

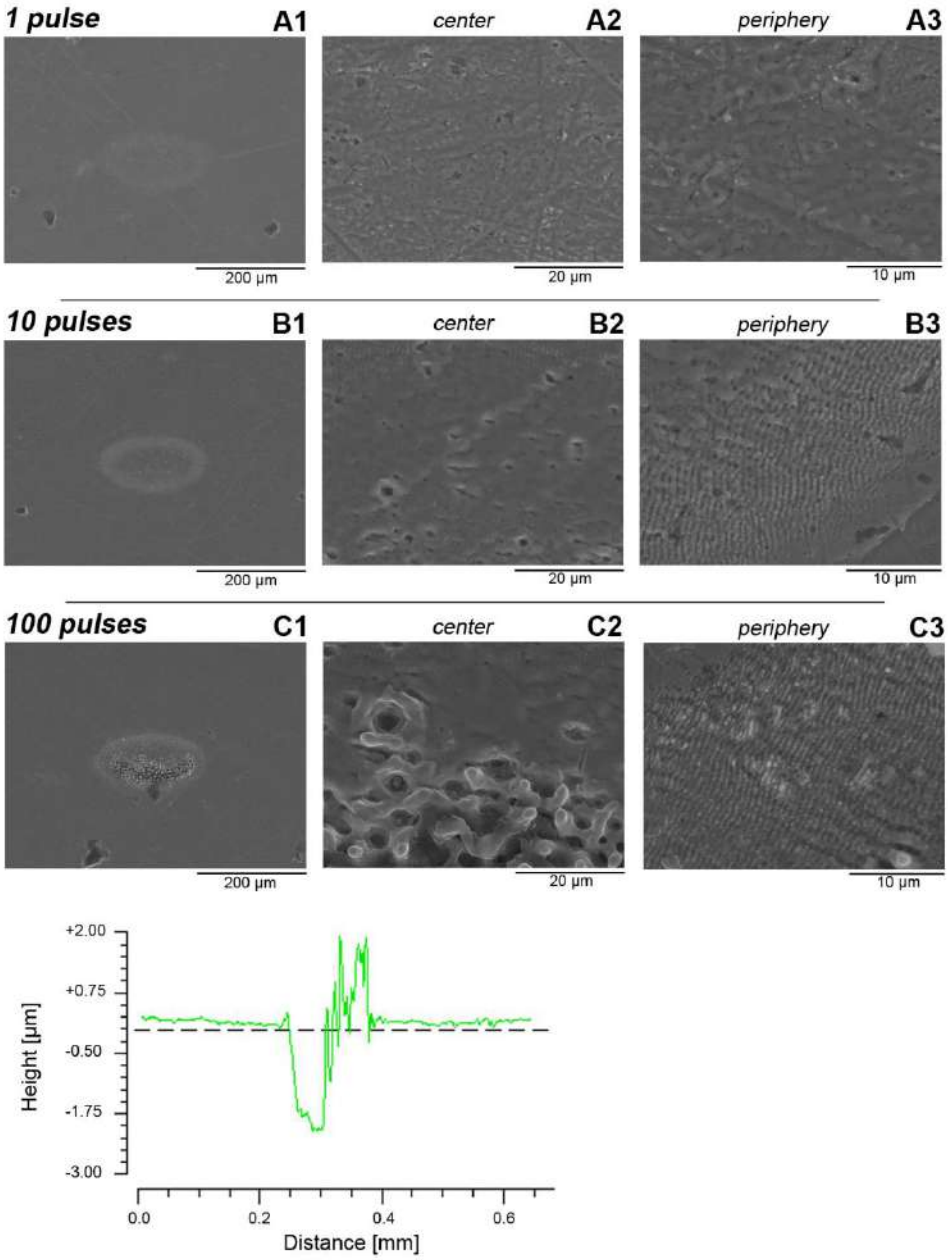

Figure 4. SEM analysis of the surface of ferritic ODS steel with Hf after irradiation in a vacuum with 1 (A), 10 (B), and 100 (C) fs laser pulses at ~10^{13} W/cm^2. Profilometric analysis conducted for damage after 100 accumulated pulses.

Phenomena in the course of fs laser-metal interaction are complex and still not completely known, including the effects of the ambiance used. In one approximation, ablation is also linked with subsequent plasma phenomena that take place above the target – namely, according to [11], two kinds of plasma are present in the helium atmosphere, i.e. plasma originating from the target itself, as well as plasma from the gas breakdown. In the case of vacuum ambiance, plasma from the gas environment is absent thus coupling should be more efficient. In the case of the applied intensity of 10^{13} W/cm^2, the shape of the obtained damages is still irregular compared to higher fluxes [9,10]. Damage is slightly deeper in vacuum compared to helium for ODS steel with no added Hf, while there is no significant difference between surroundings in the case of ODS steel with Hf. Irradiation at stronger intensities of ~10^{15} W/cm^2 shows significantly (around three times) deeper damages in a vacuum than in He [9,10].

Damage depths after laser irradiation at 10^{13} W/cm^2 are of the order of several micrometers. Generally, it can be concluded that damages in both employed ambiances are shallower in the case of ODS steel containing Hf. Namely, hafnium leads to a further strengthening effect in ODS steels through refinement of the base materials structure, and refinement of reinforcing oxides, i.e. formation of fine Y-Hf-O oxides which are formed more easily than coarser Al-containing oxides. This leads to better mechanical properties of ODS steel, and higher resistivity to laser-induced damages as shown by the results obtained.

4. Conclusion

The study presents an investigation on the surface features induced by high laser intensity, ~10^{13} W/cm^2, on ferritic ODS steel (16Cr3Al) with and without small content of hafnium. Hf is added with the aim of improving the strengthening effect through grain size refinement and the formation of smaller reinforcing oxide particles. The obtained morphological effects were observed in helium and vacuum.

Damages were generally superficial, a few micrometers deep, with not fully developed crater shape. Surface chemical analysis showed mild compositional changes. The presence of laser-induced periodic surface structures was recorded in both types of samples, with and without Hf, with less developed grooves (suprawavelength LIPSS) in the case of ODS steel with hafnium. Damage depths were typically lower in the case of Hf-containing ODS steel in both ambiances, showing better resistivity to laser irradiation at given intensities.

Acknowledgment

The expertise of Dr. Petr Hribek in the preparation of fs laser for the experiment is gratefully acknowledged. Dr. Jovan Ciganovic is acknowledged for profilometric measurements. This research was sponsored by: (i) International Atomic Energy Agency (IAEA) through CRP F13020, Contract No. 24076, “Contemporary and new IF structural-first wall materials: Conditions of high thermal and electromagnetic fluxes“; (ii) Ministry of Education, Science and Technological Development of the Republic of Serbia through Contract No. 451-03-68/2022-14/200017; (iii) Bilateral project Serbia-China No. 451-02-818/2021-09/17, “Advanced technologies based on pulsed lasers for modification/processing and synthesis of selected metal materials”; (iv) European Structural and Investment Funds and the Czech Republic through the project Centre of Advanced Applied Science [CZ.02.1.01/0.0/0.0/16_019/0000778] in the frame of the Operational Programme Research, Development and Education; (v) Czech Ministry of Education, Youth and Sports [Project LTT17015].

References

[1] Li, W., Xu, H., Sha, X., Meng, J., Wang, Z., Microstructure and Mechanical Properties of 14Cr-ODS Steels with Zr Addition, *High Temperature Materails and Processes*, 38 (2019) pp. 404-410.

[2] Macías-Delgado, J., Leguey, T., de Castro, V., Auger, M.A., Monge, M.A., Spätig, P., Baluc, N., Pareja, R., Microstructure and Tensile Properties of ODS Ferritic Steels Mechanically Alloyed with Fe_2Y, *Nuclear Materials and Energy*, 000 (2016) pp. 1-6.

[3] Zhou, X., An, Z., Shen, Z., Liu, W., Yao, C., Particles Control in Selective Laser Melting in-situ Oxide Dispersion Strengthened Method, *IOP Conference Series: Materials Science and Engineering*, 167 (2017) 012048.

[4] Yeom, H., Hoelzer, D., Maloy, S., Sridharan, K., Cold Spray Manufacturing of Oxide-Dispersion Strengthened (ODS) Steels using Gas-Atomized and Ball-Milled 14YWT Powders, *Journal of Nuclear Materials*, 574 (2023) 154187.

[5] Shabrina, N., Sugeng, B., Salam, R., Sujatno, A., Noor Haerani, D., Bandriyana, B., Synthesis of Ferritic ODS Steel with Different Electric Current in Arc Plasma Sintering Method, *Journal of Physics: Conference Series*, 2193 (2022) 012048.

[6] Zhang, G., Zhou, Z., Mo, K., Wang, P., Miao, Y., Li, S., Wang, M., Liu, X., Gong, M., Almer, J., Stubbins, J.F., The Microstructure and Mechanical Properties of Al-Containing 9Cr ODS Ferritic Alloy, *Journal of Alloys and Compounds*, 648 (2015) pp. 223-228.
[7] Zinkle, S.J., Boutard, J.L., Hoelzer, D.T., Kimura, A., Lindau, R., Odette, G.R., Rieth, M., Tan, L., Tanigawa, H., Development of Next Generation Tempered and ODS Reduced Activation Ferritic/Martensitic Steels for Fusion Energy Applications, *Nuclear Fusion*, 57 (2017) 092005.
[8] Farid, N., Harilal, S.S., El-Atwani, O., Ding, H., Hassanein, A., Experimental Simulation of Materials Degradation of Plasma-Facing Components using Lasers, *Nuclear Fusion*, 54 (2014) 012002.
[9] Trtica, M., Stasic, J., Limpouch, J., Gavrilov, P., Chen, X., Ciganovic, J., Surface Behavior of 16Cr3Al ODS Steel - Effects of High Laser Intensity 10^{14} W/cm^2 in Ambiences of Air, Helium and Vacuum, *Fusion Engineering and Design*, 150 (2020) 111360.
[10] Trtica, M., Stasic, J., Chen, X., Limpouch, J., Gavrilov, P., Zekic, A., 16Cr3Al-Hf ODS steel: Surface effects of high laser intensity of 10^{15} W/cm^2 in ambiences of air, helium and vacuum, *Fusion Engineering and Design*, in press.
[11] Vorobyev, A.Y., Guo, C., Enhanced Energy Coupling in Femtosecond Laser-Metal Interactions at High Intensities, *Optics Express*, 14 (2006) pp. 13113-13119.

Journal of Innovative Materials in Extreme Conditions
2023
Volume 4
Issue 1

THE ORIGIN OF ^{99}Tc IN THE ENVIRONMENT AND ITS REMOVAL

Đorđe Petrović*[1], Ljiljana Matović [1], Marija Egerić [1], Mia Omerašević [1], Radojka Vujasin[1], Snežana Ilić-Stojanović[2], Sanja Krstić [1]

[1]*Vinča Institute of Nuclear Sciences - National Institute of the Republic of Serbia, University of Belgrade, Mike Petrovića Alasa 12-14, 11351 Vinča, Belgrade, Republic of Serbia; djpetrovic@vin.bg.ac.rs (D.P.)*
[2]*University of Niš, Faculty of Technology, Bulevar oslobodjenja 124, 16000 Leskovac, Republic of Serbia*

Abstract: *Technetium-99 (^{99}Tc), as one of the important high-yield fission products, is a significant threat to the environment and human health. It is produced in large amounts by nuclear fission of ^{235}U or ^{239}Pu in nuclear reactions, though the quantity of Tc produced by the spontaneous fission of ^{238}U or by decay of ^{99}Mo in the nature which is very small. ^{99}Tc in the environment originates from nuclear weapons tests, discharges from nuclear power plants, nuclear medicine and radiobiology. These activities generate large volumes of low and intermediate radioactive waste which can cause a significant impact on the environment if disposed without suitable treatment. Immobilization of ^{99}Tc into a relatively small volume waste is vital for long term permanent disposal.*
High mobility and long half-life of ^{99}Tc considered to be one of the most important radionuclides in safety assessment of environmental radioactivity as well as nuclear waste management. Effective removal of radioactive technetium (^{99}Tc) from contaminated water is of enormous importance from an environmental and public health perspective, yet many current methodologies are highly ineffective.
This paper summarizes physico-chemical separation procedures emphasizing those that are the most used in practice.
Classic sorbents such as activated carbons, ion exchange resins as well, as new materials, such as metal−organic frameworks and graphene based membranes are described in the paper.

Keywords**:** *Technetium-99, nuclear fission of ^{235}U or ^{239}Pu, nuclear weapons tests waste, sorption, activated carbon, synthetic resins, MOFs, graphene oxide membranes*

1. Tc isotopes: their appearances, characteristics and ways of synthesis procedures

1.1. Radioisotope of Tc: its appearance in nature, types of isotopes, ways of synthesis

^{99}Tc, a long-lived β-emitting radionuclide, with its half life of 2.13x10^5 years, is the lightest element whose isotopes are all radioactive. There are 45 isotopes of Tc, ranging from ^{85}Tc to ^{117}Tc, that have been synthesized, and most of them are short-lived isotopes with half lives of less than 1 h. Among them most long lived are ^{97}Tc ($t_{1/2}$ = 2.6 x 10^6 y), ^{98}Tc ($t_{1/2}$ = 4.2x10^6 y) and ^{99}Tc ($t_{1/2}$ = 2.1x10^5 y). Relatively short half-life of technetium isotopes compared to the age of the Earth is responsible for its low presence in the environment, i.e. very small concentration of "natural" technetium exists in the nature [1]. Some authors mention that ^{99}Tc can be produced in nature by spontaneous fission of ^{238}U and neutron induced fission of ^{235}U in the earth [2,3], but the quantity of ^{99}Tc produced by spontaneous fission of ^{238}U or by decay of ^{99}Mo in the nature is very small [4]. Existence of ‘’natural reactors’’ et Oklo in Gabon were described by several authors [5-9]. Such ‘’reactors’’ can occur under the right geochemical conditions and if the geometry of the ore deposit is favourable. Natural fission can induce a nuclear chain reaction where ^{99}Tc appears as one of the products [10].

Nearly all available technetium is produced by nuclear fission of ^{235}U or ^{239}Pu in nuclear reactors. Half-life of ^{235}U is relatively shorter compared to ^{238}U and proportion of ^{235}U to ^{238}U has become smaller over time and present-day quantity uranium is made up of only 0.72 percent ^{235}U in the ore.

Small amounts of ^{99}Tc that occur environmentally originate from the decay of the short-lived medical radioisotope ^{99m}Tc (6.0058 h half-life), which decays by isomeric transition to technetium-99 [11]. Number of the longer-lived isotopes, such as ^{95m}Tc and ^{99m}Tc, have a plethora of research applications, especially in the medical field.

The greatest source of ^{99}Tc is its artificial production by neutron-induced fission. The fission yield of ^{99}Tc is 6.06 percent and one ton of ^{235}U-enriched fuel (3% enrichment) will produce 1 kg of ^{99}Tc at a typical burn up rate [12]. ^{99}Tc is produced in large amounts by nuclear fission of ^{235}U or ^{239}Pu in nuclear reactors in comparison to spontaneous fission of ^{238}U in the Earth's crust or by decay of ^{99}Mo in nature [13]. The fission of ^{235}U produces a spectrum of fission products including ^{99}Mo, ^{131}I, and ^{133}Xe. These fission products are produced in the same proportions to each other whether highly enriched uranium or low enriched uranium targets are used. All these isotopes can be recovered when the targets are processed to obtain ^{99}Mo [14].

Reprocessing of spent uranium fuel rods to recover ^{235}U, ^{239}Pu, and other fissile elements is the chief means by which Tc becomes part of the waste stream. Technetium has found its way into the environment over the last 40 years principally through the approved or accidental discharge of processing fluids [15].

^{99}Tc can be also produced by thermal neutron induced fission of ^{235}U with a relatively high accumulated fission yield of 6.1%, making ^{99}Tc relatively high abundant among fission products [16, 17]. The decay of ^{99}Mo is shown graphically on Figure 1.

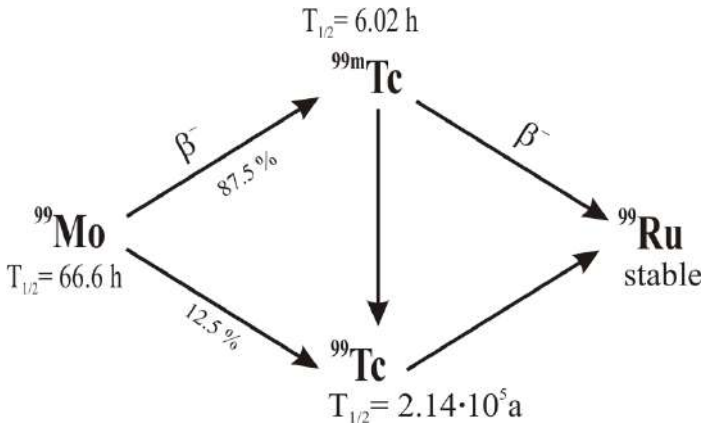

Figure 1. Decay scheme of ^{99}Mo

The predominant form of technetium is Tc_2O_7, which rapidly reacts with water vapor to form pertechnetic acid ($HTcO_4$). Technetium sorbs onto particles in the atmosphere and settles through precipitation. The nuclear weapons industry is also responsible for increasing the amount of radioactive waste producing hundreds of tons of plutonium during the Cold War and the generation of over 300 million liters of hazardous liquid wastes among which hundreds of liters of ^{99}Tc liquid waste [18-20].

Dissolution of U during reprocessing and fluorination to produce $U(VI)F_6$ also produces fluoride complexes of Tc, such as $Tc(VI)F_6$ and $Tc(VII)O_3F$, with the former more abundant than the latter. Although these species are volatile and potentially mobile to the atmosphere, most of the contamination caused by technetium fluorides is due to accidental release into water, where it hydrolyzes and disproportionates into Tc(IV) and Tc(VII). In localities where gaseous diffusion operations occurred, such as Paducah, Kentucky, and Oak Ridge, Tennessee, nearly 97.5 percent ^{99}Tc was discharged to the environment through aqueous solution and only 2.5 percent by gaseous pathways [21].

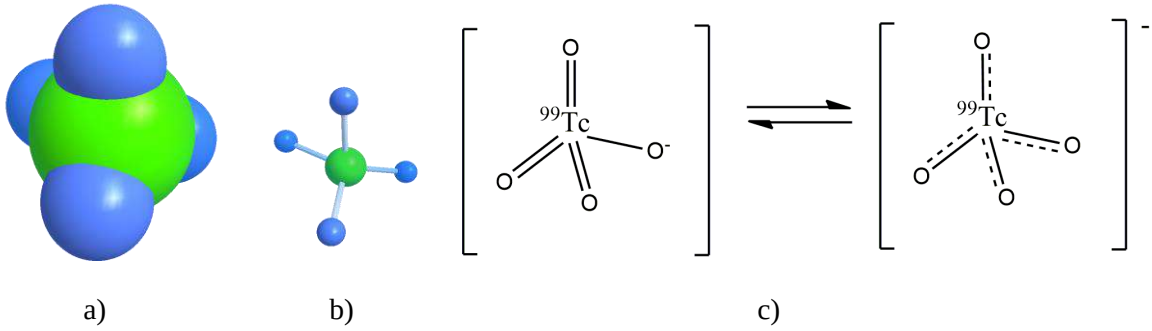

a) b) c)

Figure 2. Pertechnetate anion. Different views: space-filling model (a), stick and ball model (b), and structure view (c).

2. Technetium in the environment

Besides pertechnetate oxyanion (TcO_4^-), the tanks with nuclear waste also contain other oxyanions of concern, such as chromate (CrO_4^{2-}) and nitrate (NO_3^-), which can form spinels thus weakening the integrity of the vitrified waste glass and provoke leaching of the radioactive waste from the tanks used for disposal. After several incidents around the world, these radioactive materials entered the groundwaters and caused aquatic contamination. High toxicity, non-biodegradability, and mobility of oxyanions have become an urgent challenge that resulted in putting oxyanions in the Environmental Protection Agency, U.S. (EPA) priority pollutant list. Therefore, the importance of treatment of industrial wastewater containing oxyanions before their dischargement into the water resources is of great importance to avoid detrimental effects on living organisms after exposure to higher concentrations of oxyanions.

Transport of radionuclides to the geosphere is generally controlled by their solubility and possible sorption onto surrounding materials. It is highly soluble in surface and near-surface environments. It is known that Tc is not sorbed on negatively charged surfaces such as layered silicate [22]. The retention of Tc in soils is enhanced however, by the presence of organic materials whereas the sorption of Tc in soils containing low amounts of organic materials is negligible [23, 24].

The most stable oxidation state of ^{99}Tc under aerobic environments is the pertechnetate anion (TcO_4^-) over a broad range of pH and Eh [25, 26]. Pertechnetate (TcO_4^-) will not be significantly sorbed by anions colloids and suspended sediments and is therefore highly mobile under aerobic conditions. However, physical, chemical, and biological processes can strongly influence the fate of Tc [27].

In aqueous solutions technetium may exist in the valence states + 7, + 4, and 0 [28, 29]. Standard redox potentials of Tc species in aqueous solution are lower than the O_2/ H_2O redox couple (1.23 V), thus, the spontaneous oxidation by air of Tc species in the intermediate oxidation states (i.e., Tc^{IV} to Tc^{VII}) is thermodynamically favorable [30]. In non-complexing media, Tc^{V} and Tc^{VI} are thermodynamically unstable and disproportionate to Tc^{IV} and Tc^{VII} species.

However, Tc(VII) is reducible to lower valence states by Zn, HCl, hydrazine, hydroxylamine, ascorbic acid, tin(II) chloride, and dilute sulfuric acid [31].

To avoid the usage of a radioactive element at high concentrations for laboratory testing and development, Tc can be replaced by studying non-radioactive rhenium (^{75}Re), its chemical analogue [32].

2.1. Determination of ^{99}Tc

Technetium is silvery-gray coloured metal which tarnishes slowly in moist air. It dissolves in HNO_3, aqua regia, and concentrated H_2SO_4, but is not soluble in any strength of HCl solution [40]. Chemical separation combined with radiometric and mass spectrometric measurement techniques, has been developed for the determination of ^{99}Tc in different environmental samples [34]. Pre-treatment of solid samples consists of drying and ashing, alkali fusion, and combustion. Until then, water

samples are only filtered and acidified. Further treatment for both types of samples is the same and consists of pre-concentration by precipitation, evaporation, or ion exchange. After chemical separation like solvent extraction, ion exchange, or extraction chromatography, measurement of samples was provided by β counting or ICP-MS. Several new ion-selective electrodes for the electrochemical determination of ^{99}Tc were recently presented [35-37].

2.2. Removal of technetium

Removal of ^{99}Tc from contaminated soil and groundwater is very difficult because of the influence of other anions presented in the environment. Sorption was and still is one of the most popular and widely used methods for removing heavy metals from the environment. Sorption of ^{99}Tc on activated carbon was investigated [38-40], as well as various synthetic resins and sponges [41,42], elemental iron [43], magnetic iron sulphide material [44], organic polymers [45], chitin, chitosan [46-48] and commercial resins [49-50].

2.2.1. Organic materials for removal of pertechnetate

A simple and effective technology to remediate Tc (as TcO_4^-) contaminated groundwaters was proposed by Gu et al. [51]. *Purchased granular activated carbon* was only washed with purified water (Milli-Q) by repeated decanting and sedimentation to remove tine carbon particles and then air dried and stored in a plastic bottle. Batch sorption of TcO_4^- on activated carbon was performed in various background electrolyte solutions including 0.01 M $CaCl_2$, 0.01 M $NaNO_3$, 0.01 M Na_2SO_4, Na-salicylate, and phthalate at pH - 6.5. The conclusion was that activated carbon adsorbs TcO_4^- selectively and effectively over a wide range of pH values and from various dilute electrolyte solutions.

Demir *et al*. [42] also used *activated carbon* as an adsorbent to remove $^{99m}TcO_4^-$ from an aqueous solution. Although there is no explanation why ^{99m}Tc was used instead of ^{99}Tc, the assumption is that it is due to easier measurement of gamma radiation. They reported good adsorption capacity value obtained from the Langmuir isotherm model.

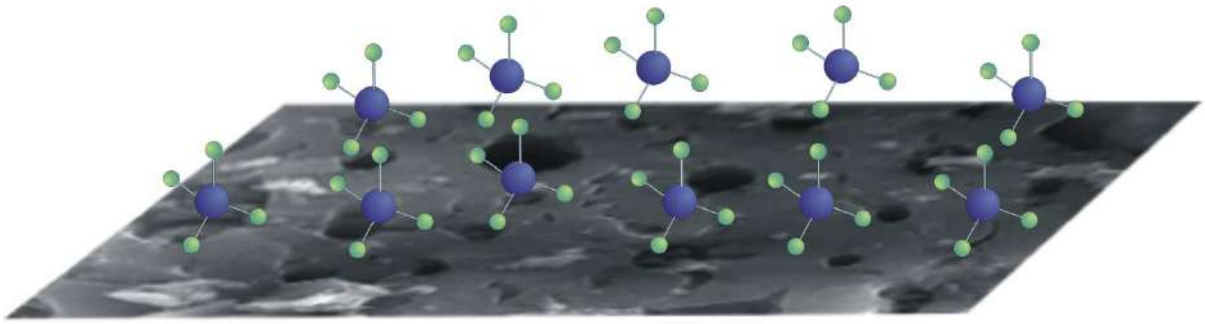

Figure 3. Schematic representation of the adsorption of pertechnetate anions on the modified carbon surface

Hexadecylpyridinium chloride monohydrate modified bentonite (HDPy-bent) was synthesized and used as an adsorbent to remove $^{99}TcO_4^-$ [52]. The adsorption behaviours of ReO_4^- as an analogue for TcO_4^- were investigated as functions of contact time, solution pH, initial concentration, and competing anions using batch techniques. Research demonstrated that the HDPy-bent showed an excellent adsorption ability for ReO_4^- at the pH range of 2–11, fast adsorption kinetic (reaching equilibrium within 3 min at room temperature), and maintained desirable ReO_4^- adsorption in the presence of concomitant anions at an excessive concentration of 500 times (Cl^-, HCO_3^-, NO_3^-, CO_3^{2-}, SO_4^{2-} and PO_4^{3-}). As for the adsorption mechanism, the authors propose the anion exchange process at a low concentration of Re(VII) and precipitation reaction at a high concentration.

Chromatographic Experiments Flowsheet Feasibility Studies Using *ABEC Resins* for Removal of Pertechnetate from Nuclear Wastes was proposed by Bond *et al* [53]. The chromatogram in which $^{99}TcO_4^-$ was loaded from 4.0 M NaOH was collected using a modified formulation of the gel-type resin ABEC G2. This material was prepared in a 110 L reactor using Me-PEG-2000, 2% divinylbenzene (DVB), and 10% vinyl benzyl chloride (VBC) in diglyme.

Some commercially available resins {Amberlite IRA-904 and IRA-900 (Rohm and Haas), Reillex HPQ (Lot 40404AD) from Reilly Industries, Inc., Indianapolis, IN; Purolite A-520E and A-850 from The Purolite Company, Bala Cynwyd, PA; and Sybron Ionac SR-6 and SR-7 from Sybron Chemicals, Inc., Birmingham}, were compared with laboratory synthesized resins based on divinylbenzene-cross-linked poly(vinylbenzyl) chloride in their efficiency for pertechnetate removal [54]. The authors reported that the 24-h *Kd* for the synthesized bifunctional resins is the highest, being approximately twice the 24-h *Kd* of any commercial resin and 50% better than any of the laboratory-prepared monofunctional resins.

Further, ReO_4^- and $^{99}TcO_4^-$ removal from aqueous solutions using a *polyethylenimine–epichlorohydrin resin* was investigated in the absence and presence of background electrolyte (0.01 and 0.50 M NaCl) [55]. The investigated polyethylenimine–epichlorohydrin resin showed a strong tendency to remove significant amounts of perrhenate and pertechnetate ions (up to 4.9 mmol/g resin) from aqueous solutions in the absence and presence of competing ions ($[Cl^-] \leq 0.5$ M) over a wide pH-range ($2.3 \leq pH \leq 8.9$). The sorption of ReO_4^- and TcO_4^- anions is pH and $[Cl^-]$-dependent, with the highest capacity and R_d values observed for $pH \leq 4.4$ and $[Cl^-] \leq 0.01$ M.

A new anion exchanger with pyridine groups was prepared by grafting *2-vinyl pyridine* onto polypropylene nonwoven fabrics by pre-irradiation grafting technique, followed by quaternization of pyridine rings in grafted chains in reaction with bromoethane [56]. The results showed that the grafting yield increased with the monomer concentration and the conversion ratio of quaternization increased with time. The possibility of adsorption of perrhenate, as a nonradioactive analogue to pertechnetate, from an aqueous solution by an anion exchanger was investigated. The experiments performed at pH = 0.1-6 showed that pH = 2.2 was the optimal acidity for ReO_4^- adsorption and adsorption equilibrium was achieved in 30 min. The reaction enthalpy was -12.55 kJ/mol, indicating that the adsorption process is exothermic. XPS tests indicated that the ReO_4^- uptake was a typical ion exchange between Cl^- anion exchanger and ReO_4^-.

Katayev *et al*. considered the possibility of using *organic molecules* that are used as radiopharmaceuticals to remove Tc [57]. The most effective way, according to them, to achieve strong binding in aqueous environments is to exploit Coulombic interactions. Using soft acids, such as low charge density cations, e.g., metal-based receptors, CTVs, polycations, phosphinimium-based receptors or structures containing guanidinium sites is the best way of binding soft bases such as perrhenate and pertechnetate anions.

A class of *two-dimensional nanostructured anionic clays* named Layered double hydroxides (LDH) was also used for the removal harmful oxyanions such as arsenate, chromate, phosphate, pertechnetate, etc. from contaminated waters [58]. Calcined Mg–Al LDHs and uncalcined Mg–Al LDHs were the most used materials for the removal of pertechnetate and perrhenate oxyanions [59-62].

2.2.2. Inorganic materials for removal of pertechnetate

Also, different inorganic materials for selective separations have become abundant in the nuclear industry. Glassy, nanocrystalline *antimony-doped hydrous tin dioxide* was used for butch experiments and after 24 h achieved almost quantitative removal of Tc from solutions. The material obtained by alkali precipitated from an acidic metal chloride solution has good thermal stability and granular physical form that enables its use in a conventional column [63]. It shows excellent, almost quantitative, uptake properties for ^{99}Tc radionuclide.

Manganese oxide nanoparticles loaded into activated carbon were presented as an improved method for pertechnetate sorption [64]. Composite was formed by co-precipitation by loading a nanoparticle into a modified activated carbon by different ratios.

^{99}Tc radionuclide (activity 257.4 CPM/ml) was extracted from residual ^{99m}Tc columns from the technetium generator used in nuclear medicine centers. Batch experiments were performed with 0.05

mg of sorbent which was added to 5 ml of radioactive waste solutions in a polypropylene centrifuge tube. The synthesized composite during a contact time of 60 minutes gave a higher adsorption efficiency of about 93% compared to nano manganese oxide and activated carbon whose efficiency was about 40%. Isotherms belonged to Freundlich model, the adsorption data followed the pseudo-second order model and the thermodynamic study indicated that the adsorption of nanocomposites was an exothermic and spontaneous process.

Low-cost adsorbents, *magnesium ferrite* ($MgFe_2O_4$) nanoparticles were synthesized using three different types of fuels such as urea, oxalic acid, and citric acid via sol-gel auto-combustion method [65]. Batch experiments were carried out to examine the sorption of pertechnetate, from aqueous solution by the synthesized nano $MgFe_2O_4$. The results revealed that the $MgFe_2O_4$ nanostructure has a high removal ability of $^{99}TcO_4^-$ from aqueous solutions (98.84%). The adsorption data were in good agreement with Freundlich and pseudo second-order isotherm models. The adsorption process was a chemisorption reaction, additionally, the results of the thermodynamic parameters indicated that the adsorption of $^{99}TcO_4^-$ on nanostructures was an exothermic and spontaneous process.

Pyrite nanoparticles were prepared by ball milling in the presence of ethanol resulting in pyrite nanoparticles capable for immobilization of ReO_4^- [66]. They offer much greater (>200 times) reduction reactivity for perrhenate than micron-scale particles due to the increased specific surface area and distortion of the crystalline lattice of the materials. The raw bulk pyrite was practically unreactive for perrhenate reduction. A much greater reduction rate and extent of ReO_4^- were observed under alkaline conditions. The favorable formation of composite ferrite and iron (hydro)xides under alkaline conditions plays important roles in the enhanced immobilization reactions. The column test data revealed that the pyrite nanoparticles may be used in a packed wall or permeable barrier configuration for in situ reductive immobilization of ReO_4^-. Compared to the loess soil, the water-leachable ReO_4^- was reduced by 44%.

Cementitious waste technology (CWT) has been considered for immobilizing pertechnetate, $Tc(VII)O_4^-$, in brine and alkaline waste solutions, as Tc(IV) oxides and/or sulfides with the use of reducing agents like slag [67]. Also, zero-valent iron (ZVI) was evaluated as a potential reducing agent in CWT as a function of pH using perrhenate, $Re(VII)O_4^-$, as an analogue for $Tc(VII)O_4^-$. Considering the thermodynamically favourable reduction of Tc(VII) over Re(VII), ZVI might have the potential for improving the reduction capacity of the current CWT. The results of this study provide insight towards the use of ZVI particles in cementitious waste technology to immobilize ^{99}Tc.

Generally, much of the ^{99}Tc at SRS is cast into a *cementitious low-level waste form*, referred to as “saltstone”, whereas at the Hanford site, both the high and low-level fractions will be immobilized into a borosilicate glass waste form a process known as vitrification [68]. Technology for *vitrification* of low-activity waste – primarily ^{99}Tc was described by Kathryn *et al* [69]. Tc removal via reductive precipitation with stannous chloride to examine the potential for diverting this stream to an alternate disposition path was investigated.

Nanoscale zero-valent iron (NZVI) supported on layered double hydroxide (LDH) was a composite applied for the reductive immobilization of Re(VII) [70]. The synergistic effect can be seen in the fact that LDH could promote a complete reduction of Re(VII) into Re(IV) by NZVI, while sorption and reduction occurred simultaneously on bare NZVI. As a scavenger for the coexisting anions, sparingly soluble products and pH buffering of LDH improve the reactivity of NZVI. The authors assumed that the immobilization performance of NZVI/LDH will provide a promising strategy for the decontamination of Tc(VII) from groundwater.

Li and Wang focused on a remediation strategy for the reduction of pertechnetate (TcO_4^-) by nanoscale *zero-valent iron* particles supported on graphene [71]. The results demonstrated that NZVI/rGOs could efficiently remove Re from the aqueous solution, with enhanced reactivity, improved kinetics (50 min to reach equilibrium), and excellent removal capacity (85.77 mg/g). Mechanisms of Re immobilization by NZVI/rGOs included adsorption and reduction, which are significant to the prediction and estimation of the effectiveness of reductive TcO_4^- by NZVI/rGOs in the natural environment.

2.2.3. Metal-organic frameworks (MOFs) as inorganic-organic hybrid porous crystalline materials for removal of pertechnetate

Metal−organic frameworks (MOF) are compounds of metal ions and organic molecules that form structured frameworks [72]. These advanced materials can be compared with sponges with unique abilities – being able to take-up, hold, and release molecules from their pores. With a highly ordered framework of pores, metal-organic frameworks exhibit the largest surface areas per gram (about 7000 m^2/g of MOF material). Banerjee with co-workers reported ReO_4^- exchange properties of a protonated amino-functionalized MOF, UiO-66-NH_3^+, in an aqueous solution in the presence of other competing anions [73]. The material has an uptake capacity of 159 mg/g, which is significantly higher than that of traditional inorganic materials such as layered double hydroxides.

A three-dimensional water-stable cationic *MOF* pillared by a neutral ligand and with Ni(II) metal nodes has been synthesized employing a rational design approach [74]. Owing to the ordered arrangement of the uncoordinated tetrahedral sulfate (SO_4^{2-}) ions in the channels, the compound has been employed for aqueous-phase ion exchange applications. The compound exhibits rapid and colorimetric aqueous-phase capture of environmentally toxic oxoanions (with similar geometries) in a selective manner. This system is the first example of a MOF-based system that absorbs both dichromate ($Cr_2O_7^{2-}$) and permanganate (MnO_4^-) ions, with the latter acting as a model for the radioactive contaminant pertechnetate (TcO_4^-). MOF containing free SO_4^{2-} ions is an unusual example of a MOF-based dual adsorbent for permanganate ions and the environmental pollutant dichromate, with the former acting as a model for the radioactive contaminant pertechnetate (TcO_4^-). In comparison with other MOF-like systems, this compound exhibits a moderately high uptake capacity of about 166 mg g^{-1} for $Cr_2O_7^{2-}$ ions.

Three-dimensional cationic *metal-organic framework material*, SCU-100, was used by Sheng, *et al*. for removing TcO_4^- [75]. Initial anion exchange studies show that SCU-100 can both quantitatively and rapidly remove TcO_4^- from water within 30 min. The exchange capacity for the surrogate ReO_4^- reaches up to 541 mg/g and the distribution coefficient Kd is up to 1.9×105 30 mL/g, which is significantly higher than all previously tested inorganic anion sorbent materials. More importantly, SCU-100 can selectively capture TcO_4^- in presence of large excess of competitive anions (NO_3^-, SO_4^2, CO_3^{2-}, and PO_4^{3-}). The sorption mechanism showed that the sorbed ReO_4^- anion is able to selectively coordinate to the open Ag^+ 36 sites, forming Ag-O-Re bonds and a series of hydrogen bonds.

An efficient and cost-effective way for the removal of radioactive pertechnetate anions from nuclear waste was proposed by Banerjee *et al* [76]. A series of functionalized hierarchical porous frameworks were evaluated for their perrhenate removal capacity in the presence of other competing anions. Functionalized PAF-1, namely PAF-1-F showed the best uptake performance, with 97% ReO_4- removal within the first 24 h. Such performance is significantly better than other reported materials including traditional inorganic materials and protonated UIO-66-NH_2.

The protonated version of an ultrastable *zirconium-based metal−organic framework* of the chemically robust MOF UiO-66-NH_2 can adsorb perrhenate (ReO_4^-) anions, a nonradioactive surrogate for TcO_4^-, from water even in the presence of other common anions aqueous medium even in the presence of other competing anions [77]. The material has an uptake capacity of 159 mg/g, which is significantly higher than that of traditional inorganic materials such as layered double hydroxides.

Hydrolytically stable and radiation-resistant cationic metal-organic framework, SCU-101, that has extremely fast removal kinetics, exceptional distribution coefficient, and high sorption capacity towards TcO_4^- was reported by Zhu *et al*. [78] This material can selectively remove TcO_4^- in the presence of large excesses of NO_3^- and SO_4^{2-}, as even 6000 times of SO_4^{2-} in excess does not significantly affect the sorption of TcO_4^-.

3. Conclusion

It can be concluded that measurable amounts of ^{99}Tc in the environment can be found after the nuclear reaction of ^{235}U or ^{239}Pu fission, whether they originate from nuclear reactors or nuclear explosions. Particle accelerators, such as linear accelerators or cyclotrons, although they provide the

possibility of different ways to obtain ^{99}Tc, they produce insignificant amounts of this isotope. Here was also mentioned the existence of ''natural reactors'', where ^{99}Tc is produced by spontaneous fission of ^{238}U.

In the environment, ^{99}Tc is presented as oxyanion (TcO_4^-) because solubility drastically decreased by the reduction of Tc(VII) to Tc(IV), where Tc(IV) exists in the sparingly soluble form of $MO_2 \cdot nH_2O$. Many authors used perrhenate (ReO_4^-) anions, a nonradioactive surrogate for TcO_4^-, to avoid the complication of directly working with radioactive elements. Technetium and rhenium both belong to the VIIB subgroup, share the same configuration of extra-nuclear electrons, have similar chemistry, and are commonly present as oxyanions (MO_4^-) in aqueous solutions.

The abundant literature that describes the removal of ^{99}Tc from water and soil gives a good basis for practical actions if it is necessary to carry out the cleaning of contaminated environment and soil. The most popular and widely used method for removing heavy metals from the environment was sorption on activated carbons and synthetic resins. Most of the carbons and synthetic resins are of commercial origin and have been used by researchers with minimal preparation. More recent studies have included elemental iron, iron sulphide material, organic polymers, chitin, and chitosan. Results of sorption on different materials ranged from 90 to 99%, but the selectivity was weak. The adsorption data in most sorption experiments were in good agreement with Freundlich and Pseudo second order isotherm models. The results of the thermodynamic parameters (where there are) indicated that the adsorption of $^{99}TcO_4^-$ on nanostructures of different origins, whether organic or inorganic or MOFs, was an exothermic and spontaneous process. Cementitious waste technology and vitrification were proposed methods for the permanent disposal of radioactive materials.

Recent works attempt to unravel the mechanism of $^{99}TcO_4^-$ / ReO_4^- sorption and determine the position of the adsorbed oxyanions within the sorbents. Comparing sorbents according to their efficiency is very unreliable because the experiments were performed in different conditions. All experiments were carried out at room temperature, but their duration was different. Most of them were batch experiments (without automation), which varied in duration, from a few hours to the whole day, to establish a steady–state equilibrium. The working procedures were simple: samples suspensions usually were shaken, then centrifuged in order to separate the solutions from the remains. Results of sorption on different materials ranged from 90 to 99%. The influence of other anions presented in the environment makes the separation of ^{99}Tc much more difficult and only a few works included the separation in addition to chlorides, nitrates, sulfates, etc.

The various materials that have been described give us different options for efficient collection and concentration of radioactive ^{99}Tc that could eventually be removed and safely disposed.

References

[1] Schwochau, K, *Technetium Chemistry and Radiopharmaceutical Applications*, WILEY-VCH Verlag GmbH. D-69469 Weinhcim (Federal Republic of Germany), 2000

[2] Wildung, R.E., McFadden, K.M., Garland, T.R., Technetium Sources and Behavior in the Environment, *Journal of Environmental Quality, 8* (1979), pp. 156–161

[3] Curtis, D., Fabryka-Martin, J., Dixon, P., Cramer, J., Nature's uncommon elements: Plutonium and technetium, *Geochimica et Cosmochimica Acta 63* (1999), pp. 275–285

[4] Rard, J.A., Rand, M.H., Anderegg, G., Wanner H., The discovery and natural occurrence of technetium and its utilisation, in: *Chemical thermodynamics of technetium*, (Ed: Sandino M. C. A, and O. sthols E.), vol. 3. Amsterdam, North-Holland, 1999. p. 74

[5]Curtis, D. B., Geochemical controls on ^{99}Tc transport and retention: *Chemical Geology*, *55* (1986), pp. 227–231

[6]Curtis, D., Benjamin, T., Gancarz, A., Loss, R., Rosman, K., DeLaeter, J., Delmore, J. E., and Maeck, W. J., Fission product retention in the Oklo Natural Fission Reactors, *Applied Geochemistry*, *4* (1989), pp. 49–62

[7] Brookins, D. G., Radionuclide behavior at the Oklo Nuclear Reactor, Gabon, *Waste Management*, *10* (1990), pp. 285–296

[8] Gauthier-Lafaye, F., Holliger, P., and Blanc, P.L., Natural fission reactors in the Franceville basin, Gabon: A review of the conditions and results of a "critical event" in a geologic system: *Geochimica et Cosmochimica Acta, 60* (1996) pp. 4831–4852

[9] Janeczek, J., Mineralogy and geochemistry of natural fission reactors in Gabon, in Burns, P. C., and Finch, R., editors, Uranium: Mineralogy, *Geochemistry and the Environment: Reviews in Mineralogy and Geochemistry, 38,* (1999) pp. 321–382
[10] Icenhower, J.P., Qafoku, N.P., Zachara, J.M., and Martin, W.J., The biogeochemistry of technetium: A review of the behavior of an artificial element in the natural environment, *American Journal of Science, 310* (2010), 8, pp. 721-752
[11] Larsen, I. L., Stetar, E. A., Glass, K. D., In-House Screening for Radioactive Sludge at A Municipal Wastewater Treatment Plant, *Radiation Protection Manager, 12* (1995), pp. 29
[12] Chen, F., Burns, P. C., and Ewing, R. C., Near-field behavior of ^{99}Tc during the oxidative alteration of spent nuclear fuel: *Journal of Nuclear Materials, 278* (2000), pp. 225–232
[13] Curtis, D.; Fabryka-Martin, J.; Dixon, P.; Cramer, J., Nature's uncommon elements: Plutonium and technetium, *Geochimica et Cosmochimica Acta, 63* (1999), pp. 275-278
[14] ***, *Molybdenum-99/Technetium-99m Production and Use in Medical Isotope Production without Highly Enriched Uranium*, https://www.ncbi.nlm.nih.gov/books/NBK215133/
[15] Schulte, E. H., and Scoppa, P., Sources and behavior of technetium in the environment, *Science of the Total Environment, 64* (1987), pp. 163–179
[16] Ihsanullah, J., Losses of technetium during various steps in the development of a procedure for environmental samples, *Journal of Radioanalytical and Nuclear Chemistry. 176* (1993), pp. 303–313.
[17] Sekine, T., Hiraga, M., Fujita, T., Mutalib, A., Yoshihara, K., Application of Laser Induced Photoacoustic Spectroscopy to the Determination of ^{99}Tc, *Journal of Nuclear Science and Technology, 30* (1993), pp. 1131–1135
[18] *Plutonium: The First 50 Years*, Report DOE/DP-0137 ; U.S. Department Of Energy: Washington, D.C., USA, 1996
[19] Offenhauer, P., *Defense Nuclear Facilities Safety Board: The First Twenty Years*; Library of Congress: Washington, D.C., 2009.
[20] Gephart, R.L., Hanford, R.E., Tank Clean up: A Guide to Understanding the Technical Issues; *Pacific Northwest Lab*, Richland, WA, 1995.
[21] Till, J.E., Source terms for technetium-99 from nuclear fuel cycle facilities, in: editors, *Technetium in the Environment* (Ed. G. Desmet, and C. Myttenaere) Elsevier Applied Science Publishers, Essex, England, 1986. pp. 1–20.
[22] Hakanen M., Technetium, neptunium and uranium in simulated anaerobic groundwater conditions. Report YJT-95-02, Nuclear Waste Commission of Finish Power Companies, Finland, 1995
[23] Stalmans, M., Maes. A., Cremers, A., Role of organic matter as a geochemical sink for technetium in soils and sediments. in: *Tc in the environment* (Ed. G. Desmet, C. Myttenaere), Elsevier, London-New York, 1986, pp. 91.
[24] Sparkes, S.T., Long, S.E., The chemical speciation of technetium in the environment: a literature survey. Report No. AERE-R 12743, HMSO, London, 1988
[25] King, W. D., Hassan, N. M., Mccabe, D. J., Hamm, L. L. & Johnson, M. E., Technetium removal from Hanford and Savannah River Site actual tank waste supernates with Superlig R 639 resin. *Separation Science and Technology, 38* (2003), pp. 3093–3114
[26] Rard, J.A., Rand, M.H., Anderegg, G., Wanner, H., Chemical thermodynamics of technetium. in:. *Chemical thermodynamics, vol. 3*. (Ed. M.C.A. Sandino, and E. ÖSTHOLS) Amsterdam: North-Holland; 1999, pp. 74.
[27] Schulte, E.H., Scoppa, P., Sources and behavior of technetium in the environment, *Science of The Total Environment, 64* (1987), 1-2, pp. 63-179
[28] Takeno, N., *Atlas of Eh−pH diagrams*, National Institute of Advanced Industrial Science and Technology (2005)
[29] Schultz, F.A., Duncan, C.T., Rigsby, M.A., Encyclopedia of electrochemistry, vol. 7a, in: *Inorganic electrochemistry* (Ed: F. Scholz, Ch.J. Pickett), Wiley-Ch, 2006, pp 435-443
[30] Kuznetsov, V. V., Chotkowski, M., Poineau, F., Volkov, M.A., German, K., Filatova, E.A., Technetium electrochemistry at the turn of the century, *Journal of Electroanalytical Chemistry 893* (2021) pp.115284
[31] Anders, E., Radiochemistry of technetium, USAEC Report, NAS-NS-3021, National Academy of Sciences, Springfield, VA, 1960

[32] Kim, E., Benedetti, M.F., Boulegue, J., Removal of dissolved rhenium by sorption onto organic polymers: study of rhenium as an analogue of radioactive Technetium, *Water Research, 38* (2004), pp. 448–454
[33] Till, J.E., Source term for technetium from muclear fuel cycle facilities, in: *Technetium in the Environment*, (Eds. G. Desmet, C. Myttenaere) Elsevier, London, 1986, pp. 1–20
[34] Shi, K., Houa, X., Roos, P., Wub, W., Determination of technetium-99 in environmental samples: A review; *Analytica Chimica Acta 709* (2012), pp. 1–20.
[35] Kopytin, A.V., German, K.E., Zhizhin, K. Yu., Tyuremnov, A.V., Zhukova, T.V., Il'in, E.G., An ion selective electrode for the determination of pertechnetate ions, *Journal of Analytical Chemistry, 75* (2020), 6, pp. 829–834
[36] Dorokhov, A.V., German, K.E., Peretrukhin, V.F., Kopytin, A.V., Pyatova, E.N., Burtsev, M.Yu., Simonoff, M., Tsivadze, A. Yu., An Ion-Selective Plasticized PVC Membrane Electrode for Tc(VII) Determination, *Doklady Physical Chemistry, 393* (2003), pp. 331-333
[37] Kopytin, A.V., German, K.E.. Zhizhin, K.Y., Safonov, A.V., Zhukov, A.F., Shpigun, L.K., A tetradecylphosphonium compounds–based membrane sensor for potentiometric quantitation of pertechnetate-ions in cementitious radioactive waste, *Sensors and Actuators B: Chemical, 310* (2020) 127853
[38] Holm, E., Gafvert, T., Lindhal, P., Roos, P., In situ sorption of technetium using activated carbon, *Applied Radiation and Isotopes, 53* (2000), pp. 153-157.
[39] Wang, Y., Gao, H., Yeredla, R., Xu, H., Abrecht, M., Control of Pertechnetate Sorption on Activated Carbon by Surface Functional Groups, *Journal of Colloid and Interface Science, 305* (2007), 209-217
[40] Rajec, P., Galamboš, M., Dano, M., Rosskopfova, O., Čaplovičova, M., Hudec, P., Horňáček, M., Novak, I., Berek, D., Čaplovič, L., Preparation and characterization of adsorbent based on carbon for pertechnetate adsorption, *Journal of Radioanalytical and Nuclear Chemistry, 303* (2015), pp. 277–286
[41] Gu B., Brown, G.M., Bonnesen, P.V., Liang, L., Moyer, B.A., Ober, R., Alexandratos, S.D., Development of Novel Bifunctional Anion-Exchange Resins with Improved Selectivity for Pertechnetate Sorption from Contaminated Groundwater, *Environmental Science and Technology, 34* (2000), 6, pp.1075–1080
[42] Demir, F., Lacin O., Bastaban B., Determined of Equilibrium Adsorption Isotherm Model Pertechnetate Oxoanion Onto Activated Carbon, *Sinop Uni J Nat Sci* 4 (2019), pp. 37-46
[43] Watson, J. H. P., Ellwood, D. C., The Removal of Pertechnetate ion and actinides from Radioactive Waste streams at Hanford, Washington, USA and Sellafield, Cumbria, UK: The Role of Iron-Sulfide-containing Adsorbent materials, *Nuclear Engineering and Design, 226* (2003) pp.375.
[44] Chen, J., Veltkamp, J. C., Pertechnetate removal by macroporous polymer impregnated with 2-nitrophenyl octyl ether (NPOE), *Solvent Extraction and Ion Exchange, 20* (2002), pp. 515-524
[45] Liang, L., Gu, B., Yin, X., Removal of Technetium-99 from Contaminated Groundwater with Sorbents and Reductive Materials, *Separations Technology, 6* (1996) pp. 111-122
[46] Chen, Q. J., Dahlgaard, H., Hansen, H. J. M., Aarkrog, A., Determination of ^{99}Tc in environmental samples by anion exchange and liquid-liquid extraction at controlled valency, *Analytica Chimica Acta, 228* (1990), pp. 163-167
[47] Suzuki, T., Fujii, Y., Yan, W., Mimura, H., Koyama, S., Ozawa, M., Adsorption behavior of VII group elements on tertiary pyridine resin in hydrochloric acid solution, *Journal of Radioanalytical and Nuclear Chemistry, 282* (2009), pp.641
[48] Hughes, L. D., DeVol, T. A., Characterization of a Teflon coated semiconductor detector flow cell for monitoring of pertechnetate in groundwater, *Journal of Radioanalytical and Nuclear Chemistry 267* (2006), pp. 287-295
[49] Duffey, C., King, W., Hamm, L., Determination of Perrhenate Adsorption Kinetics from Hanford Waste Simulants Using Superling 639 Resin; Westinghouse Savannah River Company: Aiken, SC, 2002.
[50] Nash, C., Musall, B., Morse, M., McCabe, D., Characterization of Super Lig 639 Rhenium and Technetium Resin with Batch Contact and Column Tests, *Separation Science and Technology, 50* (2015), 18, pp. 2881-2887

[51] Gu, B., Dowlena, K. E., Liang, L., Clausenb, J. L., Efficient separation and recovery of technetium-99 from contaminated groundwater; Separations Technology 6 (1996) 123-132.
[52] Yang, J., Shi, K., Wu, F., Tong, J., Su, Y., Liu, T., He, J., Mocilac, P., Hou, X., Wu, W., Shi, W., Technetium-99 decontamination from radioactive wastewater by modified bentonite: batch, column experiment and mechanism investigation, *Chemical Engineering Journal, 428* (2022), 131333
[53] Bond, A.H., Gula, M.J., Harvey, J.T., Duffey, J.M., Horwitz, E.P., Griffin, S.T., Rogers, R.D., Collins, J.L., Flowsheet Feasibility Studies Using ABEC Resins for Removal of Pertechnetate from Nuclear Wastes, *Industrial and Engineering Chemistry Research, 38* (1999), pp. 1683-1689
[54] Bonnesen, P. V., Brown, G. M., Alexandratos, S. D., Bavoux, L. B., Presley, D. J., Patel, V., Ober, R., Moyer, B. A., Development of Bifunctional Anion-Exchange Resins with Improved Selectivity and Sorptive Kinetics for Pertechnetate: Batch-Equilibrium Experiments, *Environmental Science and Technology, 34* (2000), 7, pp. 3761–3766.
[55] Sarri, S., Misaelides, P., Zamboulis, D. et al. Rhenium(VII) and technetium(VII) separation from aqueous solutions using a polyethylenimine–epichlorohydrin resin, *Journal of Radioanalytical and Nuclear Chemistry, 307* (2016), pp. 681–689
[56] Zu, Jian-Hua, Yue-ZhouYe, Mao-Song, Liu Rui-Qin, Preparation of a new anion exchanger by pre-irradiation grafting technique and its adsorptive removal of rhenium (VII) as analogue to Tc-99, *Nuclear Science and Techniques 26* (2015), pp. 69-75
[57] Katayev, E.A., Kolesnikov G.V., Sessler, J.L., Molecular recognition of pertechnetate and perrhenate, *Chemical Society Reviews, 38* (2009), pp. 1572–1586
[58] Goh, K. H., Lim, T. T., Dong, Z., Application of layered double hydroxides for removal of oxyanions: a review, Water Research, 42 (2008), pp. 1343−1368
[59] Kang, M.J., Rhee, S.W., Moon, H., Neck, V., Fanghanel, T., Sorption of MO_4^- (M = Tc, Re) on Mg/Al layered double hydroxide by anion exchange, *Radiochimica Acta, 75* (1996), pp. 169–173
[60] Kang, M.J., Chun, K.S., Rhee, S.W., Do, Y., Comparison of sorption behavior of I^- and TcO_4^- on Mg/Al layered double hydroxide, *Radiochimica Acta, 85* (1999), pp. 57–63
[61] Bryan, C.R., Wang, Y., Xu, H., Braterman, P.S., Gao, H., As, Se, and Re sorption by Mg–Al layered double hydroxides. In: *Proceedings* of the Materials Research Society Symposium, Boston, MA, USA, 2003, pp. 671–676
[62] Wang, Y., Gao, H., Compositional and structural control on anion sorption capability of layered double hydroxides (LDHs). *Journal of Colloid and Interface Science, 301* (2006), pp. 19–26
[63] Koivula R., Harjul, R., Selective Sorption of Technetium on Antimony-Doped Tin Dioxide, *Separation Science and Technology, 46* (2011), pp. 315–320
[64] Abdellah, W.M., El-Ahwany, H.I., El-Sheikh, R., Removal of Technetium (^{99}Tc) from Aqueous Waste by Manganese Oxide Nanoparticles Loaded into Activated Carbon; *Journal of Analytical Sciences, Methods and Instrumentation, 10* (2020), pp.12-35
[65] Abdellah1, W.M., Ezzat, A., Samir, I., Removal of Pertechnetate ($^{99}TcO_4^-$) from Liquid Waste by Magnesium Ferrite ($MgFe_2O_4$) Nanoparticles Synthesized Using Sol-Gel Auto Combustion Method, *Open Journal of Applied Sciences, 9* (2019), pp 68-86
[66] Ding, Q., Ding, F., Qian, T., Zhao, D., Wan, L., Reductive Immobilization of Rhenium Soil and Groundwater Using Pyrite Nanoparticles, *Water, Air, and Soil Pollution, 226* (2015), pp. 1-10.
[67] Lenell, B. A., Arai, Y., Perrhenate sorption kinetics in zerovalent iron in high pH and nitrate media. *Journal of Hazardous Materials, 321* (2017), pp. 335−343.
[68] King, W. D., Hassan, N. M., Mccabe, D. J., Hamm, L. L., Johnson, M. E. Technetium removal from Hanford and Savannah River Site actual tank waste supernates with SuperligR 639 resin. *Separation Science and Technology, 38* (2003), pp.3093–3114
[69] Taylor-Pashow, K. M. L., McCabe, D. J., Nash, C. A., Tc removal from the waste treatment and immobilization plant low-activity waste vitrification off-gas recycle, *Separation Science and Technology*, 53, (2018), Proceedings of the 19th Symposium on Separate Science and Technology for Energy Applications, pp. 1925-1934
[70] Sheng, G., Tang, Y., Linghu, W., Wang, L., Li, J., Li, H., Wang, X., Huang, Y., Enhanced immobilization of ReO_4^- by nanoscale zerovalent iron supported on layered double hydroxide via an advanced XAFS approach: implications for TcO_4^- sequestration, *Applied Catalysis B: Environmental, 192* (2016), pp. 268−276

[71] Chen, Li, J., Zhang, R. Wang, X., Reductive immobilization of Re(VII) by graphene modified nanoscale zero-valent iron particles using a plasma technique. *Science China Chemistry*, *59* (2016), pp. 150–158
[72] Islamoglu, T., Goswami, S., Li, Z., Howarth, A. J., Farha, O. K., Hupp, J. T., Postsynthetic Tuning of Metal-Organic Frameworks for Targeted Applications, *Accounts of Chemical Research*, *50* (2017), 4, pp. 805−813
[73] Banerjee, D., Xu, W., Nie, Z., Johnson, L.E.V., Coghlan, C., Sushko, M.L., Kim, D., Schweiger, M.J., Kruger, A.A., Doonan, C.J., Thallapally, P.K., Zirconium-Based Metal−Organic Framework for Removal of Perrhenate from Water, *Inorganic Chemistry*, 55 (2016), 17, pp. 8241–8243
[74] Desai, A. V.; Manna, B.; Karmakar, A.; Sahu, A.; Ghosh, S. K. A Water-Stable Cationic Metal-Organic Framework as a Dual Adsorbent of Oxoanion Pollutants, *Angewandte Chemie International Edition*, *55* (2016), 27, pp. 7811−7815
[75] Sheng, D., Zhu, L., Xu, C., Xiao, C., Wang, Y., Wang, Y., Chen, L., Diwu, J., Chen, J., Chai, Z., Albrecht-Schmitt, T. E., Wang, S., Efficient and Selective Uptake of TcO_4^- by a Cationic Metal-Organic Framework Material with Open Ag^+ Sites, *Environmental Science and Technology*, *51* (2017), 6, pp. 3471-3479
[76] Banerjee, D., Elsaidi, S. K., Aguila, B., Li, B. Kim, D., Schweiger, M. J., Kruger, A. A., Doonan, C. J., Ma, S., Thallapally, P. K., Removal of Pertechnetate-Related Oxyanions from Solution Using Functionalized Hierarchical Porous Frameworks, Chemistry A European Journal. 22 (2016), 49, pp. 17581−17584
[77] Banerjee, D., Xu, W., Nie, Z., Johnson, L. E., Coghlan, C., Sushko, M. L., Kim, D., Schweiger, M. J., Kruger, A. A., Doonan, C. J., Thallapally, P. K., Zirconium-Based Metal-Organic Framework for Removal of Perrhenate from Water, Inorganic Chemistry, 55 (2016), 17, pp. 8241−8243
[78] Zhu, L., Sheng, D., Xu, C., Dai, X., Silver, M. A., Li, J., Li, P., Wang, Y., Wang, Y., Chen, L., Xiao, C., Chen, J., Zhou, R., Zhang, C., Farha, O. K., Chai, Z., Albrecht-Schmitt, T. E., Wang, S., Identifying the Recognition Site for Selective Trapping of $^{99}TcO_4^-$ in a Hydrolytically Stable and Radiation Resistant Cationic Metal−Organic Framework, *Journal of the American Chemical Society*, *139* (2017), 42, pp. 14873−14876

Journal of Innovative Materials in Extreme Conditions
2023
Volume 4
Issue 1

ZrB_2-SiC COMPOSITES WITH RARE-EARTH OXIDE ADDITIVES

Hakan Ünsal[1], Zuzana Fürdősová[1], Zdeněk Chlup[2], Monika Tatarková[1], Alexandra Kovalčíková[3], Michal Hičák[1], Naser Hosseini[1], Inga Zhukova[1], Ivo Dlouhý[2], Pavol Šajgalík[1], [1]Peter Tatarko[1]
[1]Institute of Inorganic Chemistry, Slovak Academy of Sciences, Dúbravska cesta 9, 845 36, Bratislava, Slovak Republic
[2]Institute of Physics of Materials, Academy of Sciences of the Czech Republic, Žižkova 22, 61662 Brno, Czech Republic
[3]Institute of Materials Research, Slovak Academy of Sciences, Watsonova 49, 04001, Košice, Slovak Republic

Abstract: *The effect of different content (2, 5, and 10 wt.%) of two different types of rare earth (RE) oxides (Eu_2O_3 and Lu_2O_3) on the sintering, microstructure, room temperature mechanical properties, and ablation resistance of ZrB_2-25vol.% SiC ceramics were investigated. The materials were prepared using non-reactive Field Assisted Sintering Technology (FAST) in the temperature range of 1950°C – 2050°C, with a pressure of 70 MPa and a dwell of 7 min. No significant effect of the addition of 2 and 5 wt.% RE_2O_3 on the microstructure and the room temperature mechanical properties (hardness, indentation fracture toughness, and flexural strength) were observed. On the other hand, the coarser microstructures led to the deterioration of flexural strength and the hardness of the composites sintered with 10 wt.% RE_2O_3. The ablation resistance of the materials (tested up to ~ 2670°C) gradually increased with the increasing amount of RE oxides. The material with 10 wt.% Lu_2O_3 showed the best ablation resistance among all of the investigated compositions, with more than two times a lower ablation rate than that of the reference ZrB_2-25vol.%SiC.*
Keywords: *ultra-high temperature ceramics; zirconium diboride; rare-earth additives; mechanical properties; ablation resistance*

1. Introduction

Zirconium diboride (ZrB_2), similar to other so-called Ultra-High Temperature Ceramics (UHTC), has a high melting temperature (above 3000°C), good thermal and electric conductivity, good oxidation resistance and strength at elevated temperatures [1]. Such materials are used for applications performing at high temperatures, such as rocket propulsion, or thermal protection system for sharp leading edges of hypersonic vehicles [1, 2]. Although ZrB_2 has an extremely high melting temperature (3246°C), monolithic ZrB_2 has limited oxidation resistance [3, 4], as during oxidation in the air above 1000°C, B_2O_3 (one of the oxidation products of ZrB_2) starts evaporating, and the porous ZrO_2 layer (second oxidation product of ZrB_2) is the only phase remaining after the oxidation above 1500°C [5]. In addition, the phase transformation of ZrO_2 (1000-1200°C) leads to the volume change and the increased porosity of the layer, which significantly accelerates the oxidation rate [6].
Silicon carbide (SiC) is one of the most commonly used additives to improve the oxidation resistance of monolithic ZrB_2 ceramics. During oxidation, it forms a borosilicate glass on the surface of ZrB_2-SiC, which reduces oxygen permeation [1]. For this reason, ZrB_2 - SiC composites have been considered the most promising material systems for ultra-high-temperature environments [7]. However, the borosilicate layer can be protective only in a non-air-flowing atmosphere. Under the action of strong heat flux and high pressure, the formed silica may volatilize quickly and be blown away by high-speed airflow, leaving porous ZrO_2 on the surface of materials [8]. Since new materials for hypersonic applications need to meet the strict requirements of the aerospace industry to withstand temperatures above 2000°C, the further improvement of oxidation/ablation resistance of ZrB_2-based ceramics is still one of the most important challenges to broaden their application potential.
Therefore, the aim of the work was to investigate the effect of various amounts (2, 5, and 10 wt.%) of rare-earth oxide additives (Eu_2O_3, Lu_2O_3) on the mechanical properties of ZrB_2-25vol.%SiC materials, including their ablation resistance. It is well known that the refractoriness of the rare-earth oxides increases with the increasing cation field strength, which increases with the decreasing ionic radius of RE^{3+} (i.e. with the increasing atomic number in the periodic table) [9]. Therefore, Lu_2O_3 was chosen

[1] Corresponding author: peter.tatarko@savba.sk

as the rare-earth with the smallest radius of RE^{3+} [10], while its effect on the properties of ZrB_2-based ceramics was compared to the effect of RE from the middle of the lanthanide group (Eu_2O_3).

2. Experimental procedure

Commercially available powders of ZrB_2 (d50 ~1.5-3.0 μm, grade B, H.C. Starck), β-SiC (d50 ~0.6 μm Superior Graphite, β-SiC), and rare earth oxides, such as Eu_2O_3 and Lu_2O_3, (d50 ~3.0-15.0 μm, Treibacher,) were used as the raw materials. The ZrB_2/SiC ratio was kept constant (75 vol.% ZrB_2/25 vol.% SiC), while the amount of rare-earth oxides was 2, 5, or 10 wt.%. The powder mixtures were prepared by a planetary ball mill (Retsch PM 100) using tungsten carbide (WC) milling media and isopropanol as the solvent. The rotation speed and the milling time were 150 rpm and 6 h, respectively. The reference ZrB_2-25vol.%SiC sample without rare-earth sintering additives was also prepared for the sake of comparison.

The dried milled powders were uniaxially pressed in a graphite die with a diameter of 20 mm at a pressure of 30 MPa. The sintering was performed using Field Assisted Sintering Technology (DSP 507, Dr. Fritsch GmbH.) at the temperature range of 1950-2050°C and the pressure of 70 MPa in Argon atmosphere. Both the heating and cooling rates were 100°C/min, while the dwell time was 7 minutes. The density was measured by the Archimedes method.

The microstructures of the materials were investigated using SEM (AURIGA Compact, Zeiss). The crystalline phases were identified using X-ray diffraction (Panalytical Empyrean, Cu Kα radiation), followed by the Rietveld analysis using HighScore Plus software. The hardness and the indentation fracture toughness were evaluated using a Vickers indentation (ZWICK ROELL Z2,5), at the load of 9.81 N. The indentation fracture toughness was calculated using the formula proposed by Anstis et al. [11]. The ablation resistance of the materials was investigated by an oxyacetylene flame up to the maximum temperature of about 2660°C, measured on the surface of the materials by an optical pyrometer. The distance between the torch nozzle and the sample was 15 mm. While keeping the distance between the nozzle and the sample constant, the gas flows were changed in three steps with the C_2H_2:O_2 ratio of 1.2:1.5, 3:4, and 8:12 L/min. The dwell time at the maximum temperature was 60 s. The ablated surfaces of the specimens were observed using a confocal microscope (Lext OLS 3100, Olympus) to determine the maximum depth of the ablated zone. The maximum depth was then used to calculate the linear ablation rates of the materials when divided by the dwell time at the maximal temperature (60 s).

3. Results and discussions

a. Microstructure analysis

The addition of both Eu_2O_3 and Lu_2O_3 significantly improved the densification of ZrB_2-ceramics. While the temperature of 2050°C was necessary to use to obtain near-fully dense reference ZrB_2-25vol.% SiC materials, the maximum sintering temperature could be lowered to 2000°C after the addition of 2 and 5 wt.% RE_2O_3 to obtain the materials with similar relative densities (> 98 wt.%). The addition of 10 wt.% RE oxides further enhanced densification, and near-fully dense materials were obtained at an even lower temperature (1950°C) when compared to the materials with 2 and 5 wt.% RE_2O_3 (2000°C) or the reference ZrB_2-SiC sample (2050°C). It should be pointed out that when the ZrB_2-SiC composites with 10 wt.% RE_2O_3 were sintered at temperatures above 1950°C, and the formation of a liquid phase coming out of the die was observed during sintering.

Using the optimized sintering parameters, all of the materials were near-fully dense, having relative densities above 98 % (Table 1). The SEM analysis of the microstructures revealed the presence of uniformly distributed SiC particles (dark grey phase in Figure 1) in the ZrB_2 matrix (light grey phase in Figure 1). The materials sintered with Lu_2O_3 contained a less number of pores when compared to the materials with Eu_2O_3, which corresponds well to the relative densities of the samples. The number of elongated SiC grains increased with the increasing amount of additives, and they became predominant when 10 wt.% additives were used. This suggests that the phase transformation of SiC grains occurred during sintering, as a consequence of the presence of a greater amount of a liquid phase (RE_2O_3), which always promotes the phase transformation of SiC [12, 13]. The greater amount of the liquid phase also promoted grain growth during sintering, leading to the significantly coarser

microstructures of the composite sintered with 10 wt.% RE oxides when compared to the materials with 5 wt.% or 2 wt.% additives (Figure 1).

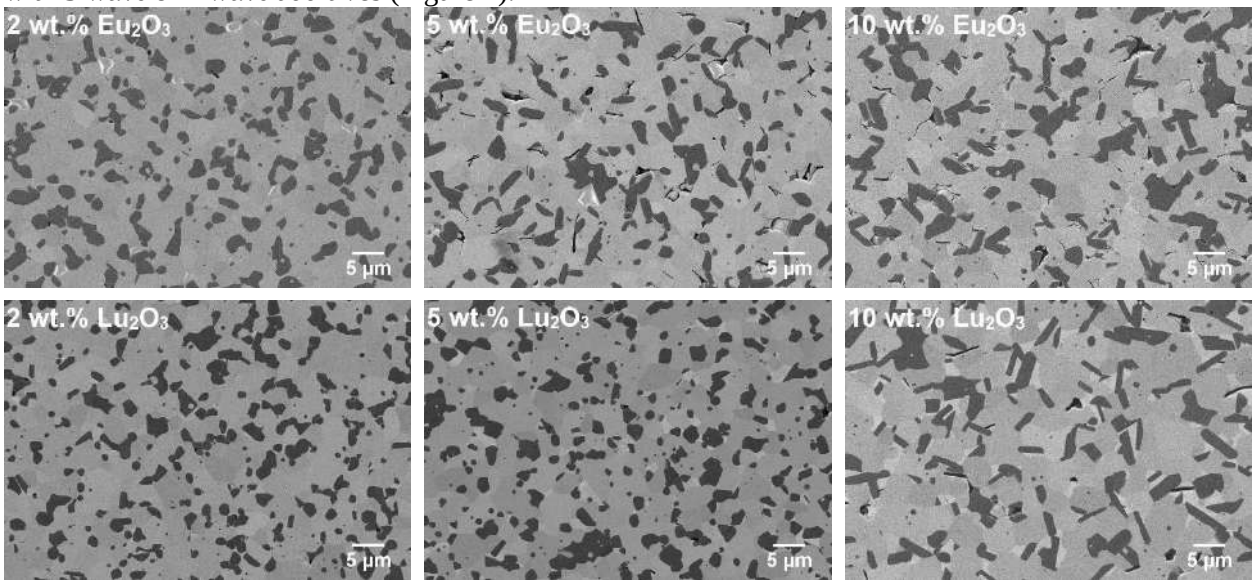

Figure 1. SEM microstructures of ZrB_2-25vol.%SiC composites sintered with different types and amounts of RE_2O_3.

b. Room temperature mechanical properties

The room temperature mechanical properties of the reference ZrB_2-25vol.%SiC material and the ZrB_2-25vol.%SiC composites with different content of RE oxides, such as hardness, indentation fracture toughness, and flexural strength, are given in Figure 2a, 2b, and 2c, respectively. In general, the hardness and strength of the materials decreased with the increasing amount of additives, while the indentation fracture toughness increased. However, it can be concluded that no significant effect of the addition of 2 wt.% and 5 wt.% RE oxides on the room temperature mechanical properties of the composites was observed, as the values were similar to those measured for the reference ZrB_2-25vol.%SiC sample without RE oxides. On the other hand, the addition of 10 wt.% RE oxides resulted in a more significant effect on the mechanical properties of ZrB_2-25vol.%SiC composites. The significantly coarser microstructures of the composites with 10 wt.% RE_2O_3 led to the deterioration of both the hardness and the strength of the materials. On the contrary, the presence of larger ZrB_2 grains and the elongated SiC grains resulted in the increased indentation fracture toughness of the samples with 10 wt.% RE_2O_3.

Although no significant difference between the mechanical properties of ZrB_2-25vol.%SiC sintered with Eu_2O_3 and Lu_2O_3 additives was observed, still the composites sintered with Lu_2O_3 exhibited slightly better room temperature mechanical properties (Figure 2). This can be attributed either to the higher relative density of the composites sintered with Lu_2O_3 additive or to the higher cationic field strength (CFS) of the Lu-based grain boundary phase, which increases with a decreasing ionic radius of RE^{3+} [14, 15].

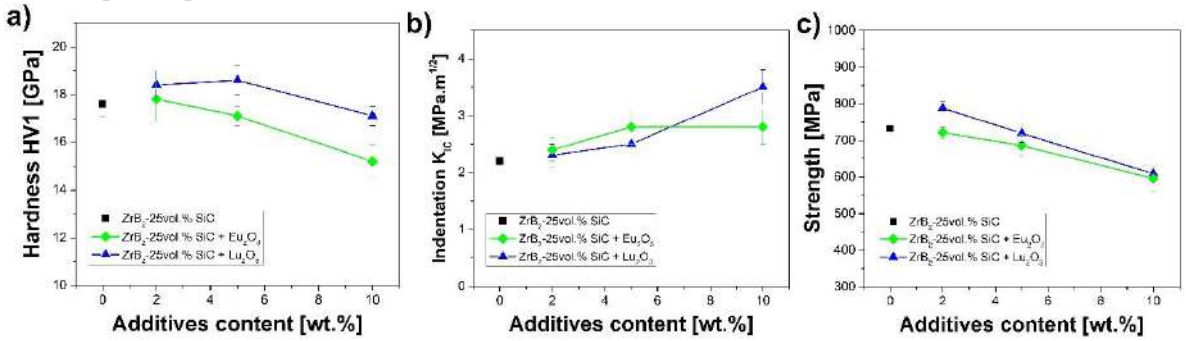

Figure 2. Hardness (a), indentation fracture toughness (b), and strength (c) of ZrB_2-25vol.%SiC composites sintered with different content of RE_2O_3 (RE = Eu, or Lu).

c. Ablation resistance

The high-temperature properties of the materials were evaluated in terms of the ablation tests up to the temperature of ~ 2600°C using an oxyacetylene flame. Figure 3 shows the examples of temperature profiles recorded during the test of the reference ZrB_2-25vol.%SiC system and the composites sintered with 5wt.% Eu_2O_3 and Lu_2O_3. The maximum temperature was reached within the three steps, while each step corresponded to the change of the gas flows, as described in the experimental procedure part. It should be pointed out that the materials were exposed to the extremely rapid heating of ~ 90°C/s, as in the final stage the temperature measured on the surface of the samples raised from ~ 1800°C to ~ 2500°C within approximately 8 s, followed by a slight steady increase of the temperature up to ~ 2670°C during the dwell of 60 s. Besides the extreme heating rate, the samples were also exposed to rapid cooling with a rate of 180-200°C/s. Figure 3 also demonstrates that all the materials were tested at the same conditions.

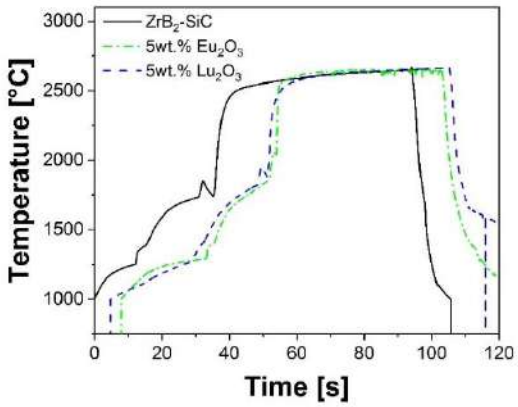

Figure 3. Temperature profile recorded during the oxyacetylene ablation test of the reference ZrB_2-25vol.%SiC material and the ZrB_2-25vol.%SiC composites sintered with 5 wt.% Eu_2O_3 and Lu_2O_3.

The macro-images of the surfaces of the samples after the ablation test are shown in Figure 4. The reference ZrB_2-25vol.%SiC sample was the only composition that cracked upon cooling from the maximum temperature. All of the other samples survived harsh testing conditions without cracking. The surface of the specimens was covered by a yellowish oxide layer, and the central part of the samples showed a significant ablation. Since the nozzle of the oxyacetylene torch was aimed at the center of the samples, both the maximum temperature and the maximum gas pressure resulted in the melting and splashing of the material from the central region. However, both the ablation and the splashing became less significant with the increase of the additive content (Figure 4).

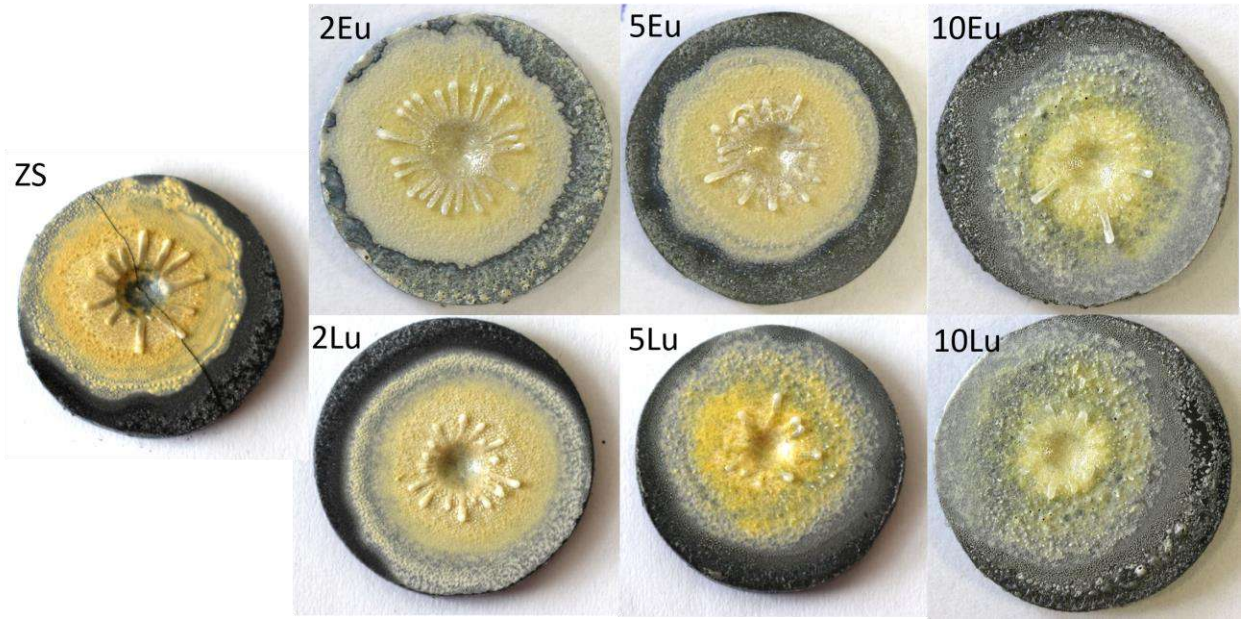

Figure 4. Macro-images of the surface of the ZrB_2-25vol.%SiC materials with different types and content of the additives after the oxyacetylene ablation test at ~ 2670°C for 60 s. All of the samples had a diameter of 20 mm.

The maximum height profiles of the ablated materials, determined by confocal microscopy, are given in Figure 5. The maximum ablated depth continuously decreased with the increasing amount of both Eu_2O_3 (Figure 5a) and Lu_2O_3 (Figure 5b) additives. In other words, the higher the content of the RE oxides the better the ablation resistance of the materials. The maximum ablated depth was then used to determine the linear ablation rates of the individual materials, which are summarized in Table 1. The lowest maximum ablated depth (so the lowest linear ablation rate) was observed for the ZrB_2-25vol.%SiC sintered with 10 wt.% Lu_2O_3, which was more than two times lower than that of the reference ZrB_2-25vol.%SiC material without any RE oxides. More importantly, the material containing 5 wt.% Lu_2O_3 exhibited a similar maximum ablated depth (Figure 5) and the linear ablation rate (Table 1) as measured for the composite with 10 wt.% Eu_2O_3. This suggests the superior effect of the Lu_2O_3 additive on the improvement of ablation resistance of ZrB_2-25vol.%SiC materials over the effect Eu_2O_3 additive.

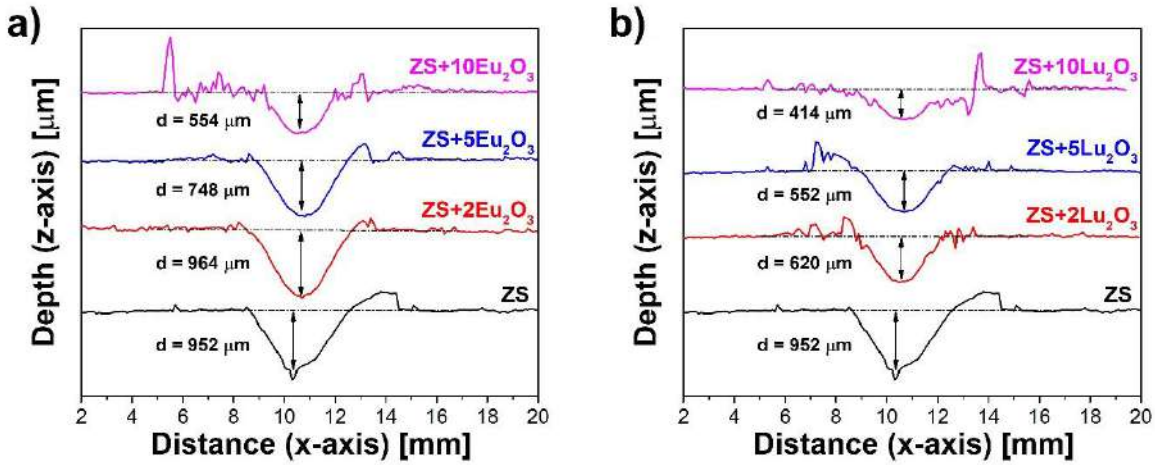

Figure 5. Maximum height profiles of the ZrB_2-25vol.%SiC materials with different content of a) Eu_2O_3 and b) Lu_2O_3 additives after the oxyacetylene ablation test at ~ 2670°C for 60 s.

Table 1. Relative densities, and linear ablation rates of ZrB_2-25vol.%SiC materials with different types (Eu_2O_3 and Lu_2O_3) and content (2, 5, and 10 wt.%) of additives after the oxyacetylene ablation test at ~ 2660°C for 60 s.

Material composition	Relative density [%]	Linear ablation rate [mm/s]
ZrB_2-25vol.%SiC	98.8	15.9×10^{-3}
ZrB_2-25vol.%SiC+2wt.%Eu_2O_3	99.0	16.1×10^{-3}
ZrB_2-25vol.%SiC+5wt.%Eu_2O_3	98.1	12.5×10^{-3}
ZrB_2-25vol.%SiC+10wt.%Eu_2O_3	98.5	9.2×10^{-3}
ZrB_2-25vol.%SiC+2wt.%Lu_2O_3	99.3	10.3×10^{-3}
ZrB_2-25vol.%SiC+5wt.%Lu_2O_3	99.8	9.2×10^{-3}
ZrB_2-25vol.%SiC+10wt.%Lu_2O_3	98.9	6.9×10^{-3}

The XRD patterns of the surfaces of the reference sample and the composites sintered with 10 wt.% RE_2O_3 after the ablation test by oxyacetylene flame at ~ 2670°C for 60 s are shown in Figure 6. While the oxide layer of the reference ZrB_2-25vol.%SiC sample was composed of monoclinic ZrO_2 phase (m-ZrO_2) only, tetragonal ZrO_2 (t-ZrO_2) was detected for the samples with 10 wt.% Eu_2O_3 and Lu_2O_3. This suggests the presence of RE_2O_3 in the microstructure of the base ZrB_2-25vol.% SiC material had a stabilizing effect to prevent the phase transformation of monoclinic ZrO_2 in the oxide layer upon cooling from the maximum temperature during the ablation test.

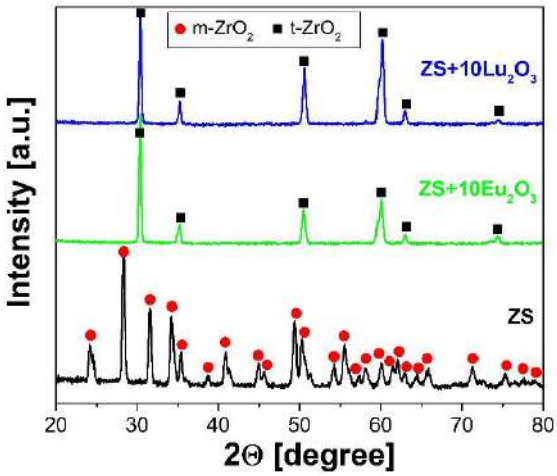

Figure 6. XRD patterns of the surfaces of ZrB_2-25vol.%SiC material and ZrB_2-25vol.%SiC sintered with 10 wt.% Eu_2O_3 and Lu_2O_3 additives after the oxyacetylene ablation test at ~ 2670°C for 60 s.

The back-scattered SEM images of the top surface of ZrB_2-25vol.%SiC with 10 wt.% Lu_2O_3 additive after the oxyacetylene ablation test is shown in Figure 7. Besides the presence of a few pores, the surface was covered by a compact oxide layer. The EDS analysis (not shown here) confirmed the presence of Zr and O_2 as the major elements in the oxide layer (in good agreement with the XRD results), while a small amount of Lu was also detected. Interestingly, the Lu element was homogenously distributed throughout the oxide layer without any significant concentration gradient observed (e.g. the concentration of Lu was 1.4 at.% and 1.2 at.% when detected in two different areas, shown as 1 and 2 in Figure 7b, respectively). Since no separated Lu-containing phases were observed in the oxide layer, the present results suggest that the formation of Lu-ZrO_2 solid solution occurred during the ablation test. This led to the stabilization of a high-temperature tetragonal modification of ZrO_2. The same effect is well known for the Y element in the commercially available Y-stabilized ZrO_2, and a similar stabilizing effect was recently reported for the ZrB_2-xSiC composites (x = 5, 10, 15, 18.5 vol.%) sintered with 5 wt.% Y_2O_3 [16]. The stabilization of t-ZrO_2 had a clear positive effect on the improvement of ablation resistance of ZrB_2-SiC materials, as the materials with 10 wt.% RE_2O_3 showed significantly lower ablation rates when compared to the reference material without any RE oxide additives.

Although the addition of both additives (Eu_2O_3 and Lu_2O_3) led to the stabilization of tetragonal ZrO_2, still the materials sintered with Lu_2O_3 showed a superior ablation resistance over the Eu_2O_3 additive. This can be explained by higher refractoriness of Lu_2O_3, as it is well known that the viscosity of RE-containing phases increases with a decreasing ionic radius of RE^{3+}. The increased viscosity then slows down the diffusion rate of oxygen through the protective surface oxide layer [9]. Therefore, the superior ablation resistance of ZrB_2-25vol.%SiC sintered with Lu_2O_3 can be attributed to the fact that the Lu_2O_3 additive has the smallest ionic radius (Lu^{3+}) among all of the RE oxides. A direct effect of the cation size of RE on the improvement of oxidation resistance was already reported for Si_3N_4-based ceramics [9], and the positive effect of RE oxides with a small RE^{3+} on the improvement of ablation/oxidation resistance of ZrB_2-SiC was clearly demonstrated in the present work. In order to reveal a clear mechanism, more detailed investigations, including SEM of cross-sections of the oxide layers and TEM analysis of the oxide layers will be carried out in the near future.

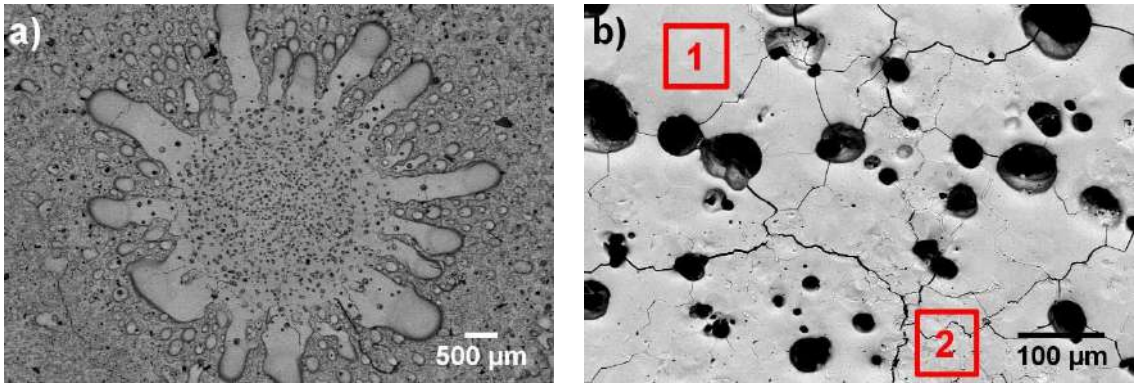

Figure 7. a) Back-scattered SEM images of the top surface of ZrB_2-25vol.%SiC with 10 wt.% Lu_2O_3 additive after the oxyacetylene ablation test at ~ 2660°C for 60 s; b) a higher magnification of the central part of the ablated zone.

4. Conclusions

Near-fully dense ZrB_2-25vol.%SiC with different content (2, 5, and 10 wt.%) of Eu_2O_3 and Lu_2O_3 additives were successfully prepared using the non-reactive FAST process at the temperature of 1950°C – 2050°C, and the pressure of 70 MPa. The following main conclusions can be made:

- The addition of RE oxides significantly improved the densification of ZrB_2-SiC, and the sintering temperature was lowered from 2050°C to 1950°C when 10 wt.% RE_2O_3 was used.
- Both the hardness and the flexural strength of the materials decreased with the increasing amount of RE_2O_3, while the indentation fracture increased. The materials with Lu_2O_3 showed slightly better room temperature mechanical properties because of their higher relative density and a higher cation field strength of the grain boundary phase.
- In general, no significant effect of RE oxides on the room temperature mechanical of ZrB_2-25vol.%SiC was observed up to 5 wt.% RE_2O_3. The coarser microstructures in the case of materials with 10 wt.% RE_2O_3 resulted in a more significant deterioration of the hardness and strength of the materials.
- The ablation resistance significantly increased with the increasing amount of RE_2O_3 additives. The addition of RE oxides stabilized the high-temperature tetragonal modification of ZrO_2 in the oxide layer.
- The material sintered with 10 wt.% Lu_2O_3 showed the best ablation resistance among all of the investigated compositions, as its linear ablation rate was more than two times lower (6.9 x 10^{-3} mm/s) when compared to the reference ZrB_2-SiC without any RE additives (15.9 x 10^{-3} mm/s).

Acknowledgment

P.T. has received funding from the European Union's Horizon 2020 research and innovation program under the Marie Sklodowska-Curie grant agreement No 798651. This work was supported by the Slovak Research and Development Agency under contract no. APVV-17-0328 and APVV-21-0402. The support of the Mobility project SAV-AVCR-21-04, VEGA project No. 2/0116/22, and JRP SAV TUBITAK project No. 546676 are also greatly acknowledged.

References

[1] W.G. Fahrenholtz, E.J. Wuchina, W.E. Lee, Y. Zhou: Ultra-high temperature ceramics – Materials for extreme environment applications, John Wiley & Sons, Inc., Hoboken, New Jersey (2014), ISBN 978-1-118-70078-5

[2] B. Berton, M. Bacos, D. Demange and J. Lahaye, "High-temperature oxidation of silicon carbide in simulated atmospheric re-entry conditions", J. Mater. Sci. vol. 27, pp. 3206-3210, 1992.

[3] M. A. Levinstein, in Proceedings of Metallurgical Society Conference on Refractory Metals and Alloys, Chicago, edited by M. Semchysen and I. Perlmutter (Interscience Publishers, New York, London, 1963).

[4] A. K. Kuriakose and J. L. Margrave, "The oxidation kinetics of zirconium diboride and zirconium carbide at high temperatures," J. Electrochem. Soc., vol. 111, no. 7, pp. 827-831, 1964.

[5] L. Kaufman, E. V. Clougherty and J. B. Berkowitz-Mattuck, "Oxidation Characteristics of Hafnium and Zirconium Diboride," Trans. Metall. Soc. AIME, vol. 239, no.4, pp.458–66, 1967.

[6] T. A. Parthasarathy, R. A. Rapp and M. Opeka, "Effects of phase change and oxygen permeability in oxide scale on oxidation kinetics of ZrB_2 and HfB_2," J. Am. Ceram. Soc., vol. 92, no.5, pp. 1079-1086, 2009.

[7] D.D. Jayaseelan, E. Zapata-Solvas, P. Brown, W.E. Lee: In situ formation of oxidation resistant refractory coatings on SiC-reinforced ZrB_2 ultra high temperature ceramics, J. Am. Ceram. Soc. 95[4] (2012)

[8] L. Luo, J. Liu, L. Duan, Y. Wang: Multiple ablation resistance of La_2O_3/Y_2O_3-doped C/SiC/ZrC composites, Ceram. Int. 41 (2015) 12878-12886

[9] P. Tatarko, M. Kašiarová, J. Dusza, P. Šajgalík: Influence of rare-earth oxide additives on the oxidation resistance of Si_3N_4-SiC nanocomposites, J. Eur. Ceram. Soc. 33[12] (2013) 2259-2268

[10] P. Tatarko, F. Valenza, H. Ünsal, A. Kovalčíková, J. Sedláček, P. Šajgalík, Design of Lu_2O_3-reinforced C_f/SiC-ZrB_2-ZrC ultra-high temperature ceramic matrix composites: Wetting and interfacial reactivity by $ZrSi_2$ based alloys, J. Eur. Ceram. Soc. 41[5] (2021) 3051-3060

[11] G.R. Anstis, P. Chantikul, B.R. Lawn, D.B. Marshall, A critical evaluation of indentation techniques for measuring fracture toughness: I, Direct crack measurements, J. Am. Ceram. Soc. 64 (1981) 533-538

[12] G. Zhan, R.J. Xie, M. Mitomo, Y.W. Kim, The effect of β→α phase transformation on the microstructural development and mechanical properties of fine-grained silicon carbide ceramics, J. Am. Ceram. Soc. 84[5] (2004) 945-950

[13] M. Nader, F. Aldinger, M.J. Hoffmann, Influence of the α/β-SiC phase transformation on microstructural development and mechanical properties of liquid phase sintered silicon carbide, J. Mat. Sci. 34 (1999) 1197-1204

[14] P. Tatarko, Š. Lojanová, J. Dusza, P. Šajgalík, Influence of various rare-earth oxide additives on microstructure and mechanical properties of silicon nitride based nanocomposites, Mat. Sci. Eng. A 527 (2010) 4771-4778.

[15] F. Lofaj, P. Hvizdoš, F. Dorčáková, R. Satet, M.J. Hoffmann, A.R. de Arellano-López, Indentation moduli and microhardness of RE-Si-Mg-O-N glasses (RE=Sc, Y, La, Sm, Yb and Lu) with different nitrogen content, Mat. Sci. Eng. A 357 (2003) 181-187

[16] S. Mungiguerra, A. Cecere, R. Savino, F. Saraga, F. Monteverde, D. Sciti, Improved aero-thermal resistance capabilities of ZrB2-based ceramics in hypersonic environment for increasing SiC content, Corros. Sci. 178 (2021) 109067

Journal of Innovative Materials in Extreme Conditions
2023
Volume 4
Issue 1

DFT STUDY OF CRYSTALLINE TiO_2 PHASE TRANSITIONS APPLICABLE IN EXTREME ENVIRONMENTS

Dušica Jovanović[1,2]*, Dejan Zagorac[1,3], Aleksandra Zarubica[2], Matej Fonović[4], Jelena Zagorac[1,3]

[1]*Institute of Nuclear Sciences Vinča, Materials Science Laboratory, University of Belgrade, Belgrade, Serbia*
[2]*Department of Chemistry, Faculty of Science and Mathematics, University of Niš, Niš, Serbia*
[3] *Center for Synthesis, Processing, and Characterization of Materials for Application in the Extreme Conditions-CextremeLab, Belgrade, Serbia*
[4]*Faculty of Engineering, University of Rijeka-RiTeh, Rijeka, Croatia*
Corresponding author: dusica.jovanovic011@gmail.com*

Abstract: *Crystalline TiO_2 has many practical applications as a photocatalytic material. The structures and relative energies of eleven different modifications of bulk structures with TiO_2 composition were theoretically investigated in this study. Calculations were performed by the DFT method with LDA-PZ functional as implemented in CRYSTAL17 code. Structural parameters, energy-volume curves and electronic band gaps were calculated and analyzed. This study aimed to gain insight into the electronic structure of various modifications of crystalline pristine TiO_2 and their phase transitions especially applicable at extreme pressure and temperature conditions. The information obtained in this study may contribute to future research on the structure and various properties (electronic, mechanical…) of such systems, as well as their potential application in various scientific fields and advanced technology.*

Keywords**:** *crystalline TiO_2, phase transitions, EV curves, DFT, ab initio*

1. Introduction

Titanium dioxide (TiO_2) is a widely investigated transition metal oxide, both experimentally and theoretically [1]. TiO_2 is attracting attention as a wide band gap semiconductor with photocatalytic properties and applicability in various fields (production of solar cells, decontamination of pollutants, elimination of microorganisms, suppression of cancer cells, etc.)[1-5]. Experimental and theoretical studies of this material can provide different data on the stability of certain crystal modifications and their transitions. In addition to the most known crystalline TiO_2 structures, anatase ($I4_1/amdz$) and rutile ($P4_2/mnm$), some modifications can be found in nature, theoretically simulated and obtained experimentally under certain conditions with the following space groups: *Pbca* (brookite), *C*2/*m* (TiO_2-B), $P2_1/c$ (ZrO_2), $P3_12_1$ (quartz-low), *Pa*-3 (pyrite), *Fm*-3*m* (fluorite), *Pbcn* (TiO_2-II), *P*-62*m* (Fe_2P type), *Pbnm* (TiO_2-R) [6-8], which structural parameters obtained experimentally or theoretically can be found in ICSD (Inorganic Crystal Structure Database) [9, 10]. The most thermodynamically stable TiO_2 modification is tetragonal rutile, but at elevated temperatures, metastable tetragonal anatase and metastable orthorhombic brookite irreversibly transform to rutile[1]. By investigating a wide range of TiO_2 modifications and their phase transitions, one can gain insight into their structure-property relation and the necessary conditions for future potential experimental/theoretical research [11-13]. The important information on their optical and electronic properties is a direct band gap energy value determined for rutile 3.02 eV and for anatase 3.2 eV [6-8, 14] which narrowing can be enabled by doping with different cations and anions [15-17]. In this theoretical study, we will present the structural parameters, band gap values, and energy-volume curves for different modifications of crystalline TiO_2.

2. Computational details

We have completed *ab initio* calculations using the CRYSTAL17 [18, 19] software package, which is based on the linear combination of atomic orbitals (LCAO) as the basis set. We have used all-electron basis sets (AEBS) for calculations – a [4s3p1d] for titanium [20, 21] and [4s3p] for oxygen [17, 22, 23]. Local optimizations have been performed by the density functional theory (DFT) method with exchange-correlation functional, local density approximation (LDA) with the Perdew–Zunger (PZ) correlation functional[24]. A search for structure candidates that might exist in extreme conditions has been conducted adopting experimental data as initial structures for calculations from the Inorganic Crystal Structure Database (ICSD) [9, 10]. It is of great importance to analyze the effect of extreme conditions on structural and electronic properties, as well as on the structure-property relationship.[25-28] All obtained results have been analyzed in the KPLOT software package [29] and visualized by the VESTA program [30].

3. Results and discussion

3.1. Structural properties of various bulk TiO_2 modifications

For TiO_2 composition, we have performed a data mining-based search of the Inorganic Crystal Structure Database (ICSD). In this way, we have found 11 different structure candidates for local optimization. Most of the candidates already exist for the TiO_2 composition (anatase, rutile, *Pbca* (brookite), *C*2/*m* (TiO_2-B), $P2_1/c$ (ZrO_2), $P3_12_1$ (quartz-low), *Pbcn* (TiO_2-II), *P*-62*m* (Fe_2P), *Pbnm* (TiO_2-R). Additionally, we have considered two more structure candidates with the general formula AB_2 that have been found in some common minerals: *Pa*-3 (pyrite), and *Fm*-3*m* (fluorite).

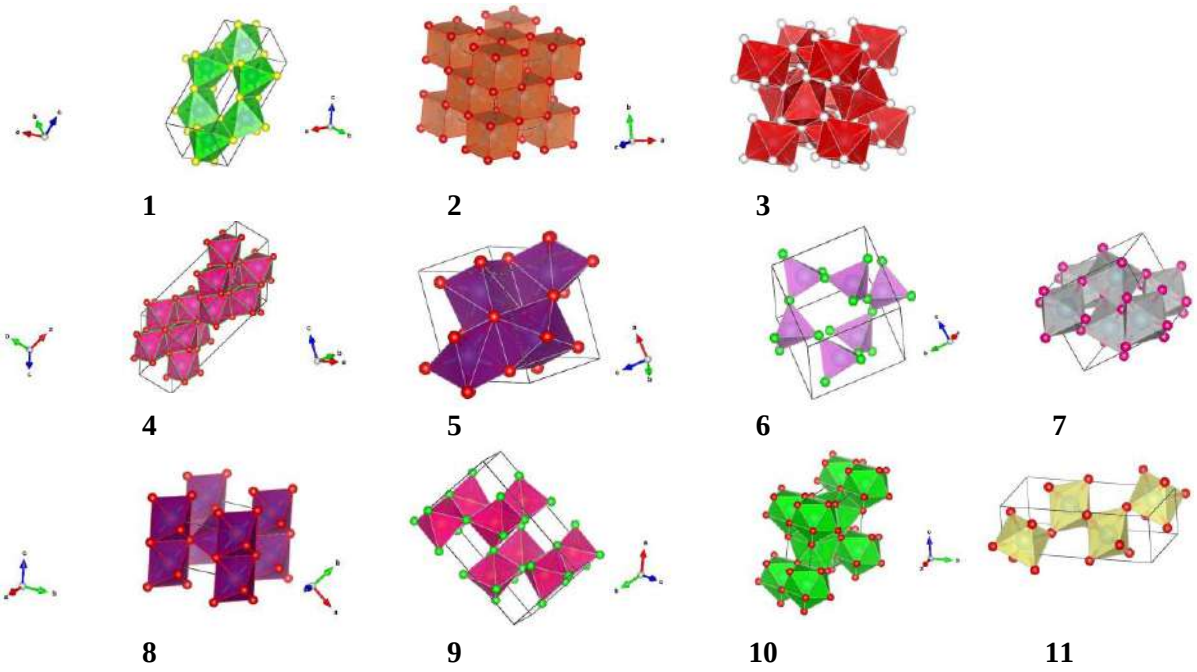

Figure 1. Structures of eleven different TiO_2 modifications: **1**) anatase, **2**) fluorite, **3**) pyrite, **4**) TiO_2-B, **5**) ZrO_2, **6**) quartz-low, **7**) TiO_2-II, **8**) rutile, **9**) brookite, **10**) Fe_2P, **11**) TiO_2-R, adopted from the ICSD database and visualized by VESTA program.

Figure 1 shows 11 different structure types that were considered as the starting modifications for TiO_2 composition during local *ab initio* optimization. Structures have been visualized in the

VESTA program.[30] For each structure shown above the coordination polyhedra around titanium cation and the connection between them differs.

Optimized structure parameters for 11 different starting structure types in TiO_2 and presented in Table 1. Furthermore, total energies per formula unit and detailed crystallographic analysis of the calculated structures using LDA-PZ functional and comparison to the experimental data from the ICSD database [9, 10] have been performed and presented in Table 1. Structures are ranked according to the total energy values in Hartrees (Ha). For each investigated modification, the band gap value has been also calculated and presented in Table 1.

Table 1. Experimental and calculated unit cell parameters, total energies per formula unit, and band gap energies of TiO_2 bulk crystalline modifications investigated by the DFT method and LDA-PZ functional, using CRYSTAL17 code

	Modification	Space group, unit cell parameters (Å) and atomic coordinates		Energy/ formula unit (Ha)	Band gap energy (eV)
		Experimental data	Calculated data		
1.	**TiO_2-II (Columbite)**	*Pbcn* (SG 60) a = 4.53, b = 5.50 c = 4.90 **Ti1** 0 0.1704 0.25 **O1** 0.2716 0.3814 0.4142	*Pbcn* (SG 60) a = 4.50, b = 5.41 c = 4.87 **Ti1** 0 0.6724 0.75 **O1** 0.2746 0.8820 0.9175	−997.1031	2.8
2.	**Rutile**	$P4_2/mnm$ (SG 136) a = 4.65, c = 2.96 **Ti1** 0 0 0 **O1** 0.305 0.305 0	$P4_2/mnm$ (SG 136)[a] a = 4.52, c = 2.94 **Ti1** 0 0 0 **O1** 0.6965 0.6965 0	−997.1018	1.9
3.	**ZrO_2**	$P2_1/c$ (SG 14) a = 4.87, b = 4.92 c = 5.11, β = 99.90 **Ti1** 0.276 0.058 0.217 **O1** 0.062 0.321 0.355 **O2** 0.449 0.759 0.459	$P2_1/c$ (SG 14) a = 4.72, b = 4.82, c = 4.95, β = 98.92 **Ti1** 0.276 0.542 0.211 **O1** 0.071 0.836 0.339 **O2** 0.443 0.258 0.476	−997.1008	2.5
4.	**Brookite**	*Pbca* (SG 61) a = 9.28, b = 5.52 ***c*** = 5.18 **Ti1** 0.129 0.092 0.862 **O1** 0.230 0.108 0.536 **O2** 0.010 0.149 0.183	*Pbca* (SG 61) a = 5.37, b = 5.10 c = 9.09 **Ti1** 0.597 0.854 0.629 **O1** 0.609 0.528 0.730 **O2** 0.649 0.182 0.513	−997.1006	2.7
5.	**TiO_2-B**	*C*2/*m* (SG 12) a = 12.19, b = 3.75 c = 6.53, β = 107.04 **Ti1** 0.196 0 0.292 **Ti2** 0.101 0 0.701 **O1** 0.142 0 0.025 **O2** 0.060 0 0.360 **O3** 0.365 0 0.298 **O4** 0.266 0 0.667	*C*2/*m* (SG 12) a = 12.17, b = 3.68 Å c = 6.49, β = 106.85 **Ti1** 0.805 0 0.712 **Ti2** 0.900 0 0.290 **O1** 0.863 0 0.996 **O2** 0.941 0 0.630 **O3** 0.638 0 0.701 **O4** 0.738 0 0.353	−997.0993	3.1
6.	**Anatase**	$I4_1/amdz$ (SG 141) a = 3.78 c = 9.53 **Ti** 0 0.25 0.3750 **O** 0 0.25 0.1678	$I4_1/amdz$ (SG 141)[a] a = 3.71 c = 9.69 **Ti** 0 0.25 0.8750 **O** 0.5 0.75 0.1701	−997.0983	2.7

7.	**TiO_2-R**	*Pbnm* (SG 62) *a* = 4.90, *b* = 9.46 *c* = 2.96 **Ti1** 0.935 0.137 0.25 **O1** 0.637 0.266 0.25 **O2** 0.208 −0.0276 0.25	*Pbnm* (SG 62) *a* = 5.21, *b* = 3.04 *c* = 6.09 **Ti1** 0.744 0.75 0.618 **O1** 0.859 0.75 0.927 **O2** 0.526 0.25 0.841	−997.0882	2.2
8.	**Fe_2P**	*P*-62*m* (SG 189**)** *a* = 5.33, *c* = 3.13 Å **Ti1** 0.3333 0.6667 0.5 **Ti2** 0 0 0 **O1** 0.263 0 0.5 **O2** 0.601 0 0	*P*-62*m* (SG 189**)** *a* = 5.24, *c* = 3.03 **Ti1** 0.333 0.667 0 **Ti2** 0 0 0.5 **O1** 0.261 0 0 **O2** 0.599 0 0.5	−997.0863	1.3
9.	**Pyrite**	*Pa*-3 (SG 205) *a* = 4.90 **Ti** 0 0 0 **O** 0.341 0.341 0.341	*Pa*-3 (SG 205) *a* = 4.81 **Ti** 0 0.5 0 **O** 0.659 0.159 0.341	−997.0839	1.6
10.	**Fluorite**	*Fm*-3*m* (SG 225) *a* = 4.84 **Ti** 0 0 0 **O** 0.25 0.25 0.25	*Fm*-3*m* (SG 225) *a* = 4.74 **Ti** 0 0 0 **O** 0.75 0.75 0.75	−997.0802	1.4
11.	**Quartz-low**	$P3_12_1$ (SG 152) *a* = 5.29, *c* = 6.13 **Ti1** 0.453 0 0.333 **O1** 0.408 0.303 0.215	$P6_422$ **(**SG 181) *a* = 5.70, *c* = 6.28 **Ti1** 0.5 0 0 **O1** 0.438 0.219 0.833	−997.0688	3.7

[a]**Ref. [17]**

Results of local *ab initio* optimization for eleven different TiO_2 crystalline modifications, using LDA-PZ, showed the lowest total energy calculated for the TiO_2-II (SG 60), suggesting it as the most stable modification. Under normal conditions, rutile is the most stable TiO_2 modification and according to the literature, it undergoes a first-order phase transition to a denser orthorhombic phase, TiO_2-II at pressures above 4 GPa and temperature above 400 °C. [31, 32] The TiO_2-II phase is also known as columbite and in previous research, it has been found that LDA functional produces a stability sequence, $E_{columbite} < E_{anatase} < E_{rutile}$.[33], as has been observed in our study. However, the LDA approximation in combination with the LCAO basis set could be a very good tool for the exploration of materials at extreme conditions of pressure and temperature.

It should be noted that the initial symmetry of the two different structure types (anatase and rutile) did not change after DFT structure optimization[17], while modification quartz-low (SG 152) become more symmetrical and appeared in space group $P6_422$ **(**SG 181), characteristic for quartz-high modification. These newly appeared space groups could be subgroups of the same structures, (or caused by the initial layer structure type adopted from the ICSD database).

Considering electronic properties and band gap values given in Table 1, we can see that all structure types exhibit semiconducting properties, where the lowest value for the band gap (1.3 eV) is found in Fe_2P modification and the highest value (3.7 eV) in the quartz-low modification. It can be noticed that the calculated band gap values for anatase (2.7 eV) and rutile (1.9 eV) were lower than the known, experimentally obtained values (3.2 for anatase and 3.02 for rutile), which is to be expected since DFT-LDA usually underestimates the size of the band gap.

3.2. Phase transitions of crystalline TiO_2 modifications

To further study the crystal structures and their relationship with energy versus volume, *E(V)* curves have been computed on the *ab initio* level (Figure 2). When comparing the minima of the total energy for seven selected different structure types in pure TiO_2, the TiO_2-II type appears to be the most stable. This structure type can exist in TiO_2 in a high-pressure regime[34]. The rutile structure type was found second according to total energy ranking. Brookite and anatase are also found in the negative pressure regions according to the *E(V)* diagram.

According to the enthalpy-pressure curves in Figure 3, the transition from the most stable TiO_2-II modification to the ZrO_2 modification appears at the pressure of 4 GPa. With further pressure increment, ZrO_2 modification can transform to TiO_2-R at approximately 23 GPa.

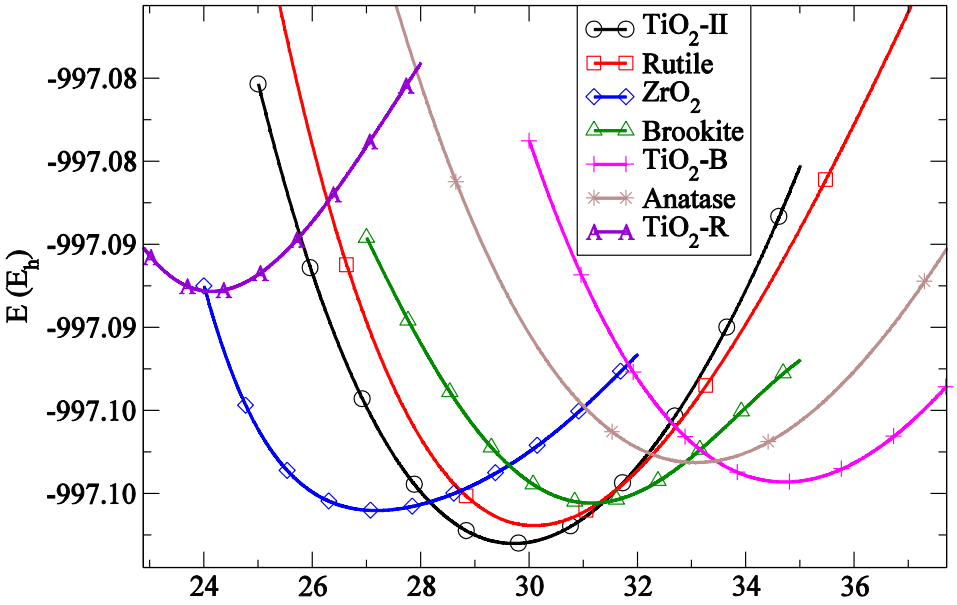

Figure 2. Energy-volume, *E(V)* curves of seven different crystalline TiO_2 modifications computed using LDA-PZ functional.

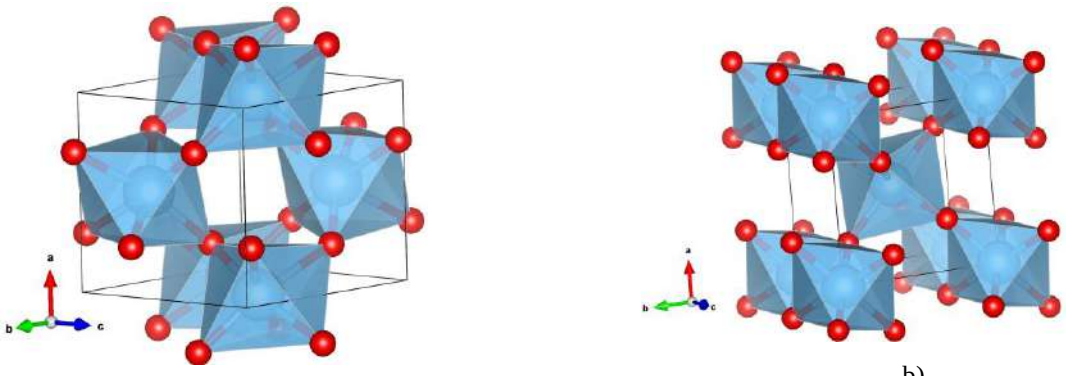

a) b)

Figure 3. Crystal structure of a) TiO_2-II (columbite) and b) rutile structure. Titanium and oxygen atoms are represented by blue and red spheres, respectively.

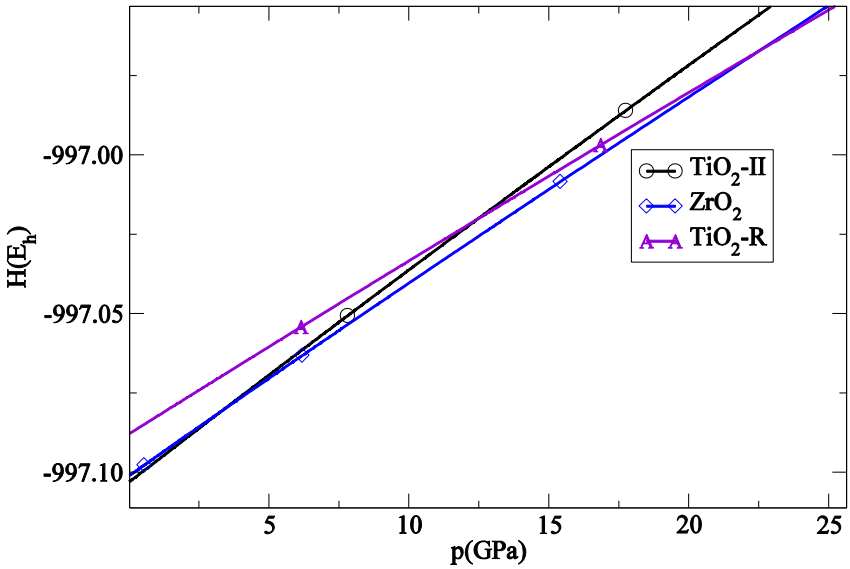

Figure 3. Enthalpy-pressure, *H(p)* curves in the high-pressure region computed using LDA-PZ functional.

4. Conclusion

In this study, we have performed *ab initio* calculations using DFT approximation with an exchange-correlation functional LDA-PZ within the CRYSTAL17 software package. Detailed structural properties after *ab initio* optimization for eleven different crystalline TiO_2 modifications are obtained. According to the *E(V)* curves for seven different modifications and ranking in total energy, the most stable modification is the TiO_2-II. This structure type in a high-pressure regime transforms to ZrO_2 and TiO_2-R modification. We can conclude that *ab initio* results for TiO_2 polymorphs are very sensitive to the choice of the functional and basis sets, and thus, one should be careful when selecting a computational methodology to investigate it. However, chosen LDA-PZ method with the LCAO basis set can be a useful tool for the investigation of structures under extreme conditions.

The band gap values for all investigated modifications have been calculated. The experimental data implicates the rutile structure as the most thermodynamically stable, while previous theoretical data suggest the lowest total energy for the TiO_2-II (columbite) type structure. *E(V)* curves diagram shows very close minimums of TiO_2-II and rutile structures, which is more in agreement with the available literature. After the DFT structure optimization, the quartz-low modification $P3_12_1$ (SG 152) shifted into the higher space group $P6_422$ (SG 181), characteristic of quartz-high modification. The band gap values calculated in this research are lower than those obtained experimentally for anatase and rutile structures, as expected from the LDA functional. The results obtained in this study provide information that should contribute to future research of these systems, as well as to their potential scientific and technological applications, especially in extreme conditions.

Acknowledgments

This work was financially supported by the Ministry of Science, Technological Development and Innovation of the Republic of Serbia through Contract No. 451-03-47/2023-01/200017. The authors are grateful to Prof. R. Dovesi, Prof. K. Doll, and Crystal Solutions for software support with CRYSTAL code. The authors thank the Max Planck Institute for Solid State Research, Stuttgart, Germany, for collaboration and for providing computational support. Furthermore, authors acknowledge the support of the Center of Advanced Computing and Modelling at the University of Rijeka for providing computing resources.

References

[1] M. Vasic, Optimisation and photocatalytic application of nanostructured TiO_2, Department of chemistry of the Faculty of Science and Mathematics, University of Nis, Nis, 2017.
[2] K. Hashimoto, H. Irie, A. Fujishima, TiO_2 Photocatalysis: A Historical Overview and Future Prospects, *Japanese Journal of Applied Physics*, 44 (2005) 8269-8285.
[3] S.M. Gupta, M. Tripathi, A review of TiO_2 nanoparticles, *Chinese Science Bulletin*, 56 (2011) 1639.
[4] M.P. Vinardell, M. Mitjans, Antitumor Activities of Metal Oxide Nanoparticles, *Nanomaterials* (Basel), 5 (2015) 1004-1021.
[5] K. Huang, L. Chen, J. Xiong, L. Meixiang, Preparation and Characterization of Visible-Light-Activated Fe-N Co-Doped TiO_2 and Its Photocatalytic Inactivation Effect on Leukemia Tumors, *International Journal of Photoenergy*, 2012 (2012).
[6] I.J. Ani, U.G. Akpan, M.A. Olutoye, B.H. Hameed, Photocatalytic degradation of pollutants in petroleum refinery wastewater by TiO_2 and ZnO-based photocatalysts: Recent development, *Journal of Cleaner Production*, 205 (2018) 930-954.
[7] B. Babić, A. Zarubica, T.M. Arsić, J. Pantić, B. Jokić, N. Abazović, B. Matović, Iron doped anatase for application in photocatalysis, *Journal of the European Ceramic Society*, 36 (2016) 2991-2996.
[8] A. Krstic, Stankovic, H., Rubezic, M., Vasic, M., Zarubica, A., Chemical modifications of nanostructured titania-based materials in photocatalytic decomposition/conversion of various organic pollutants: A short review, *Advanced Technologies*, 7(2) (2018) 78-84.
[9] G. Bergerhoff, I.D. Brown, Crystallographic Databases, International Union of Crystallography, Chester, UK, 1987.
[10] D. Zagorac, H. Muller, S. Ruehl, J. Zagorac, S. Rehme, Recent developments in the Inorganic Crystal Structure Database: theoretical crystal structure data and related features, *Journal of Applied Crystallography*, 52 (2019) 918-925.
[11] Q.-J. Li, B.-B. Liu, High pressure structural phase transitions of TiO_2 nanomaterials, *Chinese Physics B*, 25 (2016) 076107.
[12] Q.-J. Liu, Z. Ran, F.-S. Liu, Z.-T. Liu, Phase transitions and mechanical stability of TiO_2 polymorphs under high pressure, *Journal of Alloys and Compounds*, 631 (2015) 192-201.
[13] S. Kalaiarasi, A. Sivakumar, S.A. Martin Britto Dhas, M. Jose, Shock wave induced anatase to rutile TiO_2 phase transition using pressure driven shock tube, Materials Letters, 219 (2018) 72-75.
[14] R. Sikora, Ab initio study of phonons in the rutile structure of TiO_2, *Journal of Physics and Chemistry of Solids*, 66 (2005) 1069-1073.
[15] C. Byrne, L. Moran, D. Hermosilla, N. Merayo, Á. Blanco, S. Rhatigan, S. Hinder, P. Ganguly, M. Nolan, S.C. Pillai, Effect of Cu doping on the anatase-to-rutile phase transition in TiO_2 photocatalysts: Theory and experiments, *Applied Catalysis B: Environmental*, 246 (2019) 266-276.
[16] N. Khatun, S. Tiwari, C.P. Vinod, C.-M. Tseng, S.W. Liu, S. Biring, S. Sen, Role of oxygen vacancies and interstitials on structural phase transition, grain growth, and optical properties of Ga doped TiO_2, *Journal of Applied Physics*, 123 (2018) 245702.
[17] D. Jovanović, D. Zagorac, B. Matović, A. Zarubica, J. Zagorac, Anion substitution and influence of sulfur on the crystal structures, phase transitions, and electronic properties of mixed TiO_2/TiS_2 compounds, *Acta Crystallographica Section B*, 77 (2021) 833-847.
[18] R. Dovesi, A. Erba, R. Orlando, C.M. Zicovich-Wilson, B. Civalleri, L. Maschio, M. Rérat, S. Casassa, J. Baima, S. Salustro, B. Kirtman, Quantum-mechanical condensed matter simulations with CRYSTAL, *WIREs Computational Molecular Science*, 8 (2018) e1360.
[19] R. Dovesi, F. Pascale, B. Civalleri, K. Doll, N.M. Harrison, I. Bush, P. D'Arco, Y. Noël, M. Rérat, P. Carbonnière, M. Causà, S. Salustro, V. Lacivita, B. Kirtman, A.M. Ferrari, F.S. Gentile, J. Baima, M. Ferrero, R. Demichelis, M.D.L. Pierre, The CRYSTAL code, 1976–2020 and beyond, a long story, *The Journal of Chemical Physic*s, 152 (2020) 204111.

[20] J. Scaranto, S. Giorgianni, A quantum-mechanical study of CO adsorbed on TiO_2: A comparison of the Lewis acidity of the rutile (110) and the anatase (101) surfaces, *Journal of Molecular Structure: THEOCHEM*, 858 (2008) 72-76.
[21] I. Cvijović-Alagić, Z. Cvijović, D. Zagorac, M.T. Jovanović, Cyclic oxidation of Ti_3Al-based materials, *Ceramics International*, 45 (2019) 9423-9438.
[22] M.D. Towler, N.L. Allan, N.M. Harrison, V.R. Saunders, W.C. Mackrodt, E. Aprà, Ab initio study of MnO and NiO, *Physical Review B*, 50 (1994) 5041-5054.
[23] J. Zagorac, J.C. Schön, B. Matović, T. Škundrić, D. Zagorac, Predicting Feasible Modifications of Ce_2ON_2 Using a Combination of Global Optimization and Data Mining, *Journal of Phase Equilibria and Diffusion*, 41 (2020) 538-549.
[24] J.P. Perdew, A. Zunger, Self-interaction correction to density-functional approximations for many-electron systems, *Physical Review B*, 23 (1981) 5048-5079.
[25] D. Zagorac, Zagorac, J., Doll, K, Čebela, M., Matović, B., Extreme pressure conditions of BaS based materials: Detailed study of structural changes, band gap engineering, elastic constants and mechanical properties, *Processing and Application of Ceramics* 13 (2019) 401-410.
[26] D. Jovanović, Zagorac, J., Matović, B., Zarubica, A., Zagorac, D., Structural, electronic and mechanical properties of superhard B4C from first principles, *Journal of Innovative Materials in Extreme Conditions*, 1 (2020) 12-18.
[27] J. Zagorac, Zagorac, D., Jovanović, D., Pejić, M., Škundrić, T., Matović, B., Ab initio investigations and behaviour of the α-Ce_2ON_2 phase in the extreme pressure conditions, *Journal of Innovative Materials in Extreme Conditions*, 2 (2021).
[28] J.C. Schoen, Energy Landscape Concepts for Chemical Systems under Extreme Conditions, *Journal of Innovative Materials in Extreme Conditions*, 2 (2021) 5-57.
[29] R. Hundt, KPLOT: A Program for Plotting and Analysing Crystal Structures, Technicum Scientific Publishing, Stuttgart, 2016.
[30] K. Momma, F. Izumi, VESTA: a three-dimensional visualization system for electronic and structural analysis, *Journal of Applied Crystallography*, 41 (2008) 653-658.
[31] S.K. Filatov, N.A. Bendeliani, B. Albert, J. Kopf, T.I. Dyuzheva, L.M. Lityagina, Crystalline structure of the TiO_2 II high-pressure phase at 293, 223, and 133 K according to single-crystal x-ray diffraction data, *Doklady Physics*, 52 (2007) 195-199.
[32] I.E. Grey, C. Li, I.C. Madsen, G. Braunshausen, TiO_2-II. Ambient pressure preparation and structure refinement, *Materials Research Bulletin*, 23 (1988) 743-753.
[33] M.E. Arroyo-de Dompablo, A. Morales-García, M. Taravillo, DFT+U calculations of crystal lattice, electronic structure, and phase stability under pressure of TiO2 polymorphs, *The Journal of Chemical Physics*, 135 (2011).
[34] P.Y. Simons, F. Dachille, The structure of TiO2II, a high-pressure phase of TiO_2, *Acta Crystallographica*, 23 (1967) 334-336.

Journal of Innovative Materials in Extreme Conditions
2023
Volume 4
Issue 1

DATA-MINING *AB INITIO* STUDY OF GYPSUM AND $CaCO_3$ MODIFICATIONS AT STANDARD AND EXTREME CONDITIONS

Tamara Škundrić[1,2,3], Branko Matović [1,2], Aleksandra Zarubica [3], Dorota Chudoba[4], Dejan Zagorac[1,2]

[1]*Institute of Nuclear Sciences "Vinča", University of Belgrade, Belgrade, Serbia*
[2]*Centre of Excellence "Cextreme Lab", Centre for synthesis, processing, and characterization of materials for application in extreme conditions, Belgrade, Serbia*
[3]*Department of Chemistry, Faculty of Science and Mathematics, University of Niš, Niš, Serbia*
[4]*Joint Institute for Nuclear Research (JINR), Frank Laboratory of Neutron Physics, Dubna, Russia*

Corresponding author: tamara.skundric@vin.bg.ac.rs*

Abstract: *Calcium carbonate and gypsum are very common and widespread minerals widely used in many fields. However, in order to investigate their behavior under extreme conditions of pressure and temperature, a data-mining ab initio approach has been performed. To analyze structural stability and explore different $CaCO_3$ and gypsum phases in these extreme conditions, the most interesting modifications have been submitted to the DFT calculations. Local optimizations have been performed using the CRYSTAL17 solid-state-quantum-chemical program. Total energies of different gypsum phases are presented and it seems that among the calcite phases, the Calcite I ($CaCO_3$ I) phase has the lowest calculated total energy using the three different functionals in agreement with experimental data. Each of the modified phases of these minerals has been discussed and presented in this study. Due to the very wide industrial and technological application of these natural minerals, further investigation could be of great importance, especially their performances in extreme environments.*

Keywords**:** *calcium carbonate, gypsum, DFT, crystal structure prediction, data-mining, extreme pressures, high temperatures*

1. Introduction

There are several studies investigating phase transitions in gypsum and calcium carbonate in extreme conditions, using different pressure and temperature ranges within the research. Raman spectroscopy is the most used technique for phase transformations research, often combined with x-ray diffraction [1], or electrical conductivity experiments [2], but to investigate a phase transformation of gypsum into bassanite and anhydrite, one new original apparatus has also been developed, that combines an acoustic levitator and a pressure-compatible process chamber [3].

Results from the experiments indicate that gypsum dissolves in water at ambient temperature and pressure above 496 MPa, but the solubility increases significantly with increasing pressure and finally entirely dissolves at a pressure of around 866 MPa [4]. At the pressure of 2 GPa under cold compression, a phase transition from anhydrite to a monazite type has been observed [1]. However, between 2 and 5 GPa, anhydrite undergoes a gradual phase change from orthorhombic to monoclinic monazite structured phase, with a 6-8% volume change, strongly dependent on pressure [5]. At the higher pressures of 33.2 GPa and after laser heating, another phase transition has been observed and a change in color of the sample is noted, from transparent to black, with an indication that this newly discovered phase can persist to 53.5 GPa and 1800 K [1]. Accordingly, with the pressure of 5,8 GPa and atmospheric temperature, a structural phase transition in gypsum has been confirmed [2]. Thereby, at a relatively low pressure of around 0.3 GPa, starting gypsum transforms to anhydrite in only one step dehydration reaction [2].

However, at the pressure of 2,5 GPa, a two-step dehydration reaction has been confirmed as the gypsum firstly transforms into bassanite, $CaSO_4$ hemihydrate, at around 428 K [6] or 523 K[2], and then completely dehydrates to anhydrite at 673K [2]. According to another study, firstly γ-

anhydrite is formed at 488 K, and then at 593 K γ-anhydrite irreversibly transforms to the β-anhydrite form [6]. At room temperature and a pressure of 2 GPa, a further polymorphic transition of β-anhydrite to monazite has been observed and this transformation is described as completely reversible due to the Raman spectra of recovered samples [6]. Besides, with temperature increase, the anhydrite phase ($CaSO_4$) precipitates at 250-320°C and in the pressure range of 1.0 – 1.5 GPa. Hence, both conditions, a stable range of pressure and temperature along with the supersaturation of Ca and SO_4 ion concentrations in an aqueous solution are crucial for the anhydrite formation [4]. This transition that involves two processes, dissolution, and precipitation is defined as irreversible [4], while anhydrite is also described as a possible oxygen carrier particle (OCP) material [7].

Thus, in extreme conditions of high temperature and pressure, besides the monazite-type, denoted as a metastable phase to pressures up to almost 30 GPa [5], barite-type phases have also been found, and these phases are described as mechanically stable polymorphs of the ambient phases – anhydrite [8]. There is also a suggestion that anhydrite and monazite-structured phases are the only phases that can be observed under shock loading of $CaSO_4$ to pressures above 100 GPa [5]. However, even at room temperature, a phase transition from anhydrite to monazite can be induced by a pressure of around 3 GPa [8]. However, the transition from monazite to barite requires higher temperatures (>1500 K and ~20 GPa), though this phase cannot always be quenched from high temperatures, and can be distorted to some other structures as well [8]. According to the Raman and Infrared spectra of gypsum at high pressures, up to 21 GPa and 300 K, gypsum retains molecular-like sulphate groups and water molecules to pressures up to 20 GPa and 300 K [9]. Its water and sulphate vibrations remain discrete, indicating that highly rigid molecular units are maintained throughout this pressure range [9]. Due to the progressive removal of water molecules from the gypsum, the peaks reduce in amplitude and the removal of water molecules affects the crystallographic environment, hence the distortion of the $SO4^{2-}$ tetrahedra [3]. There is also a suggestion that the compression of the monazite structured phase is remarkably anisotropic, as the pressure-induced compaction is mostly accommodated by a and b axes [5].

Calcium carbonate is a very widespread mineral found in the Earth's crust. At atmospheric pressure, it crystalizes in the calcite phase, but with an increase in pressure, this ambient phase of $CaCO_3$ undergoes several phase transitions [10]. Starting from the ambient temperature, at the pressure of 1.7 GPa calcite I transform into calcite II, which further changes to calcite III at the pressure of approximately 2 GPa and this structure can be retained up to at least 10 GPa [11]. Also, using the single-crystal synchrotron X-ray diffraction, high-pressure polymorphs have been detected, $CaCO_3$-III and $CaCO_3$-VI phases [10]. $CaCO_3$ that is noted in the pressure range of 2,5 to 15 GPa is triclinic and presents two closely related structural modifications ($CaCO_3$-III and $CaCO_3$-IIIb) with an indication that different experimental paths can stabilize one or the other polymorph [10].

There is also a report of $CaCO_3$ polymorph found in extreme conditions of pressure and temperature, referred to as a calcite-Vb phase [12]. It occurs at pressures >3,5 GPa and temperatures more than 1200°C, as an intermediate between aragonite and calcite V, and this new $CaCO_3$ phase has the $KClO_3$-type structure and appears in the monoclinic $P2_1/m$ space group [12]. At pressures above 15 GPa up to 40 GPa, a triclinic $CaCO_3$-VI polymorph has been noted with 10 atoms in the unit cell [10]. However, after the pressure release, three phases $CaCO_3$-III, $CaCO_3$-IIIb, and $CaCO_3$-VI transform back to the calcite, with the sample recovered as a single crystal [10]. Additionally, first principle calculations have been performed to calculate the elastic properties for the three high-pressure phases of $CaCO_3$, aragonite, post-aragonite, and *P21/c-h* $CaCO_3$ structure with a conclusion that these high-pressure polymorphs have low isotropic wave velocity and high wave velocity anisotropies [13].

Investigation of the stability of $CaCO_3$ at high pressures and temperatures has also revealed that the $CaCO_3$ in the aragonite structure transforms into $CaCO_3$-VII (*P21/c*) at 27 GPa and 1500 K and it appears that this phase is stable between 23 and 38 GPa at 2300 K while at 42 GPa and 1400 K, it transforms into post-aragonite [14]. Further, by combining the density functional theory with the exchange-correlation functional augmented by the dispersive vdW interaction with quasi-harmonic approximations, the thermodynamic properties of $CaCO_3$ phases have been calculated and the *P*21/*c*-*l* phase has a very narrow region of stability, according to the results [15]. Besides, these simulations also suggested that this *P*21/*c*-*l* phase is structurally identical to the $CaCO_3$-VII phase [15], which is

also in agreement with some previous results [14, 16]. In 2020, a newly discovered phase named disarag, have been found, and described as a dynamically disordered aragonite with freely rotating CO_3 groups which is similar to that in the $CaCO_3$-V phase with a calcite-like structure [17]. This new phase, disarag is referred to as a stable phase in the pressure range of 3 to 10 GPa and from 1600 to 2000K [17]. Also, the increase of temperature at 3,4, and 6 GPa, led to a series of transitions starting from calcite that transformed to aragonite, which further changed to disordered calcite and finally to liquid, and upon rapid cooling of the liquid, aragonite was retained [11]. Besides the earlier known calcite-type disordered structures such as $CaCO_3$-IV, $CaCO_3$-V, rhombohedral $SrCO_3$, rhombohedral $BaCO_3$, and cubic $BaCO_3$, the existence of the disordered aragonite has been also proved, though at the high pressures [17].

Moreover, a reversible temperature-induced aragonite-amorphization transition in $CaCO_3$ has been found at 3.9 to 7.5 GPa and temperatures above 1000K [18]. This amorphous $CaCO_3$ shares a similar structure as liquid $CaCO_3$, but also a mechanism of lattice collapse for the temperature-induced amorphous phase has been suggested [18]. Moreover, using a combination of advanced *ab initio* simulation techniques and high-pressure experiment, a crystal structure of $CaCO_3$ post-aragonite that has been enigmatic for a long time, has been finally determined and this is the phase that is experimentally known to be stable above 40 GPa. [19]. Also, some novel energetically competitive structures have been identified with one of them being even more stable than aragonite above 42 GPa, which appears in the orthorhombic space group *Pmmn* and belongs to a new structure type, which is also adopted by the high-pressure post-aragonite phases of $SrCO_3$ and $BaCO_3$ [19]. When heated to high temperatures (>1500K) and at pressures >130 GPa, calcium carbonate transforms into an orthopyroxene-type structure that is also in agreement with theoretical predictions from *ab initio* calculations [20]. Particularly, at the pressure of 137 GPa, a pyroxene-type structure that appears in the orthorhombic space group *C2221*, becomes more stable than aragonite [19]. Besides the post-aragonite phase with a threefold coordination of carbon cations that manifest strongly anisotropic compressibility of each axis of the unit cell parameter, there is no obvious anisotropy in the pyroxene-type phase [20].

2. Materials and methods

In order to gain insight into the structural stability of the $CaCO_3$ and gypsum phases in extreme conditions of pressure and temperature, a data mining *ab initio* approach has been performed. We performed data-mining-based explorations of the ICSD database [21, 22] via resemblance to known crystallographic structures. A well-known KDD (knowledge discovery in databases) process, which involves selection, preprocessing, transformation, and interpretation/evaluation (or postprocessing) has been used, which also proved to be successful in some previous studies [23-25]. Also, it is of great importance to the effect of extreme conditions on structural properties, as well as the structure-property relationship that has been studied previously [26-30]. All potential structure candidates that have been obtained from data mining search are subsequently submitted to local optimization at an *ab initio* level and a combination of data mining and *ab initio* methods can be found elsewhere [31, 32].

Further, these structure candidates have been submitted to the density functional theory (DFT) calculations and local optimizations (including the cell parameters and atom positions) were performed using the CRYSTAL17 code [33-35], which is based on the linear combination of atomic orbitals. Structure optimizations were performed on the DFT level, employing three different functionals: the Generalized Gradient Approximation (GGA) with the Perdew–Burke–Ernzerhof (PBE) functional [36], the Local Density Approximation (LDA) with the Perdew–Zunger (PZ) correlation functional [37], and the hybrid B3LYP functional (Becke's three-parameter functional in combination with the correlation functional of Lee, Yang, and Parr) [38], for comparison. An all-electron basis set based on Gaussian-type orbitals was employed; in particular, in the case of calcium carbonate modifications, Ca_86-511d3G_catti_1991 for calcium [39], C_6-21G*_catti_1993 for carbon [27, 40] and O_8-411_towler_1994 for oxygen [41, 42] and H_5-11G*_dovesi_1984 for hydrogen [43, 44], respectively. In each structural optimization, Fock/KS matrix mixing was set to 30%, and the tolerances for the convergence on energy were set to 10^{-7}. K-point meshes of 8 _ 8 _ 8

Monkhorst-Pack scheme have been used. A computational strategy implemented in the CRYSTAL17 solid-state, quantum-chemical program has been performed for the accurate *ab initio* simulation of elastic and mechanical properties of crystalline materials [45]. The symmetries of the analyzed structures were determined using the SFND [46] and RGS [47] algorithms implemented in the program KPLOT [48]. The structures were visualized using the Vesta3 program [49].

3. Results and Discussion

Aiming to investigate the structural stability of different gypsum phases in extreme conditions of pressure and temperature, the most interesting formations have been modified. Local optimizations of CaO, CaOH, anhydrite, hemihydrate, and gypsum have been performed using the two different functionals, the GGA-PBE and the LDA-PZ, due to comparison. Calculated total energies and full structural data are given in Tables 1 and 2, respectively.

Table 1. The total energies of the most interesting formations calculated with the GGA-PBE and the LDA-PZ functional. Note that the energies per formula unit are given in hartrees (*Eh*).

Compound/ Modification	Total Energy (*Eh*)	
	GGA-PBE	LDA
CaO	-752.709	-750.663
CaOH	-829.109	-826.592
$CaSO_4$-anhydrite	-1376.289	-1371.709
$CaSO_4$-hemihydrite	-1414.476	-1409.666
$CaSO_4x2H_2O$	-1529.057	-1523.551

The first modification was computed in the CaO chemical system that appears in the rock salt (NaCl) type of structure. The CaO modification shows space group *Fm-3m* (no. 225) with unit cell parameters of a=4.828 Å, calculated with the GGA-PBE functional. Within this cubic structure, calcium ions are in 6-fold coordination by oxygen atoms, thus forming edge-connected octahedra. The distance between atoms is 6 × 2.4144 Å-O, and the structure is presented in Figure 1a. This is in agreement with previous observations [50], and such a structure is capable of withstanding high pressure and temperature conditions.

The next modified structure is CaOH which appears in space group *P-3m1* (no. 164) [51]. This structure is visualized in Figure 1b, with unit cell parameters a=3.613 and c=4.974 Å, calculated with the GGA-PBE functional. Within this trigonal structure, calcium ions are 6-fold coordinated by oxygen and form two layers of edge-connected octahedra with an interatomic distance of 6 × 2.3825 Å-O. The hydrogen atom is connected to only one oxygen atom with a distance between atoms of 0.9857 Å-O.

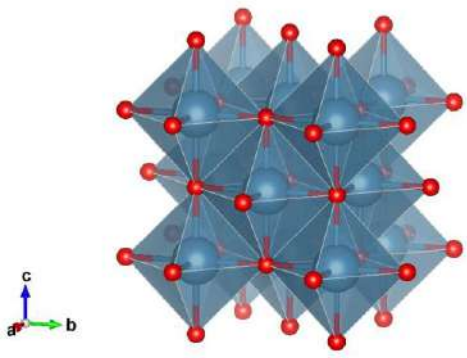

(**a**)

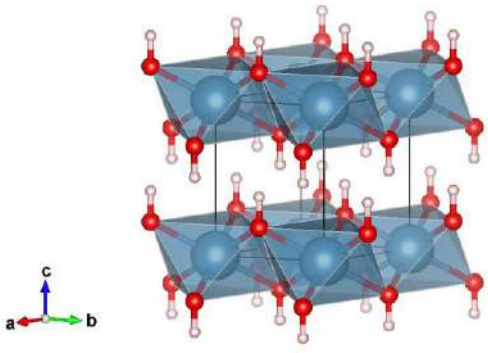

(**b**)

Figure 1. Visualization of the a) CaO that appears in *Fm-3m* (no. 225) and b) CaOH in *P-3m1* (no. 164), calculated with the GGA-PBE functional. Blue, red and pink spheres denote calcium, oxygen, and hydrogen atoms, respectively.

Following modification is a hexagonal calcium sulphate anhydrite that appears in space group *P*6222 (no. 180) and is visualized in Figure 2a [52]. Anhydrite is an anhydrous compound (it does not contain water in its crystal structure), and such is a unique material with outstanding properties beneficial to many industrial applications. This hexagonal structure has unit cell parameters of *a*=7.093 Å and c=6.450 Å, calculated with the GGA-PBE functional, while full structural data are given in Table 2. Sulphur ions are in 4-fold coordination with oxygen and form tetrahedra with an interatomic distance of 4 × 1.5323 Å-O.

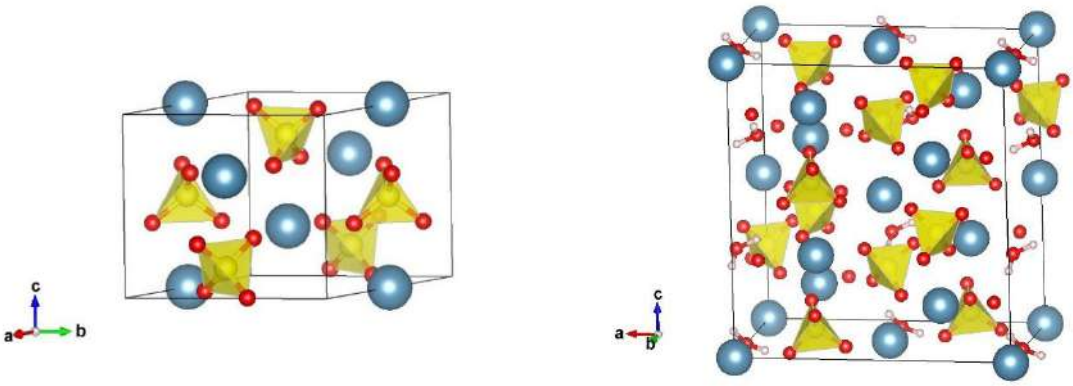

(**a**) (**b**)

Figure 2. Visualization of the a) $CaSO_4$-anhydrite that appears in *P6222* (no. 180); b) $CaSO_4$-hemihydrate in space group *C2* (no. 5), calculated with the GGA-PBE functional. Blue, yellow, red, and pink spheres denote calcium, sulphur, oxygen, and hydrogen atoms, respectively.

The only optimized structure within this group that crystallizes in a lower symmetry group is $CaSO_4$-hemihydrate [53]. This compound has been used as a building material for thousands of years and it can endure extreme conditions. It appears in space group *C2* (no. 5) with unit cell parameters of a=12.181, b=7.063, c=13.010 Å, and β=90.353, and the structure is visualized in Figure 2b. Sulphur atoms are surrounded by four oxygen atoms, and form three different tetrahedra with interatomic distances in a range of 1.5261 Å-O as the smallest distance, to 1.5422 Å-O as the largest interatomic distance, while there are also three different water molecules with distances between hydrogen and oxygen atoms of (H_1) 0.9852 Å-O, (H_2) 0.9898 Å-O, and (H_3) 0.9893 Å-O, respectively. The total energy of this modification calculated with two different functionals, GGA-PBE and the LDA-PZ are presented in Table 1, while full structural data on the GGA level of calculation are given in Table 2, respectively.

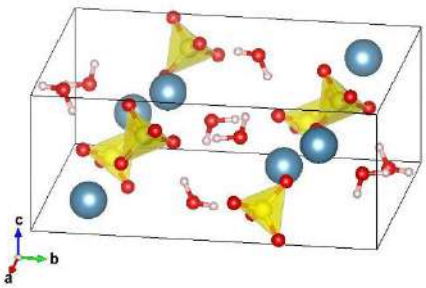

Figure 3. Visualization of the $CaSO_4x2H_2O$ in *C12/c1* (no. 15), calculated with the GGA-PBE functional. Blue, yellow, red, and pink spheres denote calcium, sulphur, oxygen, and hydrogen atoms, respectively.

The final optimized structure is the calcium sulphate dihydrate (gypsum), a material that contains water in the structure (unlike previously computed anhydrite). Anhydrite closely resembles gypsum, however, it is slightly harder and denser compared to gypsum. Gypsum crystallizes in space group *C12/c1* (no. 15) with unit cell parameters a=6.495, b=15.237, c=5.725Å and β=115.105, on the GGA-PBE level of calculation. Our DFT calculations concur with the literature data [54]. Within this structure, sulphur is in 4-fold coordination with oxygen and forms tetrahedra with interatomic distances of 2 × 1.5304 Å-O and 2 × 1.5409 Å-O, respectively. Oxygen atoms are connected to two hydrogen atoms making a water molecule, with distances of 0.9940 Å-O and 1.0013 Å-O, and the structure is presented in Figure 3.

Table 2. Full structural data of the most interesting modifications calculated with the GGA-PBE functional.

Modification	**Cell parameters (Å)**	**Position of atoms**
CaO *Fm-3m* (no. 225)	a= 4.828	Ca 0.00000 0.00000 0.00000 O 0.50000 0.50000 0.50000
CaOH *P-3m1* (no. 164)	a=3.613 c=4.974	Ca 0.00000 0.00000 0.00000 O 0.33333 0.66667 0.23120 H 0.33333 0.66667 0.42934
$CaSO_4$-anhydrite *P6222* (no. 180)	a=7.093 c=6.450	Ca 0.50000 0.00000 0.00000 S 0.50000 0.00000 0.50000 O 0.44708 0.13836 0.35497
$CaSO_4$-hemihydrate *C2* (no. 5)	a=12.181 b=7.063 c=13.010 β=90.353	Ca 0.000000 0.000000 0.000000 Ca 0.000000 0.041583 0.500000 Ca 0.229284 0.334845 0.832602 Ca 0.785512 0.355078 0.666962 S 0.774689 0.337691 0.918828 S 0.003088 0.015067 0.747868 S 0.225092 0.353110 0.582985 O 0.184487 0.879947 0.997289 O 0.177234 0.886982 0.487903 O 0.756804 0.677884 0.155160 O 0.747738 0.694063 0.660660 O 0.063107 0.140685 0.826257 O 0.566288 0.630726 0.327812 O 0.795609 0.511872 0.851283 O 0.803214 0.526497 0.350968 O 0.123944 0.289525 0.015938 O 0.129134 0.301407 0.511457 O 0.070755 0.883506 0.187990 O 0.081886 0.901355 0.681216 O 0.000000 0.656480 0.000000 O 0.957252 0.524710 0.693614 H 0.944784 0.572042 0.968707 H 0.953515 0.639334 0.737217 H 0.030584 0.525407 0.661366
$CaSO_4x2H_2O$ *C2/c* (no. 15)	a=6.495 b=15.237 c=5.725 β=115.105	Ca 0.00000 0.83275 0.75000 S 0.00000 0.32925 0.75000 O 0.70390 0.88624 0.92265 O 0.08718 0.27274 0.58994 O 0.79439 0.93198 0.41972 H 0.74821 0.91178 0.23796 H 0.75732 0.99546 0.41385

To investigate the $CaCO_3$ under extreme conditions, an *ab initio* data mining approach has been performed. High-pressure phases of calcite and aragonite, two different modifications of $CaCO_3$,

are optimized using the three different functionals (GGA-PBE, LDA-PZ, B3LYP). Calculated total and relative energies for the five high-pressure calcite and aragonite modifications are listed in Table 3.

Table 3. Calculated total and relative energies per formula unit for different $CaCO_3$ modifications.

Modifications	**GGA-PBE**		**LDA-PZ**		**B3LYP**	
	Total Energy (Eh)	**Relative Energy (kcal/mol)**	**Total Energy (Eh)**	**Relative Energy (kcal/mol)**	**Total Energy (Eh)**	**Relative Energy (kcal/mol)**
Calcite I ($CaCO_3$ I)	-941.1793	0	-937.9360	0	-941.4953	0
Calcite IIIa	-941.1740	3.326	-937.9357	0.188	-941.4888	4.079
Calcite IIIb	-941.1767	1.631	-937.9359	0.063	-941.4924	1.820
Calcite IIIc	-941.1775	1.129	-937.9339	1.318	-941.4934	1.192
Calcite VI	-941.1763	1.882	-937.9351	0.565	-941.4929	1.506
Aragonite	-941.1709	5.271	-937.9317	2.698	-941.4843	6.903

Calculated energies for all computed $CaCO_3$ modifications show similar rankings. Thus, the first modification, Calcite I ($CaCO_3$ I) has the lowest calculated energy regardless of the computational approach, while the highest computed energies were found in aragonite modification, which is expected as a high-pressure and/or high-temperature phase [55]. A structure with the highest calculated energy among calcite phases proved to be calcite IIIa modification using the GGA-PBE and the B3LYP functional, while calcite IIIc modification was energetically highest using the LDA-PZ functional (Table 3). On the other hand, Aragonite, another naturally occurring crystal form of $CaCO_3$, has the highest computed energies of all $CaCO_3$ modifications, which is expected at high pressures and/or temperatures.

The lowest energy minimum found using the data mining *ab initio* method was denoted as Calcite I ($CaCO_3$ I) modification. It crystallizes in space group *R3c* (SG no. 167) with unit cell parameters a=5.084 and c=17.002 Å, calculated using the GGA-PBE functional. It is visualized in Figure 4a, while full structural data are given in Table 4, on the GGA-PBE level of calculation. Within this structure calcium has 6-fold coordination by oxygen atoms, thus forming corner-connected octahedra. Besides, carbon atoms are in 3-fold coordination with oxygen atoms and form an equilateral triangle. Interatomic distances for calcium ions are 2.3862 Å-O and for carbon 1.3044 Å-O, respectively. The present calculation for the Calcite I type of structure agrees very well with previous reports [56-59] regardless of the computational approach. Furthermore, we have observed polytypic structures at high-pressure and/or high-temperature conditions which were recently discovered in $CaCO_3$ [60] and other chemical systems [61, 62].

Following modification on the energetic ranking using the GGA and the B3LYP functional is denoted as Calcite IIIc, which is visualized in Figure 3b. The Calcite IIIc modification is predicted within this study. We have started the DFT optimization from a metastable structure found at about 4 GPa, [63] and found a new Calcite IIIc type confirmed with all three *ab initio* methods. It crystallizes in space group *P321* (SG no. 150) with unit cell parameters a=5.062 c=8.631 Å, on the GGA-PBE level of calculation. Similar to the previous structure, calcium atoms are in 6-fold coordination with oxygen, however, form slightly distorted octahedra, with interatomic distances of (Ca_1) 2.4017 Å-O, (Ca_2) 2.3814 Å-O and 2.3863 Å-O, respectively. Octahedra positioned in the corners of the structure are connected to those inside the structure, but not to each other. Carbon atoms are 3-fold coordinated by oxygen and form an equilateral triangle, while distances between atoms are (C_1) 1.3043 Å-O and (C_2) 1.3046 Å-O. When calculated using the LDA-PZ functional, this structure proved to be much higher in energy.

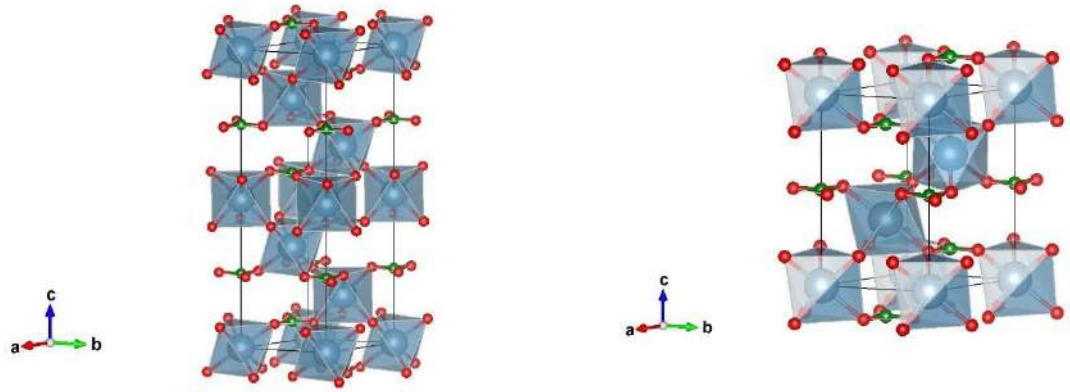

(**a**) (**b**)

Figure 4. Visualization of a) Calcite I ($CaCO_3$ I) modification in space group *R-3c* (no. 167); b) Calcite IIIc modification that appears in space group *P321* (SG no. 150). Blue, green, and red spheres denote calcium, carbon, and oxygen atoms, respectively.

Structure denoted as Calcite IIIb has a lower symmetry and appears in space group *P-1* (SG no. 2) with unit cell parameters a=6.418, b=6.635, c=6.474 Å, α=97.853, β=103.890, and γ=104.796, on the GGA-PBE level of calculation. This is an interesting modification, as calcium atoms are in 7-fold coordination with oxygen atoms, thus forming edge, and corner connected polyhedra (Figure 5a), with interatomic distances of (Ca_1) 2.3297 Å-O, 2.3595 Å-O, 2.3626 Å-O, 2.4340 Å-O, 2.4780 Å-O, 2.5773 Å-O, 2.6136 Å-O, and (Ca_2) 2.3178 Å-O, 2.3528 Å-O, 2.3804 Å-O, 2.3829 Å-O, 2.5002 Å-O, 2.5179 Å-O, 2.6824 Å-O, respectively. Carbon atoms are 3-fold coordinated by oxygen atoms and represent the center of the equilateral triangle, with interatomic distances of (C_1) 1.2993 Å-O, 1.3011 Å-O, 1.3012 Å-O and (C_2) 1.2915 Å-O, 1.3088 Å-O, 1.3168 Å-O.

Another low symmetry candidate that appears in space group *P-1* (SG no. 2) is referred to as Calcite VI modification, and it is visualized in Figure 5b with unit cell parameters a=3.870, b=5.156, c=6.661 Å, α=93.569, β=106.600, and γ=90.655, calculated using the GGA-PBE functional. Calcium atoms are 6-fold coordinated by oxygen and form distorted octahedra, while carbon remains in 3-fold coordination with oxygen. The interatomic distances are for Ca 2.3437 Å-O, 2.3772 Å-O, 2.3945 Å-O, 2.3987 Å-O, 2.4077 Å-O, 2.4576 Å-O, 2.7909 Å-O, and for C 1.2963 Å-O, 1.2997 Å-O, 1.3131 Å-O, respectively.

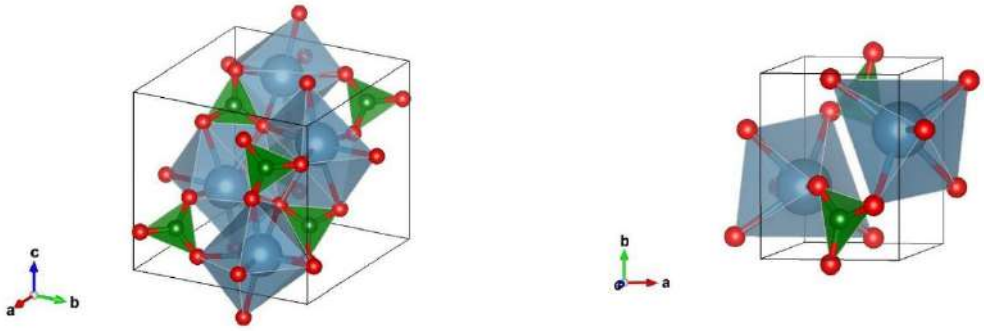

(**a**) (**b**)

Figure 5. Visualization of a) Calcite IIIb that appears in space group *P-1* (SG no. 2); b) Calcite VI in space group *P-1* (SG no. 2). Blue, green, and red spheres denote calcium, carbon, and oxygen atoms, respectively.

With the highest calculated energy using the GGA-PBE functional, there is another calcite modification denoted as Calcite IIIa that appears in space group *P-1* (SG no. 2) with unit cell

parameters a=6.422, b=7.775, c=12.764 Å, α=94.000, β=98.457, and γ=106.902. Within this structure, calcium is in 6-fold coordination and forms more or less distorted, corner-connected octahedra (Figure 6). Carbon atoms are positioned in the center of the planar group of oxygen atoms thus defining an equilateral triangle. The smallest interatomic distance for Ca_1 is 2.3974 Å-O, and it goes to the 2.4850 Å-O as the biggest distance, for Ca_2 these values are from 2.3271 Å-O to 2.5895 Å-O, for Ca_3 are from 2.3375 Å-O to 2.5313 Å-O, Ca_4 from 2.2785 Å-O to 2.5097 Å-O and for Ca_5 from 2.3921 Å-O to 2.4789 Å-O. As there are also five different carbon atoms, the distance between atoms for C_1 goes from 1.2818 Å-O to 1.3256 Å-O, C_2 from 1.2805 Å-O to 1.3143 Å-O, for C_3 from 1.2917 Å-O to 1.3123 Å-O, for C_4 from 1.2838 Å-O to 1.3203 Å-O and for the C_5 from 1.2862 Å-O to 1.3131 Å-O, respectively.

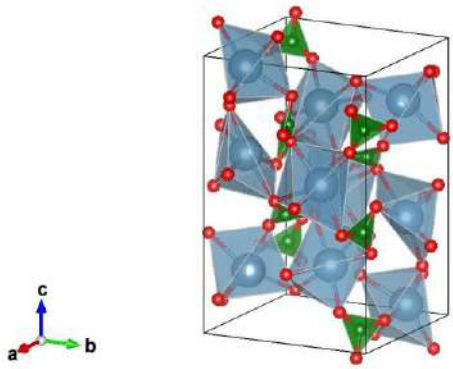

Figure 6. Visualization of the calcite IIIa modification that appears in space group *P-1* (SG no.2). Blue, green, and red spheres denote calcium, carbon, and oxygen atoms, respectively.

Table 4. Structure parameters of $CaCO_3$ phases calculated using the GGA-PBE functional.

Modifications and space group	**Cell parameters**	**Position of atoms**
Calcite I ($CaCO_3$ I) *R-3c* (SG no.167)	a=5.084 c=17.002	Ca 0.00000 0.00000 0.00000 C 0.00000 0.00000 0.25000 O -0.33333 0.07678 0.58333
Calcite IIIa *P-1* (SG no.2)	a=6.422 b=7.775 c=12.764 α=94.000 β=98.457 γ=106.902	Ca 0.83462 0.64293 0.55924 Ca 0.27128 0.87970 0.38168 Ca 0.51488 0.47742 0.78791 Ca 0.41574 0.93374 0.82704 Ca 0.01694 0.74906 0.02117 C 0.99275 0.51712 0.79004 C 0.37539 0.68572 0.59994 C 0.55816 0.73875 0.00473 C 0.04951 0.03662 0.20200 C 0.71839 0.84037 0.38697 O 0.40827 0.81383 0.02410 O 0.92103 0.50234 0.88222 O 0.19745 0.59060 0.78622 O 0.64116 0.87984 0.47193 O 0.84181 0.45775 0.70391 O 0.20124 0.66297 0.52665 O 0.46198 0.55223 0.60636 O 0.62683 0.75132 0.91286 O 0.16557 0.92323 0.19489 O 0.05542 0.12624 0.29132 O 0.91926 0.04956 0.11465 O 0.90052 0.80032 0.39877 O 0.65061 0.66033 0.07542

		O 0.46275 0.83329 0.66278 O 0.59692 0.82731 0.29282
Calcite IIIb *P-1* (SG no. 2)	a=6.418 b=6.635 c=6.474 α=97.853 β=103.890 γ=104.796	Ca 0.51812 0.77288 0.67988 Ca 0.01562 0.27830 0.78316 C 0.98359 0.23170 0.27066 C 0.53432 0.73685 0.22034 O 0.99382 0.62867 0.85160 O 0.59827 0.16370 0.71566 O 0.60747 0.60947 0.33919 O 0.09011 0.08982 0.26329 O 0.85879 0.23751 0.40146 O 0.39323 0.23050 0.94549
Calcite IIIc *P321* (SG no. 150)	a=5.062 c=8.631	Ca 0.00000 0.00000 0.00000 Ca 0.66667 0.33333 0.33496 C 0.00000 0.00000 0.50000 C 0.33333 0.66667 0.17030 O 0.25761 0.25761 0.50000 O 0.33133 0.92334 0.16998
Calcite VI *P-1* (SG no. 2)	a=3.870 b=5.156 c=6.661 α=93.569 β=106.600 γ=90.655	Ca 0.92367 0.67890 0.74171 C 0.50368 0.80485 0.24598 O 0.70086 0.63736 0.36650 O 0.58346 0.05181 0.27417 O 0.21578 0.71498 0.10313
Aragonite *Pnma* (SG no. 62)	a=5.769 b=5.061 c=8.103	Ca 0.73787 0.75000 0.58612 C 0.42084 0.25000 0.76246 O 0.41324 0.25000 0.92198 O 0.41753 0.02722 0.68106

Aragonite is another naturally occurring crystal form of calcium carbonate that is stable at high pressures and/or temperatures [55, 64]. The aragonite type modification crystallizes in space group *Pnma* (SG no. 62) with calculated unit cell parameters a=5.769, b=5.061, and c=8.103 Å, on the GGA-PBE level of calculation. Calcium atoms are in 7-fold coordination with oxygen atoms, thus forming edge-connected polyhedra, and interatomic distances are 1 × 2.4127 Å-O, 2 × 2.4447 Å-O, 2 × 2.5694 Å-O, 2 × 2.6004 Å-O, respectively. Carbon atoms are in 3-fold coordination by oxygen atoms and form equilateral triangles with interatomic distances of 1 × 1.2933 Å-O and 2 × 1.3064 Å-O, respectively. The structure is visualized in Figure 7, while full structural data are given in Table 4, calculated with the GGA-PBE functional.

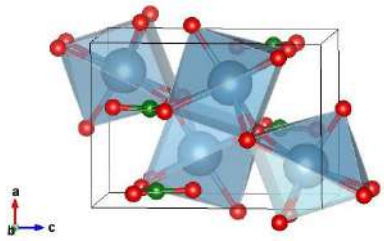

Figure 7. Visualization of the Aragonite that appears in space group *Pnma* (SG no. 62). Blue, green, and red spheres denote calcium, carbon, and oxygen atoms, respectively.

4. Conclusion

To investigate the behavior of calcite and gypsum modifications at standard and extreme conditions of pressure and temperature, a data-mining *ab initio* approach has been performed. Local structure optimizations have been carried out using the DFT approach with LDA-PZ and GGA-PBE functionals, as well as combined with the hybrid B3LYP functional. In total five gypsum-related

compounds and modifications, and six $CaCO_3$ modifications have been investigated. Computed structural and energetic properties of different gypsum phases are presented and in agreement with previous reports. In the case of the $CaCO_3$ chemical system, the calcite I ($CaCO_3$ I) phase has the lowest calculated total energy regardless of the computational approach, while aragonite modification appears energetically the highest, which is expected as a high-pressure phase. It is of great importance to the findings of polytypic behaviors in $CaCO_3$ at high pressures, which has been recently confirmed. Moreover, this study shows new predicted calcite IIIc phase in the high symmetry *P321* (no. 150) space group, which should withstand extremely high-pressure conditions. The discovery of these new modifications with possible use in extreme conditions and their eventual synthesis might have possible very wide industrial and technological applications.

Acknowledgments

This work was financially supported by the Ministry of Science, Technological Development and Innovation of the Republic of Serbia through Contract No. 451-03-47/2023-01/200017. The authors are grateful to Prof. R. Dovesi, Prof. K. Doll, and Crystal Solutions for software support with CRYSTAL code. The authors thank the Max Planck Institute for Solid State Research, Stuttgart, Germany, for collaboration and for providing computational support.

References

[1] Y. Ma, Q. Zhou, Z. He, F. Li, K. Yang, Q. Cui, G. Zou, High-pressure and high-temperature study of the phase transition in anhydrite, Journal of Physics: Condensed Matter, 19 (2007) 425221.
[2] L. Yang, L. Dai, H. Li, H. Hu, Y. Zhuang, K. Liu, C. Pu, M. Hong, Pressure-induced structural phase transition and dehydration for gypsum investigated by Raman spectroscopy and electrical conductivity, Chemical Physics Letters, 706 (2018) 151-157.
[3] S.J. Brotton, R.I. Kaiser, In situ Raman spectroscopic study of gypsum ($CaSO_4 \cdot 2H_2O$) and epsomite ($MgSO_4 \cdot 7H_2O$) dehydration utilizing an ultrasonic levitator, The Journal of Physical Chemistry Letters, 4 (2013) 669-673.
[4] C.-J. Liu, H.-F. Zheng, In situ observation of gypsum-anhydrite transition at high pressure and high temperature, Chinese Physics Letters, 29 (2012) 049101.
[5] S. Bradbury, Q. Williams, X-ray diffraction and infrared spectroscopy of monazite-structured $CaSO_4$ at high pressures: Implications for shocked anhydrite, Journal of Physics and Chemistry of Solids, 70 (2009) 134-141.
[6] P. Comodi, A. Kurnosov, S. Nazzareni, L. Dubrovinsky, The dehydration process of gypsum under high pressure, Physics and Chemistry of Minerals, 39 (2012) 65-71.
[7] J. Kirtley, V. Leichner, B.R. Anderson, H. Eilers, A comparison of pulsed and continuous lasers for high-temperature Raman measurements of anhydrite, Journal of Raman Spectroscopy, 49 (2018) 862-871.
[8] T. Fujii, H. Ohfuji, T. Inoue, Phase relation of CaSO4 at high pressure and temperature up to 90 GPa and 2300 K, Physics and Chemistry of Minerals, 43 (2016) 353-361.
[9] E. Knittle, W. Phillips, Q. Williams, An infrared and Raman spectroscopic study of gypsum at high pressures, Physics and Chemistry of Minerals, 28 (2001) 630-640.
[10] M. Merlini, M. Hanfland, W. Crichton, $CaCO_3$-III and $CaCO_3$-VI, high-pressure polymorphs of calcite: possible host structures for carbon in the Earth's mantle, Earth and Planetary Science Letters, 333 (2012) 265-271.
[11] K. Suito, J. Namba, T. Horikawa, Y. Taniguchi, N. Sakurai, M. Kobayashi, A. Onodera, O. Shimomura, T. Kikegawa, Phase relations of $CaCO_3$ at high pressure and high temperature, American Mineralogist, 86 (2001) 997-1002.
[12] D. Druzhbin, S.V. Rashchenko, A. Shatskiy, W.A. Crichton, New High-Pressure and High-Temperature $CaCO_3$ Polymorph, ACS Earth and Space Chemistry, (2022).
[13] D. Huang, H. Liu, M.-Q. Hou, M.-Y. Xie, Y.-F. Lu, L. Liu, L. Yi, Y.-J. Cui, Y. Li, L.-W. Deng, Elastic properties of $CaCO_3$ high pressure phases from first principles, Chinese Physics B, 26 (2017) 089101.

[14] X. Li, Z. Zhang, J.F. Lin, H. Ni, V.B. Prakapenka, Z. Mao, New high-pressure phase of $CaCO_3$ at the topmost lower mantle: Implication for the deep-mantle carbon transportation, Geophysical Research Letters, 45 (2018) 1355-1360.
[15] S.S. Santos, M.L. Marcondes, J.F. Justo, L.V. Assali, Calcium carbonate at high pressures and high temperatures: a first-principles investigation, Physics of the Earth and Planetary Interiors, 299 (2020) 106327.
[16] L. Bayarjargal, C.-J. Fruhner, N. Schrodt, B. Winkler, $CaCO_3$ phase diagram studied with Raman spectroscopy at pressures up to 50 GPa and high temperatures and DFT modeling, Physics of the Earth and Planetary Interiors, 281 (2018) 31-45.
[17] P.N. Gavryushkin, N. Sagatov, A.B. Belonoshko, M.V. Banaev, K.D. Litasov, Disordered aragonite: The new high-pressure, high-temperature phase of $CaCO_3$, The Journal of Physical Chemistry C, 124 (2020) 26467-26473.
[18] M. Hou, Q. Zhang, R. Tao, H. Liu, Y. Kono, H.-k. Mao, W. Yang, B. Chen, Y. Fei, Temperature-induced amorphization in $CaCO_3$ at high pressure and implications for recycled $CaCO_3$ in subduction zones, Nature communications, 10 (2019) 1-8.
[19] A.R. Oganov, C.W. Glass, S. Ono, High-pressure phases of $CaCO_3$: crystal structure prediction and experiment, Earth and Planetary Science Letters, 241 (2006) 95-103.
[20] S. Ono, T. Kikegawa, Y. Ohishi, High-pressure transition of $CaCO_3$, American Mineralogist, 92 (2007) 1246-1249.
[21] G. Bergerhoff, I. Brown, F. Allen, Crystallographic databases, International Union of Crystallography, Chester, 360 (1987) 77-95.
[22] D. Zagorac, H. Müller, S. Ruehl, J. Zagorac, S. Rehme, Recent developments in the Inorganic Crystal Structure Database: theoretical crystal structure data and related features, Journal of applied crystallography, 52 (2019) 918-925.
[23] J. Zagorac, D. Zagorac, M. Rosić, J.C. Schön, B. Matović, Structure prediction of aluminum nitride combining data mining and quantum mechanics, CrystEngComm, 19 (2017) 5259-5268.
[24] D. Zagorac, J.C. Schön, M. Jansen, Identification of promising chemical systems for the synthesis of new materials structure types: An ab initio minimization data mining approach, Processing and Application of Ceramics, 7 (2013) 37-41.
[25] T. Škundrić, D. Zagorac, J.C. Schön, M. Pejić, B. Matović, Crystal structure prediction of the novel Cr_2SiN_4 compound via global optimization, data mining, and the PCAE method, Crystals, 11 (2021) 891.
[26] D. Zagorac, J.B. Zagorac, K. Doll, M. Čebela, B. Matović, Extreme pressure conditions of bas based materials: Detailed study of structural changes, band gap engineering, elastic constants and mechanical properties, Processing and Application of Ceramics, 13 (2019) 401-410.
[27] D. Jovanović, J.B. Zagorac, B. Matović, A.R. Zarubica, D. Zagorac, Structural, electronic and mechanical properties of superhard B4C from first principles, Journal of Innovative Materials in Extreme Conditions, 1 (2020) 19-27.
[28] J.B. Zagorac, D. Zagorac, D. Jovanović, M. Pejić, T. Škundrić, B. Matović, Ab Initio Investigations and Behaviour of the α-Ce_2ON_2 Phase in the Extreme Pressure Conditions, Journal of Innovative Materials in Extreme Conditions, 2 (2021) 36-43.
[29] J.C. Schön, Energy Landscape Concepts for Chemical Systems under Extreme Conditions, Journal of Innovative Materials in Extreme Conditions, 2 (2021) 5-57.
[30] D. Zagorac, K. Doll, J. Schön, M. Jansen, Ab initio structure prediction for lead sulfide at standard and elevated pressures, Physical Review B, 84 (2011) 045206.
[31] A.A. Sokol, C.R.A. Catlow, M. Miskufova, S.A. Shevlin, A.A. Al-Sunaidi, A. Walsh, S.M. Woodley, On the problem of cluster structure diversity and the value of data mining, Physical Chemistry Chemical Physics, 12 (2010) 8438-8445.
[32] G. Ceder, D. Morgan, C. Fischer, K. Tibbetts, S. Curtarolo, Data-mining-driven quantum mechanics for the prediction of structure, MRS bulletin, 31 (2006) 981-985.
[33] R. Dovesi, A. Erba, R. Orlando, C.M. Zicovich-Wilson, B. Civalleri, L. Maschio, M. Rérat, S. Casassa, J. Baima, S. Salustro, Quantum-mechanical condensed matter simulations with CRYSTAL, Wiley Interdisciplinary Reviews: Computational Molecular Science, 8 (2018) e1360.

[34] R. Dovesi, R. Orlando, B. Civalleri, C. Roetti, V.R. Saunders, C.M. Zicovich-Wilson, CRYSTAL: a computational tool for the ab initio study of the electronic properties of crystals, Zeitschrift für Kristallographie-Crystalline Materials, 220 (2005) 571-573.
[35] R. Dovesi, F. Pascale, B. Civalleri, K. Doll, N.M. Harrison, I. Bush, P. D'arco, Y. Noël, M. Rérat, P. Carbonnière, The CRYSTAL code, 1976–2020 and beyond, a long story, The Journal of chemical physics, 152 (2020) 204111.
[36] J.P. Perdew, K. Burke, M. Ernzerhof, Generalized gradient approximation made simple, Physical review letters, 77 (1996) 3865.
[37] J.P. Perdew, A. Zunger, Self-interaction correction to density-functional approximations for many-electron systems, Physical Review B, 23 (1981) 5048.
[38] A.D. Becke, Density-functional thermochemistry. III. The role of exact exchange, The Journal of Chemical Physics, 98 (1993) 5648-5652.
[39] M. Catti, A. Pavese, V. Saunders, Elastic constants and electronic structure of fluorite (CaF_2): an ab initio Hartree-Fock study, Journal of Physics: Condensed Matter, 3 (1991) 4151.
[40] M. Catti, A. Pavese, R. Dovesi, V. Saunders, Static lattice and electron properties of $MgCO_3$ (magnesite) calculated by ab initio periodic Hartree-Fock methods, Physical Review B, 47 (1993) 9189.
[41] M.D. Towler, N.L. Allan, N.M. Harrison, V.R. Saunders, W.C. Mackrodt, E. Aprà, Ab initio study of MnO and NiO, Physical Review B, 50 (1994) 5041-5054.
[42] D. Zagorac, J. Schön, J. Zagorac, M. Jansen, Prediction of structure candidates for zinc oxide as a function of pressure and investigation of their electronic properties, Physical Review B, 89 (2014) 075201.
[43] R. Dovesi, C. Ermondi, E. Ferrero, C. Pisani, C. Roetti, Hartree-Fock study of lithium hydride with the use of a polarizable basis set, Physical Review B, 29 (1984) 3591.
[44] D. Jovanović, D. Zagorac, J.C. Schön, B. Milovanović, J. Zagorac, A new theoretical model for hexagonal ice, Ih (d), from first principles investigations, Zeitschrift für Naturforschung B, 75 (2020) 125-128.
[45] W. Perger, J. Criswell, B. Civalleri, R. Dovesi, Ab-initio calculation of elastic constants of crystalline systems with the CRYSTAL code, Computer Physics Communications, 180 (2009) 1753-1759.
[46] R. Hundt, J.C. SchoÈn, A. Hannemann, M. Jansen, Determination of symmetries and idealized cell parameters for simulated structures, Journal of applied crystallography, 32 (1999) 413-416.
[47] A. Hannemann, R. Hundt, J. Schön, M. Jansen, A new algorithm for space-group determination, Journal of applied crystallography, 31 (1998) 922-928.
[48] R. Hundt, A. Kplot, Program for Plotting and Analyzing Crystal Structures, Technicum Scientific Publishing, Stuttgart, 2016.
[49] K. Momma, F. Izumi, VESTA 3 for three-dimensional visualization of crystal, volumetric and morphology data, Journal of applied crystallography, 44 (2011) 1272-1276.
[50] W. Gerlach, Die gitterstruktur der erdalkalioxyde, Zeitschrift für Physik, 9 (1922) 184-192.
[51] W.R. Busing, H.A. Levy, Neutron diffraction study of calcium hydroxide, The Journal of chemical physics, 26 (1957) 563-568.
[52] O. Flörke, Crystallographic and X-Radiographic Investigations in the System CaSO4–CaSO4. 2H2O, Neves Jahrbuch fur Mineralogie, Geologie und Paleontologie, Abhandlung, 84 (1952) 189-240.
[53] W. Abdel, Bestimmung der Kristallstruktur von $CaSO_4(H_2O)_{0,5}$ mit Röntgenbeugungsmethoden und mit Potentialprofil-Rechnungen, Zeitschrift für Kristallographie-Crystalline Materials, 205 (1993) 99-116.
[54] R. Khasanov, N. Nizamutdinov, N. Khasanova, A. Gubaĭdullin, V. Vinokurov, Low-temperature dehydration of gypsum single crystals, Crystallography Reports, 53 (2008) 806-811.
[55] D. Bevan, E. Rossmanith, D.K. Mylrea, S.E. Ness, M.R. Taylor, C. Cuff, On the structure of aragonite–Lawrence Bragg revisited, Acta Crystallographica Section B: Structural Science, 58 (2002) 448-456.
[56] S.M. Antao, I. Hassan, W.H. Mulder, P.L. Lee, B.H. Toby, In situ study of the orientational disorder in calcite, Physics and Chemistry of Minerals, 36 (2009) 159-169.

[57] V. Borodin, V. Lyutin, V. Ilyukhin, N. Belov, The isomorphous series calcite-otavite, Doklady Akademii Nauk SSSR, 245 (1979) 1099-1101.
[58] H. Chessin, W.C. Hamilton, B. Post, Position and thermal parameters of oxygen atoms in calcite, Acta Crystallographica, 18 (1965) 689-693.
[59] S.M. Antao, I. Hassan, Temperature dependence of the structural parameters in the transformation of aragonite to calcite, as determined from in situ synchrotron powder X-ray-diffraction data, The Canadian Mineralogist, 48 (2010) 1225-1236.
[60] P.N. Gavryushkin, A.B. Belonoshko, N. Sagatov, D. Sagatova, E. Zhitova, M.G. Krzhizhanovskaya, A. Recnik, E.V. Alexandrov, I.V. Medrish, Z.I. Popov, Metastable structures of CaCO3 and their role in transformation of calcite to aragonite and postaragonite, Crystal Growth & Design, 21 (2020) 65-74.
[61] D. Zagorac, J. Schön, J. Zagorac, M. Jansen, Theoretical investigations of novel zinc oxide polytypes and in-depth study of their electronic properties, RSC Advances, 5 (2015) 25929-25935.
[62] D. Zagorac, J. Zagorac, J.C. Schoen, N. Stojanović, B. Matović, ZnO/ZnS (hetero) structures: Ab initio investigations of polytypic behavior of mixed ZnO and ZnS compounds, Acta Crystallographica Section B: Structural Science, Crystal Engineering and Materials, 74 (2018) 628-642.
[63] J.R. Smyth, T.J. Ahrens, The crystal structure of calcite III, Geophysical Research Letters, 24 (1997) 1595-1598.
[64] T. Pilati, F. Demartin, C. Gramaccioli, Lattice-dynamical estimation of atomic displacement parameters in carbonates: calcite and aragonite $CaCO_3$, dolomite $CaMg(CO_3)_2$ and magnesite $MgCO_3$, Acta Crystallographica Section B: Structural Science, 54 (1998) 515-523.

Journal of Innovative Materials in Extreme Conditions

Volume 4, Issue 2, Year 2023

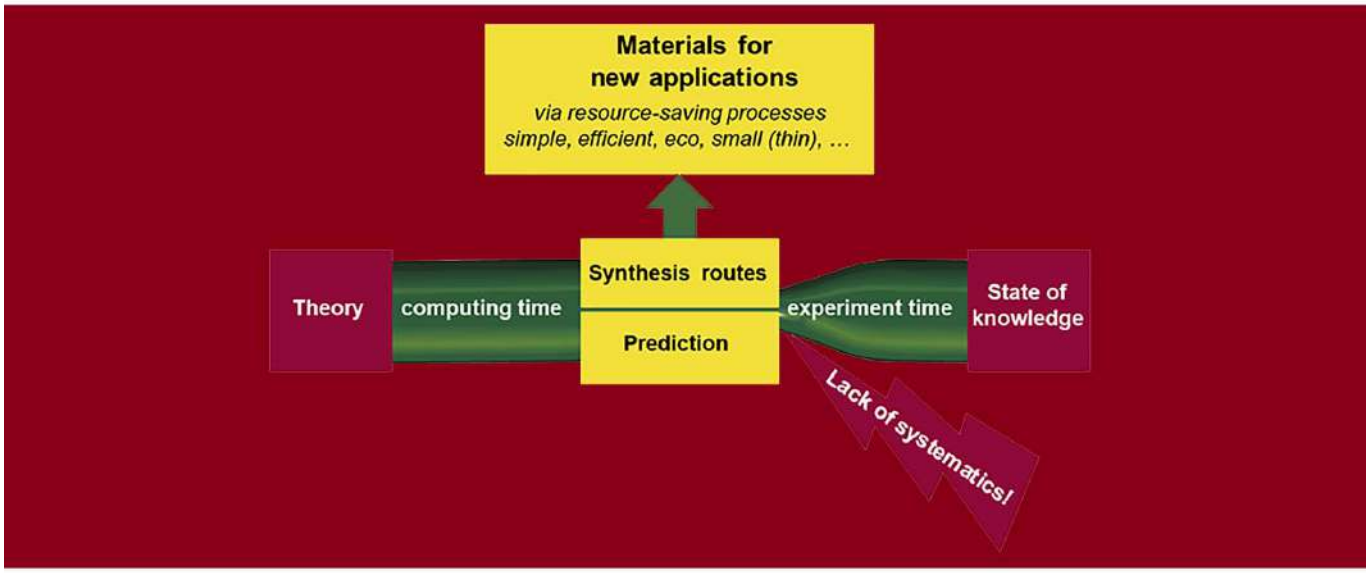

Published by:

SIM-EXTREME

Serbian Society for
Innovative Materials in
Extreme Conditions

Journal of Innovative Materials in Extreme Conditions (*abbr*. JIMEC)

Volume 4, Issue 2, Year 2023

Volume 4, year 2023

JIMEC: Table of Contents

Volume 4, Issue 2, Year 2023

-Issue 2

1. **THIN FILMS AND MONOLAYERS – PREDICTION, MODELING, AND EXPERIMENTS**
   J. Christian Schön, Dieter Fischer, *Journal of Innovative Materials in Extreme Conditions*, **Vol. 4**, Issue 2, page 52-76 (2023).
   (PDF Free Download)

2. **A REVIEW OF THE SYNTHESIS OF COMPOSITIONALLY COMPLEX ULTRA-HIGH-TEMPERATURE CERAMICS**
   Dharma Teja Teppala, Samuel Aeneas Kredel, Emanuel Ionescu, Branko Matović, *Journal of Innovative Materials in Extreme Conditions*, **Vol. 4**, Issue 2, page 77-103 (2023).
   (PDF Free Download)

Journal of Innovative Materials in Extreme Conditions
2023
Volume 4
Issue 2

THIN FILMS AND MONOLAYERS – PREDICTION, MODELING, AND EXPERIMENTS

J. Christian Schön[1,*], Dieter Fischer[1]

[1]Max Planck Institute for Solid State Research, D-70569 Stuttgart, Germany
Corresponding author: C.Schoen@fkf.mpg.de*

Abstract: *The development of new materials in an efficient fashion requires progress both in the computational search for promising targets and in the design of suitable synthesis routes by a combined effort of theory and experiment. This applies not only to bulk materials but also to low-dimensional systems such as thin films and monolayers. In this presentation, we will discuss some of the methodological features specific to the prediction and synthesis of (meta)stable (quasi)-low-dimensional systems, together with examples of structure prediction and modeling for crystalline and amorphous atom- and molecule-based monolayers and thin films. This is complemented by direct comparisons with experiments, and the discussion of additional thin film experiments that focus on new structural insights in seemingly completely understood systems like gallium and ZnO films.*

1. Introduction

New chemical materials and compounds serve as the foundation for the modern technology of our civilization, where these materials should be environmentally friendly, with stable and controllable properties for a multitude of applications, and at the same time energy efficient in their synthesis as well as easily recyclable.[1,2] In particular, the development of new devices, of ever greater sophistication yet smaller size at the same time, requires providing new types of inorganic or hybrid materials, whose structure can be controlled down to the atomic level, in order to fine-tune their physical, and chemical and/or biological properties.[3-5] Traditionally, such materials are generated in bulk and then chemically machined down to whatever size is needed.[6,7] But such materials are also often grown in a bottom-up approach on a substrate, and in the extreme, we are dealing with and aiming for low-dimensional systems with bespoke properties, where details of their structure and the stability of such materials often become an issue of concern.[8,9]

The ability to predict such (meta)stable nanomaterials via the investigation of their energy landscapes, followed by a computation of their properties and stability, is of great value in their design and synthesis.[10] Over the past three decades, the structure prediction of 3D bulk crystalline compounds, atom clusters, and (bio)molecules has shown great progress,[11-13] and the computational approaches used are expected to be also applicable to low-dimensional systems.[14] Such landscape explorations are of great value since the synthesis and design - within the limitations of physical laws - of such materials often lead to compounds or modifications that are metastable or only stable under certain specific structural or thermodynamic boundary conditions. Thus, further insights come from modeling and simulating the synthesis process, and the detailed experimental study of the structure and properties of these materials.

Furthermore, since we are not necessarily dealing with macroscopic bulk phases that are thermodynamically stable, the outcome will be greatly influenced by the details of the synthesis route. But trying to design a path to a desired compound, whose structure is controlled on the atomic level, is only possible if we know the many feasible (meta)stable phases, as a function of the thermodynamic and process parameters, that might appear along the road as intermediary modifications or even constitute traps to be avoided. Conversely, studying the energy landscape of the system, on which these modifications are located, allows us to identify promising targets for such a synthesis, especially if they are predicted to exhibit useful properties.

Besides such targets and competing phases, a full design of a synthesis route requires information about the evolution of the structures on both the atomic and the mesoscopic levels. Both reliable comprehensive experimental data and extensive input from theory are needed to provide this information about the processes involved. [15] Once such descriptions are available, optimal control

methods can be applied to identify the choice of an (optimal) synthesis route or the optimal schedule of the parameters for a given type of route [16-18], yielding the desired outcome.

The theoretical tools as such are well-known - molecular dynamics and Monte-Carlo simulations or through global explorations of the energy landscape on the one hand and in the form of differential equations representing, e.g., reaction-diffusion and various growth laws on the other hand, thus describing the evolution of the system on the atomic and mesoscopic level, respectively - although need to be adjusted for every chemical system and proposed synthesis route, and encounter obvious limitations due to numbers of atoms involved and the computational cost of the energy and force calculations when performed on the ab initio level. In contrast, sufficient input from the experiment is usually lacking in the case of solid-state synthesis. The reason for this is a "psychological" one, due to the historical focus on describing the one synthesis route that yielded the new never-before-seen compound. However, in order to provide the necessary information for modeling and optimizing a synthesis route, one needs not only a careful analysis of the specific synthesis route (including the associated parameters) that has been successful in producing the desired compound but also analogous detailed information about the outcome of unsuccessful routes or parameter choices for the synthesis of this specific compound! This includes, e.g., which byproducts have been produced, what parameter choice increases the yield, what influence certain impurities have, etc., ideally not only at the end but also along the various stages of the different synthesis routes and studied parameter schedules.

While such information is often available for organic syntheses, for inorganic compounds such data are commonly lacking or, if available, have not been published, since the focus of the solid-state chemist and materials scientist usually is on the "successful" synthesis of a new compound and not on the analysis of the synthesis route as such. One reason for this is the very time-consuming investigation of all the parameters involved in the synthesis. But such data are highly valuable, since they greatly increase our knowledge of the chemical system itself, allow the formulation of general laws effectively describing solid-state syntheses, and would be expected to be transferable, with slight modifications, to other chemical systems, for which successful syntheses are still lacking, especially in combination with theoretical analyses of the system and the attempted synthesis routes.

This issue will take on an even greater urgency as the availability of sufficient computer resources and general expertise in machine learning [19,20] will allow us to attempt to train large neural networks to predict the outcome of proposed synthesis routes for achieving a given chemical systems - or even directly suggest the best route for a given target compound or modification. In a way, this would be the computer science equivalent of incorporating the knowledge of many experienced experimental chemists into the "ideal wise chemist". However implementing this approach will require the availability, as input, of a plethora of detailed information about both the successful syntheses and those which have "failed" to produce the desired outcome.

Another related issue is often the lack of full and detailed information about the structures of the synthesized compounds of interest, ideally as a function of the synthesis route. Due to the overwhelming pressure to generate new compounds with exciting new properties, one frequently observes that the structures of the published compounds are known only in quite a rough fashion - if at all -, where reflections in diffraction patterns, bands in Raman or IR spectra, UV-VIS measurements, etc., are not fully explained or just attributed to some unspecified disorder in the system. Here, theory can only assist by pointing out that these peaks should not appear in the data assuming that the compound exhibits the proposed "ideal" structure. But theory by itself cannot identify, in a definitive way, where to look for explanations, unless we can fully model the whole synthesis starting from the educts and taking all admixtures or surfaces of reactions, etc., into account. Clearly, clarifying such issues and identifying the underlying structural peculiarities of the material is an important challenge that needs to be answered by the experimentalist.

However, although these subtle quasi-invisible features can influence the properties of a material to a large extent, it is not easy to extract such information for macroscopic 3D-bulk systems. Besides explaining the physical properties of a given material, we need to address even more fundamental questions regarding our control of a chemical system: Can we specifically synthesize all polymorphic forms of a compound? Do we understand which differences in synthesis procedures and choices of synthesis parameters are responsible for the formation of these different crystal structures? But such detailed information can often be obtained, and much control over the synthesis is expected,

if the system is of lower dimension. Examples of such systems are two-dimensional monolayers of atoms or molecules, either free-standing or on a substrate, and thin films that have been deposited from a gas phase of controlled composition without impurities in high vacuum at low temperatures, thus avoiding the complication of the presence of a solvent or flux and the high temperatures and pressures often used in solid-state syntheses.

The amount of work that has been done on such thin films and monolayers is enormous and doing it justice in a comprehensive fashion would result in a large review far beyond the purview of this contribution.[21,22] Instead, we will present some prototypical examples drawn from our work, which illustrate the issues and challenges mentioned above.

2. Methods

In order to avoid getting into technical details in the example section, we are summarizing the methods - theoretical and experimental ones - that have been applied in the examples presented below. For more details on the algorithms and synthesis methods mentioned, we refer to the literature and the original publications.

2.1. Theory

In the examples below, a variety of computational methods have been employed. To start with, global optimizations have been performed on the energy landscape of the chemical systems, in order to predict the structure of molecules and atom clusters in vacuum and on surfaces, to predict the arrangement of monolayers of atoms and molecules on a substrate or as a free-standing 2D-monolayer, and to predict the structure of bulk crystalline modifications in 3D. The algorithms employed have been simulated annealing (SA) [23], both with and without large jumpmoves - sometimes combined with local minimizations directly after the jumpmove -, the threshold algorithm (TA) [24,25] and the closely related threshold minimization (TM) algorithm [26], and the IGLOO algorithm [27].

All of these are stochastic optimization and energy landscape exploration algorithms that are based on random Monte Carlo (MC) walks in configuration space employing both simple and complex moveclasses, with or without a prescribed energy threshold, and often combined with periodic local optimizations. These are performed at different temperatures: $T = 0$ K (stochastic quench where only downhill steps are accepted), $T = \infty$ (unbiased random walk where every step is accepted), and $0 < T < \infty$ (every step is accepted according to the Metropolis criterion [28]).

Next, molecular dynamics (MD) simulations have been employed for modeling monolayers of molecules and atoms and their evolution with time, for the simulation of the deposition processes and growth of thin films, and for the computation of properties such as diffusion constants or the phonon density of states. We note that the global optimizations and MD simulations are usually performed with robust generic or specially adapted empirical potentials, but in some cases, ab initio energies were employed.

All promising structure candidates obtained during the global optimization were locally optimized on ab initio level. For those 3D crystalline modifications with low energies, the energy was also computed as a function of volume, or the enthalpy as a function of pressure, respectively, in order to be able to estimate, which ones would be classified as standard pressure, high pressure or effective negative pressure phases.

Finally, various properties were computed, on ab initio level, such as band gaps, Raman spectra of clusters or of crystalline modifications - with and without defects -, in order to interpret the peaks in the experimental data of molecules/clusters in the gas phase and of the thin films that exhibit nucleation and growth of crystalline phases.

2.2. Experiments

For the study of single non-reactive molecules and monolayers thereof on a metal substrate with smooth surfaces, the electrospray ionization (ESI) method was employed [29], while for the deposition of precursor molecules that react to form periodic or amorphous monolayers on a substrate, the gas phase resulted from sublimation of the precursor molecules. The thin films were generated using the low-rate/low-temperature deposition technique, which works on the border of the beginning of crystallization. Here, a beam of atoms and/or few-atom cluster fragments was generated by thermal evaporation [30] or via pulsed laser ablation [31] of materials with the same composition as the thin film that should be grown. In special cases, the electron beam gun evaporation combined with a plasma activation of gases was used [32,33]. The deposition usually takes place at reduced mobility conditions (low deposition temperatures T_D between -240 °C and + 450 °C) which allows the local addition of individual atoms or cluster fragments on the atomic level without large atom movement on the surface, thus forming a homogeneous, originally amorphous, deposit. Thus, a large variety of (meta)stable phases can readily nucleate and grow even when one tempers at quite low temperatures, and subsequently transform into other modifications upon slow heating and cooling of the deposit.

3. Examples

In this section, we will present a number of prototypical examples that illustrate a variety of aspects of the modern view of syntheses, ranging from structure prediction of target compounds to complete synthesis modeling as far as theory is concerned. Regarding the experiments, they deal with the deposition of monolayers via the gas phase and the systematic analysis of phase formation and transformation as a function of synthesis and subsequent treatment parameters for thin films in the experiment. These investigations are moreover combined with a detailed analysis of the generated phases and their properties as a function of the deposition parameters.

3.1. Prediction of 2D monolayers in the Si/C system

Monolayer graphene being a material with exciting properties, it is a natural question to ask, how the admixture of Si atoms would affect its behavior. Since only (meta)stable compounds should be considered for such a hypothetical material, in the first step, the energy landscape of Si_xC_{1-x} two-dimensional structures was globally explored for a range of values of x (x = 1/4, 1/3, 1/2, 2/3, 3/4).[10,34] For each choice of x, the global minimum consisted of a graphene-analogue structure, where a fraction x of the carbon atoms in graphene were replaced by Si atoms; however, many other network structures consisting of a mixture of rings of three, four, five, six, seven, eight or more atoms, were also frequently found as kinetically stable structures. Since there is no efficient robust empirical potential for the Si/C system, the global optimizations using the SA algorithm with jumpmoves were performed on ab initio level (DFT).

When comparing the energy of these configurations with the energy of decomposition into a fraction (1-x) of pure C-graphene and fraction x of pure Si-graphene, only the alternating (see Figure 1) graphene analog with composition Si : C = 1:1 was thermodynamically stable [34]. Considering the band structures of Si-, C-, and SiC-graphene, we find that those of C-graphene and Si-graphene are very similar with both exhibiting Dirac points, while the SiC-graphene structure is a semiconductor with a finite band gap of about 2.5 eV.

We note that recently, Polley et al. [35] have succeeded in preparing the alternating SiC-graphene analog by first depositing an ultrathin transition metal carbide film (TaC) on a silicon carbide substrate. Then the system was slightly heated such that Si and C atoms of the substrate diffused in equal amounts onto the TaC surface, and with Si and C atoms being in close proximity to each other, a monolayer of SiC-graphene could form as the "nearest" thermodynamically stable minimum.

This example nicely demonstrates the successful application of suitably modified versions of the well-established crystal structure prediction methods to low-dimensional systems, with a subsequent realization of the predicted structure in the experiment. However, it also demonstrates that the successful synthesis method is not a very straightforward one, at least for the non-expert in thin film and surface layer modification and growth.

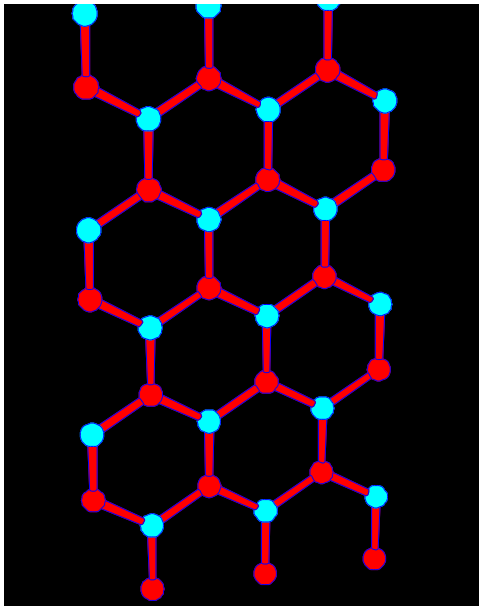

Figure 1. Structure of the global minimum of a monolayer of SiC. Red spheres and blue spheres represent carbon and silicon atoms, respectively.

3.2. Prediction and synthesis of monolayers of sucrose molecules on a Cu(100) substrate

As a second example, we consider the formation of periodic monolayers of sucrose molecules on a Cu(100) surface [36]. From a theoretical point of view, modeling the full synthesis, i.e., the generation of the gas phase via ESI, the deposition of the gas of protonated or deprotonated or otherwise charged sucrose molecules on the surface and the diffusion based re-arrangement of these molecules into possible amorphous and periodic structures would be highly complex and computationally extremely expensive: already the analysis of the deprotonated molecule in a vacuum takes a large effort to describe and analyze because of the many (22) hydrogen atoms that can be involved in the deprotonation [37]. Thus, we have employed global optimization techniques in a stepping stone approach, to obtain structure candidates for the (periodic) sucrose monolayer on the surface for comparison with the experiment.

As a first step, the TM algorithm using an AMBER force field was used to obtain the optimal shape of the neutral sucrose molecule in vacuum [26], where all angles and atom-atom-distances were allowed to vary. Next, this molecule was placed on the metal surface in various orientations as the initial configurations for a second round of global optimizations, where the optimal shape, orientation, and location of the molecule on the metal surface were identified [38], using the IGLOO algorithm. Here, the interaction with the surface was via a Lennard-Jones term and an image charge term, while only a limited number of internal degrees of freedom of the sucrose molecule, the dihedral angles, were allowed to be varied, together with the orientation and location of the molecule with respect to

the atoms in the Cu-surface. The best candidates were locally re-optimized on the ab initio level on the Cu-surface, where all atoms in the molecule were allowed to vary.

The optimal structure of the single molecule on the surface was used as input to the global search for low-energy periodic configurations of the sucrose monolayer, represented by a finite number of sucrose molecules in a variable 2D-periodic simulation cell with the actual Cu-surface being replaced by a featureless metal-like surface. Here, the individual molecules were treated as rigid, but they were allowed to be shifted and rotated in the plane of the surface, together with the variation of the cell parameters of the simulation cell. The result was a very large number of low-energy structures that all corresponded to slightly different compact packings of the sucrose molecules [38] (see Figure 2 for a typical example).

In parallel, the experiments produced STM images, which showed a periodic arrangement of bright and dark regions of sizes on the order of about half a sucrose molecule, with a more or less quadratic arrangement of these elements, suggesting a square-like unit cell.[39] By computing the STM images of the individual sucrose molecules arranging these in a compact fashion analogous to the results of the global optimization, and comparing these arrangements with the experimental STM images, a good agreement between theory and experiment was achieved [36].

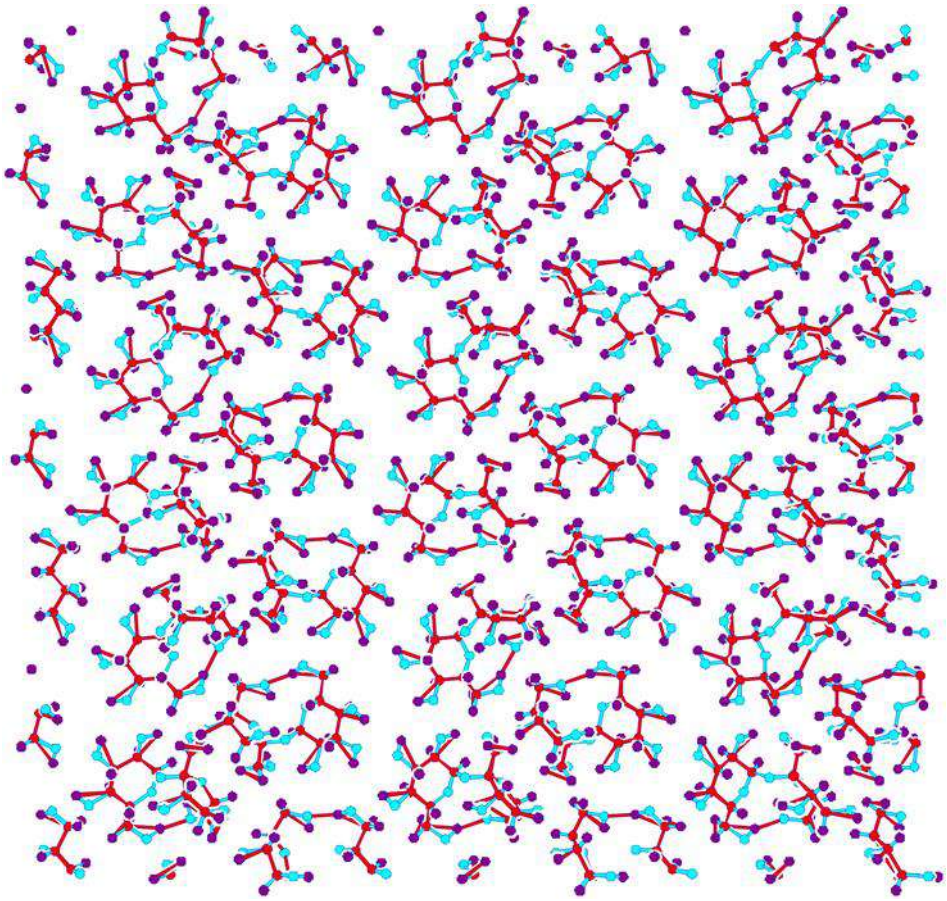

Figure 2. Low-energy local minimum of a monolayer of sucrose molecules, with four molecules in the variable periodically repeated simulation cell. Red, blue, and purple spheres correspond to carbon, oxygen, and hydrogen atoms. Note that each molecule contains 45 atoms, many of which are projected on top of each other in this view along the vertical to the surface.

This study underlines the importance of close collaboration between theory and experiment, in particular, if the system consists of many (large) molecules and surface atoms with a large variety of interaction types involved. In such a case, the number of atoms that need to be taken into account is so large, and in addition, the synthesis process is so complex, that a complete synthesis modeling and

structure prediction on ab initio level is not feasible. As a consequence, the structure prediction needs to take place in stages [38]; however, the gain in "efficiency" is paid for by the price of potentially large inaccuracies when the hand-over between two stages of the modeling process occurs.

3.3. Modeling and synthesis of amorphous monolayers of 1,3,5-tris-(4-bromophenyl)-benzene on an Au(111) substrate

The periodic arrangement of sucrose molecules on the Cu-surface was due to a combination of dense packing - thus maximizing the van-der-Waals interactions among the molecules -, hydrogen bridge bonds, and relatively weak (mostly dipole and quadrupole) electrostatic interactions between the molecules. As a consequence, the molecules could quite easily move about and rearrange themselves within a certain temperature window-, thus achieving energetically optimal (periodic) packings. However, if the temperature was too low, the molecules remained essentially frozen where they were deposited, as could be seen during the analogous deposition of trehalose, where a variety of arrangements of the molecule in small groups of molecules were observed [40], while at higher temperatures the molecules diffused very rapidly on the surface thus preventing the formation of any stable structures visible in the STM. The characteristic features of these packings could be predicted within the limitations of the purely global optimization approach to structure prediction, which typically aims at the structure that has the lowest energy and thus would be guaranteed to be the thermodynamically stable one at a temperature of 0 K. These limitations include imperfect energy functions - even on ab initio level, van-der-Waals and hydrogen-atom mediated bonding are non-trivial to account for -, small energy barriers against molecular re-arrangements combined with a multitude of low-energy arrangements. Adding finite temperatures that allow the molecules to switch between different arrangements, these limitations makes a perfect prediction nearly impossible, although one on the level of the experimental (STM) accuracy - where the resolution is usually not higher than ca. 1/2 nm - is possible.

This contrasts with the case of precursor molecules that react with one another on the surface, usually via reactive functional groups at the rim of the molecule, releasing, e.g., X_2 (X = F, Cl, Br, ...) gas molecules in the process. The resulting network of covalently bound molecules (actually, the remaining molecular cores of the precursor molecules) is thus quite stable, and rearrangements are exponentially slow at temperatures below those at which the molecules themselves decompose or the network degrades. As a consequence, the network largely reflects the original more or less random amorphous arrangement of the precursor molecules, analogous to the case of a network-type glass former like SiO_2 when cooled below the glass transition temperature [41]. Once the network has formed, changes in the frozen-in yet energetically non-optimal structure take place on logarithmically slow time scales, similar to the aging processes in glasses [42-45].

From a theoretical point of view, the appropriate approach thus takes its inspiration from the modeling of the glass transition or precursor-based 3D network formation and the simulation of the evolution of glasses and other amorphous compounds, i.e., one performs very long MC or MD simulations, while including the formation (and subsequent rare breaking) of bonds between the precursor molecules via appropriate empirical potentials.

As an example, we consider the amorphous network of 1,3,5-tris-(4-bromophenyl)-benzene on an Au(111) substrate, where each of the molecules could form three covalent bonds to neighbor molecules in a triangular fashion [46]. The experiment yielded an irregular network of triangular nodes (each representing one of the molecules) with a wide distribution of ring sizes - predominantly ranging from 4 to 8 -, where the optimal arrangement would have been a perfect hexagonal lattice. For the simulations, we performed long-time MD simulations of partly rigid molecules, i.e., the atoms inside each of the four rings consisting of six atoms each, which together constituted the individual molecules, were rigidly connected. The resulting structures (for example, see Figure 3) were very similar to the experiment. They showed good agreement with the experiment regarding both the ring-size distributions and the distribution, overall molecule nodes of the network, of the sets of the possible combinations of the sizes of the three rings that share a common corner molecule. Furthermore, the plot of the average energy of the network vs. the logarithm of simulation time

exhibited a smooth linear decrease over many orders of magnitude as expected from a typical system with standard aging behavior.

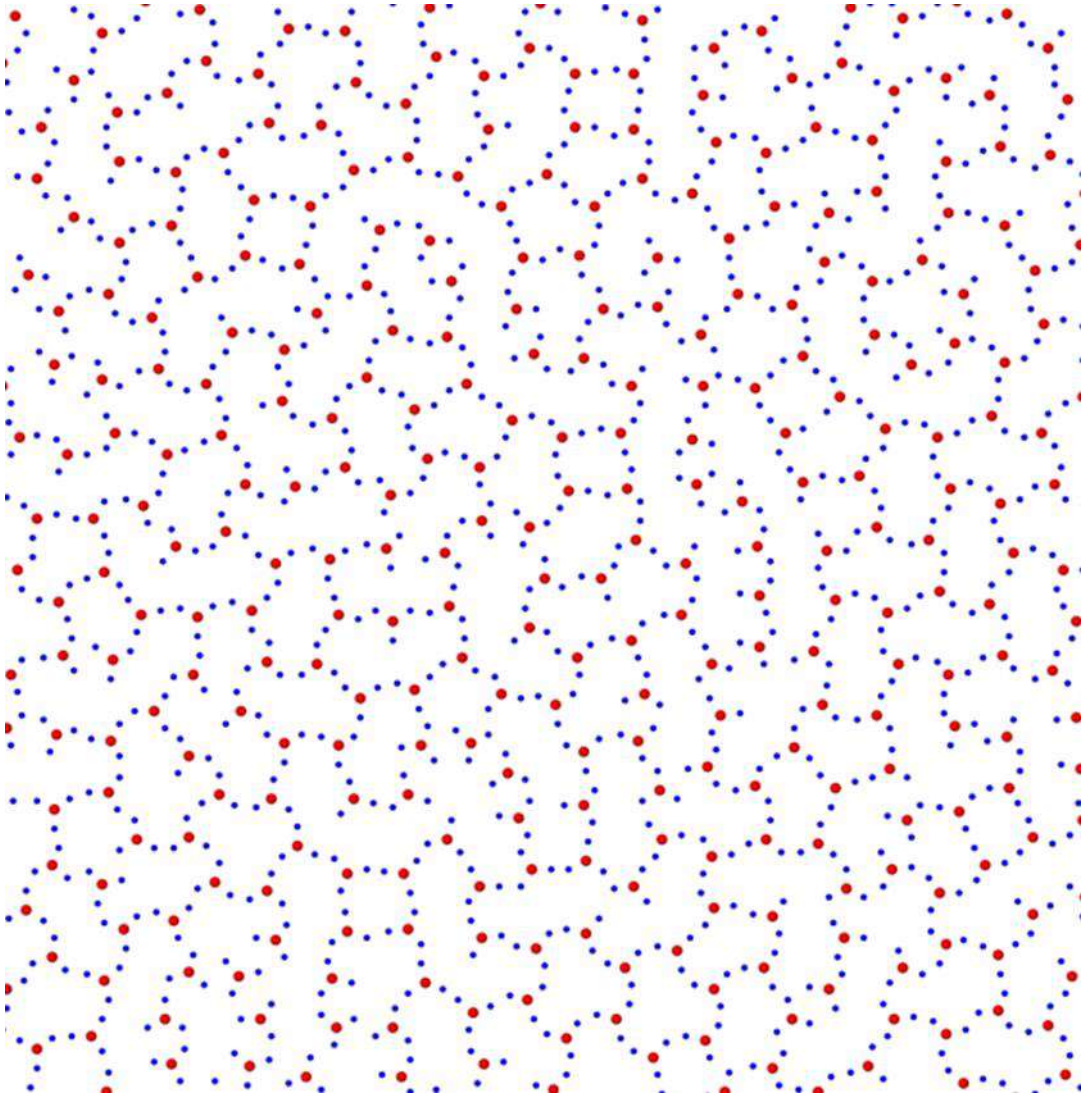

Figure 3. Except from an amorphous two-dimensional network of 1,3,5-tris-(4-bromophenyl)-benzene during a MD simulation of 5750 model molecules. The red and blue dots represent the central benzene and the three bromophenyl groups of the molecules, respectively.

While the modeling did not take into account the atom level processes that occurred during the reactions that formed the covalent bonds between the molecules, it captured the creation and evolution of the network of the molecules in a satisfactory manner. In particular, by changing the parameters in the effective potential describing both the molecule-molecule interactions and the interior flexibility of each molecule, it would be possible to suggest the outcome of the network formation for other (triangular) molecules that interact more weakly or more strongly or exhibit different degrees of internal flexibility, than the original molecular system studied. This would allow us to select a-priori the right kind of molecular building blocks to achieve specific networks (defined by their ring-size distributions) with a high probability and predict their stability as a function of evolution time.

3.4. Prediction of 3D crystalline LiBr modifications and their realization in thin films

Turning to the investigation of thin films, the analysis of LiBr thin films deposited at low temperatures is a classical example of a true 3D crystal structure prediction followed by a successful synthesis of one of the predicted yet previously not observed (meta)stable modifications [47-49]. Using the SA algorithm for global optimization on the empirical potential energy landscape followed by ab initio level local optimizations of the promising structure candidates, the resulting E(V) curves indicated that besides the known rocksalt type modification, a number of other ones, including a wurtzite, sphalerite and 5-5 type [50,51] modification, should be accessible and stable at standard pressure and moderately low temperatures. In fact, depending on the density functional employed, one of the structures with four-fold coordination, such as the wurtzite-, sphalerite-, or the β-BeO-type, might have a lower energy than the known rocksalt-type structure of LiBr.[47,48]

To explore the configuration space experimentally, the low-rate/low-temperature approach was employed using evaporation from a heated LiBr solid as a source to deposit Li/Br atoms and cluster fragments on a sapphire substrate.[49] The deposition rate (characterized by the vapor pressure p_D) was systematically varied ($1 \leq p_D < 8x10^{-4}$ mbar) as well as the temperature of the substrate (typically called the deposition temperature T_D) using a resistance heater (-100 °C $\leq T_D \leq$ 0 °C), and the outcome was carefully recorded (see Figure 4). As a result, an optimal combination of pressure and T_D was determined for which the new predicted wurtzite modification β-LiBr could be obtained in 100% of the syntheses. Furthermore, this study demonstrates the importance of a dense mesh size of the (p_D,T_D) parameter set. In the experiments with T_D below -100 °C, at low vapor pressures amorphous samples were obtained, which transform during heating into the stable rock salt modification, while at higher vapor pressures broad reflections of the rock salt modification directly emerged in the diffraction patterns. Similarly, for depositions above 0 °C the rock salt type is detected, too. However, for T_D between -100 °C and 0 °C, the β-LiBr can be stabilized where the likelihood of obtaining this modification systematically varies as a function of p_D and T_D.

Besides being a very nice example of a true successful prediction with subsequent experimental verification, this case also provides a demonstration of the proper way to not only present a newly synthesized modification but also to perform a quantitative analysis of the outcomes for a large range of the synthesis parameters. We note that an analogous successful validation of prediction was achieved for LiCl, where again the prediction of a wurtzite modification [47,48] was confirmed by the experiment [52].

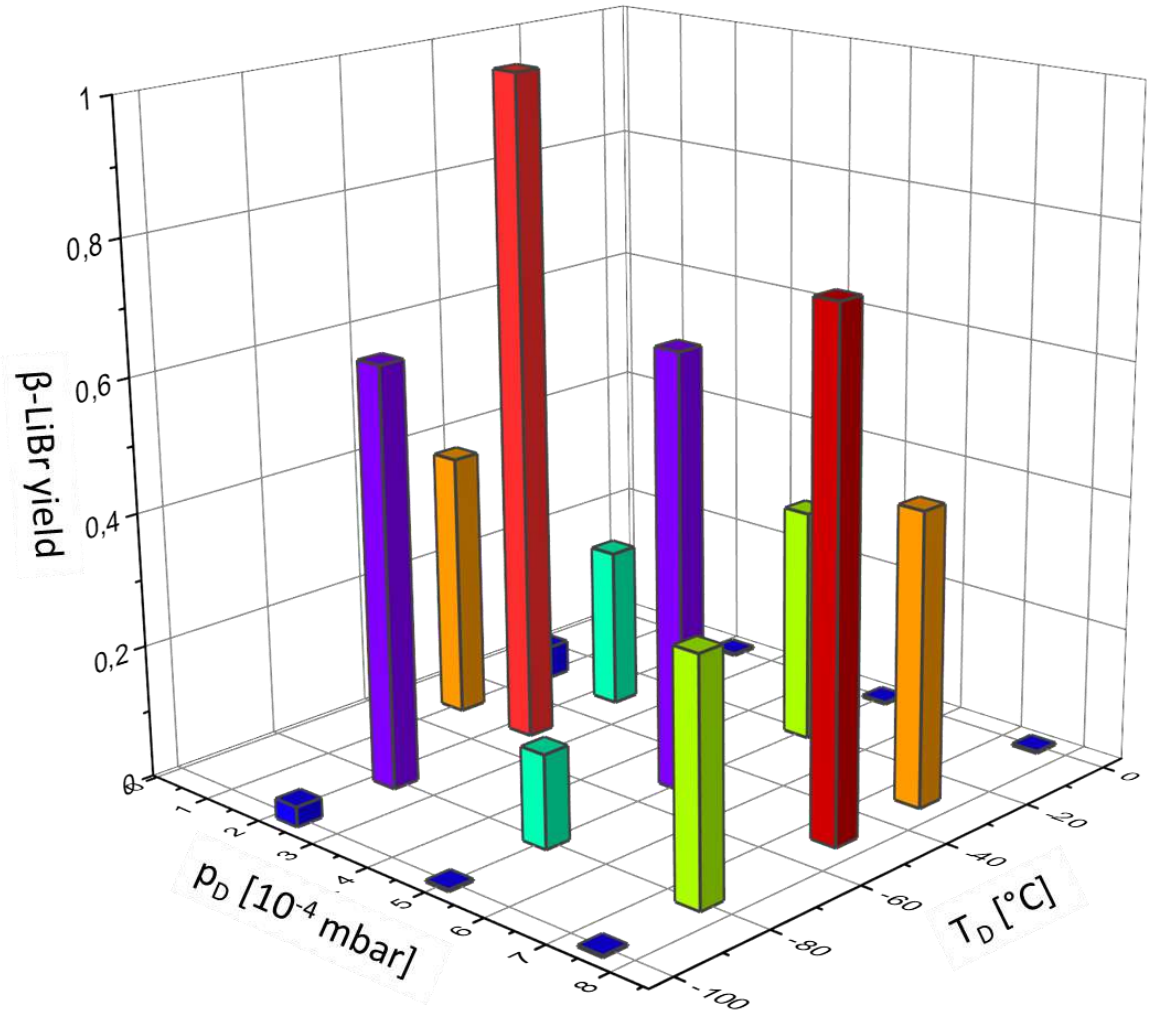

Figure 4. Yield of β-LiBr (wurtzite structure type) as a function of LiBr vapor pressure p_D and substrate temperature T_D for a set of depositions of LiBr on a sapphire substrate.

3.5. Theoretical modeling of the deposition of thin films of MgF_2 on a sapphire substrate and their tempering at elevated temperatures combined with their experimental realization

Considering the great success of the deposition at low temperatures combined with the variation of the deposition rate in generating new compounds or new crystalline modifications of known compounds, the question arises, what is happening during the deposition-annealing process on the atomic level? The fact that several of the first test systems yielded so-called high-temperature phases inside an amorphous film deposited and tempered at temperatures far below those at which the HT-modification is usually synthesized,[32,53] suggests that a competition among nuclei of several different crystalline phases of the compound of interest exists inside the amorphous deposit. These studies require an in-situ characterization of the samples during the annealing process, which was realized by a transfer of the samples from the deposition chamber to the various measurement apparatuses while maintaining cooling and vacuum. To achieve this, a special cart system was employed that allows a suitable transfer of the deposited films as well as of an argon matrix containing embedded gas phase species to an X-ray diffractometer with an integrated Raman spectrometer. Furthermore, the films can also be directly deposited on a TEM sample holder at low

temperatures and subsequently transferred in a vacuum to an electron microscope for in-situ TEM characterizations.

Quite generally, since the density of the deposit is usually lower than the ones of the feasible crystalline modifications, each nucleus of a crystalline phase will have a higher density than the surrounding amorphous material and thus will experience an effective negative pressure due to forces exerted by the atoms in the amorphous phase on those belonging to the "surface" of the nucleus. Thermodynamically, this clearly favors the nuclei with the lowest density, and once such a nucleus has reached a critical size, it can continue to grow even after the direct contact with the enclosing amorphous matrix has been lost thus eliminating the effective negative pressure, and become a kinetically stable though thermodynamically metastable crystal. This argument is also supported by the E(V) curves of the various crystalline modifications, where we can estimate the effective negative pressure at which the low-density modification would become the thermodynamically stable one.

While being a convincing thermodynamic argument and yielding a plausible easily visualized scenario of the processes taking place inside the amorphous film during the tempering stage of the synthesis, it lacks both experimental and theoretical evidence. In particular, since it is not clear at all that the hypothetical nuclei are really nearly spherical enough with a well-defined surface separating them from the atoms belonging to the amorphous phase to allow the establishment of a "real" negative pressure, we need direct atom-level information, either from theory or experiment or both.

Thus, we have investigated the deposition and growth of thin films of MgF_2 on a sapphire substrate at low temperatures to generate the films,[54,55] and complemented this by computer simulations of the complete process [55,56].

Regarding the experiments, depositions were performed at different deposition temperatures ($-228\ °C \leq T_D \leq 450\ °C$) and a variety of vapor pressures, where the gas phase was generated via an effusion cell. Directly after deposition at low temperatures, the deposit was X-ray amorphous, and upon tempering at slowly increasing temperatures, first, a slightly disordered $CaCl_2$-type phase was identified, which at somewhat higher temperatures transformed first into a disordered and finally into a fully ordered rutile phase, which is the well-known modification of MgF_2 at standard pressure.[54]

Regarding the theoretical simulations, we note that ca. 25 years ago, global optimizations with empirical potentials had identified a variety of promising structure candidates for MgF_2 besides the global rutile minimum, such as an anatase-type, a CdI_2-type, or a half-filled rocksalt-structure (reminiscent of an AB_2 analogue of the Li_3N structure but with MgF_6 square bipyramids, i.e., slightly squeezed octahedra, instead of the NLi_8 hexagonal bipyramids).[57,58] While in other analogous AB_2 systems distortions of the rutile structures resembling the $CaCl_2$ structure appeared as local minima for some of the empirical potential parameters [57], for the MgF_2 system relaxations on both the empirical potential and ab initio level had shown that the $CaCl_2$-type structure was kinetically unstable transforming instantaneously into the rutile-type structure, contradicting the claim of the experiment to have observed a $CaCl_2$-type modification in the tempered MgF_2 films.

In order to clarify this issue and to fully reproduce the synthesis of the MgF_2 films, the theoretical modeling proceeded in three stages. First, global optimizations on empirical potential and ab initio level for neutral and charged Mg/F clusters of various compositions including $(MgF_2)_n$ (n = 1,...,10) clusters were performed using SA and TA. [59,60] For many of the small low-energy clusters, Raman spectra were computed and compared with the spectra taken from the gas phase in the experiment, thus identifying both MgF_2 monomer and MgF_2 dimer species, plus some charged molecules, as the dominant components of the gas phase after thermal evaporation.[60]

In the second stage, these clusters were deposited on a cold sapphire substrate at a constant rate, using MD simulations with empirical potentials. This resulted in an amorphous phase that was in good agreement with the experiment, according to the X-ray diffraction data.[55]

In the final stage, the deposit was tempered at elevated temperatures, again using MD, yielding a layered structure of alternating Mg- and F-atom sheets.[56] Upon closer analysis, it was found that the structure consisted of a multitude of small regions that exhibited the $CaCl_2$-type or the CdI_2-type structure (see Figure 5), where these crystalline regions shared all the sheets of F-atoms that extended throughout the film parallel to the xy-plane, i.e., to the surface of the substrate. In general, the $CaCl_2$-type regions were larger than the CdI_2-type regions, though both were clearly identifiable.

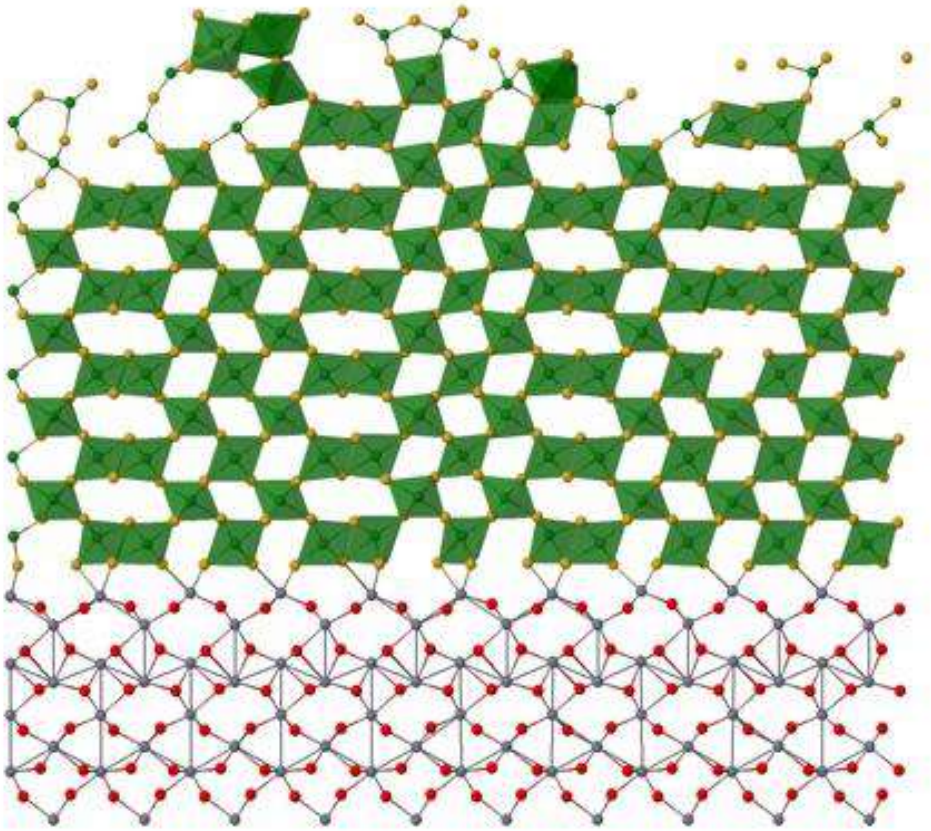

Figure 5. Outcome of a typical simulation of the deposition and annealing of MgF_2 on Al_2O_3 substrate. The substrate was kept at T_D = 50 K during the deposition, and the deposit was subsequently annealed for 3 ns at 1500 K. Al, O, Mg, and F atoms are shown as grey, red, green, and golden spheres, respectively. In order to allow easier visualization of the nano-size regions of crystallites of the $CaCl_2$- and CdI_2-type, we also depict the MgF_6 coordination polyhedra as semi-transparent slightly distorted green octahedra. (Reprinted with permission from S. Neelamraju, J. C. Schön, M. Jansen, Inorg. Chem., (2015), 54, 782-791; Copyright 2015 American Chemical Society.)

In the case of the CdI_2-type regions, only every second layer between the F-sheets was filled with Mg-atoms, as expected for a CdI_2-type structure. In contrast, in the $CaCl_2$-type regions, all in-between layers contained Mg-atoms, being about half-occupied, and where these positively charged Mg^{2+}-ions tried to stay far away from each other on average, leading to a slightly disordered $CaCl_2$-type structure, but which would still be recognized in an X-ray pattern as $CaCl_2$. Since the two modifications shared all the densely packed F-atom sheets throughout the film, the presence of the small CdI_2-type nuclei stabilized the - by themselves unstable - $CaCl_2$-type regions, because they prevented the execution of shearing motion (with zero activation energy required) that otherwise transforms the $CaCl_2$-type structure to the rutile-type structure without requiring any barrier crossings.

Continuing the tempering for very long times, the CdI_2-type regions vanished due to the effective diffusion of some of the Mg-atoms into the "open" empty zones between the individual CdI_2-type layers. We note here that the presence of the $CaCl_2$-type phase prevented the CdI_2-type "FMgF-monolayers" to move towards each other along the c-axis, which usually closes the gap between these layers and thus helps stabilize the CdI_2-type structure due to a gain of van-der-Waals energy. Therefore, it was comparatively easy for the Mg-atoms to enter the region between the "monolayers" thus leading to a relatively fast destabilization of the regions exhibiting the CdI_2-type phase. But once these stabilizing CdI_2-type regions had vanished, no barriers existed that prevented a shearing motion, and the remaining (mostly) pure $CaCl_2$-type regions right away transformed into the stable rutile modification throughout the simulated MgF_2 film.

Thus, the theoretical modeling and simulation not only reproduced the experimental results of the various stages of the deposition-tempering process of the thin films of MgF_2 but also were able to explain, on the atomic level, the existence of an, in principle, kinetically unstable phase via the presence of a second - invisible to simple X-ray measurements - modification. Clearly, the simple picture of spatially separated nuclei of various modifications that compete on purely thermodynamic grounds in an effective negative pressure environment is too simple, and one needs to take the interactions among the different kinds of nuclei into account.

3.6. Phase formation in thin films of gallium as a function of deposition temperature and phase transformations during heating and cooling cycles

In the next example, the focus is on the experiment, where even in a supposedly well-known system, elemental gallium, new (meta)stable phases can appear. At standard pressure, four modifications of gallium are known in the literature [61]: the, presumably, thermodynamically stable α-Ga phase, whose density is even lower than the density of the melt, and β-, γ- and δ-Ga phases (ranked by order of energy, according to ab initio calculations, $E_\alpha < E_\beta < E_\gamma < E_\delta$), where the three metastable phases all have a higher density than the melt: $\rho_\alpha < \rho_{melt} < \rho_\gamma <\approx \rho_\beta <\approx \rho_\delta$.

These phases can be reached, more or less reproducibly, by rapid quenches from the melt (β,γ,δ) or via heterogeneous nucleation (α) from the melt, respectively. However, no direct transformations from the metastable modifications to the α-phase are observed. In order to gain more insight into the energy landscape of the gallium system, the femtosecond pulsed-laser-deposition (PLD) method [31] was employed to generate thin Ga films for many deposition temperatures (-190 °C ≤ T_D ≤ +25 °C),[62] the highest T_D being just below the melting point of gallium, +29.8 °C. [63] The stability ranges and the phase transitions of the initially obtained gallium allotropes were in-situ investigated during subsequent cooling and heating cycles over the same temperature range from -190 °C to +25 °C.). [62] (see Figure 6).

For the lowest deposition temperatures (-190 °C to -80 °C), the deposited films show the α-phase. Between -60 °C and -40 °C, the β-phase was observed, while between -40 °C and -20 °C, the γ-phase formed, and above -20 °C to room temperature amorphous films were obtained. Again, the modification with the lowest density (α-Ga) formed at the lowest deposition temperatures where the density of the deposit was even lower than the density of the melt. However, since this phase is the thermodynamically stable one, none of the other modifications appeared when tempering the α-phase at temperatures up to +25 °C. Similarly, the "high-density" phases, β– and γ–Ga, appeared at higher deposition temperatures than the low-density α-phase. This behavior appears to correlate with the expected density of the deposited films, which presumably is larger for higher deposition temperatures. Furthermore, upon tempering at somewhat higher temperatures (> -40 °C), the γ-phase transforms into the β-phase, as one might expect. However, even when tempering the β-phase at temperatures up to +25 °C, we never observe a transformation to the α-modification. Instead, a solid amorphous phase appears, which resembles a quenched super-cooled melt of liquid Ga, with a density in-between the one of the melt and the one of the β-modification.

The reason for this difficulty in reaching the α-phase is the great difference in density between the α- and the β-modifications, such that the thermodynamic fluctuation needed to generate a stable nucleus of the α-phase of critical size inside the β-phase or even inside the amorphous phase is extremely unlikely. On the other hand, the energy landscape accessible to the system when starting from the β-modification slightly below the thermodynamic melting temperature of gallium (i.e., the one defined by thermodynamic equilibrium between the α-phase and the liquid Ga-phase), is highly complex, with a multitude of accessible local minima that exhibit structural similarities to the pure β-modification and the "quenched" melt-like phase.

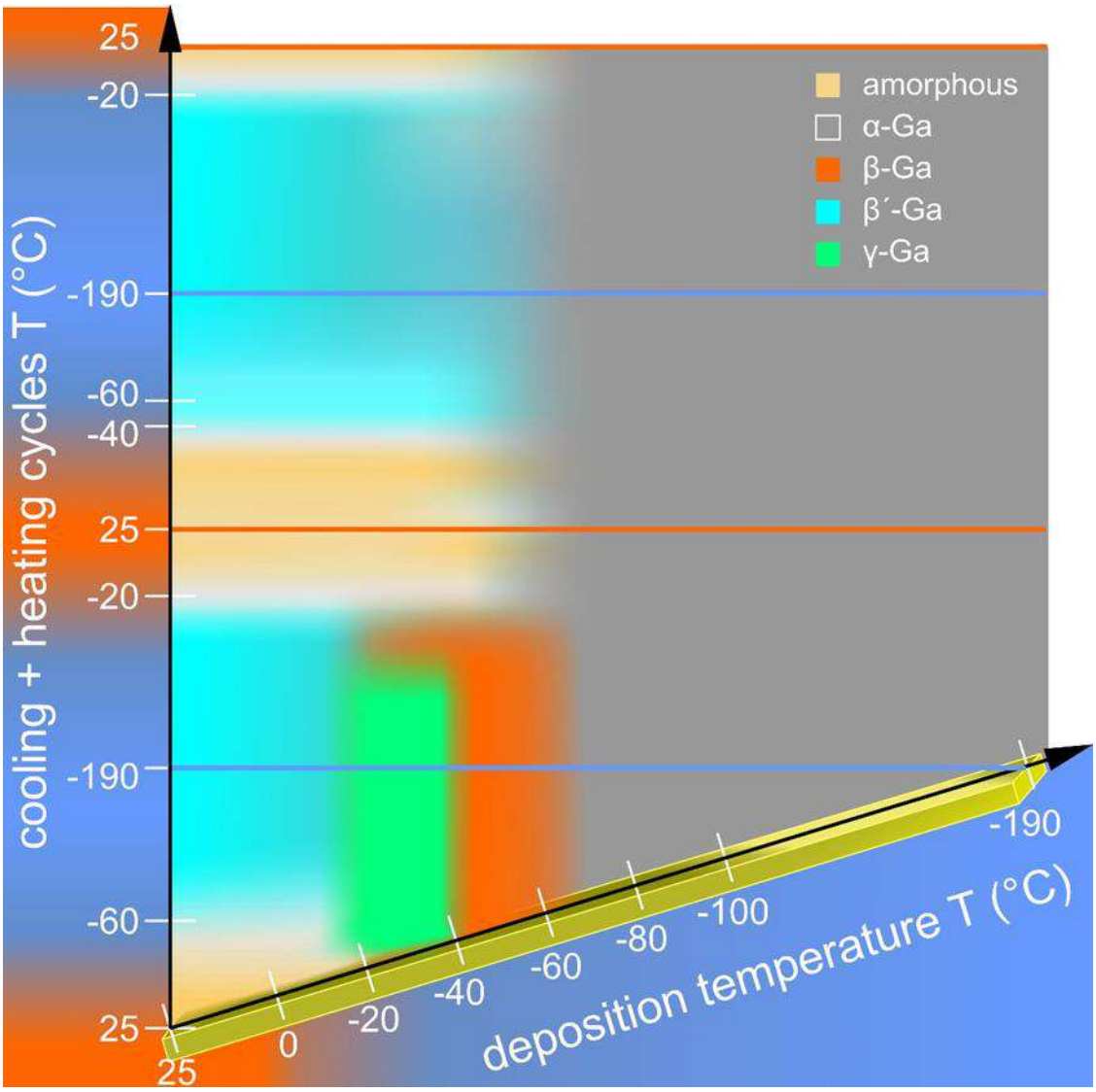

Figure 6. Deposition-temperature-annealing-schedule phase diagram, summarizing the allotropes formed during the pure gallium deposition (x-axis), followed by the phase evolution of the gallium deposits through the cooling+heating cycles (y-axis). The stability ranges of the allotropes are extrapolated from the experimental data.

This has a fascinating consequence: when cooling the system in its amorphous phase down to temperatures around -40 °C we reproducibly obtain not the β-modification, but a structurally related yet distinct new phase, which we have denoted as the β'-phase. The density of this β'-phase is larger than the one of the β-phase, and this β'-modification is preserved down to the lowest temperatures studied (-190 °C). Upon heating the β'-phase to +25 °C, we again obtain the amorphous gallium phase, from which we reproducibly regain the β'-phase upon cooling. Again, we never observe a transition from either the β'-phase or the amorphous phase to the α-modification even after long annealing cycles. Again, this is connected to the difference in the density; if we add the β'-phase and the amorphous phase to the list of densities, we obtain $\rho_{\alpha} < \rho_{melt} < \rho_{highT\text{-}amorph} < \rho_{\gamma} <\approx \rho_{\beta} <\approx \rho_{\delta} < \rho_{\beta'}$; i.e., there is a sizeable gap in density between the α-phase and both the amorphous and the β'-phase. In this context, one should also note that for depositions of Ga atoms at temperatures below liquid nitrogen temperature, e.g., at liquid He temperature, one obtains a second amorphous phase,[64] whose density $\rho_{lowT\text{-}amorph}$ should be comparable or even lower than the one of α-Ga, $\rho_{lowT\text{-}amorph} <\approx \rho_{\alpha}$,

and which would quickly evolve into the α-modification upon heating to liquid nitrogen temperature and above.

On the other hand, the α-phase remains unchanged over many heating and cooling cycles between -190 °C and +25 °C. However, we note that we observe some slight variations in the structure of the α-modification depending on the deposition temperature, which can be recognized in the relative arrangements of the (distorted) Ga-hexagons that characterize the α-Ga structure.

Ab initio calculations on various levels of refinement [65] indicate a close competition in the energy ranking among the α-, β- and β'-modifications, with the most sophisticated methods that include d-electrons and a large basis set suggesting that $E_\alpha < E_\beta < E_{\beta'}$. We also note that the simple structure suggested based on the X-ray powder data for the β'-modification might actually be an average over a multitude of structurally closely related local minima on the energy landscape inside the large multi-minima mega-basin that contains the original β-modification and many slightly different alternative structures of very similar energy (c.f. supplementary information in [62]).

From the point of view of the energy landscape of the gallium system, the stability of the β'-modification is not so much due to high-energy barriers that prevent the transformation of one unit cell of the β'-phase into a similar size unit cell of the β-phase, which is the situation one often finds in crystalline systems and is reflected in standard tree graph models of the energy landscape of crystal-forming compounds. Instead, we are dealing with a combination of entropic barriers separating the different sub-regions of the megabasin containing both the β- and β'-phases, which greatly slow down the transformation kinetics - similar to the aging kinetics in glasses mentioned earlier -, and of an entropic stabilization on the thermodynamic level due to the great malleability of the structural motifs in the β'-structure resulting in many distinct but structurally related local minima with similar energy. This is reminiscent of the currently very popular so-called high-entropy materials [66,67], where a large configurational entropy, often due to a solid solution kind of behavior, is observed to stabilize the multi-minima compound.

Besides demonstrating the importance of synthesis routes in accessing different phases of a chemical system in a reproducible manner, the example highlights the necessity of trying to explore the energy landscape of a chemical system as fully as possible not only theoretically but also experimentally, in order to get a complete overview over the structures and their stability for the many feasible modifications that are (meta)stable on physically and technically relevant time scales.

3.7. Structural details of films of ZnO as a function of the deposition temperature

The final example again demonstrates the great variety in the results of a synthesis of thin films as a function of the synthesis parameters. The system chosen, ZnO, is well-known and is employed in many technological applications, but the real material exhibits some curious properties that do not appear to be consistent with the pure ZnO compound with the ideal wurtzite structure and a clean band gap of ca. 3.4 eV [68]: essentially all crystals of ZnO are transparent, as expected, but with a (mostly) yellow color, [69] and they exhibit an intrinsic n-type conductivity [70]. In the literature, these phenomena are commonly attributed to the presence of impurities that are supposed to cause resonances in the yellow or green band and serve as the origin of impurity bands in the band structure that are then associated with the n-type conductivity.[71] Furthermore, the Raman spectra show bands at high wavenumbers, which are ascribed to the combination/overtones of some first-order Raman bands.[72]

However, these explanations are rather unsatisfying in their non-specificity and generality. Especially with regard to the Raman band at ca. 1140 cm^{-1}, assigned as multi-phonon modes derivatives from the predicted LO bands, one notes that this band is visible even if the corresponding first-order LO-bands are missing! Furthermore, they imply that essentially all samples of ZnO are not pure, and raise the question of whether the various synthesis methods employed are suitable to create pure ZnO. Thus, we have decided to generate ZnO in the form of thin films employing the femtosecond PLD method.[73,74] We are using laser ablation of a pressed, pure powder of ZnO to

create the gas phase that is deposited on a sapphire substrate, where we vary the deposition temperature from -240 °C to +300 °C. This ensures that the spurious inclusion of impurities is eliminated as much as possible.

At very low deposition temperatures, we observe a transparent colorless film of ZnO, and similar films are found at high deposition temperatures. However, at intermediate deposition temperatures, we find yellow, greyish, and opaque films. At the same time, Raman spectra of these films exhibit noticeable peaks beyond 800 cm^{-1} wavenumbers [73]. These bands fit perfectly well with the bands associated with various dioxygen species (O_2, O_2^-, O_2^{2-}). We next note that these species fit perfectly into the trigonal bipyramids formed by the Zn-sub-lattice of the ideal wurtzite structure. Usually, these bipyramids are visualized as two face-connected tetrahedra present in the hcp arrangement of the Zn-atoms, where only half of the tetrahedra are occupied by the O^{2-}-ions in the ideal wurtzite structure (c.f. Figure 7). Thus, in the ideal wurtzite crystal, all the normally filled Zn-tetrahedra are only connected via corners, with no face connection being present.

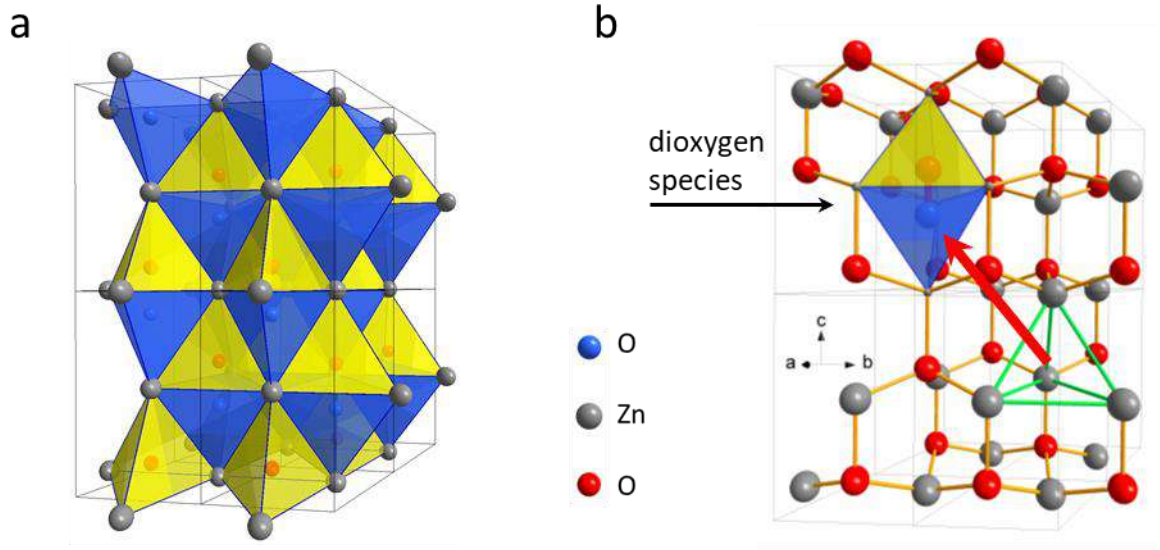

Figure 7. a) ZnO wurtzite structure (2x2x2 supercell) highlighting the OZn_4 tetrahedra arrangement, yellow tetrahedra with the tip pointing up along the c-axis (normally filled in ideal ZnO), and blue tetrahedra with tip down along the c-axis (normally empty). b) Structural realization of possible disorder in the ZnO wurtzite structure (2x2x2 supercell, distortions neglected) where one oxygen atom has moved: The figure depicts an occupied inverse tetrahedron (blue) adjacent to a filled regular tetrahedron (yellow), forming a dioxygen species, e.g., a superoxide ion (red bond); in addition, the empty (normally filled, yellow) Zn_4-tetrahedron (void) is shown by green lines.

However, during the deposition and tempering of the film, it is very easy to fill, once in a while, a tetrahedron of the orientation opposite to the normally filled Zn-tetrahedra, which results in a dioxygen species; of course, this implies that an empty Zn tetrahedron is also generated. The presence of such a filled "inverse oriented" tetrahedron is not detectable via, e.g., additional X-ray reflections. Instead, we obtain indirect evidence when analyzing the electron density derived from the diffraction patterns.[74] Here, the presence of additional occupants of the tetrahedra makes itself felt in a large broadening of the difference in electron density in the oxygen positions compared to what we would expect from an ideal ZnO wurtzite structure.

A fascinating consequence of such rearrangements of the oxygen atoms in the wurtzite structure during the film growth is the fact that the Zn-atoms no longer need to be all in the Zn^{2+} oxidation state. The formation of superoxide ions generates excess electrons ($2\ O^{2-} \rightarrow (O_2)^- + 3\ e^-$). It follows that there are additional "free" electrons in the structure, which account for the intrinsic n-type conductivity. Furthermore, in the intermediate range of deposition temperatures, the local depletion of the Zn tetrahedra is quite concentrated in nanometer-sized regions, and X-ray reflections typical of

metallic zinc are present in the diffraction pattern, where the width of the peaks indicates that the size of these Zn metal regions is in the nanometer range. From this, one concludes that mesoscopic regions of metallic zinc are formed throughout the film at intermediate temperatures, whose existence is further supported by the greyish color of the films. In addition, we note that the yellowish tinge is caused by the yellow superoxide ion O_2^- present in the film.

This example demonstrates, how the systematic use of special synthesis methods can result in different compounds or variations of a given compound represented on the energy landscape of the ZnO system, ranging from the pure wurtzite ZnO to a combination of Zn metal and ZnO, including the presence of superoxide ions.

Still, perhaps more important than the variability of synthesis outcomes even for pure systems of a well-defined overall composition, ZnO, this example system highlights our general underappreciation of the structural and compositional flexibility of supposedly simple, even binary, ceramic-type compounds; in alloys such flexibility is well-recognized, of course. This is going to be an even more relevant issue in the future since such detailed knowledge of the structural variability of a compound will become more and more crucial as we try to control a system's properties on smaller length scales down to the atomic level. Furthermore, when we try to employ such materials, we need to be able to establish time scales for the stability of the metastable modifications of the compounds of interest, which includes detailed information about the pathways for their decay or transformation to other (meta)stable or intermediary modifications. Clearly, the degree of control we have over such a material that is tuned and exploited down to the atomic level greatly relies on the completeness of our structural knowledge about the system.

4. Discussion and conclusions

In the preceding section, we have considered several examples of thin films and monolayers, the interplay of theory and experiment - including chemical synthesis and in-situ physical measurements - concerning the prediction of possible modifications and their structures, and demonstrated the influence of the synthesis parameters and subsequent treatment of a deposited film on the formation of additional modifications, the transformations between modifications and their properties. Furthermore, we have highlighted the importance of using such tools for the analysis of the whole field of possible stable and metastable phases that exist on the energy landscape of the chemical system, and for elucidating the structural basis of unusual physical properties.

All this work can be seen as contributing to the field of systematic synthesis exploration in a chemical system, which encompasses the theoretical prediction of synthesis targets via the study of the energy landscapes of a chemical system, the simulation of synthesis routes that are employed in attempts to reach such targets in the experiment, and finally the careful reproducible performance of such syntheses on well-defined chemical systems, where the syntheses are accompanied by, e.g., X-ray, IR, Raman or other measurements that yield structural data about the current state of the system at all stages of the syntheses and subsequent transformations of the material. The long-term goal of this joined theoretical and experimental enterprise is to achieve such a high degree of control in the experiment, that we are able to reach all regions of the energy landscape not only in the computer but also in the experiment - in some ways this can be understood as the final aim and highest possible achievement of the field of solid state chemistry.[15]

In particular in the field of thin films and monolayers which are essentially two-dimensional and thus allow us much more access than a bulk 3D system, such a control should, in principle, be feasible on the atomic level. In the ideal case, one would place the atoms or molecules one-by-one on a smooth surface, next to and on top of one another, at extremely low temperatures, such that their arrangement is as close as possible to one of the metastable structural arrangements we have found on the energy landscape. Activating the formation of bonding by adding heat or radiation, we could thus realize essentially all metastable modifications of the chemical system.

In the examples presented above, the starting point of the growth of the monolayers of molecules (c.f. sections 3.2 and 3.3) were individual molecules that were deposited on the surfaces and then rearranged themselves into islands with common (periodic) structural features or reacted to

form an amorphous layer. These structures corresponded to typical local minimum structures found during global optimizations or molecular dynamics simulations of the monolayers. We note that the periodic islands seen in the experiment exhibited one of the many possible very similar dense periodic packings of the molecules with similar energies found on the energy landscape. This is a typical problem with molecular crystals, where the energy differences between many similar arrangements are so small that the quality of the energy function is not always sufficient to establish the correct energy ranking among the local minima needed to identify the true global minimum. [75,76] Similarly, the amorphous arrangement was not the global minimum, which was a perfect periodic hexagonal arrangement of the reacted precursor molecules, according to the simulations; since in this case chemical bonds were involved as the major stabilizing force of the possible structures, the theoretical prediction of the global minimum is more reliable than in the case of a molecular packing controlled by van-der-Waals and hydrogen-bond interactions.

In contrast, for the thin films grown from the gas phase (3.4 - 3.7), the constituents of the entities that were to be deposited on a substrate were generated by global, i.e., thermal, or local, i.e., via laser ablation, heating of a solid compound with the same composition as the final product of interest. As a consequence, the gas phase before deposition consisted of various small or larger clusters or molecules with essentially the same composition as the source material; in particular, we note that in these fragments the various atoms already have neighbor atoms in similar numbers as in the source material, although the detailed structure of small clusters usually is quite different from cut-outs of the bulk crystal. This fact clearly might prejudice the resulting deposit when these clusters reach the surface and form the thin (amorphous) film at low temperatures, thus locking the system into a small region of the energy landscape. In some fashion, this method is reminiscent of the classical gas phase transport synthesis method [77] for the synthesis of out-of-equilibrium solids starting from a stable modification of the compound.

Such a lock-in can be possibly avoided by synthesizing the thin film directly from the individual elements, ideally in the form of single atoms being deposited on the substrate, usually at random unless STM/AFM or related techniques are available that allow a single atom placement on a given surface; however, the latter are not yet ready for macroscopic thin film production. For such a separate-atom deposition procedure, multiple evaporation and/or plasma sources are needed, one for each type of atom involved in the system. Only a few studies have been performed in this fashion, most notably the synthesis of the two metastable nitrides Na_3N [33] and K_3N [78] about twenty years ago.

However, in contrast to the deposition of the fragments with well-defined ratios of the different atom types involved, we need to fine-tune the strength of the various sources, in order to achieve a certain desired composition of the initial deposit. On the one hand, this is a serious complication of the synthesis method, since it is nearly impossible to guarantee that what arrives on the substrate exhibits exactly the target composition. On the other hand, by employing a narrow mesh of evaporation parameters, we can scan a large range of compositions in the thin films we generate, even for binary, and much more so for ternary or higher-order compounds of interest. We already have seen in the example of LiBr, how the control of the evaporation rate, i.e., of the gas phase pressure, allowed us to identify the exact range of deposition temperature-vapor pressure combinations that yielded the desired metastable LiBr modification. Thus, controlling the composition of an atom-level mixed deposit at low temperatures via small variations of the source parameters, allows us, in principle, to scan the whole phase spectrum of a chemical system, including not only thermodynamically stable but also metastable phases as a function of composition and deposition and process temperatures. Of course, this requires a large effort, ideally performed with modern robotic assistant high-throughput techniques employing multiple synthesis chambers at the same time. But once enough information has been accumulated about a given chemical system or many related ones, this can be fed into modern machine learning neural networks, with the goal to be able to obtain fast suggestions of optimal control parameters for the sources and other synthesis parameters when targeting a certain kind of metastable phase in a given chemical system. Similarly, the analysis of, e.g., the thousands of X-ray patterns produced by a high-throughput experiment that had been performed by hand in the past, can be assisted by an automated (pre-)screening in the future, using (self-learning) neural network based pattern recognition and pattern learning systems.

To demonstrate the power of the atom-separated deposition approach even without the high-throughput machinery, we want to discuss some curious features of two other examples that have been investigated using separate sources for each atom type: the synthesis of $AgNO_3$ films [32] from Ag, N and O atoms deposited at random on a sapphire substrate, and a study of the Mg/N system [79], where the ratio between Mg and N atoms was systematically varied during the deposition.

In the case of the Ag/N/O system, silver was deposited together with plasma-activated nitrogen and oxygen in approximately the ratio of N:O = 1:3 at -180 °C, and while the material was slowly heated up to +130 °C, powder patterns were acquired at a number of intermediary temperatures. At the lowest temperatures up to ca. -150 °C, only a broad amorphous hump could be seen, indicating that the deposit was still in the amorphous state. At -110 °C, we observe first reflections indicating the formation of a crystalline phase, but this phase corresponds to the molecular crystal of N_2O_4, with the silver in the system still being in the amorphous state. Here, we note that we are already close to the temperature range where the N_2O_4 molecular crystal begins to evaporate.[32,80]

But once we reach -70 °C, the X-ray reflections indicating the N_2O_4 molecular crystals vanish, and are replaced by a set corresponding to the high-temperature phase of $AgNO_3$, which remains present up to room temperature (even though HT-$AgNO_3$ is metastable at these low temperatures). Sometimes small impurities of AgO were also detected as a byproduct. While this outcome was unexpected at the time of the experiment, this is no real surprise, since the density of the amorphous material is lower than the one of the HT-$AgNO_3$ modification which in turn is lower than the one of the low-temperature modification of $AgNO_3$, and thus the nuclei of the high-temperature phase are enthalpically preferred over those of the low-temperature phase inside the amorphous matrix. When increasing the temperature to 85 °C, the compound transforms into the thermodynamically stable low-temperature modification LT-$AgNO_3$, and at even higher temperatures, we recover the - by now thermodynamically stable - HT-$AgNO_3$ phase.[32,80]

While this sequence of amorphous, HT-, LT- and again HT-phases of $AgNO_3$ with increasing temperature is quite fascinating in its own right, perhaps the most thought-provoking aspect is the observation that inside the semi-amorphous film the same kind of chemical reaction appears to take place, which occurs in the standard aqueous solution chemistry ($Ag + HNO_3(aq) \rightarrow AgNO_3(aq)$), under seemingly completely different circumstances. Seen from the point of view of time scales, we realize that the atom-level mixing present in the amorphous thin film allows chemical processes to take place at experimental time scales, which are completely analogous to the fast processes in melts or aqueous solutions that are enabled by the fast diffusion of the reaction participants in the melt or solution.

In this context, we note that when we repeat the same procedure by replacing Ag with Au in the deposition process, the N_2O_4 crystals form already at the lowest temperature (-180 °C), which indicates that no strong Au-O bonds are formed that would compete with the crystallization of N_2O_4. Upon heating the sample, the N_2O_4 crystals again vanish at around -100 °C, but instead of $AuNO_3$, we now find only tiny crystalline gold particles (with a diameter of only a few dozen nanometers, based on the width of the diffraction peaks), again in agreement with the solution chemistry experiments where Au does not dissolve in nitric acid.[80]

Similarly, the study of the Mg/N system with a wide variation of compositions deposited at room temperature (T_D = +25 °C) from atom-type separated sources, resulted in the formation of unusual phases as a function of source parameters and annealing temperature. If we consider the powder patterns of a sample prepared employing an intermediate rate of Mg deposition (Mg source at 320 °C, nitrogen flux of 1.5 cm^3/min activated by a 80 mA microwave-plasma) at room temperature, we observe the reflections of a fcc-atom arrangement of the Mg atoms (called β-Mg), the presence of which is supported by corresponding Rietveld refinements (Fm-3m, a=451.6 pm) and XPS studies. In contrast, after annealing up to 300 °C the reflections correspond to a mixture of the standard hcp-packing of Mg atoms (α-Mg) and the crystalline Mg_3N_2 compound. We note that the first reflections characteristic of crystalline Mg_3N_2 begin to be observed already at around +200 °C, together with clear peaks belonging to the β-Mg modification, while the presence of crystalline α-Mg is only confirmed at around +300 °C where no peaks of β-Mg remain. It appears that when the amorphous Mg/N matrix is transformed into crystallized Mg_3N_2, β-Mg loses its stability and transforms into the

global minimum α-Mg on the energy landscape of magnesium. We recall (see section 3.5) the case of the unstable, in principle, $CaCl_2$ phase in the thin films of MgF_2, which was stabilized by the presence of essentially invisible nanometer-size crystals of the metastable CdI_2 modification, where the $CaCl_2$ phase transformed, without requiring activation energy, into the stable rutile modification once the CdI_2 phase had vanished.

Regarding the outcome for different deposition rates of magnesium, we find that if the Mg rate is reduced (Mg source running at 300 °C) only Mg_3N_2 is formed on the substrate and if the Mg rate is increased (Mg source at 340 °C) then a mixture of Mg_3N_2, β-Mg, and α-Mg is obtained. Thus, with increasing Mg content the reaction of magnesium and nitrogen reaches a point where only a part of Mg reacts to magnesium nitride, and thus first β-Mg and later α-Mg remains as a byproduct. If we now vary the parameters of the plasma source (while keeping the Mg source at 320 °C), we find that as long as we supply a high activation of nitrogen atoms, the β-phase of Mg is present, possibly together with some crystals of Mg_3N_2. However, when we reduce the activation of nitrogen, we only obtain pure α-Mg, which clearly indicates that the presence of some additional amorphous Mg/N phase is needed for the stabilization of β-Mg. In this context, we note that β-Mg would be kinetically stable against the transformation into α-Mg, at least at low temperatures, since it constitutes a low-energy local minimum on the energy landscape of elementary Mg, in contrast to the $CaCl_2$ structure in the MgF_2 system, which does not correspond to a local minimum on the landscape of MgF_2.

These two short examples display not only the richness of the landscape of the chemical system investigated, but also the subtle features of the synthesis in the solid state, and how even small changes in synthesis and processing conditions can stabilize or destabilize the many competing metastable phases in the system. Together with the examples discussed in more detail in section 3, which have demonstrated the strength of combining theory and experiment in the realization and analysis of metastable compounds, these studies and their surprising results also highlight the many gaping holes in our understanding of chemical systems, e.g., why does β-Mg seem to require the presence of amorphous Mg_2N_3 for its stabilization, or why does the aqueous solution reaction that produces $AgNO_3$ take place in a seemingly analogous fashion in the solid film?

Although the aim of developing a rational approach to the planning of solid-state syntheses in analogy to the toolbox of organic chemistry was formulated already in the 1990s [81] and discussed as a vision even earlier [82], it often feels as if we were still at the beginning. The past three decades have seen much progress in the field of structure prediction of crystalline modifications [11,83], and the concept of the energy landscape of a chemical system as the world where the chemistry of a material takes place is by now well-established among theorists and experimentalists [11,84] Nevertheless, in the field of solid-state chemistry, the focus still appears to remain on the ideal crystal structure, and the path to the synthesis of such ideal modifications is chosen by analogy to successful syntheses in similar systems. But the examples discussed here in the context of low-dimensional materials clearly show that one needs to explore the whole energy landscape of the chemical system, including the complex barrier structure that lies beyond the singular local minima that correspond to the ideal crystals, from both a theoretical and experimental point of view. In reality, we never obtain such an ideal flawless arrangement of atoms, neither in the experiment nor during a molecular dynamics simulation containing a sufficiently large number of atoms to represent a real macroscopic system (unless we start with the ideal structure and stay at very low temperatures). Instead, in both the experiments and the simulations, we explore the landscape's mega basins or locally ergodic regions, each of which contains the many minima associated with defect structures that together represent the real crystals for each given crystalline phase. Furthermore, we need to identify the true pathways the system follows during synthesis and transformation processes for given external boundary conditions (temperature, pressure, etc.), both in the experiment and on a theoretical level. But this means, we must not only study the successful routes but also learn about the dead-ends, learn to understand why they are "failures", and how we can exert control over the path the system takes on the landscape according to the laws of physics. From a theoretical point of view, this means that it is not sufficient to study the energy landscape of the isolated chemical system, but we also need to investigate the landscape of the system in contact with the environment. This includes not only variations in the thermodynamic boundary conditions such as temperature, pressure, electromagnetic fields, etc., but also the presence of atoms belonging to a substrate, a solution, or a melt that serve as surface or

medium, respectively, where the synthesis takes place.[11,85] Dealing with these influences via modeling and simulations is a tremendous challenge, of course. Both the sheer number and diversity of the atoms involved and the large time scales of the chemical processes during the synthesis push the boundaries of the feasible as far as computational resources are concerned, in particular since the simulations should take place on an ab initio level wherever possible. Nevertheless, great progress has been made in recent years, both regarding the development of faster algorithms and with respect to suitable energy functions, where the use of machine-learning for accelerating the computation of ab initio energies and forces is a highly active field[86] although surely no panacea.

Once we have gained such an understanding, we can complement the atom level description by an appropriate and useful continuum description of the chemical system, for which phenomenological models describing various combinations of reaction-, diffusion-, growth-, etc. processes can be formulated with spatio-temporal resolution. To achieve this, both theory and experiment have to contribute: the theorist by studying the landscape of the system for substantial numbers of atoms, in order to acquire some realism as far as the atom level processes are concerned, while the experimentalist needs to carefully analyze the seemingly uninteresting results of his syntheses as these also tell us important information about the chemistry, i.e., the structural and compositional changes, in a material.

Together, they can open up a comprehensive view of the whole chemical system, and the surprising richness of the chemistry in even those systems that are often declared "dead" and uninteresting. Once such a full understanding has been achieved, the road is open to the systematic generation of new materials for future technological applications.

References:

[1] R. Arroyave, D. L. McDowell: Systems Approaches to Materials Design: Past, Present, and Future, Annu. Rev. Mater. Res., (2019), 49, 103-126.
[2] D. Banerjee: Towards a Sustainable Future with Materials, J. Ind. Inst. Sci., (2022), 102, 5-9.
[3] C. N. R. Rao, H.S.S. Ramakrishna, U. Maitra: Graphene Analogous of Inorganic Layered Materials, Angew. Chem. Int. Ed., (2013), 52, 13162-13185.
[4] W. Zhang, H. Li, E. Hopmann, A. Y. Elezzabi: Nanostructured inorganic electrochromic materials for light applications, Nanophotonics, (2021), 10, 825-850.
[5] X. Titan, Y. Zhang, R. Zheng, D. Wei, J. Liu: Two-dimensional organic-inorganic hybrid Ruddlesden-Popper perovskite materials: preparation, enhanced stability, and applications in photodetection, Sustainable Energy Fuels, (2020), 4, 2087-2113.
[6] A. Gutiérrez-Cruz, A. R. Ruiz-Hernández, J. F. Vega-Clemente, et al.: A review of top-down and bottom-up synthesis methods for the production of graphene, graphene oxide and reduced graphene oxide, J. Mater. Sci., (2022), 57, 14543–14578.
[7] M. Li, L. Li, Y. Fan, F. Jiao, D. Geng, W. Hu: From top to down – Recent advances in etching of 2D materials, Adv. Mater. Interfaces, (2022), 9, 2201334.
[8] H. Zheng, S. Ravaine: Bottom-up assembly and applications of photonic materials, Crystal, (2016), 6, 54.
[9] K. Ariga, J. P. Hill, Q. Ji: Layer-by-layer assembly as a versatile bottom-up nanofabrication technique for exploratory research and realistic application, Phys. Chem. Chem. Phys., (2007), 9, 2319-2340.
[10] J. C. Schön: Nanomaterials - What energy landscapes can tell us, Proc. Appl. Ceram., (2015), 9, 157-168
[11] J. C. Schön: Energy landscapes in inorganic chemistry, in Comprehensive Inorganic Chemistry III, eds. J. Reedijk, K. Poeppelmeier (Elsevier, Amsterdam, 2023), Chapter 127 (3.11), 262-392; DOI: 10.1016/B978-0-12-823144-9.00127-8
[12] R. Ferrando, J. Jellinek, R. L. Johnston: Nanoalloys: From Theory to Applications of Alloy Clusters and Nanoparticles, Chem. Rev., (2008), 108, 845-910
[13] D. H. Bowskill, I. J. Sugden, S. Konstantinopoulos, C. S. Adjiman, C. C. Pantelides: Crystal Structure Prediction Methods for Organic Molecules: State of the Art, Annu. Rev. Chem. Biomol. Eng., (2021), 12, 593-623
[14] J. C. Schön: Structure prediction in low dimensions - concepts, issues and examples, Phil. Trans. Roy. Soc. A, (2023), 381, 20220246
[15] J. C. Schön: On the way to a theory of solid state synthesis: Issues and open questions, Adv. Chem. Phys., (2015), 157, 125-134
[16] J. C. Schön: Finite-Time Thermodynamics and the Optimal Control of Chemical Syntheses, Z. Anorg. Allg. Chem., (2009), 635, 1794-1806
[17] K. H. Hoffmann, J. C. Schön: Controlled dynamics on energy landscapes, Eur. Phys. J. B, (2013), 86, 220_1-10
[18] K. H. Hoffmann, J. C. Schön: Combining pressure and temperature control in dynamics on energy landscapes, Eur. Phys. J. B, (2017), 90, 84
[19] F. Musil, S. De, J. Yang, J. E. Campbell, G. M. Day, M. Ceriotti: Machine learning for the structure-energy-property landscapes of molecular crystals, Chem. Sci., (2018), 9, 1289-1300
[20] J. Wei, X. Chu, X.-Y. Sun, K. Xu, H.-X. Deng, J. Chen, Z. Wei, M. Lei, Machine learning in materials science, InfoMat, (2019), 1, 338-358
[21] H. Ünlü, N. J. M. Horing, Eds.: Progress in Nanoscale and Low-Dimensional Materials and Devices: Properties, Synthesis, Characterization, Modelling and Applications, (SpringerNature, Cham, 2022)
[22] P. Miro, M. Audiffred, T. Heine: An atlas of two-dimensional materials, Chem. Soc. Rev. (2014), 43, 6537-6554
[23] S. Kirkpatrick, C. D. Gelatt, Jr., M. P. Vecchi: Optimization by Simulated Annealing, Science, (1983), 220, 671-680
[24] J. C. Schön: Studying the Energy Hypersurface of Multi-Minima Systems - the Threshold and the Lid Algorithm, Ber. Bunsenges., (1996), 100, 1388 - 1391

[25] S. Neelamraju, C. Oligschleger, J. C. Schön: The threshold algorithm: Description of the methodology and new developments, J. Chem. Phys., (2017), 147, 152713
[26] S. Neelamraju, R. L. Johnston, J. C. Schön: A threshold-minimization scheme for exploring the energy landscape of biomolecules: Application to a cyclic peptide and a disaccharide, J. Chem. Theo. Comp., (2016), 12, 2471-2479
[27] W. Margerit, A. Charpetier, C. Maugis-Rabusseau, J. C. Schön, N. Tarrat, J. Cortes: IGLOO: an Iterative Global exploration and LOcal Optimization algorithm to find diverse low-energy conformations of flexible molecules, submitted to "Algorithms", (2023)
[28] N. Metropolis and A. W. Rosenbluth and M. N. Rosenbluth and A. H. Teller and E. Teller: Equation of State Calculations by Fast Computing Machines, J. Chem. Phys., (1953), 21, 1087-1092
[29] Z. Ouyang, Z. Takats, T. A. Blake, B. Gologan, A. J. Guymon, J. M. Wiseman, J. C. Oliver, V. J. Davisson, R. G. Cooks: Preparing Protein Microarrays by Soft-Landing of Mass-Selected Ions, Science, (2003), 301, 1351-1354
[30] D. Fischer, A. Müller, M. Jansen: Existiert eine Wurtzit-Modifikation von Lithiumbromid? - Untersuchungen im System LiBr/LiI -, Z. Anorg. Allg. Chem., (2004), 630, 2697-2700.
[31] D. Fischer, L. V. Meyer, M. Jansen, K. Müller-Buschbaum: Highly Luminescent Thin Films of the Dense Framework [$EuIm_2$] with Switchable Transparency Formed by Scanning Femtosecond-Pulse Laser Deposition, Angew. Chem. Int. Ed., (2014), 53, 706-710.
[32] D. Fischer, M. Jansen: Low-Activation Solid-State Syntheses by Reducing Transport Lengths to Atomic Scales as Demonstrated by Case Studies on $AgNO_3$ and AgO, J. Am. Chem. Soc., (2002), 124, 3488-3489
[33] D. Fischer, M. Jansen: Synthesis and Structure of Na_3N, Angew. Chem. Int. Ed., (2002), 41, 1755-1756
[34] R. Gutzler, J. C. Schön: Two-dimensional Silicon-Carbon Compounds: Structure Prediction and Band Structures, Z. Anorg. Allg. Chem., (2017), 643, 1368-1373
[35] C. M. Polley, H. Fedderwitz, T. Balasubramanian, A. A. Zakharov, R. Yakimova, O. Bäcke, J. Ekman, S. P. Dash, S. Kubatkin, S. Lara-Avila: Bottom-Up Growth of Monolayer Honeycomb SiC, Phys, Rev. Lett., (2023), 130, 076203
[36] S. Abb, N. Tarrat, J. Cortes, B. Andriyevsky, L. Harnau, J. C. Schön, S. Rauschenbach, K. Kern: Carbohydrate Self-Assembly at Surfaces: STM Imaging of Sucrose Conformation and Ordering on Cu(100), Angew. Chem. Int. Ed., (2019), 58, 8336-8340
[37] B. Andriyevsky, N. Tarrat, J. Cortes, J. C. Schön: Dehydrogenation versus deprotonation of disaccharide moelcules in vacuum: a thorough theoretical investigation, Roy. Soc. Open Sci., (2022), 9, 220436
[38] J. C. Schön, C. Oligschleger, J. Cortes: Prediction and clarification of structures of (bio)molecules on surfaces, Z. Naturf. B, (2016), 71, 351-374
[39] S. Abb, L. Harnau, J. C. Schön, J. Cortes, S. Rauschenbach, K. Kern: Disaccharide self-assembly behavior on metal surfaces (European Conference on Surface Science-31, Barcelona, September 2015)
[40] S. Abb, N. Tarrat, J. Cortes, B. Andriyevsky, L. Harnau, J. C. Schön, S. Rauschenbach, K. Kern: Polymorphism in carbohydrate self-assembly at surfaces: STM imaging and theoretical modelling of trehalose on Cu(100), RSC Advances, (2019), 9, 35813-35819
[41] W. H. Zachariasen: The Atomic Arrangement in Glass (Continuous Random networks), J. Am. Chem. Soc., (1932), 54, 3841-3851
[42] J. Van Turnhout, P. Th. A. Klaase, P. H. Ong, L. C. E. Struik: Physical aging and electrical properties of polymers, J. Electrostat., (1977), 3, 171-179
[43] L. Lundgren, P. Svedlindh, P. Nordblad, O. Beckman: Dynamics of the relaxation time spectrum in a CuMn spin glass, Phys. Rev. Lett., (1983), 51, 911-914
[44] M. Utz, P. G. Debenedetti, F. H. Stillinger: Atomistic Simulation of Aging and Rejuvenation in Glasses, Phys. Rev. Lett., (2000), 84, 1471-1474
[45] A. Hannemann, J. C. Schön, M. Jansen, P. Sibani: Nonequilibrium Dynamics in Amorphous $Si_3B_3N_7$, J. Phys. Chem. B, (2005), 109, 11770 - 11776
[46] P. Alexa, C. Oligschleger, P. Gröger, C. Morchutt, B. Vyas, B. V. Lotsch, J. C. Schön, R. Gutzler, K. Kern: Short-Range Structural Correlations in Amorphous 2D Polymers, ChemPhysChem, (2019), 20, 2340 - 2347

[47] Z. Cancarevic: Prediction of not-yet-synthesized solids at extreme pressures, and the development of algorithms for local optimization on ab-initio level, (PhD-thesis, University of Stuttgart, 2006)
[48] Z. Cancarevic, J. C. Schön, M. Jansen: Stability of alkali metal halide polymorphs as function of pressure, Chem. Asian J., (2008), 3, 561-572
[49] Y. Liebold-Ribeiro, D. Fischer, M. Jansen: Experimental Substantiation of the "Energy Landscape Concept" for Solids: Synthesis of a New Modification of LiBr, Angew. Chem. Int. Ed., (2008), 47, 4428-4431
[50] J. C. Schön, M. Jansen: Determination of Candidate Structures for Simple Ionic Compounds through Cell Optimisation, Comp. Mater. Sci., (1995), 4, 43 - 58
[51] D. Zagorac, J. C. Schön, M. Jansen: Identification of promising chemical systems for the synthesis of new materials structure types: An ab initio minimization data mining approach, Proc. Appl. Ceram., (2012), 7, 37-41
[52] A. Bach, D. Fischer, M. Jansen: Synthesis of a New Modification of Lithium Chloride Confirming Theoretical Predictions, Z. Anorg. Allg. Chem., (2009), 635, 2406-2409
[53] A. Bach, D. Fischer, M. Jansen: Metastable Phase Formation of Indium Monochloride from an Amorphous Feedstock, Z. Anorg. Allg. Chem., (2013), 639, 465-467
[54] A. Bach, D. Fischer, X. Mu, W. Siegle, P. A. van Aken, M. Jansen: Structural Evolution of Magnesium Difluoride: from an Amorphous Deposit to a New Polymorph, Inorg. Chem., (2011), 50, 1563-1569
[55] X. Mu, S. Neelamraju, W. Sigle, C.T. Koch, N. Toto, J. C. Schön, A. Bach, D. Fischer, M. Jansen, P. A. van Aken: Evolution of order in amorphous-to-crystalline phase transformation of MgF_2, J. Appl. Cryst., (2013), 46, 1105-1116
[56] S. Neelamraju, J. C. Schön, M. Jansen: Atomistic Modeling of the Low-Temperature Atom-Beam Deposition of Magnesium Fluoride, Inorg. Chem., (2015), 54, 782-791
[57] M. A. C. Wevers, J. C. Schön, M. Jansen: Determination of structure candidates of simple crystalline AB_2-systems, J. Solid State Chem., (1998), 136, 233 - 246
[58] M. A. C. Wevers, J. C. Schön, M. Jansen: Global Aspects of the Energy Landscape of Metastable Crystal Structures in Ionic Compounds, J. Physics: Cond. Matt., (1999), 11, 6487 - 6499
[59] S. Neelamraju, J. C. Schön, K. Doll, M. Jansen: Ab initio and empirical energy landscapes of $(MgF_2)_n$ clusters (n = 3, 4), Phys. Chem. Chem. Phys., (2012), 14, 1223-1234
[60] S. Neelamraju, A. Bach, J. C. Schön, D. Fischer, M. Jansen: Experimental and theoretical study of Raman spectra of magnesium fluoride clusters, J. Chem. Phys., (2012), 137, 194319
[61] A. Defrain: Etats metastables du gallium. surfusion et polymorphisme, J. Chim. Phys. , (1977), 74, 851–62
[62] D. Fischer, B. Andriyevsky, J. C. Schön: Systematics of the allotrope formation in elemental gallium films, Mater. Res. Express, (2019), 6, 116401-1-31
[63] W.M. Haynes (Hrsg.) CRC Handbook of Chemistry and Physics 94th ed. (Boca Raton: CRC, Taylor&Francis group) 4 (2013)-121-136
[64] O. Hunderi, R. Ryberg: Amorphous gallium - a free electron metal, J. Phys. F: Met. Phys., (1974), 4, 2096-2102
[65] B. Andriyevsky, D. Fischer, J. C. Schön, (2023), unpublished
[66] M.-H. Tsai, J.-W. Yeh: High-Entropy Alloys: A Critical Review, Mater. Res. Lett., (2014), 2, 107-123
[67] E. P. George, R. O. Ritchie: High-entropy materials, MRS Bulletin, (2022), 47, 145-150
[68] H. Moroc, Ü. Özgür: Zinc oxide: Fundamentals, materials and device technology, (Wiley-VCH, Weinheim 2009), 1
[69] D. Ehrentraut, H. Sato, Y. Kagamitani, H. Sato, A. Yoshikawa, T. Fukuda: Solvothermal growth of ZnO, Prog. Crystal Growth Charact. Mater., (2006), 52, 280-335
[70] A. Wang: Electrical conductivity and doping, Springer Series in Materials Science 120 Zinc Oxide, chapter 5, (Springer, Berlin 2010), 95
[71] I. Ayoub, V. Kumar, R. Abolhassani, R. Sehgal, V. l Sharma, R. Sehgal, H. C. Swart, Y. K. Mishra: Advances in ZnO: Manipulation of defects for enhancing their technological potentials, Nanotechnol. Rev., (2022), 11, 575-619.

[72] R. Cusco, E. Alarcón-Lladó, J. Ibáñez, L. Artús, J. Jiménez, B. Wang, M. J. Callahan: Temperature dependence of Raman scattering in ZnO, Phys. Rev. B, (2007), 75, 165202
[73] D. Fischer, D. Zagorac, J. C. Schön: The presence of superoxide ions and related dioxygen species in zinc oxide - a structural characterization by in-situ Raman spectroscopy, J. Raman Spectr., (2022), 53, 2137-2146
[74] D. Fischer, D. Zagorac, J. C. Schön: Fundamental insight into the formation of the zinc oxide crystal structure, Thin Solid Films, (2023), 782, 140017
[75] X. Bidault, S. Chaudhuri: How Accurate Can Crystal Structure Predictions Be for High-Energy Molecular Crystals ?, Molecules, (2023), 28, 4471
[76] K. Kriz, L. Schmidt, A. T. Andersson, M.-M. Walz, D. van der Spoel: An Imbalance in the Force: The Need for Standardized Benchmarks for Molecular Simulation, J. Chem. Inf. Model., 2023, 63, 412-431
[77] M. Binnewies, R. Glaum, M. Schmidt, P. Schmidt: Chemical Vapor Transport Reactions, (De Gruyter, Berlin, 2012)
[78] D. Fischer, Z. Cancarevic, J. C. Schön, M. Jansen: Zur Synthese und Struktur von K_3N, Z. Anorg. Allg. Chem., (2004), 630, 160
[79] D. Fischer, M. Jansen: Does magnesium crystallize only in the Mg-type structure ? (HÄKO presentation, Regensburg, 3.3.-5.3.2005)
[80] D. Fischer: Research Report (MPI for Solid State Research, Stuttgart, 18.10.2006)
[81] J. C. Schön, M. Jansen: A first step towards planning of syntheses in solid state chemistry: determination of promising structure candidates using global optimization, Angew. Chem. Int. Ed., (1996), 35, 1286 - 1304
[82] M. Jansen: Syntheseplanung in der Festkörperchemie (Presentation at the 30th anniversary of the Fonds der Chemie, Düsseldorf, 1980)
[83] L. J. Conway, C. J. Pickard, A. Herrmann: First principles crystal structure prediction, in Comprehensive Inorganic Chemistry III, eds. J. Reedijk, K. Poeppelmeier (Elsevier, Amsterdam, 2023), Chapter 128 (3.12), 393-420
[84] A. J. Martinolich, J. R. Neilson: Pyrite Formation via Kinetic Intermediates through Low-Temperature Solid-State Metathesis, J. Am. Chem. Soc., 2014, 136, 15654-9
[85] J. C. Schön: Energy Landscape Concepts for Chemical Systems under Extreme Conditions, J. Innov. Mater. Extr. Cond., (2021), 2, 5-57
[86] F. Lu, L. Cheng, R. J. DiRisio, J.M. Finney, M. A. Boyer, P. Moonkaen, J. Sun, S. J. R. Lee, J. E. Deustua, T. F. Miller III, A. B. McCoy: Fast Near Ab Initio Potential Energy Surfaces Using Machine Learning, J. Phys. Chem. A, (2022), 126, 4013-4024

Journal of Innovative Materials in Extreme Conditions
2023
Volume 4
Issue 2

A REVIEW OF THE SYNTHESIS OF COMPOSITIONALLY COMPLEX ULTRA-HIGH-TEMPERATURE CERAMICS

Dharma Teja Teppala[1,]*, Samuel Aeneas Kredel[1], Emanuel Ionescu [1,2], Branko Matović[3]

[1]TU Darmstadt, Institute for Material Science, Otto-Berndt-Str. 3, D-64287, Darmstadt, Germany
[2]Fraunhofer IWKS, Brentanostr. 2a, D-63755 Alzenau, Germany
[3]Center for Synthesis, Processing, and Characterization of Materials for Application in the Extreme Conditions-CextremeLab, Institute of Nuclear Sciences Vinča, Belgrade, Serbia
Corresponding author: dharma.teppala@stud.tu-darmstadt.de*

Abstract: *Ultra-high temperature ceramics (UHTC) are a class of ceramics that possess melting points greater than 3000 °C and can withstand temperatures higher than 2000 °C without structural failure. The need to increase the performance inherently leads to the implementation of extreme temperatures, leading to the search for a new class of materials with better thermal properties. Compositionally complex ultra-high temperature ceramics with the inclusion of additional elements, whether resulting in an equimolar or non-equimolar site occupation in the respective sublattices, can improve properties due to the contributions of the configurational entropy. The term compositional complexity can be used as an umbrella term for the class of compositions with 3 or more elements and also their non-equimolar parts. The current review paper is based on the classification of the different compositionally complex ultrahigh temperature ceramics as borides, carbides, nitrides, etc., and reviews the different procedures employed for the bulk or powder synthesis thereof.*

Keywords**:** *UHTC, Compositional Complexity, Carbides, Nitrides, Borides, Silicides*

1. Introduction

Ultra-high-temperature ceramics (UHTC) are materials that have melting points greater than 3000 °C and may provide structural stability during operation at temperatures up to 2000 °C [58]. These ceramics are mainly based on the non-oxides of the transitional metal from group IV (Ti, Zr, Hf), and V (V, Nb Ta), among those being (di)borides, carbides, nitrides, or silicides. The high-temperature stability of these compounds is mainly due to the covalent bonds between B, C, and N with any of the group IV, and V elements. The presence of covalent bonds is the reason for high melting points, outstanding mechanical properties, and oxidation resistance. Additionally, UHTCs possess better electrical and thermal properties than oxides due to their metallic character [58].
Compositionally complex ceramics is the coinage for the group of ceramics that consist of medium, high entropy ceramics along with non-equimolar quaternary ceramics. Although the high entropy concept was introduced initially with the alloys, the use of the high entropy concept accelerated the ceramic property development. The compositional complexity is based on the Gibbs energy and the Boltzmann formula of entropy.

$$\Delta G_{mix} = \Delta H_{mix} - T\Delta S_{mix} \quad (1)$$

$$S = k_B \ln \omega \quad (2)$$

ΔG_{mix}: Gibbs free energy of mixing, ΔH_{mix}: Enthalpy of mixing, ΔS_{mix}: configurational entropy, S: entropy, k_b: Boltzmann constant, ω: number of possible configurations.
At sufficiently high temperatures, the $T\Delta S_{mix}$ term in eq. (1), with the entropy S being given by eq. (2), dominates the Gibbs energy and thus significantly contributes to a thermodynamic stabilization of the phase.

Along with the entropy, many other parameters such as VEC (Valance Electron Concentration), mixing enthalpy, and rules similar to Hume-Rothery were introduced and considered to be highly correlated to the thermodynamic stability of single-phase compositionally complex ceramics. Although the above-mentioned criteria are not definite for the formation of the high entropy material, a trend for the formation of a high entropic phase can be expected. In the case of the ceramics, additional contribution from the anionic sublattice can be expected, leading to the increase of the mixing entropy.

Substitution of the multiple transitional elements in the cationic sublattice of compositionally complex UHTCs can result in lattice distortions resulting in the hindrance of phonon propagation and increased electron scattering resulting in lower thermal and electrical conductivities over the binary UHTC themselves. The case can also be justified with substitution with an anionic sublattice or both.

The UHTC is generally used in aerospace applications involving high temperatures, resulting in their need for powder, bulk, and coatings. Traditional techniques for densification such as spark plasma sintering (SPS) and hot pressing are used. Additionally, non-traditional methods such as molten-salt-assisted methods were also employed to obtain compositionally complex powders, especially in the case of borides and carbides.

The current review paper will focus on the various compositionally complex borides, carbides, (carbo)nitrides, silicides, etc. of transitional metals of groups IV, V, and VI, summarizing the various procedures employed for their synthesis.

2. Brief consideration of compositional complexity in ceramics

In a multi-element compositional space for an alloy considering the various possible combinations, the compositions corresponding to the center region of the phase diagrams are generally considered as high entropy materials, with a preset of at least 5 or more elements, as the mixing entropy would be sufficiently large enough to overcome the effects of enthalpy. The entropy of mixing ΔS_{mix} can be derived using Stirling's approximation, eq. (3). Assuming anionic and cationic sublattice contributions, eq. (4) can be obtained.

$$\Delta S_{mix} = -R * \sum_{i=1}^{n} x_i \ln x_i \quad (3)$$

$$\Delta S_{mix} = -R\left(\sum_{i=1}^{n} c_i \ln c_i + \sum_{j=1}^{m} a_j \ln a_j\right) \quad (4)$$

R: Ideal gas constant, *x*: mole fraction, *c*: cationic site occupancy, *a*: anionic site occupancy.
In the case of the medium entropy, the number of elements is between 3 and 5 (see Figure 1).

Due to the entropic part of the Gibbs energy being able to overcome the enthalpy, a single-phase solid solution may be favored against the other possible outcomes. As the number of elements increase, due to difference in size, and chemical properties, many unexpected properties can be seen.

Based on the concept of high and medium entropy, compositionally complex ceramics are developed, where (a) the mixing entropy has a contribution from either the cationic and the anionic site (b) the number of elements inclusive of the cationic and anionic sublattices can be greater than or equal to 5.

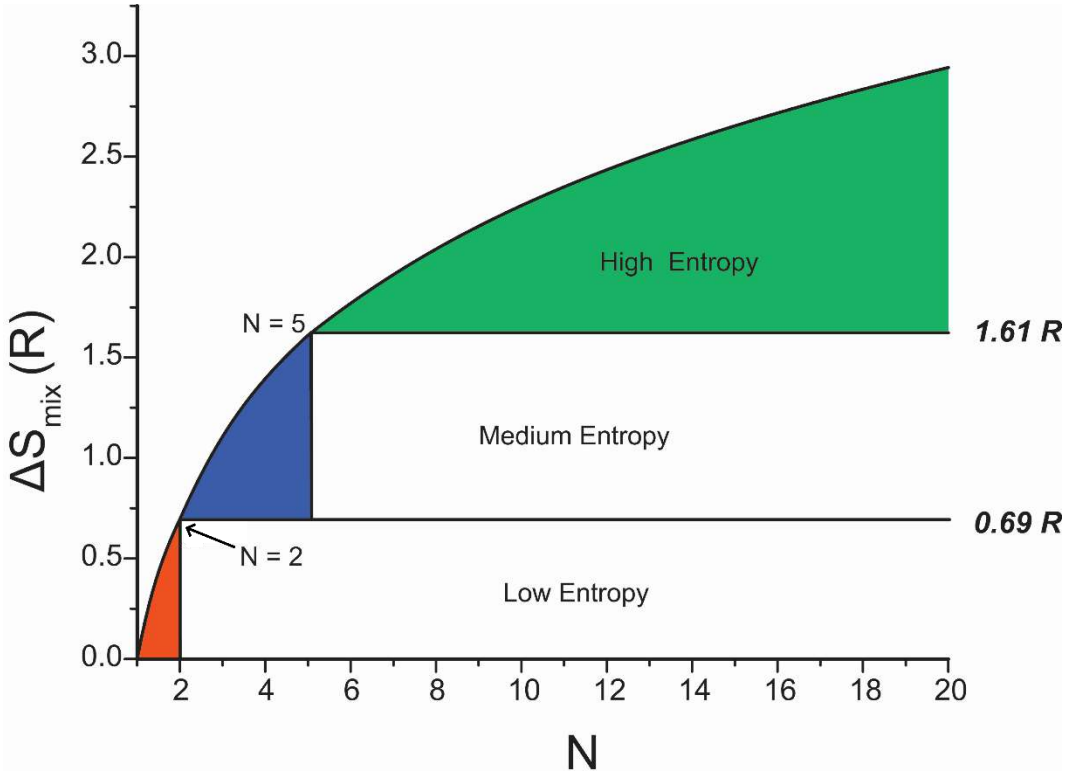

Figure 1. Configurational entropy vs number of elements in case of alloys.

Although a lot of element combinations are possible, other parameters such as the deviation parameter δ, given by eq. (5), corresponding to atomic lattice parameter mismatch were also introduced. In the case of the ceramics, it was stated that δ should have a deviation of less than 4% in order to obtain a single phase; however, various compositions with δ being greater than 4% were also observed as single-phase materials.

$$\delta = \sqrt{\sum_{i=1}^{n} c_i \left(1 - \frac{a_i}{\bar{a}}\right)^2} \qquad (5)$$

δ: deviation parameter, a: lattice constant, $\bar{a}$: mean lattice parameter, c: concentration.

To avoid the discrepancy, Gild et.al [77] suggested considering the lattice parameter instead of atomic size to better represent the single-phase formability. In the case of boride systems, the change in the c direction was observed to be more useful in predicting single-phase formability [77].

Other properties such as entropy forming ability (EFA) were computed theoretically by Sarker et.al [30] and were also considered during the design of high-entropy ceramics, EFA being a measure of the likelihood of a material system to form a single phase, obtained by observing possible unit cell configurations and evaluating their energies.

Although the high-entropy ceramics are observed and found to be promising materials, the non-equimolar combinations and ternary compositions of the high entropy compositional space were also found to exhibit similar to or better mechanical and thermal properties, thus the term compositionally complex ceramics has come into existence by grouping up the medium, non-equimolar and high entropy ceramics.

3. Synthesis Methods for Ultra-High Temperature Compositionally Complex Ceramics

As these materials need to withstand application temperatures higher than 2000 °C, a prerequisite of the present phases is a substantially high melting point (i.e., beyond 3000 °C), making high temperatures necessary to yield dense and structurally rigid materials. Thus, the fabrication of the ceramics seems difficult. Many methods are currently being employed for the synthesis to overcome these complications, and these can be majorly classified as solid-state synthesis [7],[18],[24],[26],[29],[40],[59],[60],[69].

Thus, various classes of UHTCs (see Figure 2) were preparatively accessed by using synthesis methods such as carbo- and borothermal reduction [3], [65], [85], [90], [91], reactive sintering of the elements [2], [7], [8], [16], [43], [50], [70], [72], [74], [75], [77], [87], molten salt synthesis [61], [64], [88], [89], sol-gel synthesis [29], [31], [63], [69], [96], arc melting [62], [92], [93] and high pressure [19], [94], [97]. The processing can also involve multiple steps consisting of combinations of these methods to favor the random distribution of constituents in cationic and anionic sublattices.

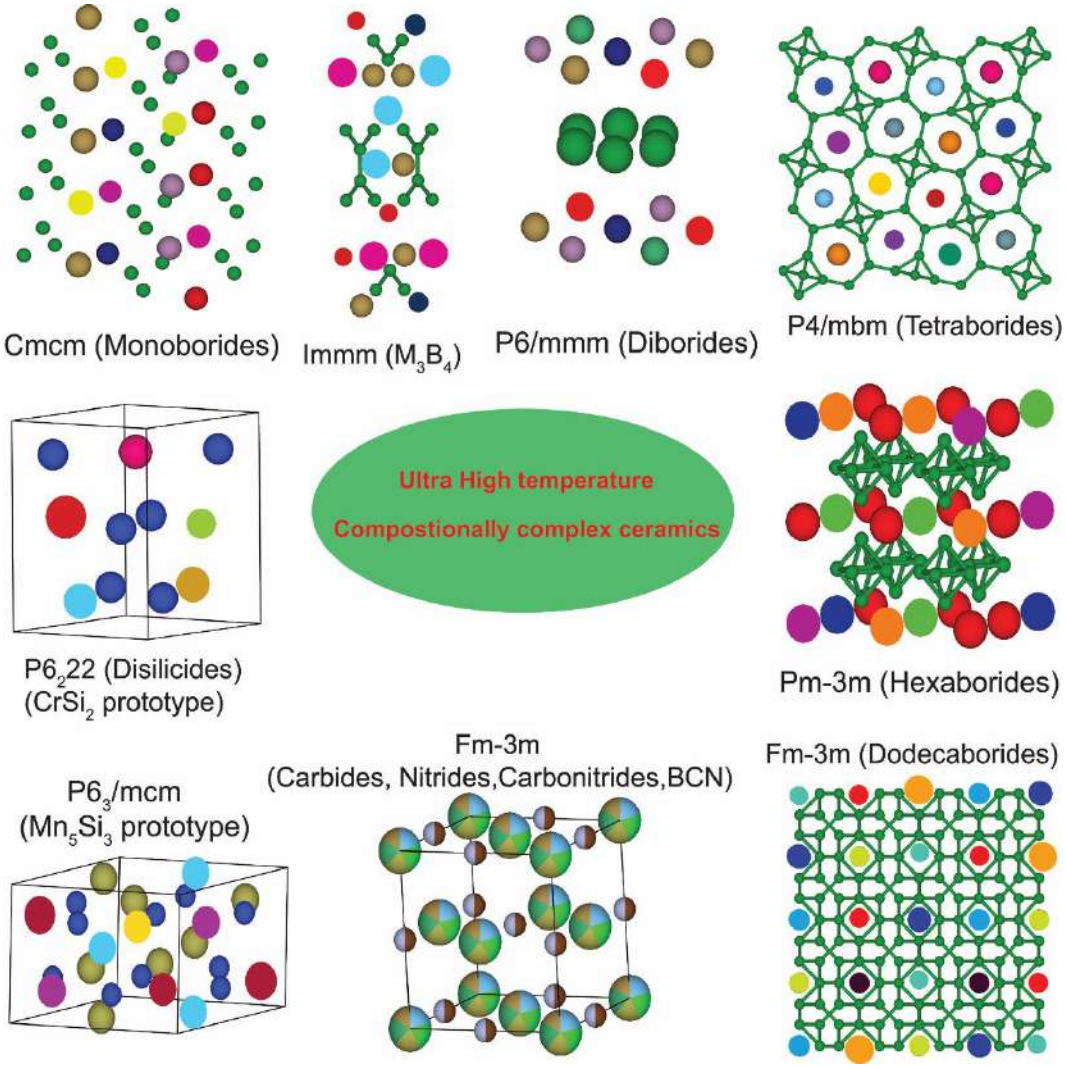

Figure 2. Various classes of compositionally complex UHTCs synthesized so far and their experimentally observed crystalline structures.

3.1 Solid State Synthesis

Solid state synthesis is a straightforward reaction, suitable for solid reactants. This process involves the reaction of the individual constituents. Tallarita et al. [7] have synthesized $(Hf_{0.2}Mo_{0.2}Ta_{0.2}Nb_{0.2}Ti_{0.2})B_2$ by reacting a ball-milled mixture of Hf, Mo, Ta, Nb, and Ti metal powders along with boron to obtain a high entropy diboride, according to the following eq. (6).

$$0.2Hf + 0.2Mo + 0.2Ta + 0.2Nb + 0.2Ti + (2 + x)B = (Hf_{0.2}Mo_{0.2}Ta_{0.2}Nb_{0.2}Ti_{0.2})B_2 \quad (6)$$

The self-propagated reaction of the mixture occurred with W filament as the heating source. Excess boron was used to reduce the oxide impurities. However, a small contribution of additional phases such as HfO_2, (Hf, Ti)B_2, (Ti, Ta)B_2, and HfB_2 were found through XRD investigations.

Recently Zhao et. al [59], [60] synthesized $(V_{0.2}Mo_{0.2}W_{0.2}Nb_{0.2}Ni_{0.2})B$, $(V_{0.2}Cr_{0.2}Mo_{0.2}Ni_{0.2}W_{0.2})B$, $(V_{0.2}Mo_{0.2}Ta_{0.2}Ni_{0.2}W_{0.2})B$, $(V_{0.2}Cr_{0.2}Mo_{0.2}W_{0.2}Ti_{0.2})B$ and $(Cr_{0.2}Mo_{0.2}Ta_{0.2}Ni_{0.2}W_{0.2})B$ via reactive hot pressing of ball milled mixtures of the compositions mentioned above. Although there were oxide and diboride phases, the sintering of these compositions at 2000 °C resulted in high entropic monoborides except for $(V_{0.2}Cr_{0.2}Mo_{0.2}W_{0.2}Ti_{0.2})B$ as significant TiB_2 was observed even at 2000 °C. However, Ye et al. [65] used ball mill-assisted hot pressing for $(Ti_{0.333}Zr_{0.333}Hf_{0.333})B_2$ at 1900 °C.

Chicardi et al. [26], [40] used a simple mechanochemical method for $(Ti_{0.2}Zr_{0.2}Hf_{0.2}V_{0.2}Nb_{0.2})C$, $(Ti_{0.2}Zr_{0.2}Hf_{0.2}V_{0.2}Ta_{0.2})C$, $(Ti_{0.2}Zr_{0.2}Hf_{0.2}Nb_{0.2}Ta_{0.2})C$, $(Ti_{0.2}Zr_{0.2}V_{0.2}Nb_{0.2}Ta_{0.2})C$, $(Ti_{0.2}Hf_{0.2}V_{0.2}Nb_{0.2}Ta_{0.2})C$ and $(Zr_{0.2}Hf_{0.2}V_{0.2}Nb_{0.2}Ta_{0.2})C$, via a long duration (/extended) ball milling at room temperature. In the case of $(Ti_{0.2}Zr_{0.2}V_{0.2}Nb_{0.2}Ta_{0.2})C$, the metallic powders were mixed with carbon and ball milled for 70 h under 5 atm of Ar, with an interval of 5 h of ball milling and 1 h of pause to avoid a temperature increment, thereby obtaining the high entropy carbide without any involvement of heating.

In the case of nitrides, Jin et al. [29] synthesized $(V_{0.2}Nb_{0.2}Cr_{0.2}Mo_{0.2}Zr_{0.2})N$ by reacting chlorides of V, Cr, Nb, Mo, and Zr with urea. The chlorides were reacted with urea under the mechanical influences of ball milling for 30 min which resulted in gelation. The gel was later pyrolyzed at 800 °C under N_2 resulting in $(V_{0.2}Nb_{0.2}Cr_{0.2}Mo_{0.2}Zr_{0.2})N$.

Similar steps were followed for $(Hf_{0.2}Nb_{0.2}Ta_{0.2}Ti_{0.2}V_{0.2})N$ by Xing et. al,[69] however ethanol was used during milling and the pyrolysis temperature was 1300 °C.

However, Guan et al. [18] have applied this method to obtain borocarbonitrides with a simple two-step mechanical alloying. $(Ta_{0.2}Nb_{0.2}Zr_{0.2}Hf_{0.2}W_{0.2})BCN$, $(Ta_{0.2}Nb_{0.2}Zr_{0.2}Hf_{0.2}Ti_{0.2})BCN$, and $(Ta_{0.2}Nb_{0.2}Zr_{0.2}Ti_{0.2}W_{0.2})BCN$ were synthesized by mechanical alloying of amorphous BCN with the respective metallic powders. The amorphous BCN was prepared by 10 h of milling of h-BN and graphite. The respective metallic powders were added in the second step of mechanical alloying, which continued for 24 hours.

Zhao et al. [24] have involved Al to obtain $(Ti_{0.25}V_{0.25}Nb_{0.25}Ta_{0.25})C$. The elements were mixed in a composition similar to 20 at% of HEC and 80 at% Al. The respective powders were ball milled using ZrO_2 and were calcinated at different temperatures leading to a high entropy carbide in the Al matrix. The aluminum formed intermetallics at low temperatures, but when pyrolyzed at high temperatures, it resulted in a single-phase carbide because Al was acting as a solvent, facilitating diffusion (see Figure 3).

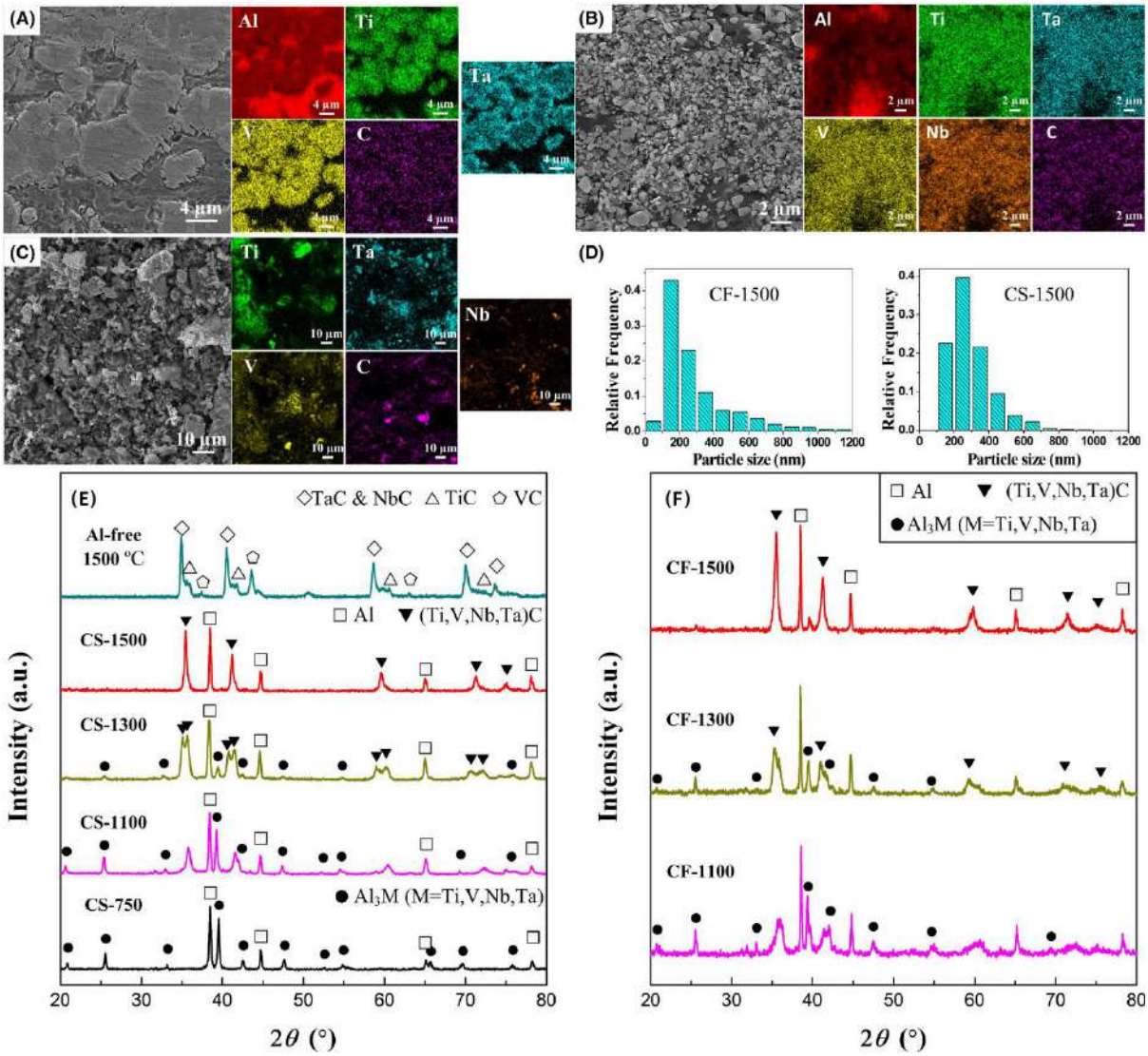

Figure 3. (A)-(C) SEM images of (TiTaNbV)C alloyed with Al, (TiTaVNb)C alloyed with Al and (TiTaVNb)C without Al. (E)-(F) displays the XRD of the compositions obtained at different temperatures and clearly shows the effect of Al on obtaining a single phase. Reprinted from Zhao et. al. [24]

3.2 Carbo-/ Borothermal Reductions

These methods are usually employed when the preparative access to the UHTCs is anticipated from oxidic precursors. A thorough mixing or milling of the respective oxides along with a reactant source forms the compositionally complex ceramic.

Zhang et al. [3] prepared $(Hf_{0.2}Zr_{0.2}Ta_{0.2}Nb_{0.2}Ti_{0.2})B_2$, $(Hf_{0.2}Zr_{0.2}Mo_{0.2}Nb_{0.2}Ti_{0.2})B_2$ and $(Hf_{0.2}Mo_{0.2}Ta_{0.2}Nb_{0.2}Ti_{0.2})B_2$ $(Hf_{0.2}Zr_{0.2}Ta_{0.2}Cr_{0.2}Ti_{0.2})B_2$ – hexagonal diboride compositions. The appropriate amounts of the oxides for the target compositions were thoroughly roll-milled (for 24 h with Si_3N_4 milling balls along with B_4C, acting as a source for both carbon and boron. The compositions were heated under vacuum at 1600 °C resulting in compositionally complex diborides and small amounts of polymorphs of HfO_2.

Zhang et al. [91] synthesized a quaternary diboride, $(Hf_{0.25}Zr_{0.25}Ta_{0.25}Sc_{0.25})B_2$, by ball milling the respective oxides and B_4C in ethanol, with zirconia as milling balls, then pressing cylindrical pellets to ensure contact during pyrolysis at 1700 °C under vacuum for 2 h, leading to the formation of a single phase compositionally complex ceramic.

Cui et. al [100] synthesized the first high-entropy dodecaboride $(Dy_{0.2}Ho_{0.2}Er_{0.2}Tm_{0.2}Lu_{0.2})B_{12}$ and subsequently $(Dy_{0.166}Ho_{0.166}Er_{0.166}Tm_{0.166}Lu_{0.166}Hf_x)B_{12}$ by reacting Dy_2O_3, Ho_2O_3, Er_2O_3, Tm_2O_3 and Lu_2O_3 with excess boron (see Figure 4). In the case of the latter composition, HfO_2 was included in the reaction. The powders were thoroughly ground in a pot for 24 h with ethanol and ZrO_2 balls, then pressed as cylindrical pellets and subsequently pyrolyzed in a vacuum at 1600 °C for 1 h. The obtained powders were either densified by spark plasma sintering (SPS) with a pressure of 30 MPa at 1500 °C, 1600 °C, 1700 °C, and 1800 °C for 5 min or high-pressure sintering at 5 GPa at 1700 °C for 30 min. This exact synthesis procedure was also followed for the hexanary composition.

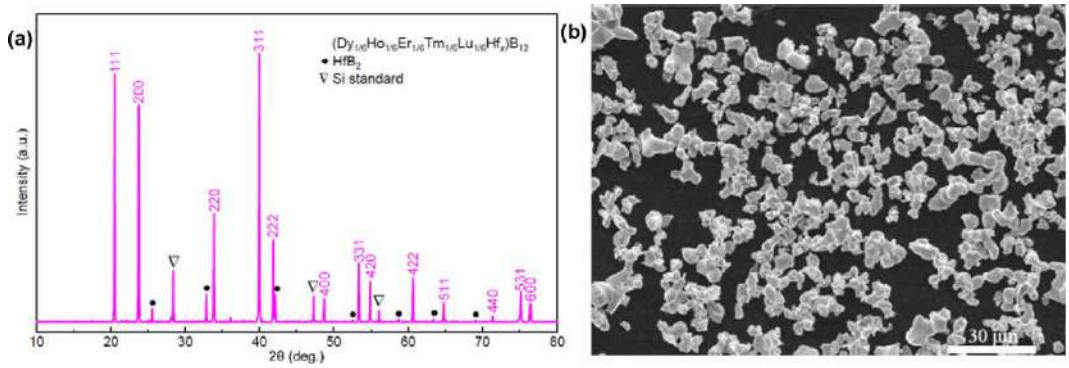

Figure 4. (a) XRD of the dodecaboride with HfB_2 impurity. (b) SEM image of the obtained powders. Reprinted with permission from Cui et al. [100]

The EDS mappings and TEM characterization were performed and the particles were segregated as Hf-rich, rare earth-rich, and B-rich, layered, phases (see Figure 5).

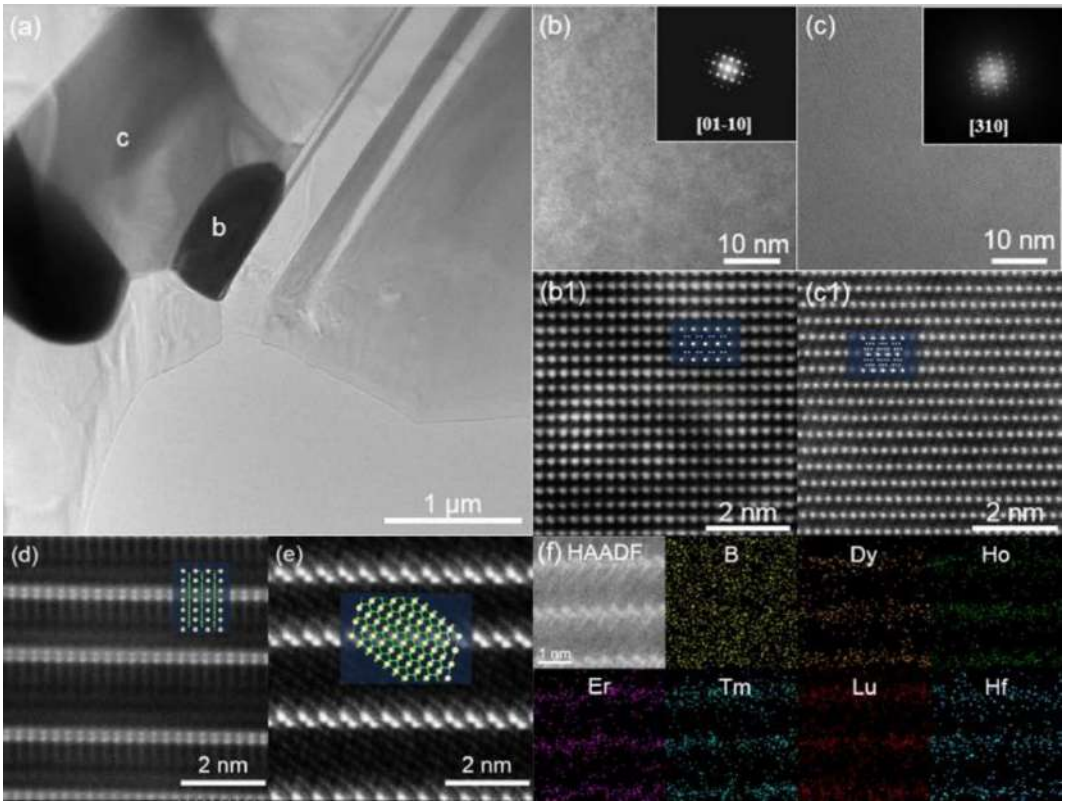

Figure 5. (a) BF-TEM image of grains with FFT in right inset. (b1), (c1), (d), (e) atomic resolved HAADF images, (f) HAADF and EDS. Reprinted with permission from Cui et al. [100]

Zhang et al. [90] have used a sol-gel assisted carbothermal reduction in the case of $(Hf_{0.2}Zr_{0.2}Ti_{0.2}Ce_{0.2}La_{0.2})C$. This method resulted initially a high entropy oxide and later the carbide phase. Hafnium(IV) acetylacetonate, zirconium(IV) acetylacetonate, titanium(IV) isopropoxide, cerium(III) acetylacetonate, and lanthanum(III) acetylacetonate were mixed in benzyl alcohol. The mixture was loaded into an autoclave and was heated to 220 °C for 48 h resulting in a metal oxide precursor, after ethyl ether was used as a gelation agent. The metal oxide precursor was heated to 220 °C for 5 h, resulting in a high entropy oxide which then was mixed with glucose (as a carbon source) and dispersed in water. After pyrolysis at temperatures higher than 1300 °C, it resulted in single-phase high entropy carbides.

The oxides that were synthesized by the sol-gel method were observed to be amorphous up to 400 °C. The sol-gel technique was used to synthesize the compositions $(HfZrTi)O_x$, $(HfZrTiCe)O_x$, $(HfZrTiLa)O_x$ and $(HfZrTiCeLa)O_x$. The similarity in the diffractograms of the synthesized compositions suggests that the mixing entropy had a low effect on nucleation [90]. At higher temperatures, the $(Hf_{0.2}Zr_{0.2}Ti_{0.2}Ce_{0.2}La_{0.2})O_x$ is found to be of fluorite structure and the elements Hf, Zr, Ti, Ce, and La are homogenously distributed with a lattice spacing d_{111} of 0.273 nm.

The presence of glucose as a carbon source resulted in $(Hf_{0.2}Zr_{0.2}Ti_{0.2}Ce_{0.2}La_{0.2})C$ only after pyrolysis at 1600 °C and as the amount of glucose was increased, the secondary phase shifted from La_2O_3 to LaC_2. After carbothermal reduction, both $(Hf_{0.2}Zr_{0.2}Ti_{0.2}Ce_{0.2}La_{0.2})C$ and $(Hf_{0.2}Zr_{0.2}Ti_{0.2}Ce_{0.2}La_{0.2})C$ with an amorphous layer of $(Hf_{0.2}Zr_{0.2}Ti_{0.2}Ce_{0.2}La_{0.2})(O)C$ formed.

$(Nb_{0.25}Ta_{0.25}Ti_{0.25}\ Zr_{0.25})C$ composition [85] was prepared directly via carbothermal reduction of Nb2O5, Ta2O5, TiO2 and ZrO2 at 2000 °C (see Figure 6).

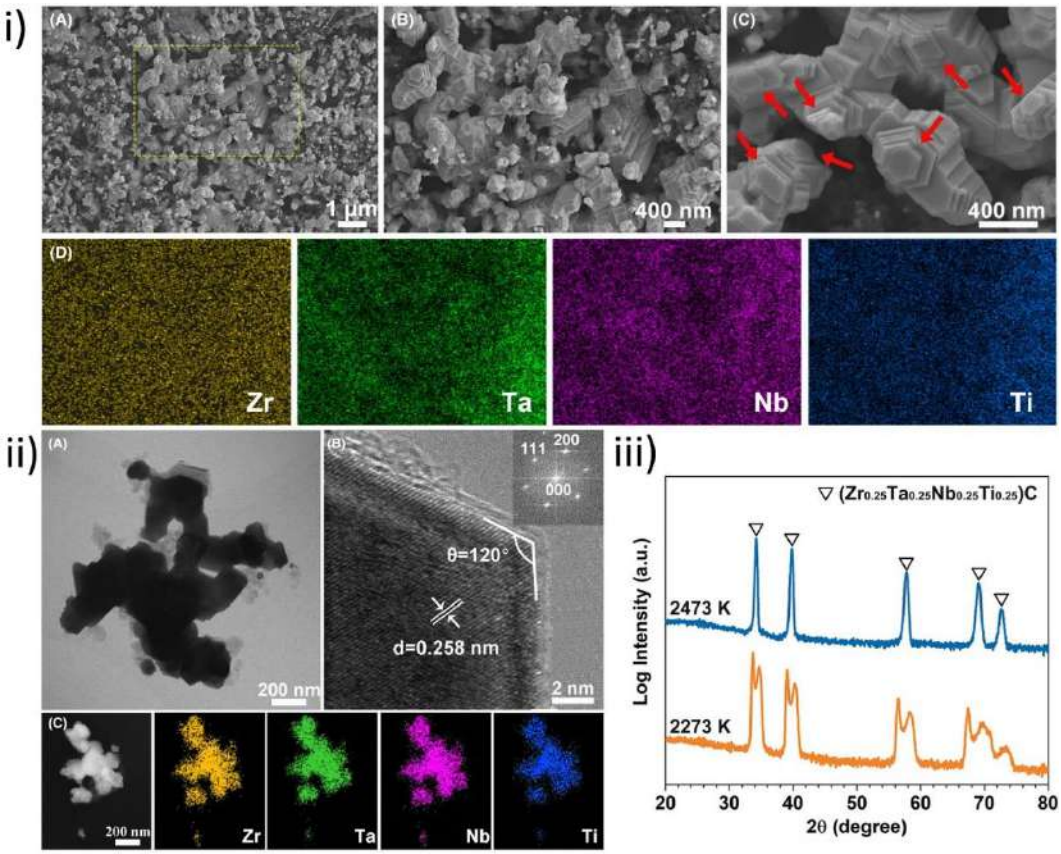

Figure 6. (i) SEM-EDS of coral-shaped $(Nb_{0.25}Ta_{0.25}Ti_{0.25}\ Zr_{0.25})C$. (ii) TEM -EDS and SAED (iii) XRD of the synthesized $(Nb_{0.25}Ta_{0.25}Ti_{0.25}\ Zr_{0.25})C$ at 2000 °C and 2200°C. Reprinted from Ye et al. [85]

Interestingly, $(Mo_{0.2}Nb_{0.2}Ta_{0.2}Ti_{0.2}Zr_{0.2})C$ was synthesized by magnesiothermic carbothermal reduction of ball-milled MoO_3, Nb_2O_5, Ta_2O_5, TiO_2, and ZrO_2 along with graphite and Mg at 1350 °C – the obtained mixture consisting of the high-entropy carbide and magnesium oxide was rinsed with HCl to obtain MgO-free carbide powders (see Figure 6) [67].

3.3 Pressure and Pressureless Sintering or Densification

Generally, the sintering involves two steps, the first step being the mechanical mixing of the respective precursors and the second step being the simultaneous compaction and heating, i.e. reactive sintering. These precursors can either be oxides, metals, or even the binary ceramics themselves.

Gild et al. [77] have synthesized several diboride ceramics, namely $(Hf_{0.2}Zr_{0.2}Ta_{0.2}Nb_{0.2}Ti_{0.2})B_2$, $(Hf_{0.2}Zr_{0.2}Ta_{0.2}Mo_{0.2}Ti_{0.2})B_2$, $(Hf_{0.2}Zr_{0.2}Mo_{0.2}Nb_{0.2}Ti_{0.2})B_2$, $(Hf_{0.2}Mo_{0.2}Ta_{0.2}Nb_{0.2}Ti_{0.2})B_2$, $(Mo_{0.2}Zr_{0.2}Ta_{0.2}Nb_{0.2}Ti_{0.2})B_2$, and $(Hf_{0.2}Zr_{0.2}Ta_{0.2}Cr_{0.2}Ti_{0.2})B_2$ by combined sintering of individual binary metal borides. The metal borides were ball-milled under Argon. The obtained ball-milled mixture was sintered at 2000 °C for 5 min with 30 MPa resulting in a single-phase phase AlB_2-type structure (see Figure 7). A Mo foil was used as an intermittent to prohibit the reaction between the powders and the graphite crucible. Also, Qin et al. [74] have synthesized $(Ti_{0.2}Zr_{0.2}Hf_{0.2}Mo_{0.2}W_{0.2})B_2$, $(Ti_{0.2}Ta_{0.2}Cr_{0.2}Mo_{0.2}W_{0.2})B_2$, $(Zr_{0.2}Hf_{0.2}Nb_{0.2}Ta_{0.2}W_{0.2})B_2$, and $(Zr_{0.225}Hf_{0.225}Ta_{0.225}Mo_{0.225}W_{0.1})B_2$ from elements through reactive sintering. The individual elements were ball milled with boron, using stearic acid as a lubricant, and were sintered in two steps, similar to the method reported by Tallarita et al. [7] The die was held at 1400 °C and 1600 °C to promote the reactions of boron with oxides as well as simultaneously occurring outgassing. Later, they were sintered at 2000 °C, resulting in a complete single phase with W and Mo being stabilized without segregations at high temperatures.

Kavak et al. [75] have synthesized quaternary diboride $(Hf_{0.25}Ti_{0.25}W_{0.25}Zr_{0.25})B_2$ in mechanochemistry-assisted SPS. The HfO_2, TiO_2, ZrO_2, and WO_3 were reacted individually with boron using magnesiothermic reactions. The obtained binary diborides were then milled along with boron under Ar with a pause of 5 min after each finished 60 min of a total milling time of 4-10 h. The obtained milled powder was sintered at 1800 °C-2050 °C to obtain a single-phase diboride with minor oxide impurities.

Qin et al. [8], [70], [72], [74] have synthesized various tetraboride compositions, i.e., $(Y_{0.17}Nd_{0.18}Sm_{0.21}Gd_{0.22}Er_{0.22})B_4$, $(Y_{0.21}Sm_{0.19}Gd_{0.21}Er_{0.18}Yb_{0.21})B_4$, $(Y_{0.22}La_{0.18}Pr_{0.20}Dy_{0.23}Er_{0.17})B_4$, $(Y_{0.22}Nd_{0.18}Gd_{0.20}Dy_{0.21}Er_{0.19})B4$, $(Y_{0.22}Nd_{0.20}Sm_{0.20}Gd_{0.19}Tb_{0.19})B_4$ and $(Nd_{0.18}Sm_{0.19}Gd_{0.23}Tb_{0.21}Yb_{0.19})B_4$ as well as hexaborides with lanthanides, obtaining relative densities of at least 98% for the compositions $(Y_{0.23}Nd_{0.21}Sm_{0.20}Gd_{0.18}Yb_{0.18})B_6$, $(Y_{0.19}La_{0.19}Pr_{0.22}Dy_{0.19}Yb_{0.21})B_6$, $(La_{0.19}Nd_{0.21}Sm_{0.23}Gd_{0.19}Yb_{0.18})B_6$, $(Y_{0.22}La_{0.20}Nd_{0.19}Sm_{0.22}Gd_{0.17})B_6$, $(Y_{0.21}La_{0.17}Nd_{0.18}Sm_{0.21}Tb_{0.23})B_6$ and $(La_{0.18}Pr_{0.21}Nd_{0.19}Sm_{0.21}Tb_{0.21})B_6$. [8] Compared to the procedure of Gild et al. [77], who performed SPS of the ball-milled mixture of metallic powders and boron, the parameters differ, as 1700 °C with a pressure of 50 MPa and a holding time of 10 min were used by Qin et al. The compacted powders were then sintered to obtain single-phase ceramics. Through this process, M_3B_4-based high entropy borides of compositions $(V_{0.2}Cr_{0.2}Nb_{0.2}Mo_{0.2}Ta_{0.2})_3B_4$ and $(V_{0.2}Cr_{0.2}Nb_{0.2}Ta_{0.2}W_{0.2})_3B_4$ were synthesized, which showed minor impurities in form of M_5B_6 phase [71]. Also, various high-entropy monoboride compositions, i.e., $(V_{0.2}Cr_{0.2}Nb_{0.2}Ta_{0.2}W_{0.2})B$, $(V_{0.2}Cr_{0.2}Nb_{0.2}Mo_{0.2}W_{0.2})B$ and $(V_{0.2}Cr_{0.2}Nb_{0.2}Mo_{0.2}Ta_{0.2})B$, were synthesized via reactive sintering with similar conditions [2].

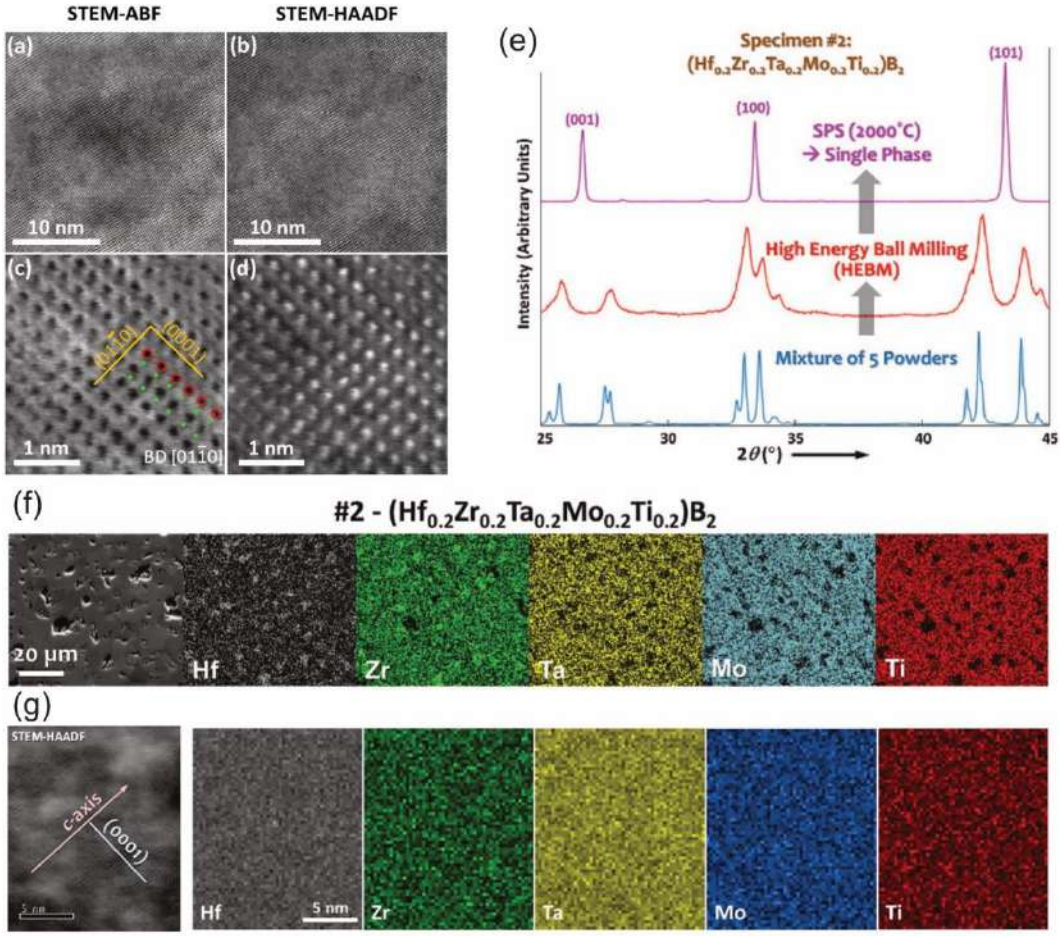

Figure 7. Structural characterization of $(Hf_{0.2}Zr_{0.2}Ta_{0.2}Mo_{0.2}Ti_{0.2})B_2$. (a), (b) ABF and HAADF, (c), (d) ABF and HAADF at higher magnification showing the cations (in red) and boron (in green) (e) XRD of $(Hf_{0.2}Zr_{0.2}Ta_{0.2}Mo_{0.2}Ti_{0.2})B_2$ at different stages of synthesis (f), (g) SEM EDS and STEM EDS of $(Hf_{0.2}Zr_{0.2}Ta_{0.2}Mo_{0.2}Ti_{0.2})B_2$. Reprinted from Gild et al. [77]

In the case of some carbide-based UHTC compositions [43], a unique route of non-reactive sintering was found. The cold-pressed green bodies of carbides were placed in an electro-resistively heated graphite felt in an argon atmosphere. Rapid heating of the cold-pressed green body leads to sintering. Although the current and heating are prone to be uneven, the process proved to be a fast and energy-efficient way to obtain dense ceramic pellets.

Dippo et al. [16] prepared several bulk high entropy (carbo)nitrides by performing SPS of milled binary nitrides and carbides under vacuum at 2000 °C. Further, Moskovskikh et al. [50] have synthesized high entropy nitrides with combustion synthesis-assisted SPS. The high energy ball milled metallic powders were combusted under N_2 of 8 atm pressure. The obtained nitride powders were then sintered at 1800 °C for 20 min with a pressure of 30 MPa under 0.8 atm N_2 (see Figure 8).

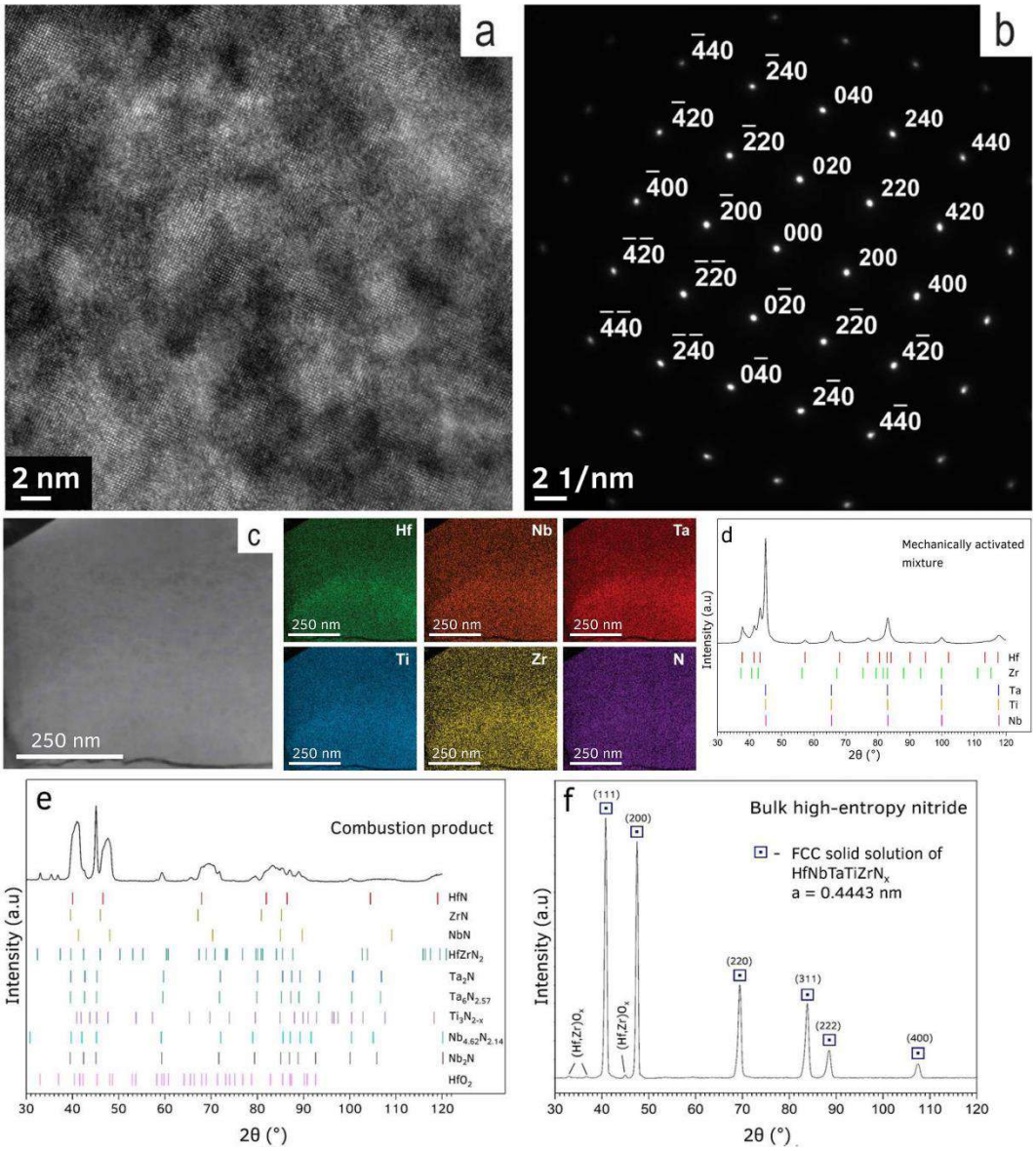

Figure 8. (a) HRTEM of $(Hf_{0.2}Ta_{0.2}Ti_{0.2}Nb_{0.2}Zr_{0.2})N$, (b) SAED pattern from [001] zone axis, (c) EDS mapping (d), (e), (f) XRD of the precursors at different stages of the synthesis. Reprinted from Moskovskikh et al. [50]

High-entropy silicides of $(V_{0.2}Cr_{0.2}Nb_{0.2}Ta_{0.2}W_{0.2})_5Si_3$ and $(Ti_{0.2}Zr_{0.2}Nb_{0.2}Mo_{0.2}Hf_{0.2})_5Si_3$ have been prepared by Sivakumar et al. [87] in ball-milled assisted SPS at 1900 °C and 1800 °C respectively, with a holding time of 20 min at 50 MPa. Interestingly, these phases were found to be of Mn_5Si_3-type hexagonal $D8_8$ structure, although the binary V, Cr, Nb, Ta, and W silicides exhibit rather tetragonal Cr_5Si_3 ($D8_1$) or W_5Si_3 ($D8_m$).

Composition $(Zr_{0.196}Hf_{0.02}V_{0.196}Nb_{0.196}Mo_{0.196}W_{0.196})C_x$ was synthesized by the Hot-pressing route by Zhang et al. [110] by ball milling the oxides with carbon for 20 h and subsequent carbothermal reduction at 1600 °C for 1 hr in a vacuum and hot pressed at 2100 °C for 60 min with the pressure of 30 MPa resulting in single phase carbide at x = 0.7 and 0.8 and the rest compositions had either spinodal decomposition or discontinuous precipitation.

3.4 Molten Salt

Molten salt synthesis was employed recently by Ning et al. for a medium entropic ceramic $(Ta_{0.25}Ti_{0.25}Nb_{0.25}V_{0.25})C$ [64]. The elements Ta, Ti, V, and Nb along with carbon were mixed in KCl and resulted in $(Ta_{0.25}Ti_{0.25}V_{0.25}Nb_{0.25})C$ ceramic without any oxidic impurities after pyrolysis under argon at 1300 °C (see Figure 9).

$(Ta_{0.25}Hf_{0.25}Ti_{0.25}Nb_{0.25})Si_2$ was prepared via the molten salt method using transition metal oxides. Thus, Ta_2O_5, HfO_2, TiO_2, and Nb_2O_5 were mixed along with 200 wt% excess SiO_2 as well as 350-400 wt% excess Mg and NaCl+KCl. The mixture was pyrolyzed under argon at 800 °C for 6 h, resulting in fine disilicide powders [88].

Ye [89] used metal oxides, B_2O_3, $MgCl_2$ and Mg for the magnesio-thermic synthesis of $(Zr_{0.25}Ta_{0.25}Nb_{0.25}Ti_{0.25})B_2$, $(Hf_{0.25}Ta_{0.25}Nb_{0.25}Ti_{0.25})B_2$, $(Hf_{0.25}Zr_{0.25}Ta_{0.25}Nb_{0.25})B_2$ and $(Ta_{0.25}Nb_{0.25}Ti_{0.25}Cr_{0.25})B_2$. As the compositionally complex ceramics supersaturate the molten salt, the fine-grained ceramics with a particle size well below 100 nm can be obtained (see Figure 9).

The underlying mechanism in a molten salt-assisted synthesis is the dissolution of cation precursors into the molten salt, causing an intermediate state where cations and delocalized electrons are present. These delocalized electrons then are accepted by the dissolved anionic precursor, resulting in delocalized anions. The recombination of the ions at the anionic surface leads to the formation of a high-entropy ceramic [64].

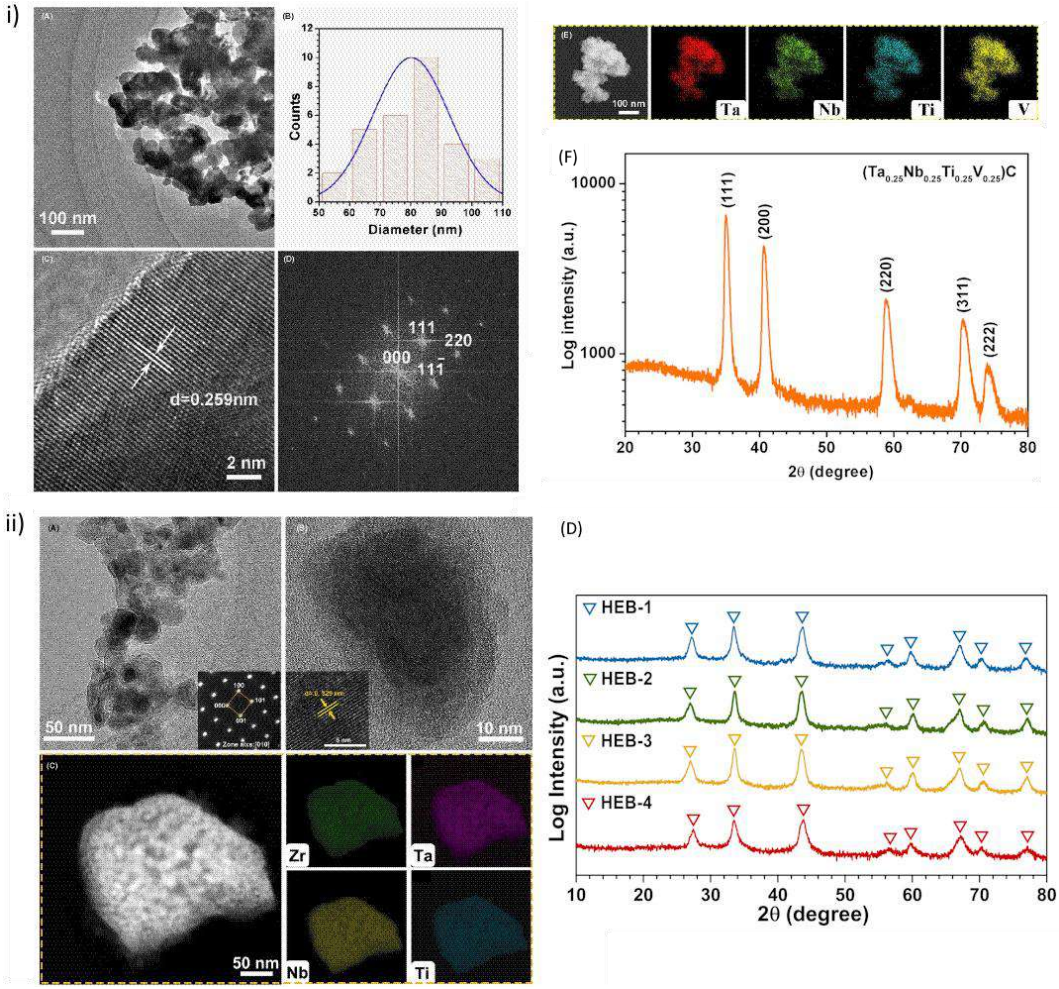

Figure 9. i) (A), (C) TEM, (B) particle size distribution, (D) SAED, (E) EDS mapping, (F) XRD of $(Ta_{0.25}Ti_{0.25}V_{0.25}Nb_{0.25})C$. Reprinted from Ning et al. [64]. ii) (A)-(C) TEM with SAED and EDS and (D) XRD of $(Zr_{0.25}Ta_{0.25}Nb_{0.25}Ti_{0.25})B_2$. Reprinted from Ye et al. [89]

3.5 Sol-Gel

The sol-gel process is a wet chemical synthesis route starting from a solution in either water, organic solvents, or a combination thereof, that is, through condensation and hydrolysis, forming a network with an enclosed solvent, a gel, depicted in Figure 10. It mostly is straightforward, without any complicated setup or processing involved – with some exceptions being supercritical drying to obtain aerogels or oxygen-free syntheses. This process can be applied to a good number of ceramic classes, such as borides, carbides, oxides, and many more. Yang et al. [63] have produced $(Cr_{0.2}Hf_{0.2}Mo_{0.2}Nb_{0.2}Ta_{0.2})B_2$ for which $HfCl_4$, $NbCl_5$, $CrCl_3.6H_2O$, Mo(II)acetylacetonate and $TaCl_5$ were dissolved in ethanol. Further, sorbitol and boric acid were mixed along with citric acid and ethylene glycol into the solution, which was heated and dried to obtain a xerogel. It was later pyrolyzed under argon resulting in a high entropy diboride powder. The sol-gel route was further used by [31] to obtain a high entropy carbide sample. [31] used the respective chlorides with the furfuryl alcohol as the gel former with butanol as the solvent, obtaining a gel which later, upon pyrolysis, resulted in a single-phase high entropy carbide. Usually, the precursor needs to feature carbon-rich functional groups, e.g., alcohol. Other precursors such as citric acid, glucose, and PEG along with water-soluble salts can be considered to obtain the target compositionally complex ceramics at high temperatures. Interestingly, this method was modified by [96] by substituting alcohols with acetyl methane and butanol and then reacting the mixture in a hydrothermal autoclave chamber to obtain the gel which after pyrolysis results in carbide.

For nitrides, however, the reaction only involved one step in which the chlorides react with urea to form metal urea gels, which later are pyrolyzed to obtain the nitride ceramics (see Figure 11). [29],[69]

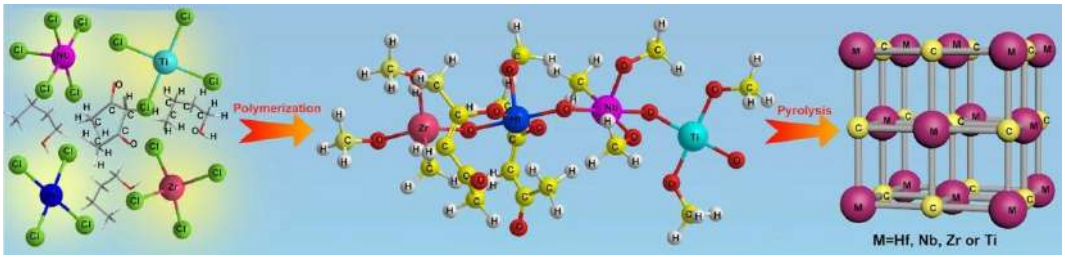

Figure 10. Schematic diagram of the sol-gel process in the case of high entropy carbides. Reprinted from Du et al. [56]

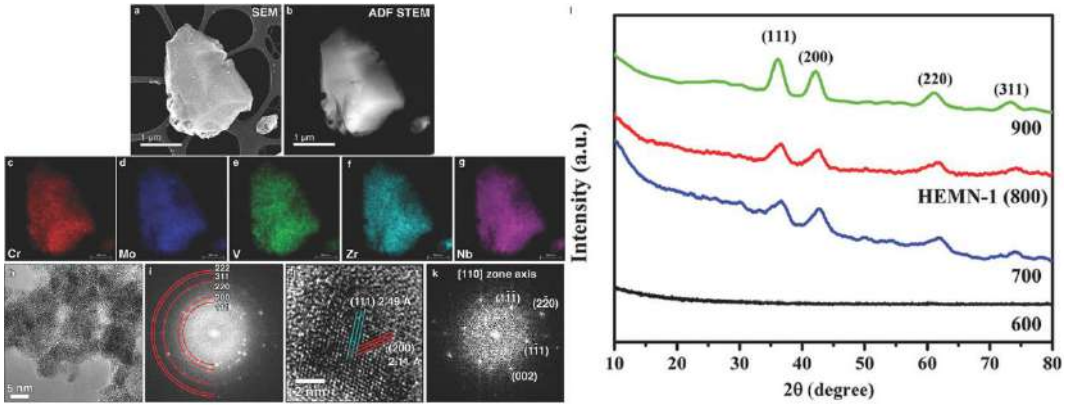

Figure 11. (a) SEM, (b-k) TEM with EDS and SAED and (l) XRD of $(Cr_{0.2}Mo_{0.2}V_{0.2}Zr_{0.2}Nb_{0.2})N$. Reprinted from Jin et al. [29]

3.6 Arc-Melting

The arc melting method involves the melting of the respective individual ceramics into a homogenized solution and later cooling to obtain homogenous high entropy ceramics. However, this method cannot be used for nitrides and other materials with high vapor pressure. As carbides and borides possess significantly lower vapor pressure, there are many studies involving these material classes. In [92], a quinary and four quaternary compositions of the (Hf, Ta, Ti, Zr, Cr)B_2 family, were obtained as single-phase compounds in all the compositions. However, the chromium-containing samples showed a decreased amount of chromium due to its relatively low melting point and high vapor pressure when compared to other borides.

For carbides, Ya et al. [62] used oxides and graphite as precursors to react them under DC arc discharge and subsequently used the resulting binary carbides to form a high entropy carbide solid solution through a further arc-melting step

In the case of Xia et al. [93], ball-milled binary carbides were directly arc melted to obtain the ceramic $(Nb_{0.25}Mo_{0.25}Ta_{0.25}W_{0.25})C$ and $(Nb_{0.2}Mo_{0.2}Ta_{0.2}W_{0.2}Hf_{0.2})C$.

3.7 High Pressure and High-Temperature Compaction/Sintering

Recently, the synthesis of high-entropy ceramics has also been realized through high-pressure high-temperature techniques. Guan et al. [14], [94], prepared the well-known $(Ti_{0.2}Zr_{0.2}Nb_{0.2}Ta_{0.2}Mo_{0.2})C$ and $(Hf_{0.2}Nb_{0.2}Ta_{0.2}Ti_{0.2}Zr_{0.2})C$ and phases by pressurizing the powder mixtures of the binary carbides to 5.5 GPa and simultaneously heating them to 1600-2000 °C, resulting in single-phase high entropy carbides.

Iwan et al. [97,99] synthesized $(Hf_{0.2}Ti_{0.2}Zr_{0.2}Ta_{0.2}Mo_{0.2})B_2$ via high-pressure high-temperature reactions (see Figure 12). The materials used were the oxides of the respective metals, i.e. HfO_2, TiO_2, ZrO_2, Ta_2O_5, and MoO_3, as well as slightly excess B_4C and C to diminish the retention of oxides at the synthesis conditions, compensating the loss of B and C as B_2O_3 and CO respectively. All powders were thoroughly milled before loading them into the high-pressure cell.

$(Hf_{0.2}Mo_{0.2}Nb_{0.2}Ta_{0.2}Ti_{0.2})B_2$ and $(Hf_{0.2}Mo_{0.2}Nb_{0.2}Ti_{0.2}Zr_{0.2})B_2$ were synthesized analogously, the setup is schematically shown in Figure 13.[97] The high entropy borides formed at a pressure of 0.9 GPa at temperatures above 1100 °C and were measured up to 9.5 GPa and 2000 °C (see Figure 14).

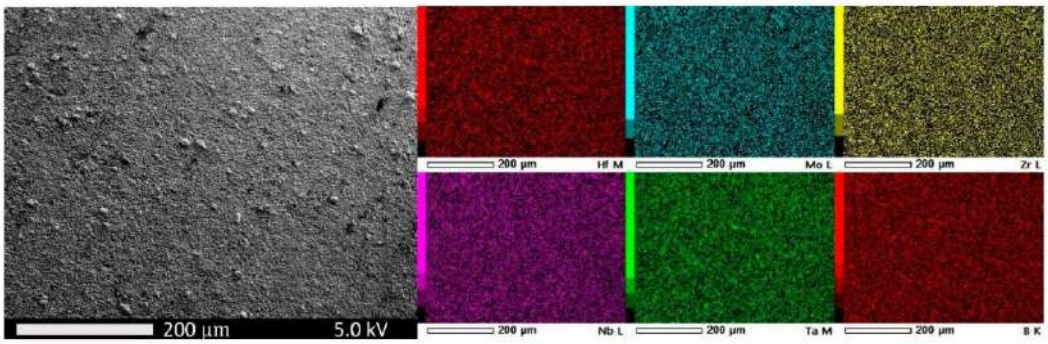

Figure 12. SEM micrographs of $(Hf_{0.2}Mo_{0.2}Zr_{0.2}Nb_{0.2}Ta_{0.2})B_2$. Reprinted from Iwan et el. [99]

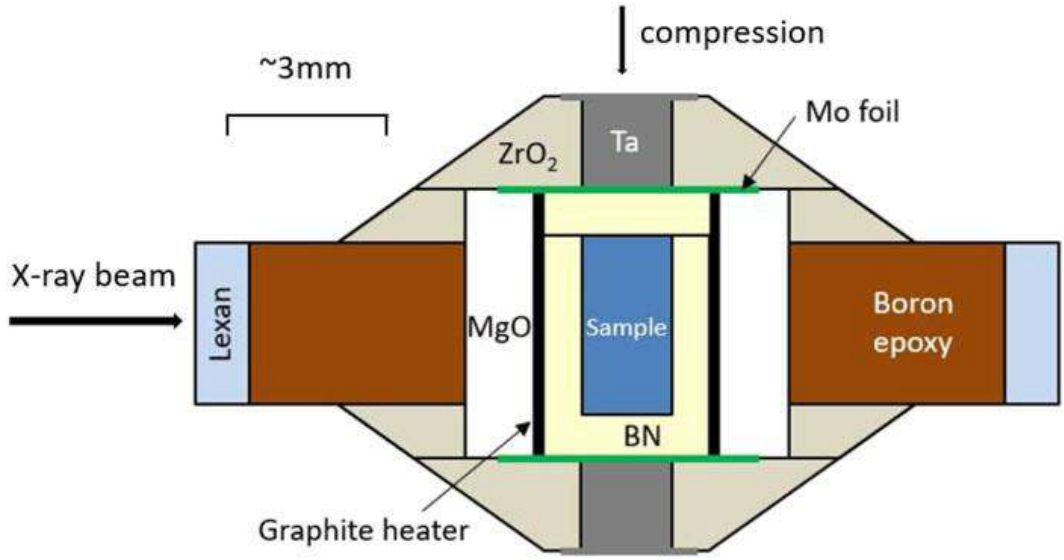

Figure 13. Schematic of a general HP-HT used by Iwan et al. up to 7.6 GPa and 1600 °C. [97]

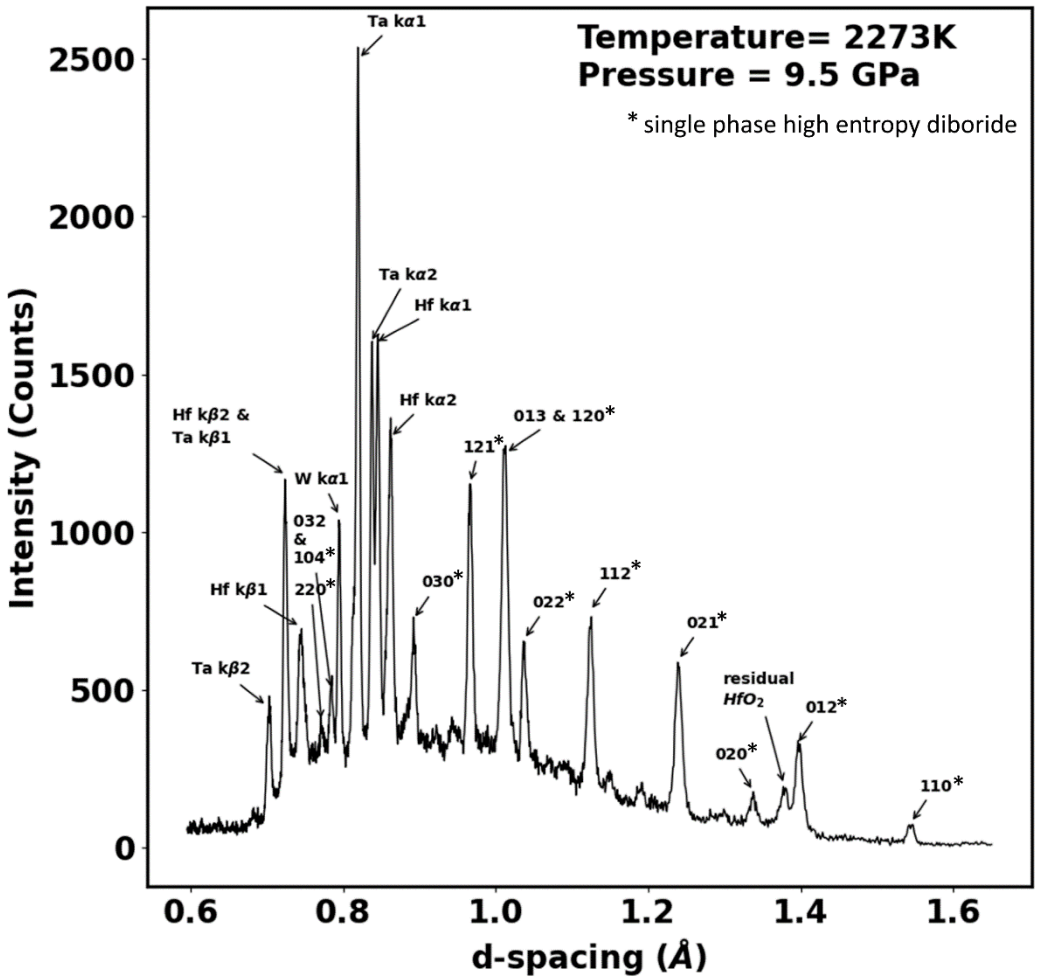

Figure 14. XRD of $(Hf_{0.2}Mo_{0.2}Nb_{0.2}Ta_{0.2}Ti_{0.2})B_2$. Reprinted from Iwan et el. [99].

All compositions up to date that were successfully synthesized as single phase including minor oxidic impurities are listed below in Table 1. The borides, especially diborides triggered the motivation of looking for UHTCs with improved ultrahigh temperature capability. The number of synthesized compositionally complex carbides is markedly high, indicating that their preparative access is less difficult- this possibly relies on their robust process (typically carbothermal reactions of oxides) as well as the high thermodynamic stability in this class of materials. The nitrogen fugacity in the materials at the temperatures of synthesis and processing results in difficulties during the preparations, due to which the number of synthesized carbonitrides and nitrides is less.

Table 1. Synthesized compositions of UHT-CCC and their crystal structures

Ceramic	Synthesized compositions	Crystal structure	Reference
Mono-borides	$(Cr_{0.2}Mo_{0.2}Nb_{0.2}\ V_{0.2}W_{0.2})B$	*Cmcm*	[2]
	$(Cr_{0.2}Mo_{0.2}Ni_{0.2}\ V_{0.2}W_{0.2})B$		[59]
	$(Cr_{0.2}\ Mo_{0.2}Nb_{0.2}Ta_{0.2}V_{0.2})B$		[2]
	$(Cr_{0.2}Mo_{0.2}Ta_{0.2}Ni_{0.2}W_{0.2})B$		[59],[60]
	$(Cr_{0.2}Nb_{0.2}Ta_{0.2}V_{0.2}W_{0.2})B$		[2]
	$(V_{0.2}Mo_{0.2}W_{0.2}Nb_{0.2}Ni_{0.2})B$		[59]
	$(V_{0.2}Cr_{0.2}Mo_{0.2}W_{0.2}Ti_{0.2})B$		[59]
	$(V_{0.2}Mo_{0.2}Ta_{0.2}Ni_{0.2}W_{0.2})B$		[59]
Di-borides	$(Hf_{0.333}Ti_{0.333}Zr_{0.333})B_2$	*P6/mmm*	[65]
	$(Cr_{0.25}Nb_{0.25}Ta_{0.25}Ti_{0.25})B_2$		[89]
	$(Hf_{0.25}Nb_{0.25}Ta_{0.25}Ti_{0.25})B_2$		[89]
	$(Hf_{0.25}Nb_{0.25}Ta_{0.25}Zr_{0.25})B_2$		[89]
	$(Hf_{0.25}Sc_{0.25}Ta_{0.25}Zr_{0.25})B_2$		[91]
	$(Hf_{0.25}Ti_{0.25}V_{0.25}Zr_{0.25})B_2$		[109]
	$(Hf_{0.25}Ti_{0.25}W_{0.25}Zr_{0.25})B_2$		[75]
	$(Nb_{0.25}Ta_{0.25}Ti_{0.25}Zr_{0.25})B_2$		[89]
	$(Hf_{0.25}Ta_{0.25}Ti_{0.25}Zr_{0.25})B_2$		[92]
	$(Cr_{0.25}Hf_{0.25}Ti_{0.25}Zr_{0.25})B_2$		[92]
	$(Cr_{0.25}Hf_{0.25}Ta_{0.25}Zr_{0.25})B_2$		[92]
	$(Cr_{0.25}Hf_{0.25}Ta_{0.25}Ti_{0.25})B_2$		[92]
	$(Cr_{0.25}Ta_{0.25}Ti_{0.25}Zr_{0.25})B_2$		[92]
	$(Hf_{0.28}Zr_{0.28}Ta_{0.28}W_{0.15})B_2$		[103]
	$(Cr_{0.2}Hf_{0.2}Mo_{0.2}Nb_{0.2}Ta_{0.2})B_2$		[63]
	$(Cr_{0.2}Hf_{0.2}Ta_{0.2}Ti_{0.2}Zr_{0.2})B_2$		[74],[92]
	$(Cr_{0.2}Mo_{0.2}Ta_{0.2}Ti_{0.2}W_{0.2})B_2$		[74]
	$(Er_{0.2}Hf_{0.2}Ta_{0.2}Ti_{0.2}Zr_{0.2})B_2$		[108]
	$(Hf_{0.2}Mo_{0.2}Nb_{0.2}Ta_{0.2}Ti_{0.2})B_2$		[7],[77],[99]
	$(Hf_{0.2}Mo_{0.2}Nb_{0.2}Ti_{0.2}Zr_{0.2})B_2$		[77]
	$(Hf_{0.2}Mo_{0.2}Nb_{0.2}Ta_{0.2}Zr_{0.2})B_2$		[99]
	$(Hf_{0.2}Mo_{0.2}Ta_{0.2}Ti_{0.2}Zr_{0.2})B_2$		[77],[97]
	$(Hf_{0.2}Mo_{0.2}Ti_{0.2}W_{0.2}Zr_{0.2})B_2$		[74]
	$(Hf_{0.2}Nb_{0.2}Ta_{0.2}Ti_{0.2}Zr_{0.2})B_2$		[77]
	$(Hf_{0.2}Nb_{0.2}Ta_{0.2}V_{0.2}Zr_{0.2})B_2$		[10]
	$(Hf_{0.2}Nb_{0.2}Ta_{0.2}W_{0.2}Zr_{0.2})B_2$		[74]
	$(Mo_{0.2}Nb_{0.2}Ta_{0.2}Ti_{0.2}Zr_{0.2})B_2$		[77]
	$(Zr_{0.225}Hf_{0.225}Ta_{0.225}Mo_{0.225}W_{0.1})B_2$		[74]
Tetra-borides	$(Y_{0.17}Nd_{0.18}Sm_{0.21}Gd_{0.22}Er_{0.22})B_4$	*P4/mbm*	[72]
	$(Y_{0.21}Sm_{0.19}Gd_{0.21}Er_{0.18}Yb_{0.21})B_4$		[72]
	$(Y_{0.22}La_{0.18}Pr_{0.20}Dy_{0.23}Er_{0.17})B_4$		[72]
	$(Y_{0.22}Nd_{0.18}Gd_{0.20}Dy_{0.21}Er_{0.19})B_4$		[72]
	$Y_{0.22}Nd_{0.20}Sm_{0.20}Gd_{0.19}Tb_{0.19})B_4$		[72]
	$(Nd_{0.18}Sm_{0.19}Gd_{0.23}Tb_{0.21}Yb_{0.19})B_4$		[72]
Hexa-borides	$(Y_{0.23}Nd_{0.21}Sm_{0.20}Gd_{0.18}Yb_{0.18})B_6$	*Pm-3m*	[8]
	$(Y_{0.19}La_{0.19}Pr_{0.22}Dy_{0.19}Yb_{0.21})B_6$		[8]
	$(La_{0.19}Nd_{0.21}Sm_{0.23}Gd_{0.19}Yb_{0.18})B_6$		[8]
	$(Y_{0.22}La_{0.20}Nd_{0.19}Sm_{0.22}Gd_{0.17})B_6$		[8]
	$(Y_{0.21}La_{0.17}Nd_{0.18}Sm_{0.21}Tb_{0.23})B_6$		[8]
	$(La_{0.18}Pr_{0.21}Nd_{0.19}Sm_{0.21}Tb_{0.21})B_6$		[8]

Ceramic	Synthesized compositions	Crystal structure	Reference
M_3B_4	$(V_{0.2}Cr_{0.2}Nb_{0.2}Mo_{0.2}Ta_{0.2})_3B_4$	*Immm*	[71]
	$(V_{0.2}Cr_{0.2}Nb_{0.2}Ta_{0.2}W_{0.2})_3B_4$		[71]
Dodeca-borides	$(Dy_{0.166}Ho_{0.166}Er_{0.166}Tm_{0.166}Lu_{0.166}Hf_x)B_{12}$	*Fm*-3*m*(UB_{12})	[100]
	$(Dy_{0.2}Ho_{0.2}Er_{0.2}Tm_{0.2}Lu_{0.2})B_{12}$		[101]
Carbides	$(Hf_{0.333}Ti_{0.333}Zr_{0.333})C$		[105]
	$(Nb_{0.333}Ta_{0.333}Zr_{0.333})C$		[95],[106]
	$(Ta_{0.333}Ti_{0.333}Zr_{0.333})C$		[86]
	$(Hf_{0.25}Nb_{0.25}Ta_{0.25}Zr_{0.25})C$		[39],[47]
	$(Hf_{0.25}Ta_{0.25}Ti_{0.25}Zr_{0.25})C$		[44]
	$(Mo_{0.25}Nb_{0.25}Ta_{0.25}W_{0.25})C$		[93]
	$(Nb_{0.25}Ta_{0.25}Ti_{0.25}\ Zr_{0.25})\ C$		[13],[57],[85],[96]
	$(Nb_{0.25}\ Ta_{0.25}Ti_{0.25}V_{0.25})C$		[24],[64]
	$(Nb_{0.25}Ti_{0.25}V_{0.25}Zr_{0.25})C$		[80]
	$(Ce_{0.2}Hf_{0.2}La_{0.2}Ti_{0.2}Zr_{0.2})C$		[90]
	$(Cr_{0.2}Nb_{0.2}Ta_{0.2}Ti_{0.2}V_{0.2})C$		[43]
	$(Cr_{0.2}Nb_{0.2}Ta_{0.2}Ti_{0.2}Zr_{0.2})C$		[43]
	$(Cr_{0.2}Nb_{0.2}Ti_{0.2}V_{0.2}Zr_{0.2})C$		[43]
	$(Hf_{0.2}Mo_{0.2}Nb_{0.2}Ta_{0.2}Ti_{0.2})C$		[41]
	$(Hf_{0.2}Mo_{0.2}Nb_{0.2}Ta_{0.2}W_{0.2})C$		[93]
	$(Hf_{0.2}Mo_{0.2}Ta_{0.2}Ti_{0.2}Zr_{0.2})C$		[41]
	$(Hf_{0.2}Nb_{0.2}Ta_{0.2}Ti_{0.2}V_{0.2})C$	*Fm*-3*m*	[26],[30]
	$(Hf_{0.2}Nb_{0.2}Ta_{0.2}Ti_{0.2}W_{0.2})C$		[41]
	$(Hf_{0.2}Nb_{0.2}Ta_{0.2}Ti_{0.2}Zr_{0.2})C$		[30],[57]
	$(Hf_{0.2}Nb_{0.2}Ta_{0.2}V_{0.2}Zr_{0.2})C$		[26]
	$(Hf_{0.2}Nb_{0.2}Ti_{0.2}V_{0.2}Zr_{0.2})C$		[26]
	$(Hf_{0.2}Ta_{0.2}Ti_{0.2}V_{0.2}Zr_{0.2})C$		[26]
	$(Hf_{0.2}Ta_{0.2}Ti_{0.2}W_{0.2}Zr_{0.2})C$		[30]
	$(Mo_{0.2}Nb_{0.2}Ta_{0.2}Ti_{0.2}V_{0.2})C$		[41]
	$(Mo_{0.2}Nb_{0.2}Ta_{0.2}Ti_{0.2}Zr_{0.2})C$		[57]
	$(Mo_{0.2}Nb_{0.2}Ta_{0.2}V_{0.2}W_{0.2})C$		[30],[45]
	$(Nb_{0.2}Ta_{0.2}Ti_{0.2}V_{0.2}W_{0.2})C$		[30]
	$(Nb_{0.2}Ta_{0.2}Ti_{0.2}V_{0.2}Zr_{0.2})C$		[30]
	$(Nb_{0.2}Ta_{0.2}Ti_{0.2}W_{0.2}Zr_{0.2})C$		[96]
	$(Zr_{0.196}Hf_{0.02}V_{0.196}Nb_{0.196}Mo_{0.196}W_{0.196})C_x$		[110]
	$(Cr_{0.16}Nb_{0.16}Ta_{0.16}Ti_{0.16}V_{0.16}Zr_{0.16})C$		[43]
	$(Hf_{0.16}Nb_{0.16}Ta_{0.16}Ti_{0.16}W_{0.16}Zr_{0.16})C$		[96]
	$(Ti_{0.16}Zr_{0.16}Hf_{0.16}Nb_{0.16}Ta_{0.16}Mo_{0.16})C$		[19]
	$(Cr_{0.143}\ Mo_{0.143}\ Nb_{0.143}Ta_{0.143}Ti_{0.143}V_{0.143}\ Zr_{0.143})C$		[43]
	$(Hf_{0.143}Nb_{0.143}Ta_{0.143}Ti_{0.143}V_{0.143}W_{0.143}Zr0_{.143})C$		[96]
	$(Cr_{0.125}\ Mo_{0.125}Nb_{0.125}Ta_{0.125}\ Ti_{0.125}V_{0.125}W_{0.125}\ Zr_{0.125})C$		[43]
	$(Hf_{0.125}Mo_{0.125}Nb_{0.125}Ta_{0.125}Ti_{0.125}V_{0.125}W_{0.125}Zr_{0.125})C$		[96]
	$(Ti_{0.11}\ Zr_{0.11}\ Hf_{0.11}\ V_{0.11}\ Nb_{0.11}\ Ta_{0.11}\ Cr_{0.11}\ Mo_{0.11}W_{0.11})C$		[111]

Ceramic	Synthesized compositions	Crystal structure	Reference
(Carbo)-nitrides	$(Ti_{0.333}Zr_{0.333}Hf_{0.333})CN$	*Fm*-3*m*	[102]
	$(Ti_{0.25}Zr_{0.25}Hf_{0.25}Nb_{0.25})CN$		[102]
	$(Hf_{0.2}Nb_{0.2}Ta_{0.2}Ti_{0.2}Zr_{0.2})N$		[50]
	$(Cr_{0.2}Mo_{0.2}Ta_{0.2}V_{0.2}W_{0.2})CN$		[16]
	$(Cr_{0.2}Hf_{0.2}Ta_{0.2}Nb_{0.2}Ti_{0.2})CN$		[16]
	$(Cr_{0.2}Nb_{0.2}Ta_{0.2}Ti_{0.2}V_{0.2})CN$		[16]
	$(V_{0.2}Nb_{0.2}Cr_{0.2}Mo_{0.2}Zr_{0.2})N$		[29]
	$(Cr_{0.2}Nb_{0.2}Ti_{0.2}Ta_{0.2}V_{0.2})N$		[16]
	$(Cr_{0.2}Hf_{0.2}Nb_{0.2}Ta_{0.2}Ti_{0.2})N$		[16]
	$(Hf_{0.2}Ta_{0.2}Nb_{0.2}Zr_{0.2}V_{0.2})N$		[69]
	$(Ti_{0.2}Zr_{0.2}Hf_{0.2}Nb_{0.2}Ta_{0.2})$ CN		[102]
	$(Ti_{0.25}W_{0.25}V_{0.25}Ta_{0.25})N$		[107]
Silicides	$(V_{0.2}Cr_{0.2}Nb_{0.2}Ta_{0.2}W_{0.2})_5Si_3$	*P*6$_3$/*mcm*	[87]
	$(Ti_{0.2}Zr_{0.2}Nb_{0.2}Mo_{0.2}Hf_{0.2})_5Si_3$		[87]
	$(Cr_{0.2}Mo_{0.2}Ta_{0.2}V_{0.2}Nb_{0.2})Si_2$	*P*6$_2$22	[61]
	$(Mo_{0.2}Nb_{0.2}Ta_{0.2}Ti_{0.2}Zr_{0.2})Si_2$		[61]
	$(Ti_{0.2}Zr_{0.2}Nb_{0.2}Mo_{0.2}W_{0.2})Si_2$		[61]
	$(Mo_{0.2}Nb_{0.2}Ta_{0.2}Ti_{0.2}W_{0.2})Si_2$		[61]
	$(Mo_{0.2}W_{0.2}Cr_{0.2}Ta_{0.2}Nb_{0.2})Si_2$		[61]
	$(Nb_{0.25}Ta_{0.25}Hf_{0.25}Ti_{0.25})Si_2$		[88]
Boro-carbo-nitrides	$(Ta_{0.2}Nb_{0.2}Zr_{0.2}Hf_{0.2}W_{0.2})BCN$	*Fm*-3*m*	[18]
	$(Ta_{0.2}Nb_{0.2}Zr_{0.2}Hf_{0.2}Ti_{0.2})BCN$		[18]
	$(Ta_{0.2}Nb_{0.2}Zr_{0.2}Ti_{0.2}W_{0.2})BCN$		[18]

4. Conclusion

Recent studies on the various synthesis techniques have aroused an interest in the UHTC area. The UHTCs in combination with compositional complexity have been proven to be high-potential candidates for applications involving extreme conditions. The thermodynamics of high entropy ceramics is not yet completely understood; however, many computational predictions and approaches are being performed to understand the behavior of the compositionally complex ceramics. All compositionally complex UHTCs consist of borides, carbides, nitrides, carbonitrides, and silicides. These were usually synthesized either as bulk samples or as powders depending on the used synthesis route. In the case of powders, mechanochemical methods such as ball milling, self-propagation high temperature, molten salt-assisted reductions, boro/carbothermal reductions, and sol-gel were used. To ensure homogenous reactions, usually mechanochemically milled samples were preferred for further process except for molten salt assisted. So far, the only compositions synthesized at room temperature are $(Ta_{0.2}Nb_{0.2}Zr_{0.2}Hf_{0.2}W_{0.2})BCN$, $(Ta_{0.2}Nb_{0.2}Zr_{0.2}Hf_{0.2}Ti_{0.2})BCN$, and $(Ta_{0.2}Nb_{0.2}Zr_{0.2}Ti_{0.2}W_{0.2})BCN$, those were prepared using a ball milling approach. Most of the carbides, nitrides, and silicides were prepared by employing spark plasma sintering as dense monoliths. Sol-gel methods have resulted in obtaining borides, carbides, and nitrides as powders which in turn can be used as prerequisites for spark plasma sintering or hot pressing to obtain dense samples.

In the case of borides, various borides have been synthesized such as mono, di, tetra, hexa, dodeca borides and M_3B_4. These borides were obtained as single-phase compounds during densification. The trend in the properties caused by the anisotropy in the crystal structure suggested to consider the lattice mismatch over atomic size mismatch for the determination of the deviation parameter δ.

In the case of carbides, the reactions were straightforward with carbothermal reductions either as powders or reactive densification. Also, the sintering of mixtures of binary carbides was also performed to obtain a dense sample. The nitrides proved to be a problem due to the intrinsically high

N_2 fugacity of nitrogen. This problem can be overcome by the sol-gel process. Although borides and carbides were also synthesized by using high-pressure high-temperature techniques, due to the air-tight conditions, the above process seems like a viable alternative for the nitrides.

Although significant work has been performed in the field of synthesis of compositionally complex UHTCs, most of the literature can be found on borides and carbides, with less focus on nitrides and silicides. The mechanical properties such as elastic moduli, density, and hardness were measured, but the other properties such as fracture toughness and high-temperature properties are yet to be investigated.

Acknowledgments

DTT gratefully acknowledges funding from the German Academic Exchange Service (Deutscher Akademischer Austauschdienst, DAAD) in the form of a doctoral fellowship grant. The authors acknowledge furthermore funding from DAAD within the frame of the Programs for Project-Related Personal Exchange (PPP, project no. 57601381, “Compositionally Complex Metal Carbides and Carbonitrides”). Also, SAK and EI received funding from the German Research Foundation (Deutsche Forschungsgemeinschaft, DFG) within the Research Training Group RTG 2561 (project no. 413956820, “Materials Compounds from Composite Materials”).

5. References

[1] H. Chen, H. Xiang, F.Z. Dai, J. Liu, Y. Zhou, Porous high entropy (Zr0.2Hf0.2Ti0.2Nb0.2Ta0.2)B2: A novel strategy towards making ultrahigh temperature ceramics thermal insulating, *J. Mater. Sci. Technol. 35* (2019) 2404–2408. https://doi.org/10.1016/j.jmst.2019.05.059.

[2] M. Qin, Q. Yan, H. Wang, C. Hu, K.S. Vecchio, J. Luo, High-entropy monoborides: Towards super hard materials, *Scr. Mater. 189* (2020) 101–105. https://doi.org/10.1016/j.scriptamat.2020.08.018.

[3] Y. Zhang, Z. Bin Jiang, S.K. Sun, W.M. Guo, Q.S. Chen, J.X. Qiu, K. Plucknett, H.T. Lin, Microstructure and mechanical properties of high-entropy borides derived from boro/carbothermal reduction, *J. Eur. Ceram. Soc. 39* (2019) 3920–3924. https://doi.org/10.1016/j.jeurceramsoc.2019.05.017.

[4] Z.Q. Linjing Qiao, Yi Liu, Yu Gao, Jianqiang Bi, Yonghan Li, Chen Liu, Jian Gao, Weili Wang, First-principles prediction, fabrication and characterization of (Hf0.2Nb0.2Ta0.2Ti0.2Zr0.2)B2 high-entropy borides, *Ceram. Int. 48* (2022) 17234–17245. https://doi.org/10.1016/j.ceramint.2022.02.281.

[5] F. Monteverde, F. Saraga, M. Gaboardi, J.R. Plaisier, Compositional pathways and anisotropic thermal expansion of high-entropy transition metal diborides, *J. Eur. Ceram. Soc. 41* (2021) 6255–6266. https://doi.org/10.1016/j.jeurceramsoc.2021.05.053.

[6] M. Li, X. Zhao, G. Shao, H. Wang, J. Zhu, W. Liu, B. Fan, H. Xu, H. Lu, Y. Zhou, R. Zhang, Oscillatory pressure sintering of high entropy (Zr0.2Ta0.2Nb0.2Hf0.2Mo0.2)B2 ceramic, *Ceram. Int. 47* (2021) 8707–8710. https://doi.org/10.1016/j.ceramint.2020.11.108.

[7] G. Tallarita, R. Licheri, S. Garroni, R. Orrù, G. Cao, Novel processing route for the fabrication of bulk high-entropy metal diborides, *Scr. Mater. 158* (2019) 100–104. https://doi.org/10.1016/j.scriptamat.2018.08.039.

[8] M. Qin, Q. Yan, Y. Liu, H. Wang, C. Wang, T. Lei, K.S. Vecchio, H.L. Xin, T.J. Rupert, J. Luo, Bulk high-entropy hexaborides, *J. Eur. Ceram. Soc. 41* (2021) 5775–5781. https://doi.org/10.1016/j.jeurceramsoc.2021.05.027.

[9] L. Qiao, Y. Liu, Y. Gao, J. Bi, Y. Li, C. Liu, J. Gao, W. Wang, Z. Qian, First-principles prediction, fabrication and characterization of (Hf0.2Nb0.2Ta0.2Ti0.2Zr0.2)B2 high-entropy borides, *Ceram. Int. 48* (2022) 17234–17245. https://doi.org/10.1016/j.ceramint.2022.02.281.

[10] Y. Yang, J. Bi, K. Sun, L. Qiao, Y. Liu, Y. Li, H. Wang, Y. Liang, M. Shang, Novel (Hf0.2Zr0.2Ta0.2V0.2Nb0.2)B2 high entropy diborides with superb hardness sintered by SPS under a mild condition, *Ceram. Int. 48* (2022) 30859–30867. https://doi.org/10.1016/j.ceramint.2022.07.040.

[11] X.F. Wei, J.X. Liu, F. Li, Y. Qin, Y.C. Liang, G.J. Zhang, High entropy carbide ceramics from different starting materials, *J. Eur. Ceram. Soc. 39* (2019) 2989–2994. https://doi.org/10.1016/j.jeurceramsoc.2019.04.006.

[12] Y. Zhang, W.M. Guo, Z. Bin Jiang, Q.Q. Zhu, S.K. Sun, Y. You, K. Plucknett, H.T. Lin, Dense high-entropy boride ceramics with ultra-high hardness, *Scr. Mater. 164* (2019) 135–139. https://doi.org/10.1016/j.scriptamat.2019.01.021.

[13] F. Wang, X. Yan, T. Wang, Y. Wu, L. Shao, M. Nastasi, Y. Lu, B. Cui, Irradiation damage in (Zr0.25Ta0.25Nb0.25Ti0.25)C high-entropy carbide ceramics, *Acta Mater. 195* (2020) 739–749. https://doi.org/10.1016/j.actamat.2020.06.011.

[14] S. Guan, H. Liang, Q. Wang, L. Tan, F. Peng, Synthesis and Phase Stability of the High-Entropy Carbide (Ti0.2Zr0.2Nb0.2Ta0.2Mo0.2)C under Extreme Conditions, *Inorg. Chem. 60* (2021) 3807–3813. https://doi.org/10.1021/acs.inorgchem.0c03319.

[15] E.W. Neuman, G.E. Hilmas, W.G. Fahrenholtz, Transition metal diboride-silicon carbide-boron carbide ceramics with super-high hardness and strength, *J. Eur. Ceram. Soc. 42* (2022) 6795–6801. https://doi.org/10.1016/j.jeurceramsoc.2022.08.019.

[16] O.F. Dippo, N. Mesgarzadeh, T.J. Harrington, G.D. Schrader, K.S. Vecchio, Bulk high-entropy nitrides and carbonitrides, *Sci. Rep. 10* (2020) 21288. https://doi.org/10.1038/s41598-020-78175-8.

[17] Y.C. Lin, S.Y. Hsu, Y.T. Lai, P.H. Kuo, S.Y. Tsai, J.G. Duh, Effect of the N2/(Ar+N2) ratio

on mechanical properties of high entropy nitride (Cr0.35Al0.25Nb0.12Si0.08V0.20)Nx films, *Mater. Chem.* Phys. *274* (2021) 125195. https://doi.org/10.1016/j.matchemphys.2021.125195.

[18] J. Guan, D. Li, Z. Yang, B. Wang, D. Cai, X. Duan, P. He, D. Jia, Y. Zhou, Synthesis and thermal stability of novel high-entropy metal boron carbonitride ceramic powders, *Ceram. Int. 46* (2020) 26581–26589. https://doi.org/10.1016/j.ceramint.2020.07.126.

[19] W. Zhang, L. Chen, C. Xu, W. Lu, Y. Wang, J. Ouyang, Y. Zhou, Densification, microstructure and mechanical properties of multicomponent (TiZrHfNbTaMo)C ceramic prepared by pressureless sintering, *J. Mater. Sci. Technol. 72* (2021) 23–28. https://doi.org/10.1016/j.jmst.2020.07.019.

[20] Z. Peng, W. Sun, X. Xiong, H. Zhang, F. Guo, J. Li, Novel refractory high-entropy ceramics: Transition metal carbonitrides with superior ablation resistance, *Corros. Sci. 184* (2021) 109359. https://doi.org/10.1016/j.corsci.2021.109359.

[21] B. Ye, T. Wen, D. Liu, Y. Chu, Oxidation behavior of (Hf 0.2 Zr 0.2 Ta 0.2 Nb 0.2 Ti 0.2)C high-entropy ceramics at 1073-1473 K in air, *Corros. Sci. 153* (2019) 327–332. https://doi.org/10.1016/j.corsci.2019.04.001.

[22] E. Ionescu, S. Bernard, R. Lucas, P. Kroll, S. Ushakov, A. Navrotsky, R. Riedel, Polymer-Derived Ultra-High Temperature Ceramics (UHTCs) and Related Materials, *Adv. Eng. Mater. 21* (2019) 1–24. https://doi.org/10.1002/adem.201900269.

[23] P. Šolcová, M. Nižňanský, J. Schulz, P. Brázda, P. Ecorchard, M. Vilémová, V. Tyrpekl, Preparation of High-Entropy (Ti, Zr, Hf, Ta, Nb) Carbide Powder via Solution Chemistry, *Inorg. Chem. 60* (2021) 7617–7621. https://doi.org/10.1021/acs.inorgchem.1c00776.

[24] Q. Zhao, J. Mei, W. Jin, Q. Jiang, A novel approach to the rapid synthesis of high-entropy carbide nanoparticles, *J. Am. Ceram. Soc. 103* (2020) 4733–4737. https://doi.org/10.1111/jace.17173.

[25] R. Adalati, M. Sharma, S. Sharma, A. Kumar, G. Malik, R. Boukherroub, R. Chandra, Metal nitrides as efficient electrode material for supercapacitors*: A review, J. Energy Storage. 56* (2022) 105912. https://doi.org/10.1016/j.est.2022.105912.

[26] E. Chicardi, C. García-Garrido, J. Hernández-Saz, F.J. Gotor, Synthesis of all equiatomic five-transition metals High Entropy Carbides of the IVB (Ti, Zr, Hf) and VB (V, Nb, Ta) groups by a low-temperature route, *Ceram. Int. 46* (2020) 21421–21430. https://doi.org/10.1016/j.ceramint.2020.05.240.

[27] T. Stasiak, P. Souček, V. Buršíková, N. Koutná, Z. Czigány, K. Balázsi, P. Vašina, Synthesis and characterization of the ceramic refractory metal high entropy nitride thin films from Cr-Hf-Mo-Ta-W system, *Surf. Coatings Technol. 449* (2022). https://doi.org/10.1016/j.surfcoat.2022.128987.

[28] T.H. Hsieh, C.H. Hsu, C.Y. Wu, J.Y. Kao, C.Y. Hsu, Effects of deposition parameters on the structure and mechanical properties of high-entropy alloy nitride films, *Curr. Appl. Phys. 18* (2018) 512–518. https://doi.org/10.1016/j.cap.2018.02.015.

[29] T. Jin, X. Sang, R.R. Unocic, R.T. Kinch, X. Liu, J. Hu, H. Liu, S. Dai, Mechanochemical-Assisted Synthesis of High-Entropy Metal Nitride via a Soft Urea Strategy, *Adv. Mater. 30* (2018) 1–5. https://doi.org/10.1002/adma.201707512.

[30] P. Sarker, T. Harrington, C. Toher, C. Oses, M. Samiee, J.P. Maria, D.W. Brenner, K.S. Vecchio, S. Curtarolo, High-entropy high-hardness metal carbides discovered by entropy descriptors, *Nat. Commun. 9* (2018) 1–10. https://doi.org/10.1038/s41467-018-07160-7.

[31] F. Li, Y. Lu, X.G. Wang, W. Bao, J.X. Liu, F. Xu, G.J. Zhang, Liquid precursor-derived high-entropy carbide nanopowders, *Ceram. Int. 45* (2019) 22437–22441. https://doi.org/10.1016/j.ceramint.2019.07.244.

[32] S.Y. Hsu, Y.T. Lai, S.Y. Chang, S.Y. Tsai, J.G. Duh, Combinatorial synthesis of reactively co-sputtered high entropy nitride (HfNbTiVZr)N coatings: Microstructure and mechanical properties, *Surf. Coatings Technol. 442* (2022) 128564. https://doi.org/10.1016/j.surfcoat.2022.128564.

[33] A. V. Pshyk, A. Vasylenko, B. Bakhit, L. Hultman, P. Schweizer, T.E.J. Edwards, J. Michler, G. Greczynski, High-entropy transition metal nitride thin films alloyed with Al: Microstructure, phase composition and mechanical properties, *Mater. Des. 219* (2022) 110798. https://doi.org/10.1016/j.matdes.2022.110798.

[34] J. Gild, J. Braun, K. Kaufmann, E. Marin, T. Harrington, P. Hopkins, K. Vecchio, J. Luo, A high-entropy silicide: (Mo0.2Nb0.2Ta0.2Ti0.2W0.2)Si2, *J. Mater. 5* (2019) 337–343. https://doi.org/10.1016/j.jmat.2019.03.002.

[35] L. Feng, W.G. Fahrenholtz, G.E. Hilmas, Y. Zhou, Synthesis of single-phase high-entropy carbide powders, *Scr. Mater. 162* (2019) 90–93. https://doi.org/10.1016/j.scriptamat.2018.10.049.

[36] K. Wang, L. Chen, C. Xu, W. Zhang, Z. Liu, Y. Wang, J. Ouyang, X. Zhang, Y. Fu, Y. Zhou, Microstructure and mechanical properties of (TiZrNbTaMo)C high-entropy ceramic, *J. Mater. Sci. Technol. 39* (2020) 99–105. https://doi.org/10.1016/j.jmst.2019.07.056.

[37] Y. Wu, J. Xiong, Z. Guo, M. Yang, J. Chen, S. Xiong, H. Fan, J. Luo, Microstructure and fracture toughness of Ti (C 0 . 7 N 0 . 3) -WC-Ni cermets, *Int. Journal of Refractory Metals and Hard Materials. 29* (2011) 85–89. http://dx.doi.org/10.1016/j.ijrmhm.2010.08.004.

[38] Z. Anwer, S. Huang, J. Vleugels, Liquid phase assisted synthesis of (Ti, V, Nb, Ta, W)C-Ni high entropy carbide cermets by conventional pressureless sintering, *Int. J. Refract. Met. Hard Mater. 107* (2022) 105914. https://doi.org/10.1016/j.ijrmhm.2022.105914.

[39] J. Song, G. Chen, H. Xiang, F. Dai, S. Dong, W. Han, X. Zhang, Y. Zhou, Regulating the formation ability and mechanical properties of high-entropy transition metal carbides by carbon stoichiometry, *J. Mater. Sci. Technol. 121* (2022) 181 189.https://doi.org/10.1016/j.jmst.2021.12.063.

[40] E. Chicardi, C. García-Garrido, F.J. Gotor, Low temperature synthesis of an equiatomic (TiZrHfVNb)C5 high entropy carbide by a mechanically-induced carbon diffusion route, *Ceram. Int. 45* (2019) 21858–21863. https://doi.org/10.1016/j.ceramint.2019.07.195.

[41] T.J. Harrington, J. Gild, P. Sarker, C. Toher, C.M. Rost, O.F. Dippo, C. McElfresh, K.Kaufmann, E. Marin, L. Borowski, P.E. Hopkins, J. Luo, S. Curtarolo, D.W. Brenner, K.S. Vecchio, Phase stability and mechanical properties of novel high entropy transition metal carbides, *Acta Mater. 166* (2019) 271–280. https://doi.org/10.1016/j.actamat.2018.12.054.

[42] J. Zhou, J. Zhang, F. Zhang, B. Niu, L. Lei, W. Wang, High-entropy carbide*:* A novel class of multicomponent ceramics, *Ceram. Int. 44* (2018) 22014–22018. https://doi.org/10.1016/j.ceramint.2018.08.100.

[43] H.R. Mao, E.T. Dong, S.B. Jin, X.M. Qiu, P. Shen, Ultrafast high-temperature synthesis and densification of high-entropy carbides, *J. Eur. Ceram. Soc. 42* (2022) 4053–4065.https://doi.org/10.1016/J.JEURCERAMSOC.2022.03.054.

[44] E. Castle, T. Csanádi, S. Grasso, J. Dusza, M. Reece, Processing and Properties of High-Entropy Ultra-High Temperature Carbides, *Sci. Rep. 8* (2018) 1–12. https://doi.org/10.1038/s41598-018-26827-1.

[45] D. Liu, Y. Hou, A. Zhang, J. Han, J. Zhang, J. Meng, H. Su, Experimental studies on critical compositions for fabricating single-phase high entropy carbides based on the calculated phase diagram of (VNbTaMoW)0.5Cx (0 < x < 0.6), *J. Eur. Ceram. Soc. 41* (2021) 7488–7497. https://doi.org/10.1016/j.jeurceramsoc.2021.08.037.

[46] Y. Wang, B. Zhang, C. Zhang, J. Yin, M.J. Reece, Ablation behaviour of (Hf-Ta-Zr-Nb)C high entropy carbide ceramic at temperatures above 2,100 °C, *J. Mater. Sci. Technol. 113* (2022) 40–47. https://doi.org/10.1016/j.jmst.2021.09.064.

[47] J. Dusza, P. Švec, V. Girman, R. Sedlák, E.G. Castle, T. Csanádi, A. Kovalčíková, M.J.Reece, Microstructure of (Hf-Ta-Zr-Nb)C high-entropy carbide at micro and nano/atomic level, *J.Eur. Ceram. Soc. 38* (2018) 4303–4307. https://doi.org/10.1016/j.jeurceramsoc.2018.05.006.

[48] C. Zhang, X. Lu, C. Wang, X. Sui, Y. Wang, H. Zhou, J. Hao, Tailoring the microstructure, mechanical and tribocorrosion performance of (CrNbTiAlV)Nx high-entropy nitride films by controlling nitrogen flow, *J. Mater. Sci. Technol. 107* (2022) 172–182.https://doi.org/10.1016/j.jmst.2021.08.032.

[49] J. Li, Y. Chen, Y. Zhao, X. Shi, S. wang, S. Zhang, Super-hard (MoSiTiVZr)Nx high-entropy nitride coatings, *J. Alloys Compd. 926 (2022) 166807*. https://doi.org/10.1016/j.jallcom.2022.166807.

[50] D. Moskovskikh, S. Vorotilo, V. Buinevich, A. Sedegov, K. Kuskov, A. Khort, C. Shuck, M. Zhukovskyi, A. Mukasyan, Extremely hard and tough high entropy nitride ceramics, *Sci. Rep.*

10 (2020) 19874. https://doi.org/10.1038/s41598-020-76945-y.

[51] A. Kretschmer, D. Holec, K. Yalamanchili, H. Rudigier, M. Hans, J.M. Schneider, P.H. Mayrhofer, Strain-stabilized Al-containing high-entropy sublattice nitrides, *Acta Mater. 224*(2022) 117483. https://doi.org/10.1016/j.actamat.2021.117483.

[52] H. Liu, B. Du, Y. Chu, Synthesis of the ternary metal carbide solid-solution ceramics by polymer-derived-ceramic route, *J. Am. Ceram. Soc. 103* (2020) 2970–2974. https://doi.org/10.1111/jace.16993.

[53] A.L. Tomas-Garcia, Q. Li, J.O. Jensen, N.J. Bjerrum, High surface area tungsten carbides: Synthesis, characterization and catalytic activity towards the hydrogen evolution reaction in phosphoric acid at elevated temperatures, *Int. J. Electrochem. Sci. 9* (2014) 1016–1032.

[54] D. Liu, A. Zhang, J. Jia, J. Meng, B. Su, Phase evolution and properties of (VNbTaMoW)C high entropy carbide prepared by reaction synthesis, *J. Eur. Ceram. Soc. 40* (2020) 2746–2751. https://doi.org/10.1016/j.jeurceramsoc.2020.03.020.

[55] A. Sedegov, S. Vorotilo, V. Tsybulin, K. Kuskov, D. Moscovskikh, Synthesis and study of high-entropy ceramics based on the carbides of refractory metals, *IOP Conf. Ser. Mater. Sci. Eng. 558* (2019). https://doi.org/10.1088/1757-899X/558/1/012043.

[56] B. Du, H. Liu, Y. Chu, Fabrication and characterization of polymer-derived high-entropy carbide ceramic powders, *J. Am. Ceram. Soc. 103* (2020) 4063–4068.https://doi.org/10.1111/jace.17134.

[57] Liu, H. L., Feng-Zhen, D. A. N. G., De-Wei, N. I., Chang-Qing, L. I. U., Yun-Long, X. U. E.,& Yuan-Ting, W. U, Preparation of Single-phase High Entropy Carbides by a Modified Citric Acid Complexing Method (2021).

[58] F. William G, G.E. Hilmas, Ultra-High Temperature Ceramics: Materials for Extreme Environments Department of Materials Science and Engineering Missouri University of Science and Technology, Rolla, MO 65049, *Scr. Mater. 129* (2017) 94–99. https://doi.org/10.1016/j.scriptamat.2016.10.018.

[59] P. Zhao, J. Zhu, M. Li, G. Shao, H. Lu, H. Wang, J. He, Theoretical and experimental investigations on the phase stability and fabrication of high-entropy monoborides, *J. Eur. Ceram. Soc. 43* (2023) 2320–2330. https://doi.org/10.1016/j.jeurceramsoc.2023.01.026.

[60] P. Zhao, J. Zhu, Y. Zhang, G. Shao, H. Wang, M. Li, W. Liu, B. Fan, H. Xu, H. Lu, Y. Zhou, R. Zhang, A novel high-entropy monoboride (Mo0.2Ta0.2Ni0.2Cr0.2W0.2)B with super hardness and low thermal conductivity, *Ceram. Int. 46* (2020) 26626–26631. https://doi.org/10.1016/j.ceramint.2020.07.131.

[61] A. Salian, P. Sengupta, I. Vishalakshi Aswath, A. Gowda, S. Mandal, A review on high entropy silicides and silicates: Fundamental aspects, synthesis, properties, *Int. J. Appl. Ceram. Technol. 20* (2023) 2635–2660. https://doi.org/10.1111/ijac.14422.

[62] A.Y. Pak, P.S. Grinchuk, A.A. Gumovskaya, Y.Z. Vassilyeva, Synthesis of transition metal carbides and high-entropy carbide TiZrNbHfTaC5 in self-shielding DC arc discharge plasma, *Ceram. Int. 48* (2022) 3818–3825. https://doi.org/10.1016/j.ceramint.2021.10.165.

[63] Y. Yang, J. Bi, X. Gao, K. Sun, L. Qiao, G. Liang, H. Wang, Facile synthesis of nanocrystalline high-entropy diboride powders by a simple sol-gel method and their performance in supercapacitor, *Ceram. Int. 49* (2023) 19523–19527. https://doi.org/10.1016/j.ceramint.2023.02.170.

[64] Y.C. Shanshan Ning, Tongqi Wen, Beilin Ye, Low-temperature molten salt synthesis of high-entropy carbide, *J. Am. Ceram. Soc. 103* (2019) 2244–2251. https://doi.org/https://doi.org/10.1111/jace.16896.

[65] S. Ye, J. Zhu, P. Li, M. Li, N. Yan, H. Wang, Study on microstructure, mechanical properties and thermal performance of single-phase (Ti, Zr, Hf)B2 solid solution, *Mater. Today Commun. 34* (2023) 105228. https://doi.org/10.1016/j.mtcomm.2022.105228.

[66] D. Yu, J. Yin, B. Zhang, X. Liu, Z. Huang, Recent development of high-entropy transitional carbides: A review, *J. Ceram. Soc. Japan. 128* (2020) 329–335. https://doi.org/10.2109/jcersj2.19242.

[67] B. Li, C. Liu, Z. Fang, Z. Yang, F. Ding, L. Bai, C. Wang, F. Yuan, Synthesis of single-phase (ZrTiTaNbMo)C high-entropy carbide powders via magnesiothermic reduction process, *J. Eur. Ceram. Soc. 42* (2022) 6767–6773. https://doi.org/10.1016/j.jeurceramsoc.2022.08.025.

[68] Y. Qin, J.X. Liu, F. Li, X. Wei, H. Wu, G.J. Zhang, A high entropy silicide by reactive spark plasma sintering, *J. Adv. Ceram. 8* (2019) 148–152. https://doi.org/10.1007/s40145-019-0319-3.

[69] J. Xing, P. Foroughi, S. Mondal, S. Sun, Z. Cheng, Facile and economical routes toward novel high-entropy metal nitride high-temperature ceramic nanograin powders, *MRS Commun. 12* (2022) 183–187. https://doi.org/10.1557/s43579-022-00159-8.

[70] M. Qin, Q. Yan, H. Wang, C. Hu, K.S. Vecchio, J. Luo, High-entropy monoborides: Towards superhard materials, *Scr. Mater. 189* (2020) 101–105. https://doi.org/10.1016/j.scriptamat.2020.08.018.

[71] M. Qin, Q. Yan, Y. Liu, J. Luo, A new class of high-entropy M3B4 borides, *J. Adv. Ceram. 10* (2021) 166–172. https://doi.org/10.1007/s40145-020-0438-x.

[72] M. Qin, Q. Yan, H. Wang, K.S. Vecchio, J. Luo, High-entropy rare earth tetraborides, *J. Eur. Ceram. Soc. 41* (2021) 2968–2973. https://doi.org/10.1016/j.jeurceramsoc.2020.12.019.

[73] J. Liu, Q.Q. Yang, J. Zou, W.M. Wang, X.G. Wang, Z.Y. Fu, Strong high-entropy diboride ceramics with oxide impurities at 1800°C, *Sci. China Mater. 66* (2023) 2061–2070. https://doi.org/10.1007/s40843-022-2287-7.

[74] M. Qin, J. Gild, H. Wang, T. Harrington, K.S. Vecchio, J. Luo, Dissolving and stabilizing soft WB2 and MoB2 phases into high-entropy borides via boron-metals reactive sintering to attain higher hardness, *J. Eur. Ceram. Soc. 40* (2020) 4348–4353. https://doi.org/10.1016/j.jeurceramsoc.2020.03.063.

[75] S. Kavak, K.G. Bayrak, M. Mansoor, M. Kaba, E. Ayas, Ö. Balcı-Çağıran, B. Derin, M.L. Öveçoğlu, D. Ağaoğulları, First principles calculations and synthesis of multi-phase (HfTiWZr)B2 high entropy diboride ceramics: Microstructural, mechanical and thermal characterization, *J. Eur. Ceram. Soc. 43* (2023) 768–782. https://doi.org/10.1016/j.jeurceramsoc.2022.10.047.

[76] Z.J. Huang, L.F. Su, L. Xu, Y.Z. Zhou, W.M. Guo, H.T. Lin, Dense (Hf0.2Mo0.2Ta0.2Nb0.2Ti0.2)B2 ceramics prepared by pressureless sintering with Ni additives, *Ceram. Int. 49* (2023) 27651–27656. https://doi.org/10.1016/j.ceramint.2023.05.192.

[77] J. Gild, Y. Zhang, T. Harrington, S. Jiang, T. Hu, M.C. Quinn, W.M. Mellor, N. Zhou, K. Vecchio, J. Luo, High-Entropy Metal Diborides: A New Class of High-Entropy Materials and a New Type of Ultrahigh Temperature Ceramics, *Sci. Rep. 6* (2016) 37946. https://doi.org/10.1038/srep37946.

[78] Y. Wang, Processing and properties of high entropy carbides, *Adv. Appl. Ceram. 121* (2022) 57–78. https://doi.org/10.1080/17436753.2021.2014277.

[79] B.R. Golla, A. Mukhopadhyay, B. Basu, S.K. Thimmappa, Review on ultra-high temperature boride ceramics, *Prog. Mater. Sci. 111* (2020) 100651. https://doi.org/10.1016/j.pmatsci.2020.100651.

[80] B. Ye, T. Wen, M.C. Nguyen, L. Hao, C.Z. Wang, Y. Chu, First-principles study, fabrication and characterization of (Zr 0.25 Nb 0.25 Ti 0.25 V 0.25)C high-entropy ceramics, *Acta Mater. 170* (2019) 15–23. https://doi.org/10.1016/j.actamat.2019.03.021.

[81] H. Xiang, Y. Xing, F. Zhi Dai, H. Wang, L. Su, L. Miao, G. Zhang, Y. Wang, X. Qi, L. Yao, H. Wang, B. Zhao, J. Li, Y. Zhou, High-entropy ceramics: Present status, challenges, and a look forward, *J Adv Ceram 10*, 385–441 2021. https://doi.org/10.1007/s40145-021-0477-y.

[82] J. Liu, X. Shen, Y. Wu, F. Li, Y. Liang, G. Zhang, Mechanical properties of hot-pressed high-entropy diboride-based ceramics, *J. Adv. Ceram. 9* (2020) 503–510. https://doi.org/https://doi.org/10.1007/s40145-020-0383-8.

[83] J. Billingham, P.S. Bell, M.H. Lewis, Vacancy short-range order in substoichiometric transition metal carbides and nitrides with the NaCl structure. I. Electron diffraction studies of short-range ordered compounds, *Acta Crystallogr. Sect. A. 28* (1972) 602–606. https://doi.org/10.1107/S0567739472001524.

[84] X.X. Yu, G.B. Thompson, C.R. Weinberger, Influence of carbon vacancy formation on the elastic constants and hardening mechanisms in transition metal carbides, *J. Eur. Ceram. Soc. 35* (2015) 95–103. https://doi.org/10.1016/j.jeurceramsoc.2014.08.021.

[85] Beilin Ye, Shanshan Ning, Da Liu, Tongqi Wen, One-step synthesis of coral-like high-entropy metal carbide powders, *J. Am. Ceram. Soc. 102* (2019) 6372–6378.

https://doi.org/https://doi.org/10.1111/jace.16514.
[86] D. Demirskyi, T. Nishimura, T.S. Suzuki, Y. Sakka, O. Vasylkiv, K. Yoshimi, High-temperature toughening in ternary medium-entropy (Ta1/3Ti1/3Zr1/3)C carbide consolidated using spark-plasma sintering, *J. Asian Ceram. Soc. 8* (2020) 1262–1270. https://doi.org/10.1080/21870764.2020.1840703.
[87] S. Shivakumar, M. Qin, D. Zhang, C. Hu, Q. Yan, J. Luo, A new type of compositionally complex M5Si3 silicides: Cation ordering and unexpected phase stability, *Scr. Mater. 212* (2022) 114557. https://doi.org/10.1016/j.scriptamat.2022.114557.
[88] H. Liu, S. Ning, Fabrication of High-Entropy Disilicide Nanopowders via Molten Salt-Assisted Magnesium Thermal Reduction, *Res. Sq. Rapid Commun.* (2020) 1–9.
[89] Beilin Ye, Che Fan, Yangjie Han, Mengdong Ma, Synthesis of high-entropy diboride nanopowders via molten salt-mediated magnesiothermic reduction, *J. Am. Ceram. Soc. 103* (2020) 4738–4741. https://doi.org/https://doi.org/10.1111/jace.17184.
[90] W. Zhang, F. Guo, R. Zhang, D. Liu, X. Wang, X. Zhao, A simple route to synthesize high-entropy carbide (Hf0.2Zr0.2Ti0.2Ce0.2La0.2)C1-δ nanoparticles with large covalent radius difference, *Ceram. Int. 49* (2023) 38566–38574. https://doi.org/10.1016/j.ceramint.2023.09.189.
[91] Z. Zhang, S. Zhu, Y. Liu, L. Liu, Z. Ma, Phase structure, mechanical properties and thermal properties of high-entropy diboride (Hf0.25Zr0.25Ta0.25Sc0.25)B2, *J. Eur. Ceram. Soc. 42* (2022) 5303–5313. https://doi.org/10.1016/j.jeurceramsoc.2022.05.066.
[92] S. Failla, P. Galizia, S. Fu, S. Grasso, D. Sciti, Formation of high entropy metal diborides using arc-melting and combinatorial approach to study quinary and quaternary solid solutions, *J. Eur. Ceram. Soc. 40* (2020) 588–593. https://doi.org/10.1016/j.jeurceramsoc.2019.10.051.
[93] M. Xia, N. Lu, Y. Chen, B. Shen, X. Liang, Microstructures and mechanical properties of (Nb0.25Mo0.25Ta0.25W0.25)C and (Nb0.2Mo0.2Ta0.2W0.2Hf0.2)C high-entropy carbide ceramics produced by arc melting, *Int. J. Refract. Met. Hard Mater. 107* (2022) 105859. https://doi.org/10.1016/j.ijrmhm.2022.105859.
[94] S. Guan, W. Lin, H. Liang, W. Liang, Y. Tian, D. He, F. Peng, The effect of pressure tuning on the structure and mechanical properties of high-entropy carbides, *Scr. Mater. 216* (2022) 114755. https://doi.org/10.1016/j.scriptamat.2022.114755.
[95] D. Demirskyi, H. Borodianska, T.S. Suzuki, Y. Sakka, K. Yoshimi, O. Vasylkiv, High-temperature flexural strength performance of ternary high-entropy carbide consolidated via spark plasma sintering of TaC, ZrC and NbC, *Scr. Mater. 164* (2019) 12–16. https://doi.org/10.1016/j.scriptamat.2019.01.024.
[96] B. Du, X. Huang, A. Wang, Y. Liu, Y. Cheng, Structure evolutions of the polymer derived medium-/high-entropy metal carbides, *J. Alloys Compd. 939* (2023) 168737. https://doi.org/10.1016/j.jallcom.2023.168737.
[97] S. Iwan, K.C. Burrage, B.C. Storr, S.A. Catledge, Y.K. Vohra, R. Hrubiak, N. Velisavljevic, High-pressure high-temperature synthesis and thermal equation of state of high-entropy transition metal boride, *AIP Adv. 11* (2021). https://doi.org/10.1063/5.0045592.
[98] X. Wang, Y. Zuo, S. Horta, R. He, L. Yang, A. Ostovari Moghaddam, M. Ibáñez, X. Qi, A. Cabot, CoFeNiMnZnB as a High-Entropy Metal Boride to Boost the Oxygen Evolution Reaction, *ACS Appl. Mater. Interfaces. 14* (2022) 48212–48219. https://doi.org/10.1021/acsami.2c11627.
[99] S. Iwan, C.M. Lin, C. Perreault, K. Chakrabarty, C.C. Chen, Y. Vohra, R. Hrubiak, G. Shen, N. Velisavljevic, High-Entropy Borides under Extreme Environment of Pressures and Temperatures, *Materials (Basel). 15* (2022) 1–11. https://doi.org/10.3390/ma15093239.
[100] J. Cui, X. Zheng, W. Bao, J. Liu, F. Xu, G. Zhang, Y. Liang, Coexistence of Super hardness and Metal-Like Electrical Conductivity in High-Entropy Dodecaboride Composite with Atomic-Scale Interlocks, *Nano Lett. 2023 23*(20), 9319–9325. https://doi.org/10.1021/acs.nanolett.3c02506.
[101] X. Zheng, J. Cui, C. Gu, W. Bao, X. Zhou, J. Liu, G. Zhang, W. Zhang, Y. Zhao, S. Wang, Y. Liang, Scripta Materialia Superhard high-entropy dodecaboride with high electrical conductivity, *Scr. Mater. 220* (2022) 114938. https://doi.org/10.1016/j.scriptamat.2022.114938.

[102] P. Zhang, X. Liu, A. Cai, Q. Du, X. Yuan, H. Wang, Y. Wu, S. Jiang, Z. Lu, High-entropy carbide-nitrides with enhanced toughness and sinterability, *Sci. China Mater. 64* (2021) 2037–2044. https://doi.org/10.1007/s40843-020-1610-9.

[103] Z. Wen, H. Meng, S. Jiang, Z. Tang, Y. Liu, Y. Chu, Non-equimolar (Hf, Zr, Ta, W)B2 high entropy diborides enable superior oxidation resistance, *Sci. China Mater. 66* (2023) 3213–3222. https://doi.org/10.1007/s40843-023-2461-y.

[104] W. Zhang, L. Chen, W. Lu, S. Huo, B. Wei, Y. Wang, Y. Zhou, Non-stoichiometry of (TiZrHfVNbTa)Cx and its significance to the microstructure and mechanical properties, *J. Eur. Ceram. Soc. 42* (2022) 6347–6355. https://doi.org/10.1016/j.jeurceramsoc.2022.07.007.

[105] H. Lun, Y. Zeng, X. Xiong, Z. Ye, T. Qian, W. Sun, Y. Wang, Z. Chen, Synthesis of carbide solid solution with multiple components using elemental powder, *Adv. Powder Technol. 31* (2020) 505–509. https://doi.org/10.1016/j.apt.2019.10.019.

[106] F. Wang, F. Monteverde, B. Cui, Will high-entropy carbides and borides be enabling materials for extreme environments?, *Int. J. Extrem. Manuf. 5* (2023). https://doi.org/10.1088/2631-7990/acbd6e.

[107] Q. Xie, X. Liu, Z. Zhang, X. Nian, L. Chen, Investigation of mechanical and electronic properties of a novel quaternary transition-metal nitride Ti0.25W0.25V0.25Ta0.25N, *Mater. Chem. Phys. 310* (2023) 128467. https://doi.org/10.1016/j.matchemphys.2023.128467.

[108] M. Qin, S. Shivakumar, T. Lei, J. Gild, E.C. Hessong, H. Wang, K.S. Vecchio, T.J. Rupert, J. Luo, Processing-dependent stabilization of a dissimilar rare-earth boride in high-entropy (Ti0.2Zr0.2Hf0.2Ta0.2Er0.2)B2 with enhanced hardness and grain boundary segregation, *J. Eur. Ceram. Soc. 42* (2022) 5164–5171. https://doi.org/10.1016/j.jeurceramsoc.2022.05.034.

[109] A.C. Feltrin, F. Akhtar, High-temperature oxidation kinetics of a metastable dual-phase diboride and a high-entropy diboride, *J. Eur. Ceram. Soc. 43* (2023) 7363–7372. https://doi.org/10.1016/j.jeurceramsoc.2023.08.001.

[110] W. Zhang, K. Li, L. Chen, Z. Shi, S. Huo, B. Wei, S.J.L. Kang, Y. Wang, Y. Zhou, The phase decomposition in non-equimolar (ZrHfVNbMoW)Cx complex concentrated carbides via carbon content regulation, *J. Eur. Ceram. Soc. 44* (2023) 1396–1403.https://doi.org/10.1016/j.jeurceramsoc.2023.10.050.

[111] Y. Qin, J.X. Liu, Y. Liang, G.J. Zhang, Equiatomic 9-cation high-entropy carbide ceramics of the IVB, VB, and VIB groups and thermodynamic analysis of the sintering process, *J. Adv. Ceram. 11* (2022) 1082–1092. https://doi.org/10.1007/s40145-022-0594-2.